SEISMOLOGICAL INVESTIGATION OF THE MECHANICAL PROPERTIES OF A HOT DRY ROCK GEOTHERMAL SYSTEM

by

Michael Fehler

B.A., Reed College, Portland, Oregon

(1974)

SUBMITTED IN PARTIAL FULFILLMENT

OF THE REQUIREMENTS FOR THE DEGREE OF

DOCTOR OF PHILOSOPHY

at the

April, 1979

Signature of Author.....
Department of Earth and Planetary Sciences
April 1979

Certified by.....
Thesis Supervisor

Accepted by.....
Chairman, Departmental Committee on Graduate Students

SEISMOLOGICAL INVESTIGATION OF THE MECHANICAL PROPERTIES OF A HOT DRY ROCK GEOTHERMAL SYSTEM

by

Michael C. Fehler

Submitted to the Department of Earth and Planetary Sciences on April , 1979, in partial fulfillment of the requirements for the degree of Doctor of Science

ABSTRACT

High frequency (8-15 KHz) seismic waves that travel between two boreholes are used to probe the detailed structure of rock in the Los Alamos Scientific Laboratory Fenton Hill geothermal energy reservoir. Because of the unique ability to control fluid pressure in the reservoir, we can make in situ seismic measurements at different fluid pressures and apply the results of pertinent laboratory measurements and theoretical models of rock containing cracks to the velocity and attenuation data obtained.

Two theoretical problems involving the interaction of seismic waves with a fluid-filled crack are studied. First the reflection and transmission of plane P and S waves incident on a fluid layer imbedded between two elastic half spaces are studied as a function of fluid layer thickness, fluid viscosity, elastic properties of fluid and solid as well as angle of incident wave. It is found that a water layer as thin as 1 mm can have a strong effect on seismic waves in the kilohertz frequency range. Transmission is frequency dependent in the range 8-15 KHz if layer thickness is greater than 1 mm. Secondly diffraction of plane P and S waves by finite two dimensional empty and fluid-filled (zero viscosity) cracks as a function of wavelength and direction of incident wave is studied. Wavelengths on the scale of the crack length are considered.

Laboratory measurements of velocity on dry cores removed from the geothermal well at the time of drilling are modeled using techniques developed by Cheng (1978) to determine the pore aspect ratio spectrum. Then, velocity vs. effective pressure for water-saturated core samples is predicted using the pore aspect ratio spectrum.

A total of 16,800 seismograms from two dual well seismic experiments, separated in time by one year, are studied. Each experiment was broken into steps where receiver was stationary in one borehole and source traversed a section of the other borehole firing at equal intervals of time. Arrival times of direct P waves traveling between two boreholes are picked by a computer algorithm developed to handle the large quantity of data available. Travel time variations due to changes in fluid pressure vary with location of source along the borehole. The variation is smooth in the periphery and becomes rough, with scale length as short as three meters, in the middle of the heat extraction region. Travel time data are inverted to find in situ velocity at two different pressure conditions. Velocity is found to be lower than predicted from estimations for core samples and is interpreted to be due to increase in porosity of microcracks due to heat extraction. Velocity decreases linearly with change in in situ temperature at a rate of 1.07 (km/sec)/100°C. The linear decrease in velocity leads to the important conclusion that P wave velocity can be used as an effective measure of change in temperature during operation of the geothermal system. In situ pore aspect ratio spectra are estimated from measurements of velocity at two effective pressures using Cheng's technique. Attenuation is predicted using results of O'Connell and Budiansky (1977). Microcrack compressibility is computed from pore aspect ratio spectrum and found to be too large to be consistent with the time dependence of fluid flow between the two boreholes and is interpreted to mean that some flow occurs along large fractures whose volumes do not change at the low fluid pressures used during flow experiments.

Spectral amplitudes of individual seismograms show little correlation even for differences in source spacing as small as 20 cm, but show a smooth decay in envelope of amplitude when averaged over many seismograms. A single scattering approach explains

well the observed change in amplitude spectrum vs. time for signals recorded, when no artificial fluid pressure is applied, in a region removed from the center of heat extraction. For signals traversing the low velocity medium in the heat extraction region a diffusion model of energy propagation adequately models the data and is used to estimate Q of seismic waves. A jump in average spectral amplitude is found for waves traversing a region on the periphery of the reservoir. The jump is interpreted as energy reflected off some inhomogeneity but the inhomogeneity cannot be located precisely because these arrivals are not coherent enough for an effective stacking.

Loss of high frequency content of direct arriving P waves during the second dual well seismic experiment is compared with observed Q found from the coda part and also with the theoretical results on frequency dependence of transmission through a water-filled fracture to determine the minimum number of large fractures in the system. Two to four fractures with thickness about 4 mm and vertical extent of as much as 200 meters are required to explain observations during the second experiment. Effective transmission of high frequencies observed during the first experiment is interpreted as meaning that fracture thickness was less than 1 mm at that time. Increased fracture thickness during the second experiment is probably due to a 75 day period of heat extraction during which in situ temperature dropped by as much as 100°C below the virgin temperature. Since coefficient of linear thermal expansion for granite is approximately 10^{-5}/°C, a decrease in temperature of 100°C in a region on the order of one meter around the fracture is required to explain the increased fracture thickness.

Acknowledgements

Many friends contributed to this work. Although it is impossible to thank them all or to list the contributions of each I will try to mention a few.

It has been a great privilege to work with Kei Aki over the last few years. He has always been accessible and eager to talk about my work and very stimulating to converse with. He showed great enthusiasm for my results and his keen insight added greatly to this thesis. To Kei go my deepest thanks.

I also had the honor of working part time with Gene Simmons on a project that seemd to have no end. I learned a lot about rock mechanics and other aspects of geophysics from Gene and I thank him for his patience and effort.

During my stay at M.I.T. I had two cell mates who spent many long nights in the office working with me and whose friendship was very important to me during my graduate student years. Shamita Das helped me during my first two years by encouraging me when I felt down as well as through many discussions about this work and other areas of geophysics. When Shamita graduated, I felt destined to spend the rest of my nights alone in the office. Fortunately Steve (stinks) Taylor, whose

desire for self punishment through long work hours usually exceeded mine, moved into my office. Steve proved to be an excellent source of information about practical seismology and had great patience at explaining and reexplaining geology to me. Steve's presence was a great inspiration to me, and I thank him deeply for his friendship.

Many of my fellow graduate students contributed to my M.I.T. experience and in one way or the other helped with this thesis. Dr. Arthur Cheng spent countless hours discussing different aspects of rock mechanics with me and allowed me to use his velocity modeling programs. Arthur also served as my sports advisor, keeping me informed of all the many happenings in the world of sports. Dr. David H. Johnston, being the local Q expert, provided many useful conversations and finally made a copy of his thesis available to me so I could examine laboratory measurements of Q. Clifford Thurber and Wook Lee were my quiet office partners whose presence often reminded me that I should shut up occasionally and think. They also provided useful feedback during various stages of this work. Other members of the fifth floor gang whose conversations helped me through the years include Jim Muller, Tony Shakal, Sara Brydges, Randy Richardson, George Zandt and Roger Buck. I also benefitted greatly

from conversations and field work in Hawaii with Bernard Chouet. I would like to thank Al Taylor, a charter fifth floor member, for allowing me to read his newspaper every day as well as for much assistance during my stay at M.I.T.

Jan Sedlacek has been my hiking partner for many years now and has encouraged and assisted me in many ways. I hope we can continue to find mountains where we can meet, explore and refresh our minds.

My cat, Nea, deserves credit for being a faithful friend, always happy to see me arrive home no matter what my mood.

This work would never have come about if it had not been for my fruitful interactions with members of the geothermal energy development group at Los Alamos Scientific Laboratory. I would especially like to thank Jim Albright for his maintaining contact with me and assisting me in many ways. I would also like to thank Jim's family for their kind hospitality during my many visits at Los Alamos. Other members of the Los Alamos group G-3 who contributed ideas and stimulating discussions include Jeff Tester (group leader), Bob Potter, Rod Spence and Lee Aamodt. Roscoe Butler did a fantastic job of preparing computer tapes of data for me and his efforts are greatly appreciated. Doris Elsner was always very helpful in arranging my trips to LASL and

was interesting to talk with. The data collection at Fenton Hill was done by the devoted workers of LASL Group G-4 under the direction of Bert Dennis.

Lisa Supinski typed every word that appears in this thesis. She also checked some of my grammar and proofread what she typed. Her assistance and cheerful spirit were of great help to me in finishing this work. Thank you very much!

I would like to thank my family for their optimistic outlook and encouragement. I would never have made it here without their support.

I was supported during part of my stay at M.I.T. by a DuPont graduate fellowship. This work was supported by U.S. Department of Energy Contract EY-76-S-02-2534. Los Alamos Scientific Laboratory of the University of California also supported this work.

TABLE OF CONTENTS

Page

Abstract 1

Acknowledgements 4

Chapter 1. Introduction 12

Figures

Chapter 2. Direct Detection of Hydrofractures Using Active Seismic Techniques 28

2.1 Interaction of Waves with a Viscous Liquid Layer of Infinite Extent

2.1.1 Plane Waves in Elastic Media

2.1.2 Plane Waves in Viscous Media

2.1.3 Incident SH Waves

2.1.4 P Waves at Normal Incidence

2.1.5 P and SV Waves at Arbitrary Angle of Incidence

2.2 Interaction of Waves with a Finite Crack 50

2.2.1 Diffraction by an Empty Crack: Boundary Conditions

2.2.2 Boundary Conditions for a Fluid-filled (zero viscosity) Crack

2.2.3 Method of Solution

2.2.4 Results of the Calculation

Tables 73

Figures 75

Page

Chapter 3. Physical Properties of Rocks: Data and Theory Relevant to a Hot Dry Rock Geothermal System 108

3.1 Effects of Microcracks on the Elastic Properties of a Rock

3.1.1 Effects of Microcracks on Compressibility

3.1.2 Effects of Microcracks on Velocity of Seismic Waves in a Rock

3.2 Attenuation of Seismic Waves in Cracked Solids

3.3 Pore Pressure Effects on Mechanical Properties of Rocks

3.4 Effects of Changes in Temperature on Physical Properties of Rocks

3.5 Permeability

3.6 Laboratory Data on Rocks from the Fenton Hill Geothermal System

3.6.1 Modeling of Laboratory Data to Obtain Pore Aspect Ratio Spectrum

3.6.2 Prediction of Attenuation from the Pore Aspect Ratio Spectrum

Tables 145

Figures 150

Chapter 4. Analysis of Seismic Data Obtained During Dual Well Seismic Experiments at the Fenton Hill Geothermal Test Site 163

4.1 Dual Well Seismic Experiment

4.1.1 Purpose of the Dual Well Seismic Experiment

4.1.2 Design of the Experiment

4.1.3 In situ Conditions at the Time of the Experiment

Page

4.2 Analysis of Data by LASL

4.3 P Wave Velocity

4.3.1 Method of Finding Velocity

4.3.2 Results of Velocity Determination

4.4 Spectral Analysis of Seismograms

4.4.1 Direct P Waves

4.4.2 Amplitude Spectra for Consecutive Time Windows

4.5 Stacking of Seismograms

4.6 Summary

Tables 216

Figures 217

Chapter 5. Discussion and Conclusion 264

5.1 Scattering

5.1.1 Single Scattering

5.1.2 Multiple Scattering

5.2 Microcracks

5.3 Modeling the Seismic Response of the Fenton Hill Geothermal System

5.4 Conclusions and Suggestions for Further Work

Tables 302

Figure 314

References 316

Appendix A. Finite Difference Method 328

Figure

Appendix B. Method of Picking Arrival Times 333

Page

Appendix C. Damped Least Squares Inversion 538

Biographical Note

CHAPTER I

INTRODUCTION

The concept of a Hot Dry Rock geothermal system provides the possibility of extracting energy virtually from anywhere a hole can be drilled into the ground (Cummings, Morris, Tester, Bivins, 1979). Figure 1 shows a conceptual diagram of a Hot Dry Rock geothermal system. Two holes are drilled into low permeability crystalline basement rock to a depth where the desired temperature of rock is found. In order to create a large surface area for heat transfer from the rock to circulating fluid, a hydrofracture is created from one of the boreholes. Once the position of the hydrofracture is determined, the second hole is directionally drilled to intersect the fracture. With both holes connected to the fracture, a circulation loop may be set up where cold water is pumped down one borehole into the fracture where the water is heated and then out the second borehole to the surface. Such a system is currently being developed at the Los Alamos Scientific Laboratory (LASL).

One of the biggest problems encountered by workers at LASL is determining the location of a hydrofracture with sufficient accuracy that a second hole may be drilled to intersect it. In addition, knowledge of mechanical

properties of rock in the vicinity of the hydrofracture would be of great help in understanding flow of fluid and heat exchange in the system. Of all non-destructive methods available for finding information about location of a hydrofracture as well as mechanical properties of the rock that contains the fracture, the seismic technique seems to be the most appropriate. For this reason, LASL has devoted a great deal of effort to developing seismology as a tool to solve their problems. It was initially speculated that surface sources and receivers could be used to locate an artificially induced hydrofracture. Unfortunately the short wavelength waves necessary to delineate these features were so severely attenuated when they propagated through the low Q rock near the surface that little information could be obrained from them. It took some time to develop seismic sources and receivers that could operate at the high temperatures encountered in a geothermal environment for a sufficient length of time to allow collection of enough high quality seismic data to justify extensive analysis. An important improvement in the acquisition of seismic data for study of Hot Dry Rock reservoirs was the development of a piezoelectric source-receiver combination by Dresser Atlas Company that could operate at temperatures up to 200°C. This equipment facilitated collection of large quantities

of seismic data.

The LASL geothermal test site is located just west of the Valles Caldera in northern New Mexico. Figure 2a shows the location of the Caldera in New Mexico as well as some of the structural features in the vicinity of the caldera. Figure 2b is a more detailed diagram of the caldera. The Hot Dry Rock site is labeled Fenton Hill in this figure. The Valles Caldera is a region of high heat flow that is related to recent (< .1 m.y.) volcanic activity (Laughlin and Eddy, 1977). The high heat flow makes the region a prime candidate for the development of geothermal energy. In fact, Union Oil Company is presently installing a hydrothermal geothermal system inside the Valles Caldera (see Figure 2b).

LASL currently has two holes drilled into Precambrian crystalline basement beneath Fenton Hill. Both holes extend to a depth of about 3 km (10,000 ft) below the surface. Figure 3 (from Pettitt, 1978) shows a plan view section of the two boreholes. Hole named EE-1 was drilled to a depth of 3.048 km (10,000 feet) below the surface and is the hole from which the hydrofracture originates. Hole GT-2 was originally drilled to a depth of about 9500 feet. In 1977 a new section of GT-2, labeled GT-2A in Figure 3, was drilled beginning at about 8100 feet below the surface

in GT-2. This redrilling was done in an attempt to intersect the fracture that originated from EE-1. GT-2A apparently passed over the top of the fracture so another attempt, GT-2B, was made to intersect the fracture. Hole GT-2B was successful in that flow properties of the system were greatly improved over flow properties of the original GT-2/EE-1 system. Throughout this thesis, reference to hole GT-2 at depths below about 8100 feet (2.5 km) refers to GT-2B in Figure 3 as this is the only section of borehole below this depth that is currently accessible.

The dual wellbore system created at Fenton Hill provides an excellent in situ laboratory for the study of rock properties. The use of high frequency (5-15Khz) signals generated by the Dresser Atlas source enables detailed structure of the rock between the boreholes to be probed.

Workers at LASL have performed many seismic experiments at Fenton Hill. Most of their experiments and results are described in their annual reports (Blair et al., 1976; LASL HDR staff, 1978). A discussion of some of their findings during the first seismic experiment using Dresser Atlas equipment may be found in Albright et al.(1978). Their results also are discussed briefly in Chapter 4.

This thesis is concerned with both theoretical and

experimental aspects of the application of seismology to problems in a Hot Dry Rock geothermal system. In Chapter 2, two theoretical problems are discussed. The first problem is the interaction of high frequency seismic waves with a fluid layer of finite viscosity. A hydrofracture is considered to be a plane layer of water of finite thickness but infinite extent. Amplitudes of transmitted and reflected waves are found as a function of fluid layer thickness, fluid viscosity and bulk modulus, elastic properties of the solid surrounding the fluid as well as frequency, angle of incidence and type of incident wave. In the second part of Chapter 2, the effects of the finite size of the hydrofracture are considered. The fracture is modeled as a crack in an infinite, isotropic elastic medium. Inside of the crack may be empty or filled with a zero viscosity fluid. Interaction of waves of wavelength on the scale of the crack length are studied using a finite difference scheme.

Chapter 3 contains a review of experimental and theoretical studies on mechanical properties of rock with emphasis on results relevant to Hot Dry Rock geothermal energy. Various models of mechanical properties are discussed. The method of Cheng (1978) is used to predict seismic velocities of fluid saturated rocks as a function of effective pressure using laboratory measure-

ments of velocity of samples from the LASL geothermal test site (Trice and Warren, 1977). Seismic attenuation as a function of frequency and effective pressure is predicted using results of O'Connell and Budiansky (1977).

Data obtained using Dresser Atlas logging tools in a dual wellbore configuration at the LASL Hot Dry Rock test site is presented in Chapter 4. Two nearly identical experiments, separated in time by one year, were performed. In situ conditions at the time of the experiments are described. A method to pick P arrival times on the large number of seismograms available from each experiment is developed. Using the large number of arrival times enables very accurate determination of in situ P wave velocity. Velocities are determined at different locations in the geothermal reservoir and for two values of fluid pressure. In one case pressure is due only to the weight of the column of water in the borehole. In the other, fluid pressure in one borehole is artificially increased by 100 bars. Changes in rock velocity resulting from removing heat from rock during the one year interval between the two experiments are found. Spectral analysis of direct P waves recorded for two effective pressures enables some constraints to be put on amount of attenuation of waves by the rock. Values of Q are found by computing the rate of decay of a given spectral component of the signal with time.

Seismograms are stacked in an attempt to find locations of scatterers that reflect coherent energy.

In Chapter 5 data is discussed in terms of its meaning about the properties in situ at the LASL geothermal test site. The seismic data collected at Fenton Hill will be discussed from three different viewpoints. First, some character of the seismograms is attributed to scattering by heterogeneities with scale length comparable to wavelength ($\sim$50 cm). Secondly, the seismic velocity and attenuation data will be interpreted in terms of microcracks with size much smaller than the wavelength. Using Cheng's (1978) technique the pore aspect ratio spectra of rocks will be estimated from the in situ velocity measurements. Finally, we trace the evolution of the model of the Hot Dry Rock geothermal reservoir from a single hydrofracture with dimension of up to 1 kilometer in otherwise impermeable rock to a system of two or more hydrofractures in heterogeneous rock whose microcrack porosity and permeability increases as heat is extracted. Major conclusions of the thesis are then summarized and proposals made for experiments that would aid in further understanding the complex structure now present in the Fenton Hill geothermal reservoir.

Figure Captions

Figure 1. Conceptual diagram of a manmade Hot Dry Rock geothermal system (from Pettitt, 1976).

Figure 2. (a) Major structural features in the vicinity of the Los Alamos Scientific Laboratory Hot Dry Rock site near the Valles Caldera, New Mexico (from Pettitt, 1978).

(b) Simplified map of Valles Caldera showing some major geologic features. Geothermal site is located at Fenton Hill (from Pettitt, 1976).

Figure 3. Plan view of lower section of EE-1 and GT-2 wellbores. Section labeled GT-2B is only section of borehole GT-2 that is currently accessible (from Pettitt, 1978).

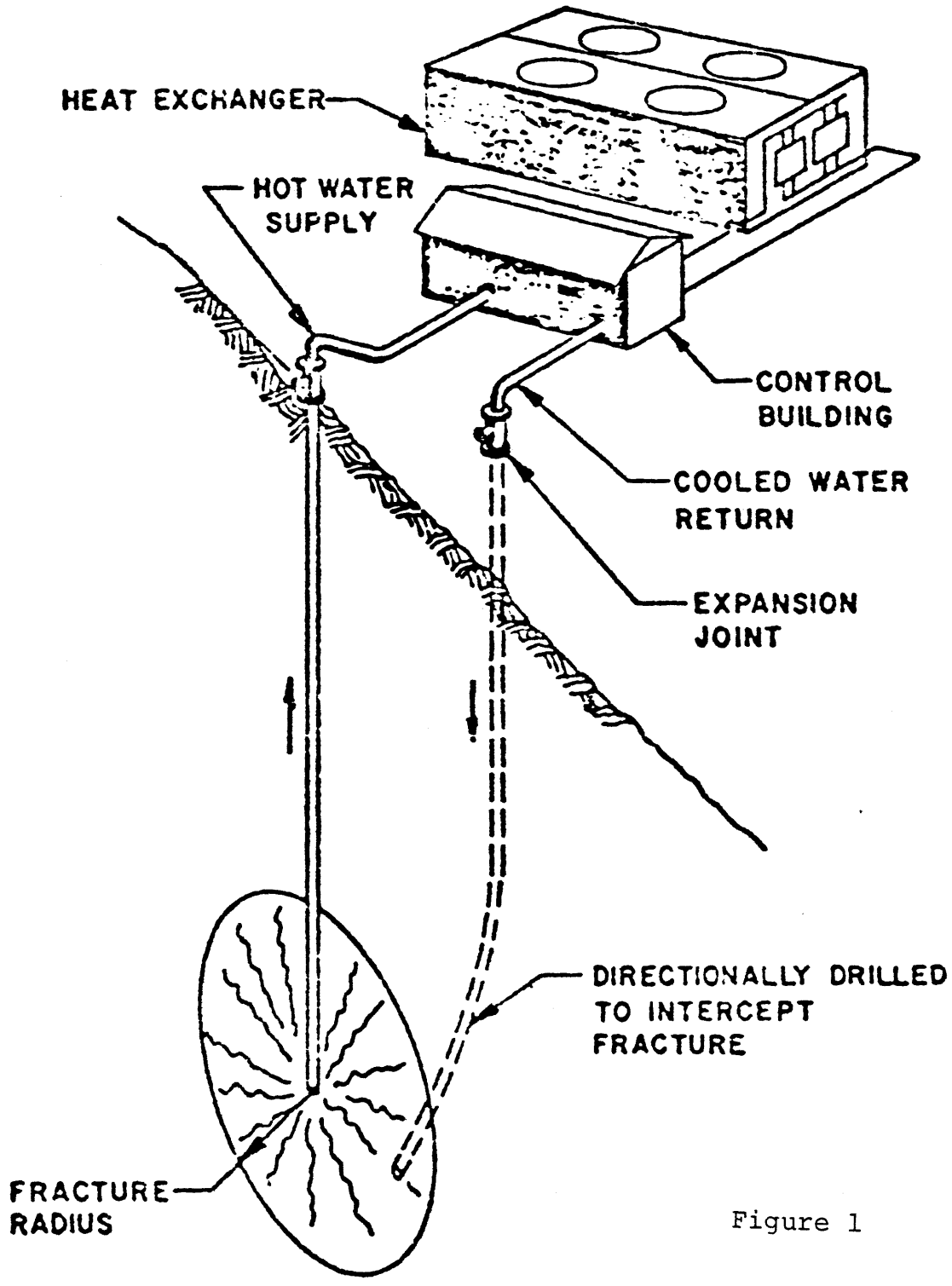
HEAT EXCHANGER
HOT WATER SUPPLY
CONTROL BUILDING
COOLED WATER RETURN
EXPANSION JOINT
DIRECTIONALLY DRILLED TO INTERCEPT FRACTURE
FRACTURE RADIUS

Figure 1

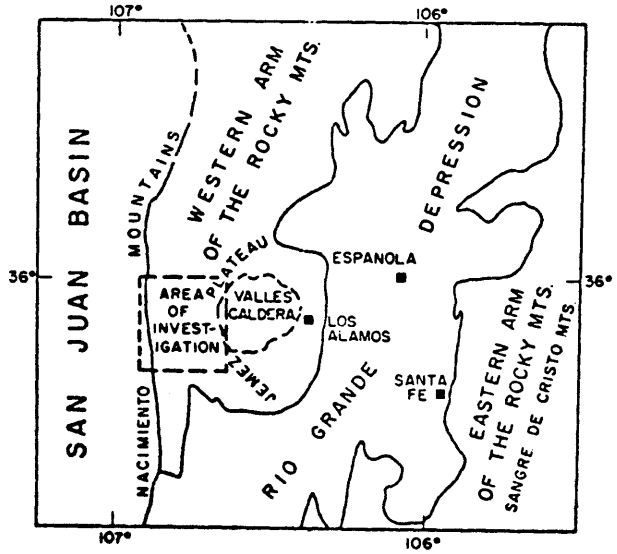

Figure 2a

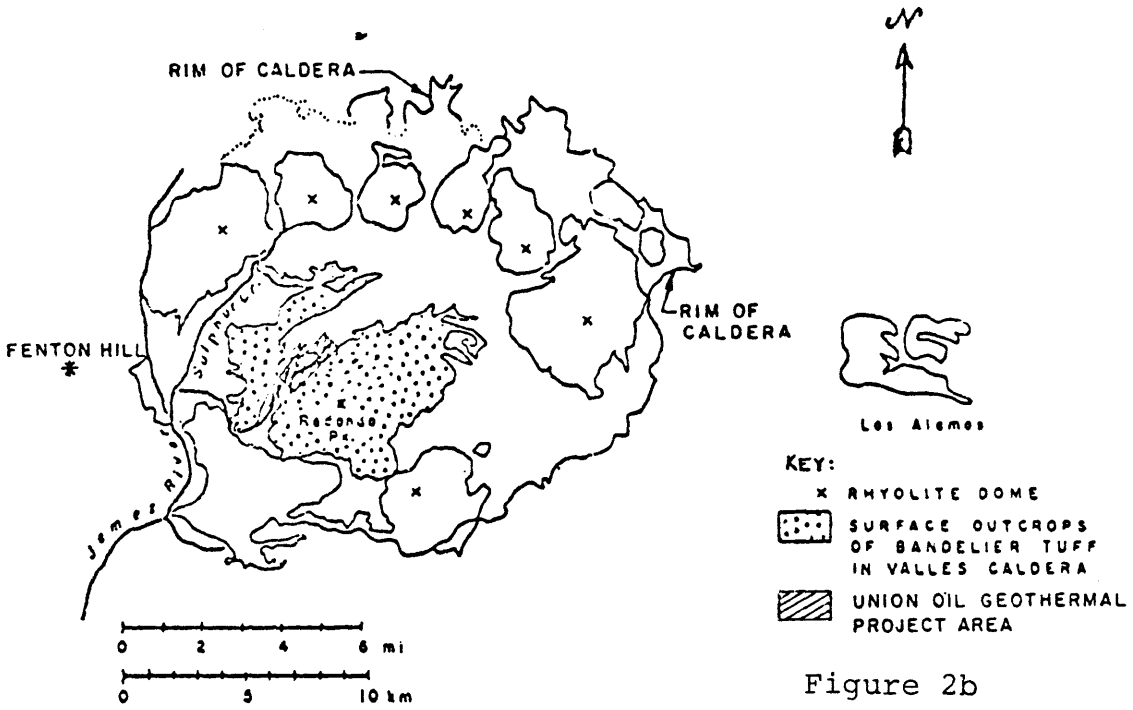

Figure 2b

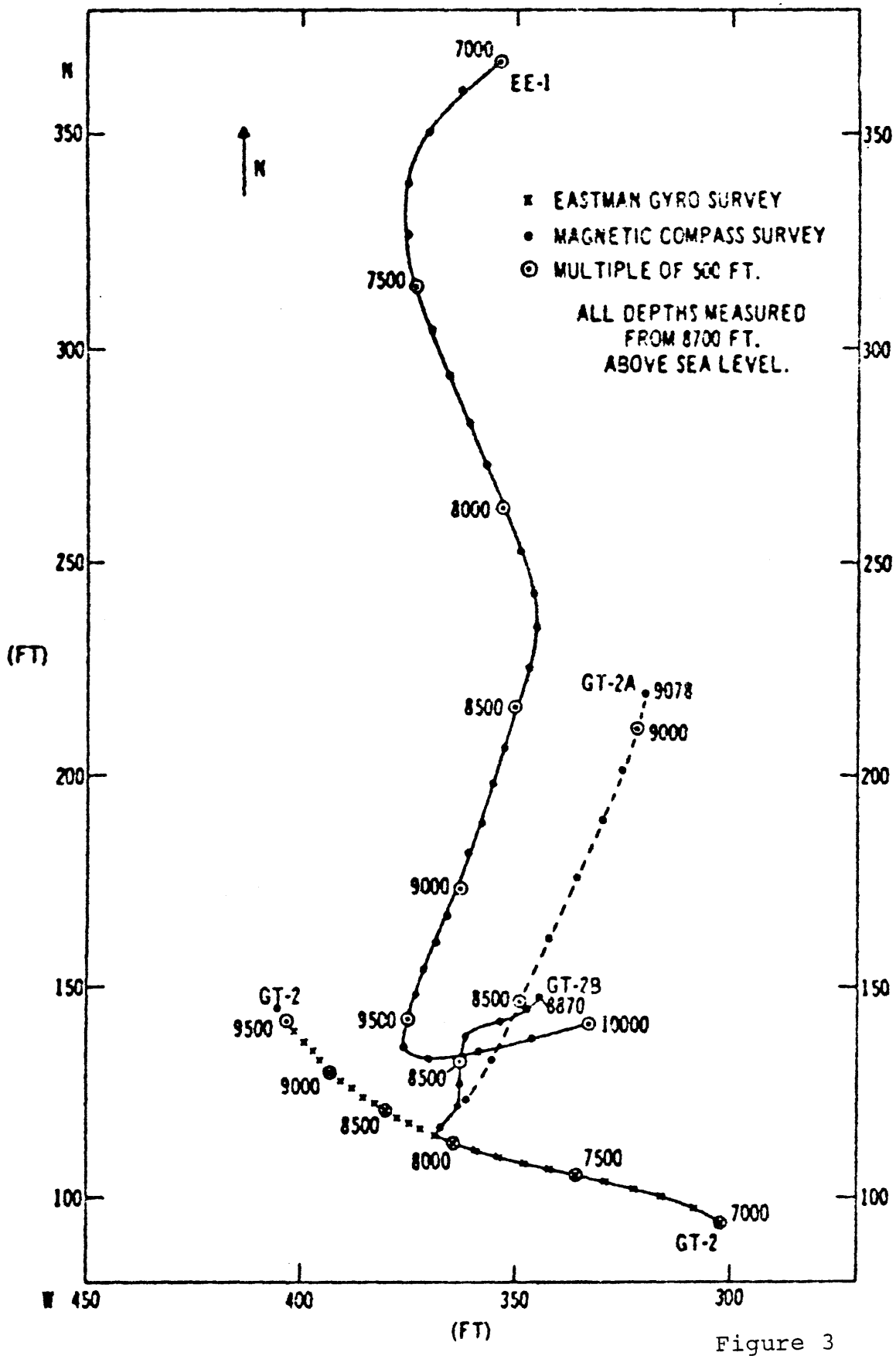
N
350
300
250
200
150
100
(FT)
W 450
400
350
300
(FT)
7000
EE-1
7500
8000
8500
9000
9500
10000
GT-2A
9078
GT-2B
8870
GT-2
9500
9000
8500
8000
7500
7000
GT-2
EASTMAN GYRO SURVEY
MAGNETIC COMPASS SURVEY
MULTIPLE OF 500 FT.
ALL DEPTHS MEASURED
FROM 8700 FT.
ABOVE SEA LEVEL.

Figure 3

CHAPTER 2

DIRECT DETECTION OF HYDROFRACTURES USING ACTIVE SEISMIC TECHNIQUES

Use of active seismic techniques provides the opportunity to carefully plan and execute an experiment so that data can be collected that is most easily interpreted. Seismic signals generated by artifical sources have been studied to obtain much information about the shallow structure of the earth's crust. Traditional applications of active techniques include reflection and refraction studies to determine crustal structure as well as for finding oil and gas. Well logging using artifical seismic sources is often used to map the fine scale structure of a formation that is cut by a borehole.

Two techniques using active seismology that have been proposed to locate hydrofractures will be discussed in this chapter. Both techniques involve studying the direct effect of a hydrofracture on the amplitude or phase of a wave. If the two opposite surfaces of a hydrofracture are considered to be completely out of contact with each other, the fracture represents a local discontinuity in elastic properties of the medium that contains the fracture. The magnitude of effect of this local change in elastic properties on seismic waves will depend on the length and thick-

ness of the hydrofracture, physical properties of the fluid filling the fracture, wavelength and type of waves (P or S) incident as well as the angle that the incident wave makes with the plane of the fracture. Incident waves are considered to be monochromatic plane waves. Once a solution for plane waves is obtained, the solution for an incident wave consisting of many frequencies or a curved wavefront can in principle be found by superposing plane wave solutions using Fourier Transforms and techniques for representing curved wavefronts as superpositions of plane waves.

The first approach that will be discussed is to consider the fracture as a planar layer of viscous fluid of infinite extent in two dimensions that is sandwiched between two homogeneous isotropic elastic half spaces. Waves are incident from one side of the layer and amplitudes of waves traveling away from the layer are computed. See Figure 1. The effects of the finite length of the fracture are ignored. If the wavelength of the incident wave is small compared to the length of the fracture and if measurements are made well away from the edges of the fracture, the effects of the edges are small and can be ignored. The problem described can be solved using analytic methods up to a point where a matrix inversion is required. The matrix equation is solved on a computer.

When the wavelength of an incident wave is of the

same scale as the length of the fracture, the finite size of the crack must be considered when computing the interaction of the wave with the fracture. The case of incident waves of wavelength on the order of the cracklength has been studied using a finite difference solution of the wave equation. Diffraction of waves by an empty two-dimensional crack are studied. In addition, an approximate solution is obtained when the crack is fluid-filled in order to study the effects of the finite compressibility of the fluid in the hydrofracture.

2.1 Interaction of Waves with a Viscous Liquid Layer of Infinite Extent

In this section a hydrofracture is assumed to be a planar layer of viscous fluid that has constant but finite thickness in one dimension and is infinite in the other two directions. This model is an approximation to a true hydrofracture that is valid so long as the wavelength of the incident wave is small compared to the crack size and the point of observation is well away from the edges of the crack. Experiments where the above conditions are met will be referred to as shadowing or reflection-transmission experiments because certain types of waves will be unable to be transmitted through the fracture, or shadowed by the fracture.

The method of solving for transmitted and reflected

waves resulting when a wave is incident on an interface is well known (Ewing, Jardetzky and Press, 1957; Brekovskikh, 1960). The extension to layered media was first done by Thomson (1950) and the method was used to compute surface wave dispersion by Haskell in 1953. Improvements in the accuracy of the matrix propagator method for high frequency waves were made by Dunkin (1965), Knopoff (1964) and more recently by Abo-Zena (1978). A study of the transmission of plane waves through layered viscoelastic material was made by Shaw and Bugl in 1968. They pose the problem in terms of stress and displacements rather than potentials and study the conditions for the existence of interface waves. Biswas (1967) studied the transmission of SH waves through a viscoelastic layer imbedded between two elastic half spaces and concluded that the effect of the imaginary components of elastic properties on the transmission of waves increases as the frequency increases. Borcherdt (1973) made a general study of plane waves in a linear viscoelastic media and discussed the types of plane waves that can propogate in such media. He derived an energy balance equation for these waves. In this study, the fluid is viscous rather than viscoelastic. By this it is meant that the fluid is characterized by a bulk modulus which is a real quantity and a viscosity that describes how the fluid will respond in shear. The elastic shear modulus of the fluid is set equal to zero.

Figure 1 shows the geometry of the problem that will be solved. In this case a plane P wave of amplitude P_{inc} is incident on the fluid from the solid at angle γ from the plane of the fluid. At each fluid-solid contact both reflected and transmitted waves are generated. A reflected P wave of amplitude P_{ref} travels away from the fluid at angle γ . A reflected S wave of amplitude S_{ref} travels away from the fluid at an angle θ given by Snell's law. The fluid is considered to have a finite viscosity so there will be both P and S waves in the fluid. These waves can be expressed as upgoing (traveling in -Z direction) and downgoing (traveling in +Z direction) waves. P and S waves leave the fluid traveling in the -Z direction. These are labeled P_{trans} and S_{trans} respectively. Physical properties of the solid are given by λ, μ, ρ where λ and μ are Lame's parameters (μ = rigidity) and ρ is rock density. The fluid is described by η, the viscosity, κ, the bulk modulus, and ρ', the fluid density.

2.1.1 Plane Waves in Elastic Media

Figure 2 shows the three types of plane waves that will be discussed. A P wave is a longitudinal wave with particle motion parallel to the direction the wave propagates. Shear or S waves are those in which particle motion is perpendicular to the direction of travel. Since the perpendicular to the direction of travel defines a

plane, study of the interaction of waves with plane boundaries is made easier if S waves are further classified by the vector components of the associated particle motion. The directions of the vectors are chosen according to the direction of the boundary to be studied. An SH wave is one whose particle motion is parallel to the interface under study. SH stands for horizontally polarized shear. The name clearly applies if the boundary under study is horizontal, e.g., the surface of the earth. A SV wave (vertically polarized shear) is one whose particle motion is perpendicular to the SH particle motion and to the direction of wave propagation. Generally a shear wave is a combination of SH and SV waves. The advantage of the classification of S waves when studying plane boundaries lies in the fact that a SH wave interacts with the boundary to produce only SH waves--no P or SV waves are generated. This is because the SH wave particle motion is in a direction unique to the P and SV waves so that no coupling of motion to these waves can occur. P and SV waves can couple so that study of their interactions with boundaries is generally more complicated than if only SH waves are present. In this study, SV and SH waves will be defined as if the fluid layer were horizontal in the earth, regardless of whether or not the hydrofracture is or is not horizontal.

The elastic wave equation for displacements in three

dimensions can be broken into four second order differential equations if displacements are defined in terms of potential functions

$$\vec{U} = \nabla\phi + \nabla x\vec{\Psi} \tag{1}$$

where $\vec{U}$ is the displacement vector, ϕ is a scalar potential that describes P waves and $\vec{\Psi}$ is a vector potential that describes S waves. The equations that ϕ and Ψ_i must satisfy are

$$\rho\frac{\partial^2\phi}{\partial t^2} = (\lambda+2\mu)\ \nabla^2\phi \tag{2}$$

$$\rho\frac{\partial^2\Psi_i}{\partial t^2} = \mu\nabla^2\Psi_i \tag{3}$$

where ρ = density, μ = rigidity and λ is a Lame parameter. For the case of P or SV waves incident with the coordinate system shown in Figure 1 displacements are only in the X and Z directions so that $\Psi_1 = \Psi_3 = 0$. For the case of SH wave incident there is motion only in the Y direction so that $\Psi_2 = 0$.

Plane wave solutions to equations (2) and (3) are of the form

$$\phi,\Psi = F(\omega t - \vec{k}\cdot\vec{x}) = A\exp\{i\omega t - ikx\cos\delta - ikz\sin\delta\} \tag{4}$$

where A is the amplitude of the wave, k is the wavenumber equal to 2π/wavelength and δ is the angle the propagation

vector makes with the X axis and ω is angular frequency.

2.1.2 Plane Waves in Viscous Media

To obtain the appropriate equations that must be satisfied in a viscous medium first replace λ by $\kappa - 2/3\mu$ where κ is the bulk modulus of the fluid. Using the correspondence principle (Ewing, Jardetsky and Press, 1957) the effect of the viscosity of the fluid is accounted for by replacing μ by the operator $\eta\frac{\partial}{\partial t}$ where η is the fluid viscosity. The equation for wave propagation in a viscous medium is

$$\rho'\frac{\partial^2\phi}{\partial t^2} = \kappa\nabla^2\phi + 4/3\eta\frac{\partial}{\partial t}\nabla^2\phi \qquad (5)$$

$$\rho'\frac{\partial^2\Psi_i}{\partial t^2} = \eta\frac{\partial}{\partial t}\nabla^2\Psi_i \qquad (6)$$

where ρ' is the fluid density.

Waves in a viscous medium attenuate because of the finite value of viscosity. This attenuation must be incorporated into expressions for ϕ and Ψ_i. The amplitude of the wave must decrease along the direction of travel of the wave and be constant parallel to the wave front. One further criterion that must be met by ϕ and Ψ_i in order to specify and satisfy boundary conditions at each interface is that there be a wavelength in the X direction which is the same for both P and S waves in both fluid and solid. This requirement can be shown to yield Snell's

Law. This ensures that peaks and troughs of waves coincide at the interface so that continuity at the boundary is possible. In order to satisfy the above two conditions, the solutions of (5) and (6) are forced to be of the form

$$\phi, \Psi \sim A\exp\{i\omega t - ik_x X \pm igZ\} \tag{7}$$

where $k_x = k\cos\delta$

$g = \ell + im$

Substituting (7) into (5) for the scalar potential, expressions for ℓ and m are found to be

$$|md| = \sqrt{\frac{-b + \sqrt{b^2 - 4ae}}{2a}} \tag{8}$$

$$|\ell d| = (4/3)C_1 md + \sqrt{(16/9)C_1^2 m^2 d^2 - (k_x^2 d^2 - m^2 d^2) + C_2^2}$$

where d = fluid layer thickness

$a = 64\, C_1^4/9 + 8C_1^2 + 9/4$

$b = -k_x^2 d^2 a + 9C_2^2/4 + 4C_2^2 C_1^2$

$e = -C_2^4 C_1^2$

$C_1 = \eta\omega/\kappa$

$C_2 = \rho'\omega^2 d^2/\kappa$

A similar procedure for the vector potential yields

$$|\ell d| = \sqrt{\frac{-k_x^2 d^2 + k_x^4 d^4 + \gamma^4 d^4}{2}}$$

$$|md| = \sqrt{\frac{k_x^2 d^2 + k_x^4 d^4 + \gamma^4 d^4}{2}} \qquad (9)$$

where

$$\gamma = \sqrt{\frac{\omega \rho'}{\eta}}$$

2.1.3 Incident SH Waves

Since no conversions from SH to other types of waves can occur at an interface, the problem of SH waves incident on a fluid layer is very easy to solve analytically. In this section, the solution of the problem of SH waves incident on a viscous fluid layer will be found and the results and implications of this solution will be discussed.

The simple case of SH waves normally incident on a fluid layer will be discussed first. The SH problem can be solved using displacements rather than potentials. This follows from (1) and (2) since

$$\rho \frac{\partial^2 U_{SH}}{\partial t^2} = \frac{\partial}{\partial X} \rho \frac{\partial^2 \Psi_3}{\partial t^2} = \frac{\partial}{\partial X} \mu \nabla^2 \Psi_3 = \mu \nabla^2 U_{SH} \qquad (10)$$

In the medium below the fluid layer ($Z \geq d/2$) the displacement can be written as the sum of up and downgoing waves

$$V(Z) = (S_i e^{ikz} + S_R e^{-ikz})\, e^{i\omega t} \qquad Z \geq d/2 \qquad (11)$$

The shear stress is

$$\tau_{xz}(z) = \mu\frac{\partial}{\partial z} V(z) = \mu ik(s_i e^{ikz} - S_R e^{-ikz}) e^{i\omega t} \qquad z \geq d/2 \qquad (12)$$

In the medium above the fluid layer there is only an outgoing wave

$$V(z) = S_T e^{i\omega t+ikz}$$

$$z \leq d/2 \qquad (13)$$

$$\tau_{xz}(z) = \mu ikS_T e^{i\omega t+ikz}$$

Inside the fluid, the displacement is obtained from (7) and (9) by setting k_x equal to 0

$$V(z) = (S_u e^{1/\sqrt{2}(\gamma+i\gamma)z} + S_d e^{-1/\sqrt{2}(\gamma+i\gamma)z}) e^{i\omega t} \qquad (14)$$

The shear stress in the fluid is

$$\tau_{xz}(z) = \eta\frac{\partial^2 V}{\partial z \partial t} = \eta i\omega\frac{(\gamma+i\gamma)}{\sqrt{2}} \{S_u e^{1/\sqrt{2}(\gamma+i\gamma)z} - S_d e^{-1/\sqrt{2}(\gamma+i\gamma)z}\} e^{i\omega t} \qquad (15)$$

Since wave amplitude in the fluid decreases as $e^{\frac{-\gamma r}{\sqrt{2}}}$ where r is the travel distance, the parameter γr is a measure of the amount of attenuation that occurs in the fluid.

Boundary conditions at each fluid-solid boundary are that the displacement, V, and shear stress, τ_{xz}, be continuous. Continuity of two properties at each of two interfaces gives four equations which can be solved to find the four coefficients S_T, S_R, S_u and S_d in terms of the incident wave amplitude, S_i. The quantities of inter-

est are the reflected wave amplitude, S_R, and the transmitted wave amplitude, S_T. Interestingly, the expressions for transmitted and reflected wave amplitudes can be written entirely in terms of dimensionless parameters. One of these parameters, γd, will be called the shear attenuation parameter because it is a measure of the decrease in amplitude of a wave that travels through the fluid layer of thickness d. The other parameter is $I = \sqrt{\frac{\eta\omega\rho'}{2\mu\rho}}$. The acoustic impedance of the solid is $\sqrt{\mu\rho}$. If $\sqrt{\frac{\eta\omega\rho'}{2}}$ is considered to be the impedance of the fluid, the dimensionless quantity I can be thought of as the ratio of the fluid to solid impedance. The transmitted and reflected wave amplitudes, in terms of γd and I are

$$\frac{S_T}{S_i} = 4GI(1+i)$$

$$\frac{S_R}{S_i} = (1-I^2(i+i)^2(e^{(\gamma+i\gamma)d/\sqrt{2}} - e^{-(\gamma+i\gamma)d/\sqrt{2}})\ G \qquad (16)$$

where

$$G = e^{i\omega d/\beta}/[(I(1+i) + 1)^2\ e^{(\gamma+i\gamma)d/\sqrt{2}} - (I(1+i)-1)^2\ e^{-(\gamma+i\gamma)d/\sqrt{2}}] \qquad (17)$$

Figure 3 shows schematically values of $|\frac{S_T}{S_i}| = T$ and

$|\frac{S_R}{S_i}|$ = R on a γd-I plane. Regions where R = 1 and T = 1 are marked. Region labeled E = 1 is that part of the plane where $T \neq 1$ and $R \neq 1$ but where $T^2 + R^2 = 1$ which means that all energy incident on the fluid layer is either reflected or transmitted. The region $E < 1$ is that region where $T^2 + R^2 < 1$ which means that some energy is lost due to viscous dissipation in the fluid.

Figure 4 is a contour plot of T and R. When I is near 1 and small there is perfect transmission of waves by the fluid layer. As γd increases energy is lost in the fluid and the transmission coefficient decreases. If frequency is small, both γd and I are small. When frequency is large the two parameters are large. At both extremes in frequency SH waves are perfectly reflected. When viscosity is high, I is large and γd is small. When viscosity is low, I is small and γd large. At both of these extremes the SH waves are perfectly reflected.

Figures 3 and 4 show that amplitudes of transmitted and reflected waves as well as the sum of energy of the two waves are not quite symmetric about the horizontal line I = 1. This departure from symmetry can be better understood by considering the energy transmitted into a fluid half-space when a wave is incident from a solid half-space. For a nomally incident wave, the kinetic energy flux through an area A parallel to the interface is

$$E = 1/2\rho\dot{\vec{U}}\cdot\dot{\vec{U}}^{*}\ AC \tag{18}$$

where C is the velocity of propagation of the wave and $\dot{\vec{U}}$ is the particle velocity. Conservation of energy requires that the sum of the energies of the reflected and transmitted waves at the interface must equal the energy of the incident wave. For a SH wave incident from a solid half space onto a fluid half space, the ratio of energy transmitted into the fluid to energy incident on the interface is

$$\frac{E_T}{E_i} = \frac{4I}{1 + 2I + 2I^2} \tag{19}$$

where I is the ratio of fluid to solid impedance discussed above. The maximum energy is transmitted into the fluid half space and the minimum reflected back into the solid when $I = 1/\sqrt{2}$. The function representing the amount of energy reflected from the solid-fluid interface as well as the function representing the amount of energy transmitted into the fluid can be shown to be symmetric in log(I) about the point $I = 1/\sqrt{2}$. This symmetry is apparent in Figure 3 by the near symmetry through $I = 1/\sqrt{2}$ of the two regions for small and large I where reflection from the fluid layer is perfect. If no energy is lost in the fluid, both reflection from and transmission through the fluid layer would exhibit symmetry through $I = 1/\sqrt{2}$.

The line $I = \gamma d$ represents a line which may be completely parameterized by frequency. If η, ρ', ρ and μ are held fixed and only frequency varied, values of I and γd will fall along a line parallel to the line $I = \gamma d$. Points A and B labeled in Figure 3 represent values of I and γd that hold for downhole Fenton Hill for cases of frequency equal to 10^4 and 10^2 Hertz, respectively if fluid thickness is .1 mm. The locations of these points in the figure imply that SH waves at normal incidence will be perfectly reflected by the crack in the frequency range 10^2-10^4 Hertz.

Computing amplitudes of transmitted and reflected waves resulting when the incident SH wave is incident at non-normal incidence requires a great deal more algebra than the computation for normal incidence. The complexity is increased for arbitrary incidence because the expressions for ℓ and m defined in equations (9) are not simple. For an SH wave incident at angle θ from the plane of the fluid layer the transmitted and reflected wave amplitudes are

$$\frac{S_T}{S_i} = 4\mu k \sin\theta \eta\omega(i\ell - m)H \qquad (20)$$

$$\frac{S_R}{S_i} = [\mu^2 k^2 \sin^2\theta - \eta^2\omega^2(i\ell - m)^2][e^{(i\ell - m)d} - e^{-(i\ell - m)d}]H \qquad (21)$$

$$H = e^{ikd\sin\theta}/[(\eta\omega(i\ell-m) + \mu k\sin\theta)^2 e^{(i\ell-m)d} -$$

$$(\eta\omega(i\ell-m) - \mu k\sin\theta)^2 e^{-(i\ell-m)d}]$$

These expressions can be reduced to a form identical to equation (11) for normal incidence if k = wave number $<<\gamma$. Redefining I by

$$I_\theta = I/\sin\theta \qquad (22)$$

equations (20) and (21) become (16) and (17) if $e^{i\omega d/\beta}$ is replaced by $e^{i\omega d/\beta\sin\theta}$. Under these conditions the plot in Figure 4 is also valid for SH waves at non-normal incidence.

2.1.4 P Waves at Normal Incidence

An analytic solution for the amplitudes of transmitted and reflected waves resulting when a P wave is normally incident on a fluid layer will now be obtained. For P waves at normal incidence on an interface there are no conversions of P to SV waves. The absence of conversions reduces the complexity of the reflection-transmission problem. The solution for wave amplitudes when P waves are normally incident on a fluid layer can be expressed in terms of three independent dimensionless parameters. The first parameter, γd, has already been discussed. Another parameter, called R, is the ratio of bulk modulus to shear modulus of the fluid ($\kappa/\eta\omega$). The

third dimensionless parameter is the ratio of elastic impedance of the solid to shear impedance of the fluid. Since there are three independent dimensionless parameters in the solution to the normally incident P wave problem, a single plot cannot be made to show the reflection and transmission properties of the fluid layer. Some physical insight can be obtained by studying the problem.

Since only one component of displacement is non-zero for a vertically traveling P wave, the work in this section can be done using displacements rather than potentials. The displacement and stress in the region below the fluid layer can be expressed as the sum of upgoing and downgoing waves

$$W(z) = P_i e^{i\omega t+ikz} + P_R e^{i\omega t-ikz} \qquad z \geq d/2 \tag{23}$$

$$\tau_{zz} = (\lambda+2\mu)\frac{\partial W}{\partial z} = ik(\lambda+2\mu)(P_i e^{i\omega t+ikz} - P_R e^{i\omega t-ikz})$$

Displacements and stress in the fluid are

$$W = P_u e^{i\omega t+igz} + P_d e^{i\omega t-igz} \qquad |z| \leq d/2 \tag{24}$$

$$\tau_{zz} = (\kappa + 4/3\eta\frac{\partial}{\partial t})\frac{\partial W}{\partial z} = ig(\kappa + 4/3\eta i\omega)(P_u e^{i\omega t+igz} - P_d e^{i\omega t-igz})$$

where $g = \ell + im$

with ℓ and m as defined in equations (8). The signs

of ℓ and m are chosen such that the component of displacement that has amplitude P_u is an upgoing wave, i.e., it travels in the negative Z direction and attenuates along its propagation path. These conditions require that ℓ be greater than zero and m be less than zero. The decrease in amplitude that a P wave suffers in passing through the fluid layer one time is e^{-md}. It is interesting that the quantity $md/\gamma d$, which is a dimensionless parameter that is the ratio of P to S attenuation in the fluid, can be written entirely in terms of the dimensionless quantity $R = \kappa/\eta\omega$.

$$m/\gamma = \sqrt{\frac{-b + \sqrt{b^2+4a}}{2a}}$$

$$a = 9R^4/4 + 8R^2 + 64/9 \qquad (25)$$

$$b = 9R^3/4 + 4R$$

The ratio of P to S attenuation computed using (25) is shown in Figure 5. For small values of R, attenuation of P and S waves are nearly equal. As R increases beyond a value of 1, the amount of P wave attenuation decreases in relation to the S wave attenuation. The frequency where R is 1 was described by Walsh (1968) as a critical frequency. For frequencies greater than critical, the viscous losses for all waves are dominated by the shear

rather than the hydrostatic component of stress.

Displacement and stress above the fluid layer are

$$W = P_T e^{i\omega t+ikz} \qquad z \leq d/2 \qquad (26)$$

$$\tau_{yy} = ik(\lambda+2\mu)P_T e^{i\omega t+ikz}$$

Boundary conditions at each solid-fluid interface are that the normal stress, τ_{zz}, and normal displacement, W, are constant. Using these boundary conditions, the reflected and transmitted wave amplitudes are found to be

$$\frac{P_R}{P_i} = \frac{J - g'(R+4i/3)\phi/\theta}{J + g'(R+4i/3)\phi/\theta} e^{ikd} \qquad (27)$$

$$\frac{P_T}{P_i} = \frac{(1 + \frac{P_R}{P_i})}{\theta} e^{-ikd} \left(1 + \frac{g'(R+4i/3)}{g'(R-4i/3)} \frac{+ J}{- J}\right) e^{igd/2} \qquad (28)$$

where

$$J = \sqrt{\frac{(\lambda+2\mu)\rho}{\eta\omega\rho'}}$$

$$\phi = e^{-igd/2}\left[\frac{g'(R+4i/3) + J}{g'(R-4i/3) - J} e^{2igd} - 1\right], \quad \theta = \phi+2e^{-igd/2}$$

$$g' = g/\gamma = \frac{\ell+im}{\gamma}$$

An example of the interaction of normally incident P

waves with a fluid layer is shown in Figure 6. Curves labeled reflection and transmission show the amplitude, normalized by incident wave amplitude, of waves reflected and transmitted through the fluid layer. Curve labeled energy is the total energy contained in the sum of transmitted and reflected waves. If the value of the energy is less than 1, energy has been absorbed in the fluid by viscous heating. Curve labeled attenuation is a plot of the value of the dimensionless parameter md which is a measure of the decrease in amplitude of a wave that passes through the fluid. Values of physical properties used to generate the curves in Figure 6 are $\kappa = 10^9$ gm/cm sec^2 $\rho' = \rho = 2.5$ gm/cm^3, $\lambda = \mu = 2.5 \times 10^{10}$ gm/cm sec^2, frequency = 10 Hz, and d = 10 meters.

Figure 6 shows that when conditions are such that the value of R is not near 1 the reflection and transmission coefficients are independent of viscosity, attenuation is small and no energy is lost in the fluid. In fact, the values of reflected and transmitted wave amplitudes computed using a viscosity of 10^4 Poise are equal to the values computed using a formulation of the same problem assuning a zero viscosity fluid. For the case of P waves in a fluid the value of R is a good indicator of the importance of viscosity on the propagation of compressional waves. For R much greater than 1, viscosity can be considered to be zero.

2.1.5 P and SV waves at Arbitrary Angle of Incidence

When a P or SV wave is incident on a fluid layer, transmitted and reflected P and SV waves will result. In this section, the method of computing amplitudes of transmitted and reflected waves will be discussed. Computations for a case thought to be appropriate to the Fenton Hill geothermal system will be presented.

Computations for arbitrary angle of incidence are best done using potentials rather than displacements and stresses. This allows easy representation of wave fields in terms of up and downgoing P and SV waves. Displacements associated with P and SV waves are easily computed once potentials are known.

The form of potentials in the region below the fluid are

$$\phi = P_i \exp\{i\omega t - ik_\alpha \cos\gamma x + ik_\alpha \sin\gamma z\} + P_R \exp\{i\omega t - ik_\alpha \cos\gamma x - ik_\alpha \sin\gamma z\}$$

$$\Psi = S_i \exp\{i\omega t - ik_\beta \cos\theta x + ik_\beta \sin\theta z\} + S_R \exp\{i\omega t - ik_\beta \cos\theta x - ik_\beta \sin\theta z\} \qquad (29)$$

where ϕ and Ψ are the dilitational and rotational potentials respectively, k_α is the wavenumber of the P wave in the solid, k_β is the wavenumber of the S wave in the solid, γ and θ are respectively the angle of propagation measured from the plane of the fluid layer of the P and

S waves and P_i, S_i, P_R, S_R are the amplitudes of potentials associated with incident, i, and reflected, R, P and SV waves. Snell's law requires that the wavenumbers measured parallel to the fluid-solid interface be a conserved quantity which will be called k_x. This gives a relation between k_x, k_α, k_β, θ and γ

$$k_\alpha \cos\gamma = k_\beta \cos\theta \equiv k_x \tag{30}$$

Displacements and stresses in the region below the fluid are calculated from

$$u = \frac{\partial\phi}{\partial x} - \frac{\partial\Psi}{\partial z} \qquad W = \frac{\partial\phi}{\partial z} - \frac{\partial\Psi}{\partial x}$$

$$\tau_{zz} = \lambda\left(\frac{\partial^2\phi}{\partial x^2} + \frac{\partial^2\phi}{\partial z^2}\right) + 2\mu\left(\frac{\partial^2\Psi}{\partial x\,\partial z} + \frac{\partial^2\phi}{\partial z^2}\right) \tag{31}$$

$$\tau_{xz} = \mu\left(2\frac{\partial^2\phi}{\partial x\,\partial z} + \frac{\partial^2\psi}{\partial x^2} - \frac{\partial^2\Psi}{\partial z^2}\right)$$

Potentials in the fluid are

$$\phi = P_u \exp\{i\omega t - ik_x x + ig_\alpha z\} + P_d \exp\{i\omega t - ik_x x - ig_\alpha z\}$$
$$\Psi = S_u \exp\{i\omega t - ik_x x + ig_\beta z\} + S_d \exp\{i\omega t - ik_x x - ig_\beta z\} \tag{32}$$

where g_α and g_β are defined in equations (8) and (9), respectively. Displacements U and W in the fluid are calculated as in (31). Stresses in the fluid are

$$\tau_{zz} = (\kappa - 2/3\eta\frac{\partial}{\partial t})(\frac{\partial^2\phi}{\partial x^2} + \frac{\partial^2\phi}{\partial z^2}) + 2\eta\frac{\partial}{\partial t}(\frac{\partial^2\Psi}{\partial x \partial t} + \frac{\partial^2\phi}{\partial z^2})$$

$$\tau_{xz} = \eta\frac{\partial}{\partial t}(2\frac{\partial^2\phi}{\partial x \partial z} + \frac{\partial^2\Psi}{\partial x^2} - \frac{\partial^2\Psi}{\partial z^2}) \qquad (33)$$

Potentials in the region above the fluid are

$$\phi = P_T \exp\{i\omega t - ik_x x + ik_\alpha \sin\gamma z\}$$

$$\Psi = S_T \exp\{i\omega t - ik_x x + ik_\beta \sin\theta z\} \qquad (34)$$

Displacements and stresses above the fluid are computed by using (34) and (31).

If viscosity is non-zero, there are four boundary conditions at each fluid-solid interface. These four conditions are that the two components of stress, τ_{zz} and τ_{xz}, and two components of displacement, U and W, be continuous functions across each interface. Four conditions at each of two interfaces yields eight equations which may be solved to find the eight unknowns: P_R, S_R, P_u, P_d, S_u, S_d, P_T, and S_T in terms of the amplitude of the potential associated with the incident P or S wave.

If viscosity of the fluid is zero, or can be assumed to be zero, then there can be no S wave in the fluid since the fluid cannot support shear. Equations (32) and (33) are adjusted by setting η,

S_u and S_d equal to zero. The stress in the solid must vanish at the point of contact with the fluid. The solid can slip parallel to the fluid-solid interface so there is no condition on the displacement U. The boundary value problem reduces to six equations in six unknowns when viscosity is zero.

It should be emphasized that each of the eight or six, equations is a complex equation and each coefficient P_T, etc., is a complex number. The modulus of each coefficient is related to the amplitude of the transmitted or reflected wave and the phase gives the phase shift of the wave relative to the incident wave.

As a check on the validity of the solution to the boundary value problem, kinetic energy flux of transmitted and reflected waves can be computed at each interface. If the solution is correct, the sum of the kinetic energy flux of all waves traveling towards the interface must equal the sum of the kinetic energy flux of all waves leaving the interface. For waves traveling with velocity C at angle δ to the interface, the kinetic energy flux through area A is

$$KE = 1/2\rho\vec{U}\cdot\vec{U}^*\sin\delta AC \qquad (35)$$

When viscosity is non-zero energy is dissipated in the fluid so the sum of the energy of all waves leaving the fluid will not equal the energy of the incident wave. If viscosity is zero, all the energy incident on the fluid must leave the fluid.

Once amplitudes of potentials associated with P or SV waves leaving the fluid have been computed it is desired to convert the results into the amplitudes of displacements of waves for comparison with field measurements. Displacements in the solid are found from potentials by using equations (31). In the region above the fluid, equations (34) and (31) give

$$\vec{U}_p = \frac{\partial\phi}{\partial x}\hat{x} + \frac{\partial\phi}{\partial z}\hat{z} = -ik_\alpha \cos\gamma\phi\hat{x} + ik_\alpha \sin\gamma\phi\hat{z}$$

$$\vec{U}_s = -\frac{\partial\Psi}{\partial z}\hat{x} + \frac{\partial\Psi}{\partial x}\hat{z} = -ik_\beta \cos\theta\Psi\hat{x} - ik_\beta \sin\theta\Psi\hat{z} \qquad (36)$$

amplitudes of P and S waves are

$$|\vec{U}_p| = k_\alpha|\phi| = k_\alpha|P_T|$$

$$|\vec{U}_s| = k_\beta|\Psi| = k_\beta|S_T| \qquad (37)$$

For P wave incident the ratio of transmitted P wave amplitude to incident P wave amplitude is simply obtained by dividing $k_\alpha|P_T|$ by $k_\alpha|P_i|$ to get $|P_T|/|P_i|$. Ratio of transmitted S wave amplitude normalized by

incident P wave amplitude is $k_\beta|S_T|/k_\alpha|P_i|$. Similar expressions can be found for reflected wave amplitudes and for the case where S waves are incident.

When S waves are incident at angle θ less than $\cos^{-1}\beta/\alpha$ the value of $\cos\gamma$ given by (30) must be greater than 1. The angle $\cos^{-1}\beta/\alpha$ is called the critical angle. When θ is less than the critical angle, then γ is complex so P waves no longer propagate as plane waves. Instead P waves travel parallel to the fluid-solid boundary and decrease in amplitude away from the boundary. These waves are called inhomogeneous waves.

Computations of amplitudes of transmitted and reflected waves as a function of incidence angle of P or SV waves have been carried out using physical properties and dimensions considered appropriate for conditions in situ at the Fenton Hill geothermal test site. Physical properties used in the calculations are listed in Table 1. For frequency of 10KHz. The values of dimensionless parameters γd and I listed in Table 1 correspond to point marked A in Figure 3 which means that SH waves are perfectly reflected by the fluid layer. The viscous impedance of the fluid, $\sqrt{\eta\omega\rho'}$, is so small that S waves cannot enter the fluid. The large value of R means that P waves are unaffected by the viscosity of the fluid.

The viscosity of the fluid is so small that it can be neglected even for frequencies as large as 10 KHz. Results obtained when viscosity is assumed to be zero and results obtained when viscosity is non-zero are in agreement which confirms the lack of importance of viscosity in the present calculation.

Figures 7 and 8 show amplitudes of reflected P and S waves respectively when a P wave is incident. Amplitudes are plotted for three frequencies. In addition, amplitudes of waves reflected when a P wave is incident from an elastic half space on a fluid half space are plotted. Figures 9 and 10 show transmitted P and SV waves for incident P wave. Figures 11-14 show reflected and transmitted P and SV waves resulting when SV wave is incident on a fluid layer. Critical angle for the case under study is 54.3°. For angles less than this value, P wave amplitudes represent the amplitude of the wave at z = 0. Amplitude of P waves away from the fluid layer are diminished by a factor

$$A(z) \sim e^{-k_\alpha |z|} \sinh(\cosh^{-1}(\alpha/\beta\cos\theta)) \qquad (38)$$

Figures 7-14 will be useful in interpreting results of experiments performed at the LASL Fenton Hill geothermal test site.

2.2 Interaction of Waves with a Finite Crack

When the wavelength of a wave is of the same scale as the lateral extent of the fracture, the effects of the finite size of the crack must be taken into account when computing the effect of the interaction of the wave with the fracture. In this section the interaction of empty and fluid-filled cracks with plane P and S waves at various angles of incidence will be investigated. The geometry of the problem is two dimensional as shown in Figure 15. The crack is of finite extent in the X-Y plane, having length L, and extends to infinity in a direction perpendicular to the plane of the figure. An empty crack represents a cut in an otherwise homogeneous and isotropic elastic medium and its surfaces are traction-free. At the surface of a fluid-filled crack, a normal stress exists but the shear stress vanishes neglecting the viscosity of the fluid.

A problem similar to diffraction by an empty crack is found in optics when an opaque screen is placed in the path of a parallel beam of rays (Sommerfeld, 1949). The optics problem, however, is different from the one discussed here in that only transversely polarized waves are present in an electromagnetic field where as both transverse and longitudinal waves must be dealt with in the elastic prob-

lem. The other difference is one of scale: in optics the wavelength is small compared with the size of the diffractor and diffraction effects are computed at distances of many wavelengths from the diffractor. In this section, diffracted fields will be computed in the near-field of the diffractor and discussion will be limited to cases where the wavelength is comparable to size of diffractor and the distance from the crack is less than two cracklengths.

Diffraction of elastic waves by a finite empty two dimensional crack is a difficult problem to solve analytically. Ang and Knopoff (1964 a,b) found a solution which is valid for wavelength λ much longer than the diffractor size L and at distances much greater than L from the crack. Loeber and Sih (1968, 1969) reduce the problem to an integral equation which can be solved numerically to find the displacement field on the crack surface for an arbitrary wavelength and incident angle. The same problem has been studied in the time domain by Thau and Lu (1970, 1971) for short time intervals, using the Wiener-Hopf technique. Their procedure requires a new equation to be solved each time a diffracted P or S wave strikes the tip of the crack and the equations become intractable when multiple reflections occur at the crack tips.

Recently Achenbach et al. (1978) obtained a high frequency solution to diffraction of waves from a point

source by a circular crack in a three dimensional medium. Their approach is to use the solution of a canonical problem, which is the diffraction of waves by a semi-infinite crack (Achenbach and Gautessen, 1977), to construct the wave field resulting from waves incident on the curved edge of a fracture. Diffractions of direct rays as well as surface, P and S waves that travel along the surface of the fracture are used in the construction. Geometrical ray theory is used to choose the rays that will eventually reach a given point of observation. The conditions for the validity of the diffracted wave solution are $kr>>1$ and $ka>>1$ where r is the distance between a diffracting edge and a point of observation and a is the crack radius. The theory developed using geometrical ray theory provides a powerful tool for studying diffraction by complicated shaped cracks. Unfortunately, the region of validity of the solution obtained does not overlap the region of validity of the solution to be presented in this section.

In view of the recent success at modeling dynamic crack propagation problems by numerical schemes (Burridge, 1969; Madariaga, 1976; Das and Aki, 1977) it seems reasonable to attempt a numerical solution to the diffraction problem. In this study, the diffraction problem is solved using the explicit leap frog finite difference scheme developed by Madariaga (1976) to

study dynamic crack propagation problems. The time domain solution for incident step function tensile stress wave at an arbitrary angle of incidence is computed and the solution in the frequency domain is found by Fourier Transforms.

2.2.1 Diffraction by an Empty Crack: Boundary Conditions

The crack is assumed to represent a cut in an otherwise infinite, isotropic and homogeneous medium. Each surface of an empty crack is a free surface, at which both the normal and shear stresses vanish. It is assumed that the crack surfaces, though considered flat to first order, are held apart by some static stress field. If the two crack surfaces were to come in contact they would no longer satisfy stress free boundary conditions and the problem would be very complicated to solve.

The diffracted wave field, denoted with superscript d, is the field that must be added to the incident field, denoted superscript i, to yield the appropriate boundary conditions on the crack surface. This can be expressed as

$$\begin{aligned} \tau^{i}_{xy} + \tau^{d}_{xy} &= 0 \\ &\text{on the crack surface} \\ \tau^{i}_{yy} + \tau^{d}_{yy} &= 0 \end{aligned} \qquad (39)$$

The problem is to find the stress field on the crack surface due to the incident wave and then find a diffracted wave, which satisfies the wave equation as well as equation (39). The problem stated in equation (39) is divided into two mixed boundary value problems in a half space. The boundary conditions for these two problems are

$$\tau_{yy}^{d^1} = -\tau_{yy}^{i} \qquad \text{in } y = 0 \text{ for } |x|<L/2$$

$$\tau_{xy}^{d^1} = 0 \qquad \text{in } y = 0 \text{ for all } x \qquad (40)$$

$$v^{d^1} = 0 \qquad \text{on } y = 0 \text{ for } |x|>L/2$$

$$\tau_{xy}^{d^2} = -\tau_{xy}^{i} \qquad \text{on } y = 0 \text{ for } |x|<L/2$$

$$\tau_{yy}^{d^2} = 0 \qquad \text{on } y = 0 \text{ for all } x \qquad (41)$$

$$u^{d^2} = 0 \qquad \text{on } y = 0 \text{ for } |x|>L/2$$

The solution to the diffraction problem is the superposition of the solutions to the two problems defined by (40) and (41). This assertion will now be justified.

Consider an incident P wave. The scalar potential associated with this wave, denoted ϕ^i, can be broken into two parts, one even in y and one odd in y.

$$\phi^i(x,y,t) = \phi^i_e(x,y,t) + \phi^i_o(x,y,t) = 1/2(\phi^i(x,y,t) + \phi^i(x,-y,t)) + 1/2(\phi^i(x,y,t) - \phi^i(x,-y,t)) \tag{42}$$

Then

$$\tau^i_{yy} = \lambda\nabla^2\phi_i + 2\mu\frac{\partial^2\phi^i}{\partial y^2} = (\lambda\nabla^2\phi^i_e + 2\mu\frac{\partial^2\phi^i_e}{\partial y^2}) + \lambda\nabla^2\phi^i_o + 2\mu\frac{\partial^2\phi^i_o}{\partial y^2}$$

$$\tau^i_{xy} = 2\mu\frac{\partial^2\phi^i}{\partial x\partial y} = 2\mu\frac{\partial^2\phi^i_e}{\partial x\partial y} + 2\mu\frac{\partial^2\phi^i_o}{\partial x\partial y} \tag{43}$$

On the plane y = 0, the plane of the crack, equation (43) can be simplified because odd continuous functions must vanish in this plane.

$$\tau^i_{yy} = \lambda\nabla^2\phi^i_e + 2\mu\frac{\partial^2\phi^i_e}{\partial y^2}$$

$$\tau^i_{xy} = 2\mu\frac{\partial^2\phi^i_o}{\partial x\partial y} \qquad \text{on } y = 0 \tag{44}$$

The problem of matching boundary conditions (39) can now be broken into two problems, one for ϕ^i_e and one for ϕ^i_o. For ϕ^i_e the normal stress, τ^d_{yy} associated with the diffracted field is symmetric in y and the shear stress , τ^d_{xy}, is antisymmetric. Requiring that displacement and shear stress parallel to the crack surface be continuous across the crack it can be shown that the

displacement perpendicular to the crack surface must be antisymmetric. Functions antisymmetric in y must vanish on y = 0 except where they are discontinuous. The only discontinuity is the displacement between the two crack faces. Thus τ_{xy}^{dl} vanishes everywhere on y = 0 and V^{dl} vanishes on y = 0 outside the crack area. A complete set of boundary conditions is obtained for the problem involving ϕ_e^i. They are displayed in equation (40).

Boundary conditions given in equation (41) correspond to satisfying equation (39) for the odd part of ϕ^i. In this case, τ_{xy}^i is symmetric and τ_{yy}^i is antisymmetric. Thus τ_{yy}^d must vanish on y = 0 and the displacement in the x-direction is antisymmetric and must therefore vanish on y = 0 except where it is discontinuous -- i.e., on the surface of the crack. The displacement in the y direction is symmetric in this problem. Equations (41) are thus justified.

A complete set of symmetry relations for the two problems appears in Table 2. Using this table a solution in the entire X-Y plane may be obtained after solving each of the problems described above in a half plane.

2.2.2 Boundary Conditions for a Fluid-Filled (zero viscosity) Crack

To obtain approximate boundary conditions for a thin fluid filled crack first consider plane P waves incident from below on a plane fluid layer imbedded in an otherwise infinite, isotropic elastic medium (see Figure 1). The amplitude of the P wave potential of the incident wave is P_i. Potentials of reflected and transmitted P and SV waves have amplitudes as shown in the figure. An approximate relationship between the stress and displacement at the fluid boundary is desired. This relation will be used as a boundary condition so that stress can be computed at the crack surface without explicit knowledge of the displacement inside the fluid. To find the relationship between stress and displacement at the surface of the fluid layer only the wave field inside the layer need be considered. Since the fluid has zero viscosity there are no S waves present in the layer. The potential associated with the P wave in the fluid is of the form

$$\phi = [M\exp\{ik_f z\sin\delta\} + D\exp(-ik_f z\sin\delta)]e^{S}$$

where $S = ik_f x\cos\delta + i\omega t$

k_f is the wavenumber in the fluid

δ is the angle in the fluid

Then displacement normal to the fluid layer is

$$V = -ik_f e^S \sin\delta [Me^{ik_f z\sin\delta} - De^{-ik_f z\sin\delta}] \qquad (45)$$

and

$$\Delta V(d/2) = \frac{V(d/2)-V(-d/2)}{2} = -k_f e^S \sin\delta (M+D) \sin(k_f d/2\sin\delta)$$

$$\simeq - k_f^2 e^S d \sin^2\delta (M+D) + O(k_f^3 d^2) \qquad (46)$$

where $O(k_f^3 d^2)$ indicates that terms of order $k_f^3 d^2$ and higher in $k_f d$ are not explicitly shown. These higher order terms are negligibly small if $k_f d$ is small. The normal stress, τ_{zz}, in the fluid layer is

$$\tau_{zz} = -\kappa k_f^2 e^S (Me^{ik_f z\sin\delta} + De^{-ik_f z\sin\delta}) \qquad (47)$$

where κ is the bulk modulus of the fluid. The average stress at the boundary of the fluid layer is

$$\tau_{zz}^{av}(d/2) = \frac{\tau_{zz}(d/2)+\tau_{zz}(-d/2)}{2} = -\kappa k_f^2 e^S (M+D)\cos(k_f d/2\sin\delta) \qquad (48)$$

$$-\kappa k_f^2 e^S (M+D) + O(k_f^3 d^2)$$

Comparing (46) with (48) it can be shown that if $\sin^2\delta = 1$

$$(k/d)\Delta V(d/2) = \tau_{zz}^{av}(d/2) + O(k_f^3 d^2) \qquad (49)$$

Assuming that the P wave velocity of the fluid is much less than that of the rock then (see equation (30))

$$\sin^2\delta = 1 - \frac{\alpha_f^2}{\alpha_m^2}\cos^2\delta \sim 1$$

where α_f and α_m are P wave velocities of fluid and rock respectively. Since τ_{zz}^{av} is the part of τ_{zz} that is symmetric in z and ΔV the antisymmetric part of V equation (40) is modified to

$$\tau_{yy}^{i} + \tau_{yy}^{d} = \kappa/d\ \Delta V^{d} \qquad y = 0,\ |x| \leq L/2 \qquad (50)$$

For an empty crack, $\kappa = 0$, and the above equation reduces to (40). Using equation (47) it is easy to show that to order $k_f d$ there is no change in the boundary conditions defined by equation (41).

For a useful presentation of numerical results non-dimensional stress and displacement are used. Unit stress is chosen to be τ_o so that $\tau_{yy} = \tau_o \tau'_{yy}$ where prime indicates a dimensionless stress. Dimensionless displacement is defined by $V = \tau_o L V'/\mu$ where L is the crack length. Inserting these quantities into (50) gives

$$\tau_{yy}^{i'} + \tau_{yy}^{d'} = \kappa/\mu\ L/d\ Vd' \qquad (51)$$

The quantity κ/μ L/d $\equiv$ C = crack stiffness factor is a dimensionless quantity which determines the effect of the fluid in the crack.

Achenbach et al. (1978) proposed that boundary conditions for a fluid filled crack be that shear stress vanish on the crack surfaces and there be no discontinuity in normal displacement across the crack. If these conditions are used, the problem defined in equations (40) does not need to be solved and the solution to equation (41) completely describes the diffracted wave field. Using these boundary conditions there will be no diffracted wave field generated when P waves are normally incident. This follows because the shear stress, τ_{xy}, associated with a normally incident P wave vanishes everywhere. When the fluid bulk modulus differs significantly from the bulk modulus of the solid it seems unlikely that the conditions used by Achenbach et al. (1978) are appropriate.

2.2.3 Method of Solution

Boundary conditions on the surface of an empty crack are given in equations (40) and (41). The modification to equations (40) for the case when a zero viscosity fluid fills the crack is given in equation (50). In all cases, radiation conditions

supply boundary conditions at y = ∞. The total diffracted field is formed by superposing the results of the two problems defined in (40) and (41) (see Table 2) as

$$U^d(x,y,t) = U^{d1}(x,y,t) + U^{d2}(x,y,t)$$
$$V^d(x,y,t) = V^{d1}(x,y,t) + V^{d2}(x,y,t) \qquad (52)$$

Once the diffracted field resulting from plane transient P or S wave with δ-function or step function time dependence has been calculated, the diffracted field resulting from any incident longitudinal or shear plane wave may be found by convolution. Choose the incident plane wave to be a step function in stress in which the jump in normal stress at the wavefront is τ_o. Then for P wave incidence, the incident wave stress components working on the plane parallel to the crack plane are

$$\tau_{yy}^i(x,y,t) = (1-2/3\sin^2\gamma)\tau_o H(\alpha/L(t + x\sin\gamma/\alpha - y\cos\gamma/\alpha))$$
$$\tau_{xy}^i(x,y,t) = -1/3\tau_o \sin 2\gamma\, H(\alpha/L(t + x\sin\gamma/\alpha - y\cos\gamma/\alpha)) \qquad (53)$$

where γ is the incidence angle and α is the compressional velocity of the solid. For S waves incident at angle γ', the stress components acting on the plane parallel to y = 0 are

$$\tau^{i}_{xy}(x,y,t) = \tau_o \cos 2\gamma' \; H(\beta/L(t + x/\beta\sin\gamma' - y/\beta\cos\gamma'))$$

$$\tau^{i}_{yy}(x,y,t) = \tau_o \sin 2\gamma' \; H(\beta/L(t + x/\beta\sin\gamma' - y/\beta\cos\gamma')) \qquad (54)$$

These expressions, along with equations (40) and (41) define the two mixed boundary value problems that must be solved to obtain the diffracted field.

The incident stress fields in (53) and (54) propagate along the x-direction on the plane of the crack (y = 0) with phase velocities $\alpha/\sin\gamma$ and $\beta/\sin\gamma'$ respectively. If $\sin\gamma' = \beta/\alpha\sin\gamma$ the expression for incident wave stresses on y = 0 in (53) are equal, to within multiplicative constants, to the expressions for incident wave stresses on y = 0 given in (54). Thus by taking the appropriate linear combination of solutions to (40) and (41), numerical solution of the diffraction of P waves incident at angle γ can be used to compute the solution for S waves incident at angle γ'.

The solutions to (41) and (42) are found using the finite difference scheme of Madariaga (1976) as discussed briefly in Appendix A. The direct

output of the finite difference calculation is the particle velocity associated with the diffracted wave at each grid point. In order to study the diffracted field as a function of wavelength, the particle velocity at each grid point is numerically Fourier Transformed in time.

As a check on the validity of the numerical solution, displacements computed by numerical integration of particle velocities are compared in Figure 16 with the displacements obtained by Thau and Lu (1971) for P wave normally incident on an empty crack. The two solutions agree well except for a small discrepancy at the early part where there is a sudden jump in the particle velocity. As another check, the y-component amplitude, V^d, of the diffracted wave field on the surface of an empty crack normalized to the amplitude of the incident wave, V^i, is compared in Figure 17 with the result of Sih and Loeber (1968) for various wavelengths of normally incident P wave. The static solution shown in the figure corresponds to infinite period or a crack under static stress. The infinite period solution can be obtained from the calculation of the diffracted wave for a finite period of time because the particle velocity due to the diffracted wave dies out quickly with increasing time, and the displacement approaches that of a static solution.

This provides a criterion for determining if the transient solution has been calculated for a sufficient amount of time to yield a complete record and also provides a convenient check on the results of the numerical computation since the static solution can be easily computed analytically. Figure 17 shows good agreement between results obtained by the two methods.

To check the validity of the approximate boundary condition for a fluid filled crack, the simple case of P waves normally incident on a fluid layer imbedded between two solid half spaces was tested. The time domain solution for transient stress wave incident was computed using the numerical scheme and the approximate boundary conditions. The time domain solution was transformed into the frequency domain and the amplitudes of transmitted waves were compared with amplitudes of incident waves. The results obtained using the finite difference approach were compared with the transmitted wave amplitudes calculated for P waves normally incident on a zero viscosity fluid layer (equation (28)). Figure 18 shows a comparison of transmission coefficients computed using the two methods. Real and imaginary parts of the coefficients are shown. Crack stiffness factor in the numerical scheme was chosen to be 2. Length scale

in the finite difference scheme is L which is arbitrarily set equal to ten grid spacings. Analytic solution was calculated for the following conditions

$$\kappa/\mu = .04$$

$$L/d = 50$$

$$\rho = \rho'$$

Specific values of physical properties are needed to compute coefficients using the analytic solution because there is no approximation involved in this case. For small values of κ/μ, transmission coefficients depend very little on the ratio of fluid density to solid density. Agreement between analytic and numeric solutions is very good provided that L/d is large and κ/μ small.

The incident wave must be added to the diffracted wave to obtain the total motion for comparison with observations. The particle velocities associated with the incident P wave of equation (53) are given by

$$\dot{U}^i(x,y,t) = (\alpha\tau_o \sin\gamma/3\mu)H(\alpha/L(t + x\sin\gamma/\alpha - y\cos\gamma/\alpha)) \tag{55}$$

$$\dot{V}^i(x,y,t) = -(\alpha\tau_o \cos\gamma/3\mu)H(\alpha/L(t + x\sin\gamma/\alpha - y\cos\gamma/\alpha))$$

and those for the incident wave of equation (54) are

$$\dot{U}^i(x,y,t) = -(\beta\tau_o \cos\gamma'/\mu)H(\beta/L(t + x\sin\gamma'/\beta - y\cos\gamma'/\beta))$$

$$\dot{V}^i(x,y,t) = -(\beta\tau_o \sin\gamma'/\mu)H(\beta/L(t + x\sin\gamma'/\beta - y\cos\gamma'/\beta)) \quad (56)$$

Their Fourier Transforms are

$$\dot{U}^i(x,y,\omega) = -(i\alpha\tau_o \sin\gamma/3\mu\omega)\exp\{i\omega(x\sin\gamma/\alpha - y\cos\gamma/\alpha)\}$$

$$\dot{V}^i(x,y,\omega) = (i\alpha\tau_o \cos\gamma/3\mu\omega)\exp\{i\omega(x\sin\gamma/\alpha - y\cos\gamma/\alpha)\} \quad (57)$$

for equation (55) and

$$\dot{U}^i(x,y,\omega) = (i\beta\tau_o \cos\gamma'/\omega\mu)\exp\{i\omega(x\sin\gamma'/\beta - y\cos\gamma'/\beta)\}$$

$$\dot{V}^i(x,y,\omega) = (i\beta\tau_o \sin\gamma'/\omega\mu)\exp\{i\omega(x\sin\gamma'/\beta - y\cos\gamma'/\beta)\} \quad (58)$$

for equation (56). Values calculated from (57) and (58) are added to the corresponding Fourier Transforms of the diffracted waves obtained by the numerical method. The particle velocity at a point associated with one frequency can be described by the absolute value, $|V(\omega)|$, of Fourier Transform and the phase delay, $\theta(\omega)$.

$$\dot{U}(t) = |\dot{U}| \cos(\omega t - \theta)$$
$$\dot{V}(t) = |\dot{V}| \cos(\omega t - \xi) \quad (59)$$

The particle motion described by (59) is generally elliptical where the shape is defined by the equation

$$\frac{\dot{U}^2}{|\dot{U}|^2} + \frac{\dot{V}^2}{|\dot{V}|^2} - \frac{2\,\dot{U}\,\dot{V}}{|\dot{U}||\dot{V}|}\cos(\theta-\xi) = \sin^2(\theta-\xi) \qquad (60)$$

This equation shows that the shape is indistinguishable between $\xi-\theta$ and $\theta-\xi$, that is between clockwise and counterclockwise sense of motion.

2.2.4 Results of the Calculation

Diffraction effects for P waves normally incident on a crack for cases where the crack stiffness factor is 0, 2, and 10 have been computed. Results for S waves at normal incidence and P waves incident at an angle of 45° on an empty crack have been obtained. Results for all these cases for various wavelengths appear in Figures 19-28. These results will now be discussed.

For a wavelength much longer than the cracklength L it is expected that the crack will have little effect on the wave motion. This is demonstrated clearly in Figure 19 which shows the result for P wave of wavelength 11.64L normally incident on an empty crack. The vertical line on the right hand of the figure directly above the figure label shows the incident wave motion, i.e., the motion observed in the absence of the crack. The incident wave arrives from below in

the figure. The crack is located between the two crosses marked on the horizontal line that bisects the figure. Each ellipse represents the particle motion at the center of the ellipse, marked by a cross. The points where ellipses are plotted are not symmetric through the center of the crack. This was done on purpose so that more details of the wave motion could be represented. The pattern of wave motion has symmetry through a vertical line cutting the center of the crack so that each ellipse could have a mirror image through this line. The amplitude of the motion along the center line at a point is represented by a straight line at that point. By symmetry there is no component of motion parallel to the plane of the crack at points along the center line if P wave is normally incident. Most of the particle motion ellipses in this figure appear to be nearly straight lines of length equal to the line representing the incident wave, showing that there is little departure from the incident wave motion in this case.

Figures 20 and 21 show results for wavelength 4.65L. Figure 20 shows the result for P wave normally incident on an empty crack and Figure 21 shows the result for P waves normally incident on a fluid-filled crack with stiffness factor, C, of 2. At this relatively long wavelength there is a surprisingly strong

diffraction effect when the crack is empty, as shown by the generally elliptical motion and the variations in orientation of the ellipses. When the crack is fluid filled (Figure 21) the effect of the crack on the particle motion is weak and there is little deviation in particle motion from the incident waves for waves of this wavelength.

The complicated pattern represented in Figure 22 shows the result for P waves with wavelength of 1.33L normally incident on an empty crack. Immediately above the crack there is a shadow zone where the amplitude of the wave motion is considerably less than that of the incident wave. There is a very rapid change of phase of particle motion as a function of position inside the shadow zone as shown by the orientation of the ellipses in this region. Below the crack, the strong amplitude modulation as a function of distance from the crack is caused by the interference between incident waves and waves reflected from the crack. The interval between maximum amplitudes is 1/2 wavelength, as expected for the case of waves normally incident on the free surface of an elastic half-space.

Figures 23 and 24 show results for P waves of wavelength 1.33L normally incident on cracks where the stiffness factors are 2 and 10, respectively.

When the stiffness factor is 2 (Fig. 23) the results look very similar to the case shown in Figure 22 for an empty crack. For larger values of the stiffness factor the effect of the crack on the particle motion decreases. The shadow zone is not present when the stiffness factor is 10 but there is still a noticeable effect on the wave motion. Apparently the finite compressibility of fluid in the crack makes it more transparent for the normal incidence of P waves.

General features of the solutions for P waves incident at 45° on an empty crack will now be discussed. The numerical solution of this problem requires more computer time than the solution for the case of normal incidence because there is no symmetry about the perpendicular axis through the center of the crack. Also, for P waves at normal incidence, equation (55) yields $\tau_{xy}^{i} = 0$ so that the second problem described by equation (41) does not have to be solved.

Figure 25 shows the result for P wave of wavelength 3.46L incident at 45° from the plane of the crack. The wave travels from the lower right corner to the upper left corner of the figure. The amplitude and direction of particle motion due to the incident wave are represented by the straight line drawn in the center right of the figure above the figure label. The shadow zone for this wavelength is not

very well defined. Immediately behind the crack, the pattern of particle motion changes drastically from point to point.

Some evidence of a shadow zone behind the crack is seen in Figure 26 which shows the result for P wave of wavelength 1.69L incident at 45° upon the crack. On the side of the crack facing the incident wave, a strong amplitude modulation due to the interference between incident and reflected waves is again found. Additional ellipses are plotted in this figure in order to make the change in motion with position more apparent.

Figures 27 and 28 show results for S waves of respective wavelengths 2.69L and 1.34L normally incident on an empty crack. For normally incident S waves the normal stress, τ_{yy}, vanishes everywhere (see equation 53) The displacement in the y direction, V^d, excited by the incident stress field is a symmetric function of y (see Table 2). The incident stress field does not excite any displacement in the y direction that is antisymmetric in y. This means that the right hand side of equations (40) vanish completely so that the diffracted field generated by a normally incident S wave is totally defined by the solutions to equations (41). Since the crack stiffness factor does not enter into equations (41) the results for the

case of normally incident S waves are independent of this parameter. In the figures, the incident S wave arrives from below with particle motion perpendicular to the direction of propagation as shown by the horizontal line on the right hand of the figure above the label. For the wavelength of 2.69L (Figure 27) the crack has little effect on the particle motion, except at a few points showing a rather large component of motion perpendicular to the particle motion of the incident wave. For the case where the wavelength is 1.33L (Figure 27) the pattern of predicted motion differs considerably from the incident wave motion but the differences are qualitatively similar to that found for P waves of the same wavelength normally incident on an empty crack.

Water at 200°C

Viscosity	.0014 poise
density	1.0 gm/cm^3
bulk modulus	1.19×10^{10} $gm/(cm\ sec^2)$

Rock

density	2.69 gm/cm^3
shear modulus	3.3×10^{11} $gm/(cm\ sec^2)$
λ	3.1×10^{11} $gm/(cm\ sec^2)$

Fluid layer thickness .1 cm

Dimensionless parameters (use F=10KHz)

$R = \kappa/\eta\omega$	1.14×10^{7}
$I = \sqrt{\eta\omega\rho'/2\mu\rho}$	7.30×10^{-6}
$\gamma d = \sqrt{\omega\rho'/\eta}\ d$	6.70×10^{2}
$J = \sqrt{(\lambda+2\mu)\rho/\eta\omega\rho'}$	1.72×10^{5}

Table 1. Physical properties used to compute transmitted and reflected wave amplitudes shown in Figures 7-14.

Table 2: Symmetry relations between stress and dis-- placements for the two boundary value problems.

Solution of A2	Solution of A3
$\tau^{d^1}_{xy}(x,y,t) = -\tau^{d_1}_{xy}(x,-y,t)$	$\tau^{d^2}_{xy}(x,y,t) = \tau^{d^2}_{xy}(x,-y,t)$
$\tau^{d^1}_{yy}(x,y,t) = \tau^{d^1}_{yy}(x,-y,t)$	$\tau^{d^2}_{yy}(x,y,t) = -\tau^{d^2}_{yy}(x,-y,t)$
$\tau^{d^1}_{xx}(x,y,t) = \tau^{d^1}_{xx}(x,-y,t)$	$\tau^{d^2}_{xx}(x,y,t) = -\tau^{d^2}_{xx}(x,-y,t)$
$u^{d^1}(x,y,t) = u^{d^1}(x,-y,t)$	$u^{d^2}(x,y,t) = -u^{d^2}(x,-y,t)$
$v^{d^1}(x,y,t) = -v^{d^1}(x,-y,t)$	$v^{d^2}(x,y,t) = v^{d^2}(x,-y,t)$

Figure Captions

Figure 1. Geometry of fluid layer imbedded between solid half spaces. Incident P wave is labeled P_{inc}, Reflected and transmitted P and S waves are labeled. Relation between γ and θ is given by Snell's law.

Figure 2. Particle motions of P, SV, and SH waves.

Figure 3. Schematic of reflection and transmission coefficients for SH waves at normal incidence on a fluid layer. R = reflection coefficient, T = transmission coefficient, E = sum of energy of reflected and transmitted waves.

Figure 4. Reflection coefficients for SH waves at normal incidence.

Figure 5. Ratio of P to S wave attenuation in a viscous fluid.

Figure 6. Amplitudes as a function of viscosity of P waves reflected and transmitted by a viscous layer when P waves are normally incident. Total energy of waves leaving the fluid normalized by energy incident on the fluid is also shown as well as the attenuation,

md, as discussed in the text. Physical properties of fluid and solid used to generate figure are given in text.

Figure 7. Amplitude of reflected P wave, normalized by incident P amplitude vs. incident P angle. Fluid thickness is 1 mm.

Figure 8. Amplitude of reflected SV wave normalized by incident P amplitude vs. incident P angle.

Figure 9. Amplitude of transmitted P wave normalized by incident P wave amplitude vs. incident P angle.

Figure 10. Amplitude of transmitted SV wave normalized by incident P wave angle vs. incident P angle.

Figure 11. Same as Figure 7, SV wave is incident.

Figure 12. Same as Figure 8, SV wave is incident.

Figure 13. Same as Figure 9, SV wave is incident.

Figure 14. Same as Figure 10, SV wave is incident.

Figure 15. Geometry of the diffraction problem. Incident wave comes from lower right corner of figure.

Angle of incidence is γ. Normal incidence occurs when $\gamma = 0$.

Figure 16. Comparison of numerical solution with that of Thau and Lu (1971). Solutions represent y-component of diffracted wave as a function of time at a point .2L from crack tip for step function tensile stress normally incident on an empty crack.

Figure 17. Comparison of numerical solution with that of Sih and Loeber. Solutions represent amplitude of displacement of diffracted wave normalized by displacement of incident wave as a funciton of position on the crack surface. Solutions for y-component of motion are shown for various incident wave wavelengths.

Figure 18. Real and imaginary parts of transmission coefficient for P waves incident on a fluid layer. Numerical solution was obtained using approximate boundary conditions for a fluid-filled crack with crack stiffness factor of 2.

Figure 19. Particle Motion diagram representing total particle motion resulting when P wave of wavelength 11.64L is normally incident on an empty crack. Crack is located between two crosses in horizontal line that

bisects the figure. Incident wave comes from below and has amplitude equal to line drawn above the figure label.

Figure 20. Same as Figure 19, wavelength = 4.65L.

Figure 21. Same as Figure 20 except that crack is fluid filled and has stiffness factor of 2. Incident wave wavelength is 4.65L.

Figure 22. Same as Figure 20, stiffness factor = 0, wavelength = 1.33L.

Figure 23. Same as Figure 20, stiffness factor = 2, wavelength = 1.33L.

Figure 24. Same as Figure 20, stiffness factor = 10,

Figure 25. Particle motion diagram representing total particle motion resulting when P-wave of wavelength 3.46L is incident at 45° on an empty crack. Incident wave comes from bottom right. Amplitude and direction of particle motion of incident wave is represented by the 45° line drawn above the figure caption.

Figure 26. Same as Figure 25, wavelength = 1.69L.

Figure 27. Particle motion diagram represents total particle motion resulting when S wave of wavelength 2.69L is normally incident on a crack. Incident wave travels from bottom to top in the figure. Particle motion for the incident shear wave is in the plane of the figure but normal to the direction in which the wave travels. The amplitude and direction of this particle motion is represented by the line drawn above the figure caption.

Figure 28. Same as Figure 27, wavelength = 1.34L.

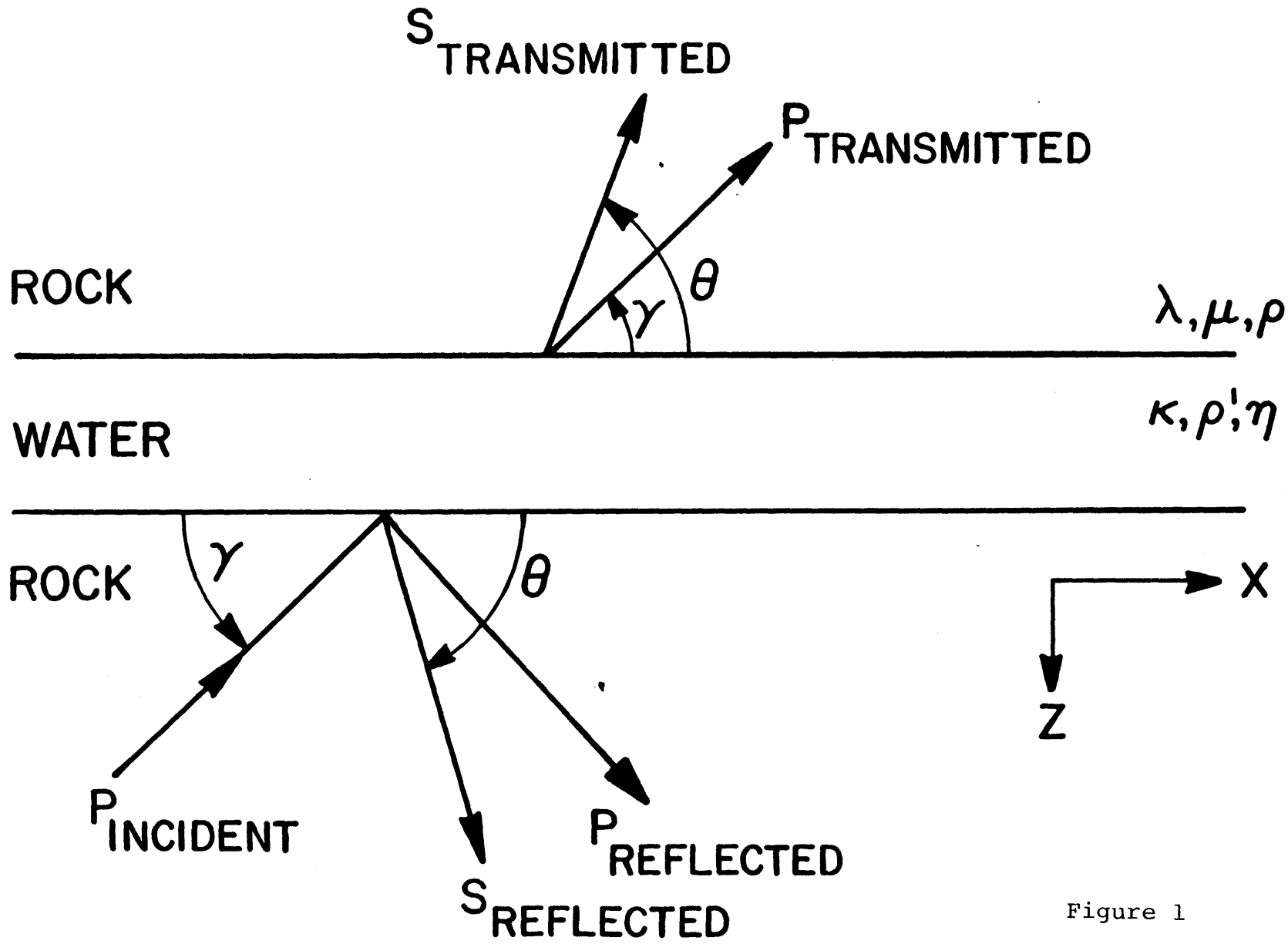
S TRANSMITTED
P TRANSMITTED
ROCK
θ
γ
λ,μ,ρ
WATER
κ,ρ',η
ROCK
γ
θ
X
Z
P INCIDENT
P REFLECTED
S REFLECTED

Figure 1

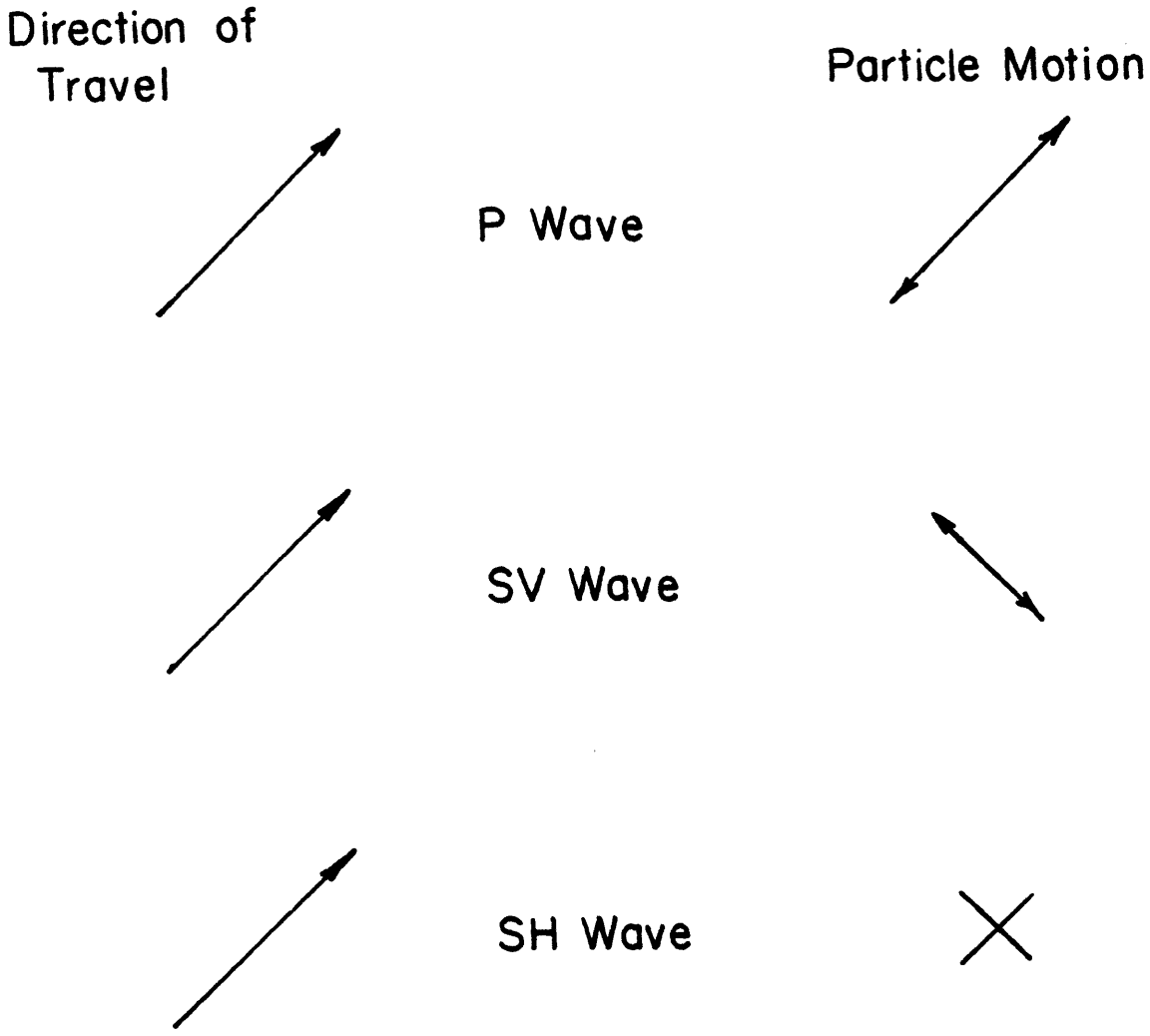

Figure 2

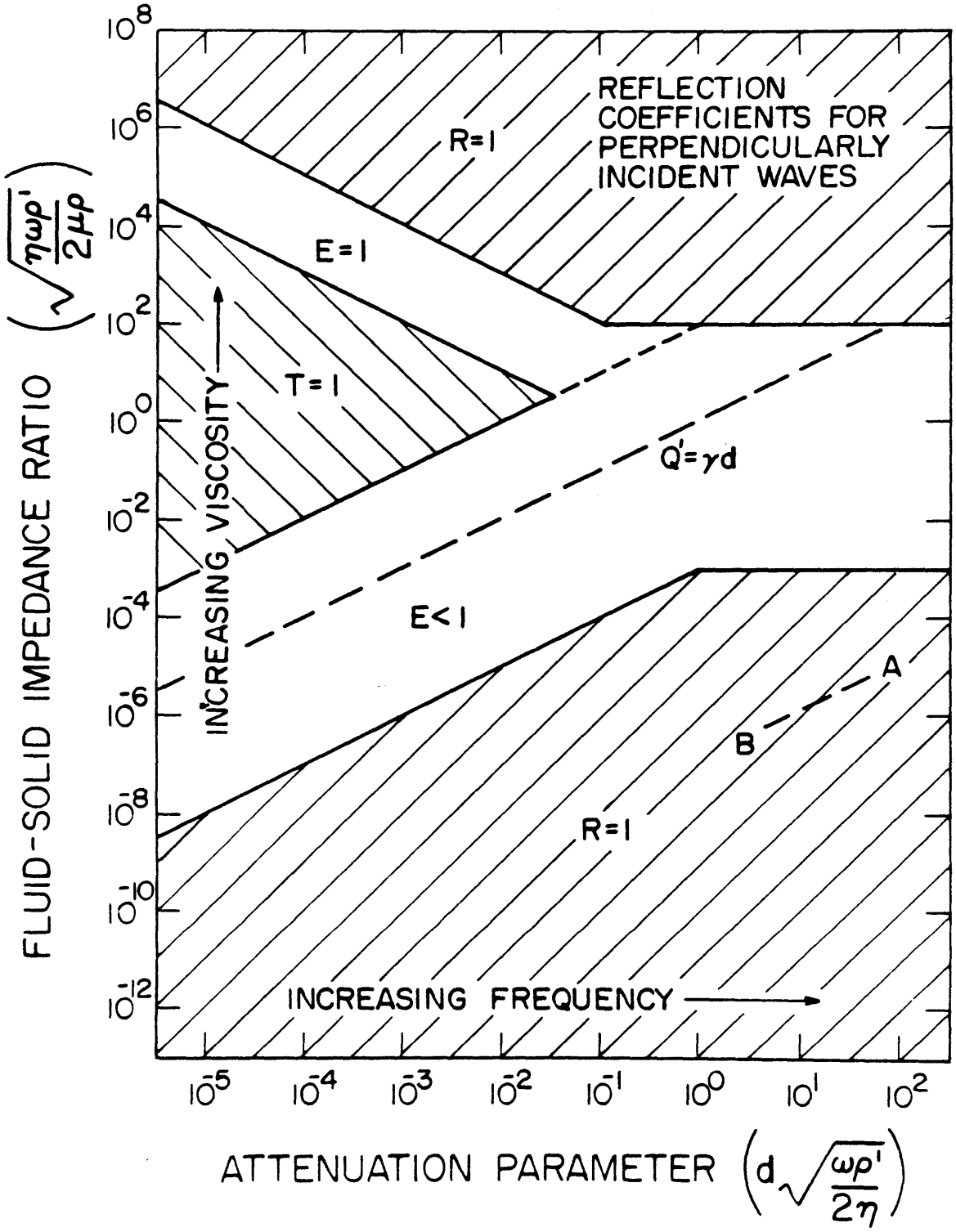
REFLECTION COEFFICIENTS FOR PERPENDICULARLY INCIDENT WAVES
R=1
E=1
T=1
INCREASING VISCOSITY
Q'=γd
E<1
A
B
R=1
INCREASING FREQUENCY
FLUID-SOLID IMPEDANCE RATIO $\left(\sqrt{\frac{\eta\omega\rho'}{2\mu\rho}}\right)$
ATTENUATION PARAMETER $\left(d\sqrt{\frac{\omega\rho'}{2\eta}}\right)$
10^{8}
10^{6}
10^{4}
10^{2}
10^{0}
10^{-2}
10^{-4}
10^{-6}
10^{-8}
10^{-10}
10^{-12}
10^{-5}
10^{-4}
10^{-3}
10^{-2}
10^{-1}
10^{0}
10^{1}
10^{2}

Figure 3

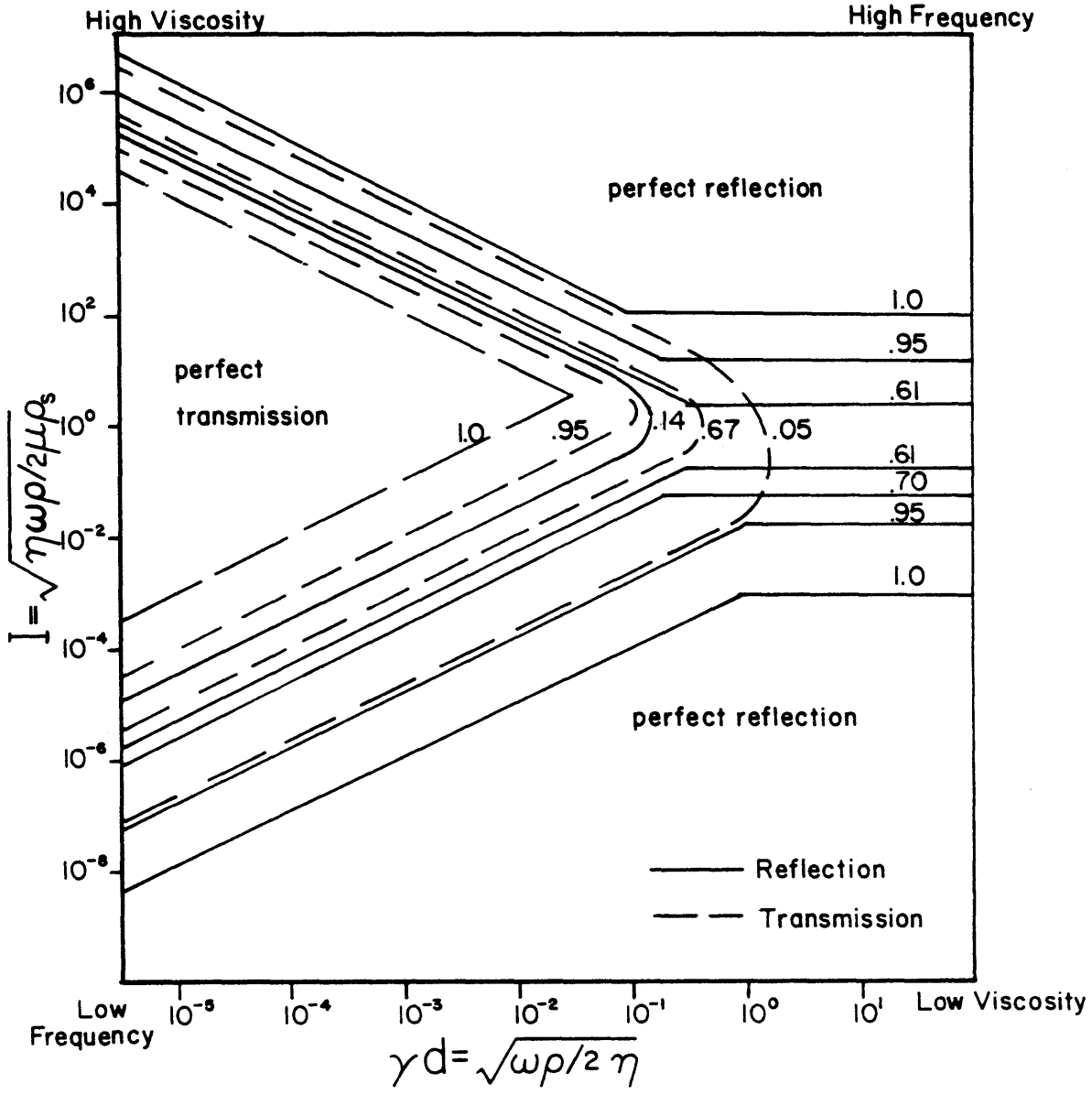
High Viscosity
High Frequency
perfect reflection
perfect
transmission
1.0
.95
.61
.14
.67
.05
.61
.70
.95
1.0
perfect reflection
Reflection
Transmission
Low
Frequency
Low Viscosity
10^{6}
10^{4}
10^{2}
10^{0}
10^{-2}
10^{-4}
10^{-6}
10^{-8}
10^{-5}
10^{-4}
10^{-3}
10^{-2}
10^{-1}
10^{0}
10^{1}
$I=\sqrt{\eta\omega\rho/2\mu\rho_s}$
$\gamma d=\sqrt{\omega\rho/2\eta}$

Figure 4

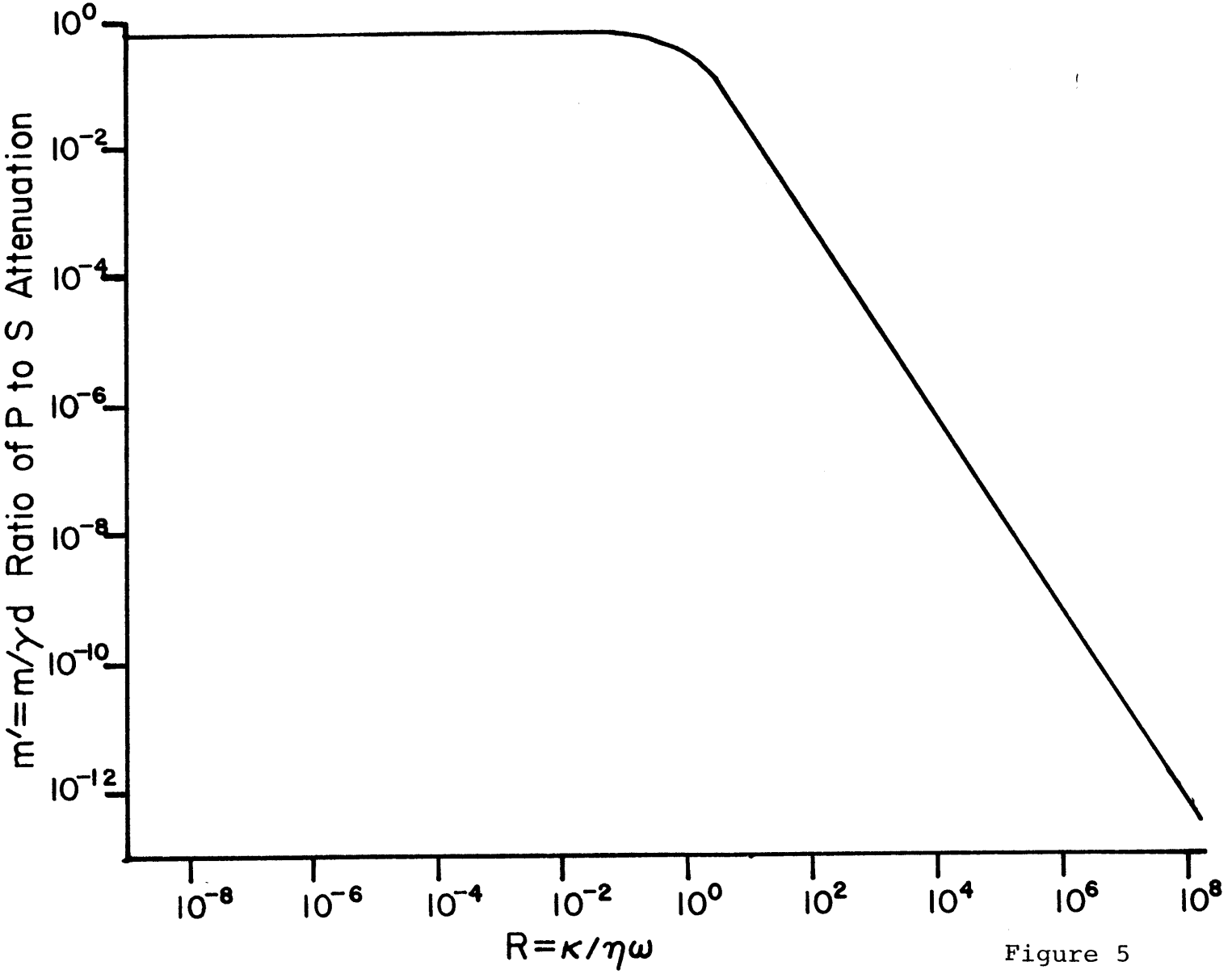
10^0
10^{-2}
10^{-4}
10^{-6}
10^{-8}
10^{-10}
10^{-12}
m′=m/γd Ratio of P to S Attenuation
10^{-8}
10^{-6}
10^{-4}
10^{-2}
10^0
10^2
10^4
10^6
10^8
R=κ/ηω

Figure 5

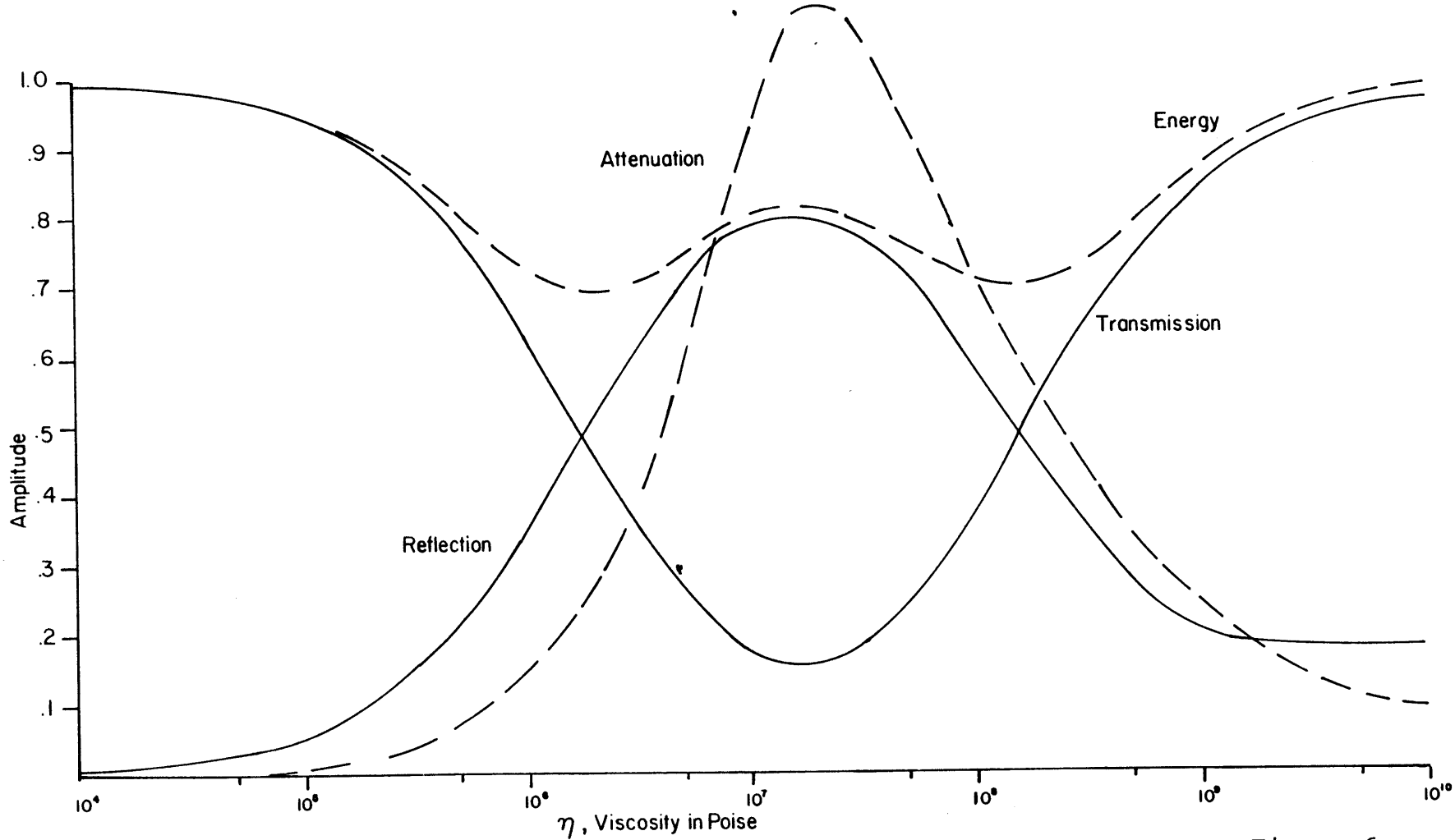
1.0
.9
.8
.7
.6
.5
.4
.3
.2
.1
Amplitude
Attenuation
Energy
Transmission
Reflection
10^4
10^5
10^6
10^7
10^8
10^9
10^{10}
η, Viscosity in Poise

Figure 6

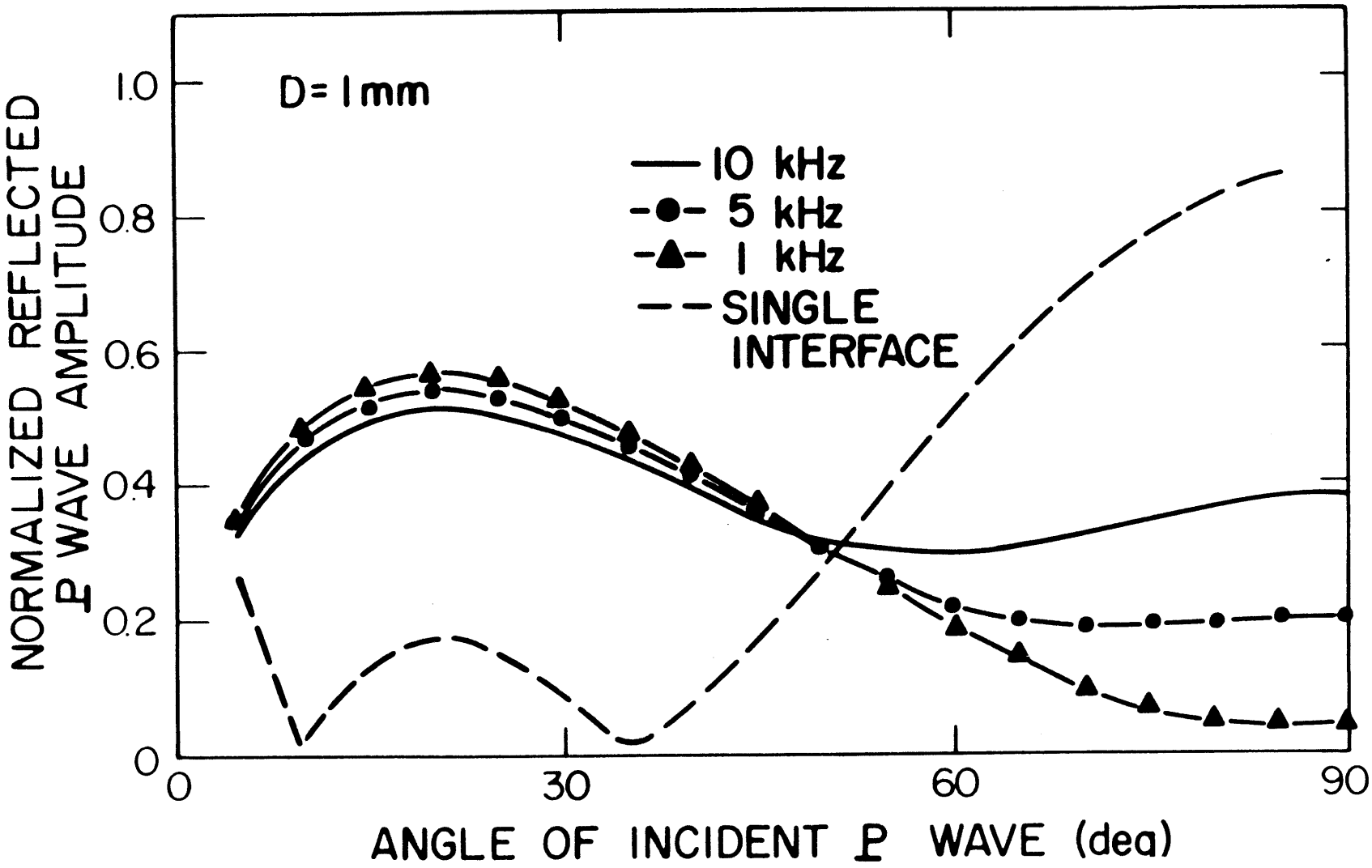
D= 1mm
10 kHz
5 kHz
1 kHz
SINGLE INTERFACE
NORMALIZED REFLECTED P WAVE AMPLITUDE
1.0
0.8
0.6
0.4
0.2
0
0
30
60
90
ANGLE OF INCIDENT P WAVE (deg)

Figure 7

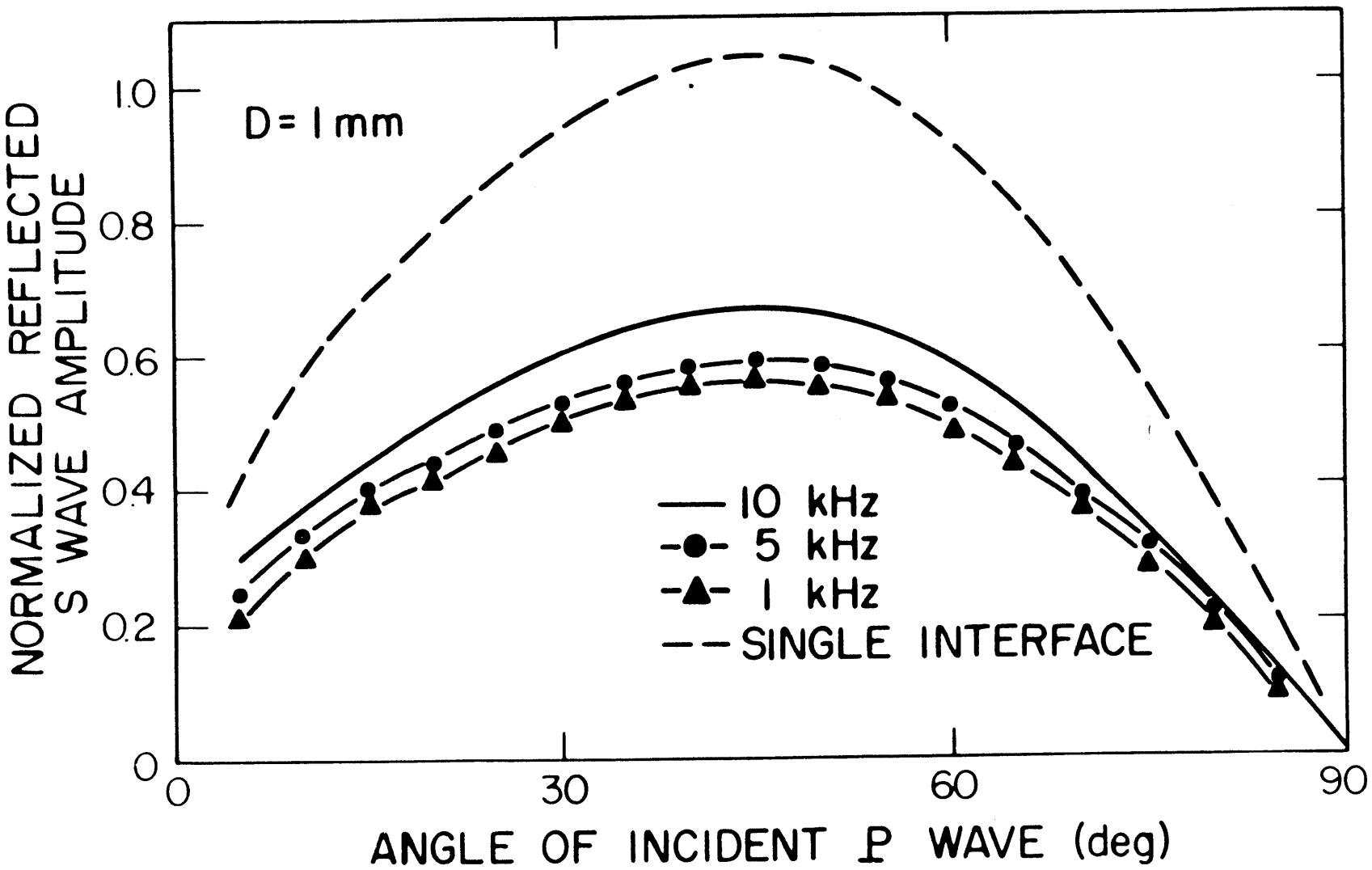
D = 1 mm
NORMALIZED REFLECTED S WAVE AMPLITUDE
1.0
0.8
0.6
0.4
0.2
0
0
30
60
90
ANGLE OF INCIDENT P WAVE (deg)
10 kHz
5 kHz
1 kHz
SINGLE INTERFACE

Figure 8

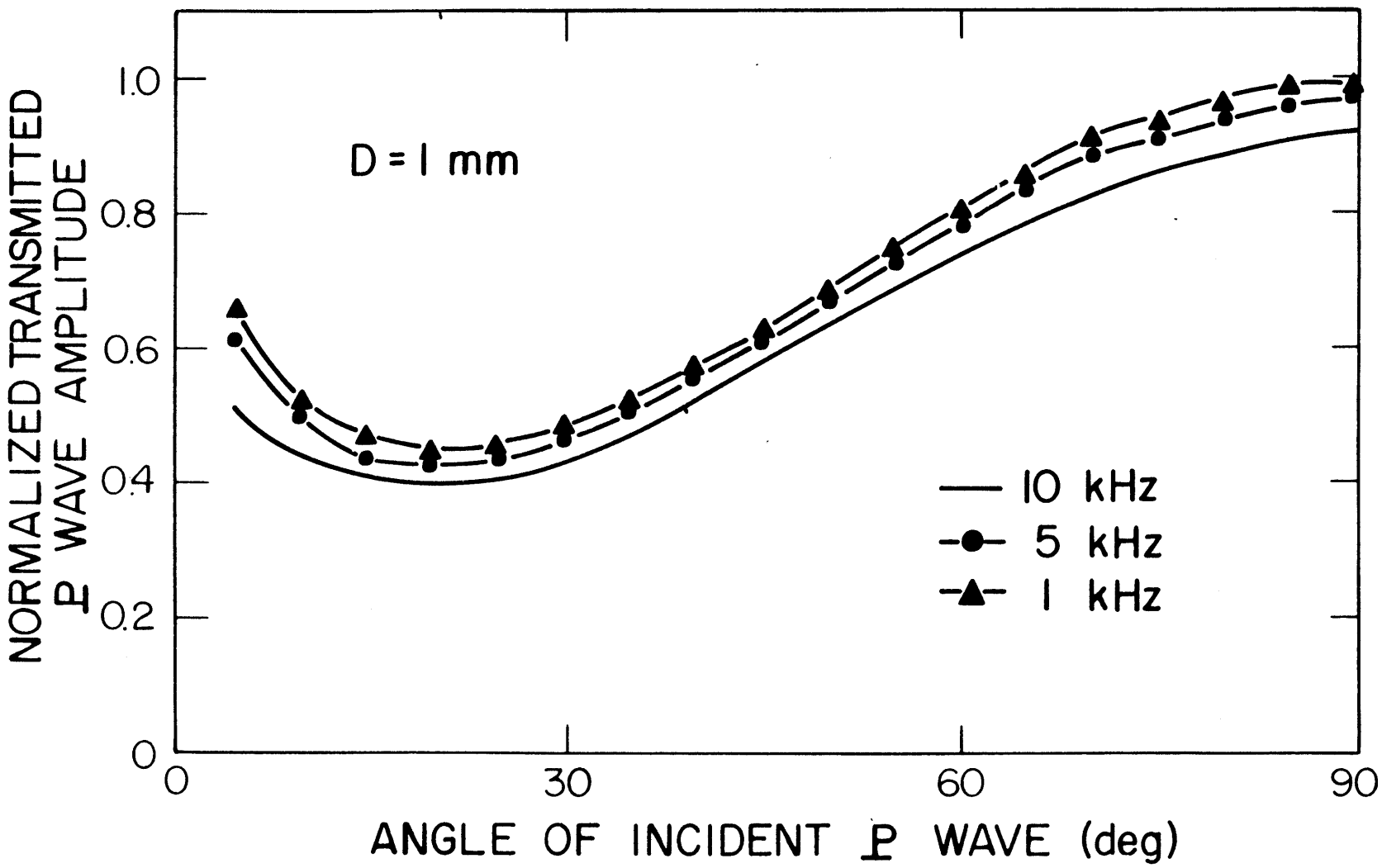
D = 1 mm
NORMALIZED TRANSMITTED P WAVE AMPLITUDE
1.0
0.8
0.6
0.4
0.2
0
0
30
60
90
ANGLE OF INCIDENT P WAVE (deg)
10 kHz
5 kHz
1 kHz

Figure 9

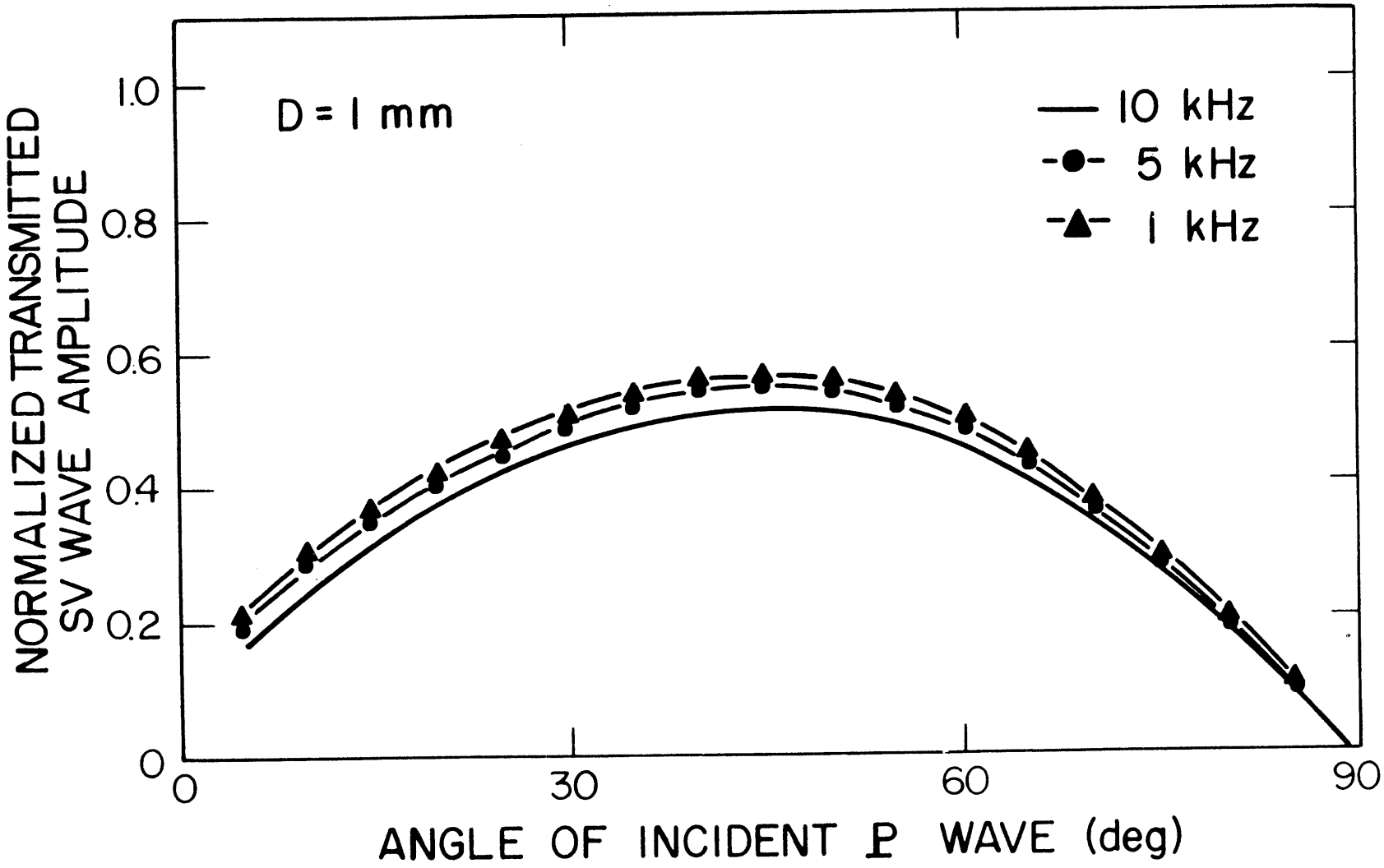
D = 1 mm
10 kHz
5 kHz
1 kHz
NORMALIZED TRANSMITTED SV WAVE AMPLITUDE
1.0
0.8
0.6
0.4
0.2
0
0
30
60
90
ANGLE OF INCIDENT P WAVE (deg)

Figure 10

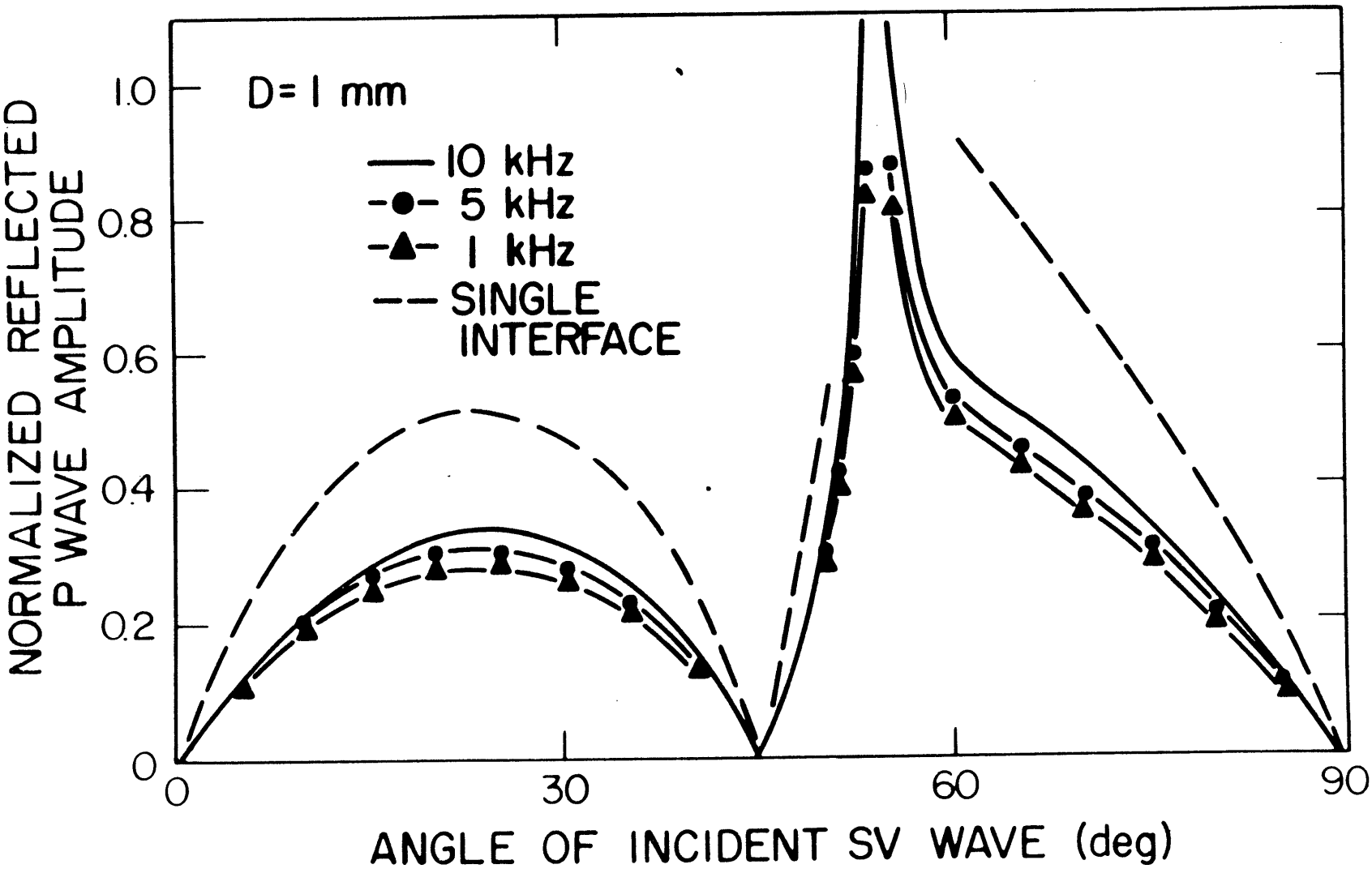
D= 1 mm
10 kHz
5 kHz
1 kHz
SINGLE INTERFACE
NORMALIZED REFLECTED P WAVE AMPLITUDE
1.0
0.8
0.6
0.4
0.2
0
0
30
60
90
ANGLE OF INCIDENT SV WAVE (deg)

Figure 11

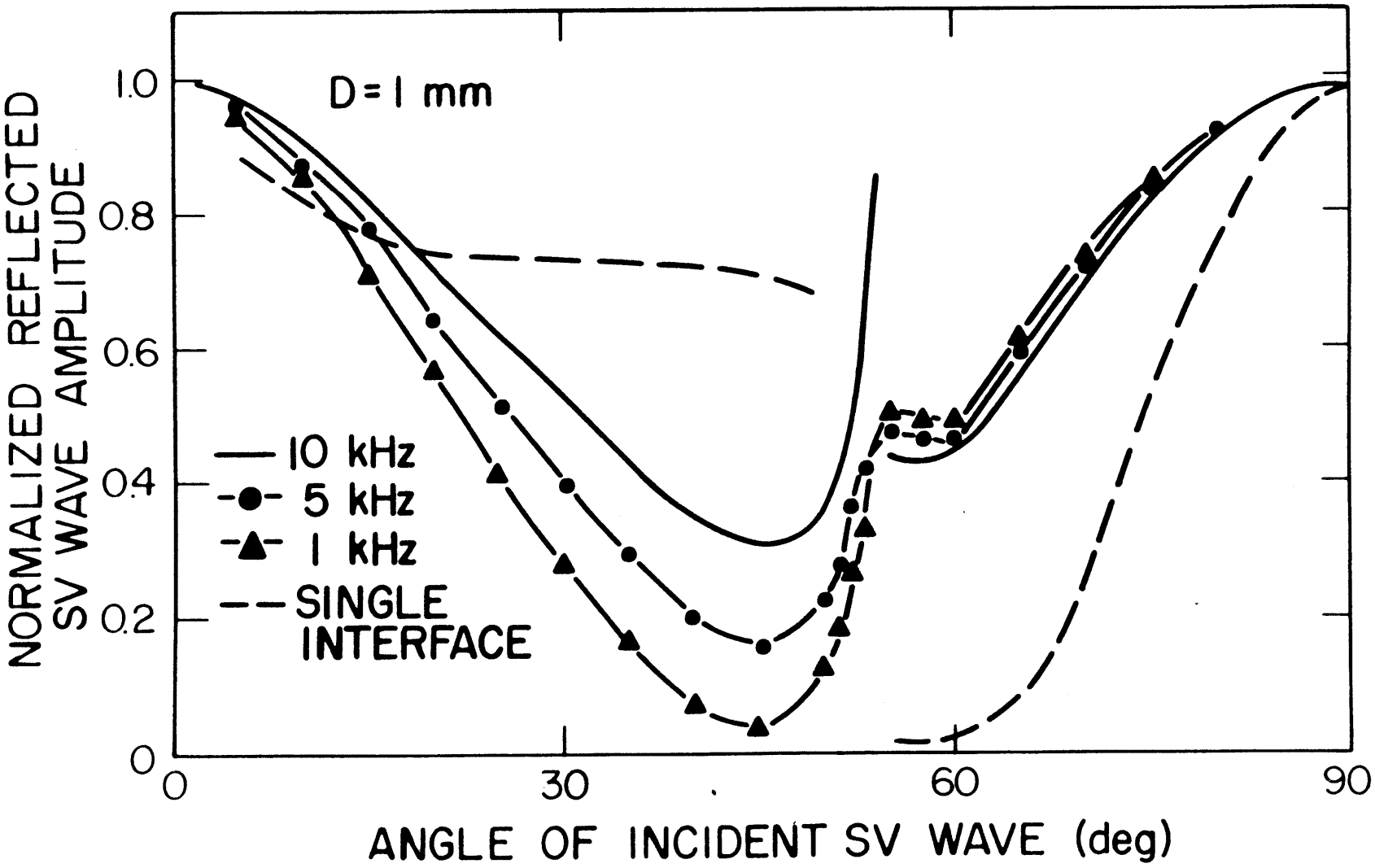
D = 1 mm
10 kHz
5 kHz
1 kHz
SINGLE INTERFACE
NORMALIZED REFLECTED SV WAVE AMPLITUDE
1.0
0.8
0.6
0.4
0.2
0
0
30
60
90
ANGLE OF INCIDENT SV WAVE (deg)

Figure 12

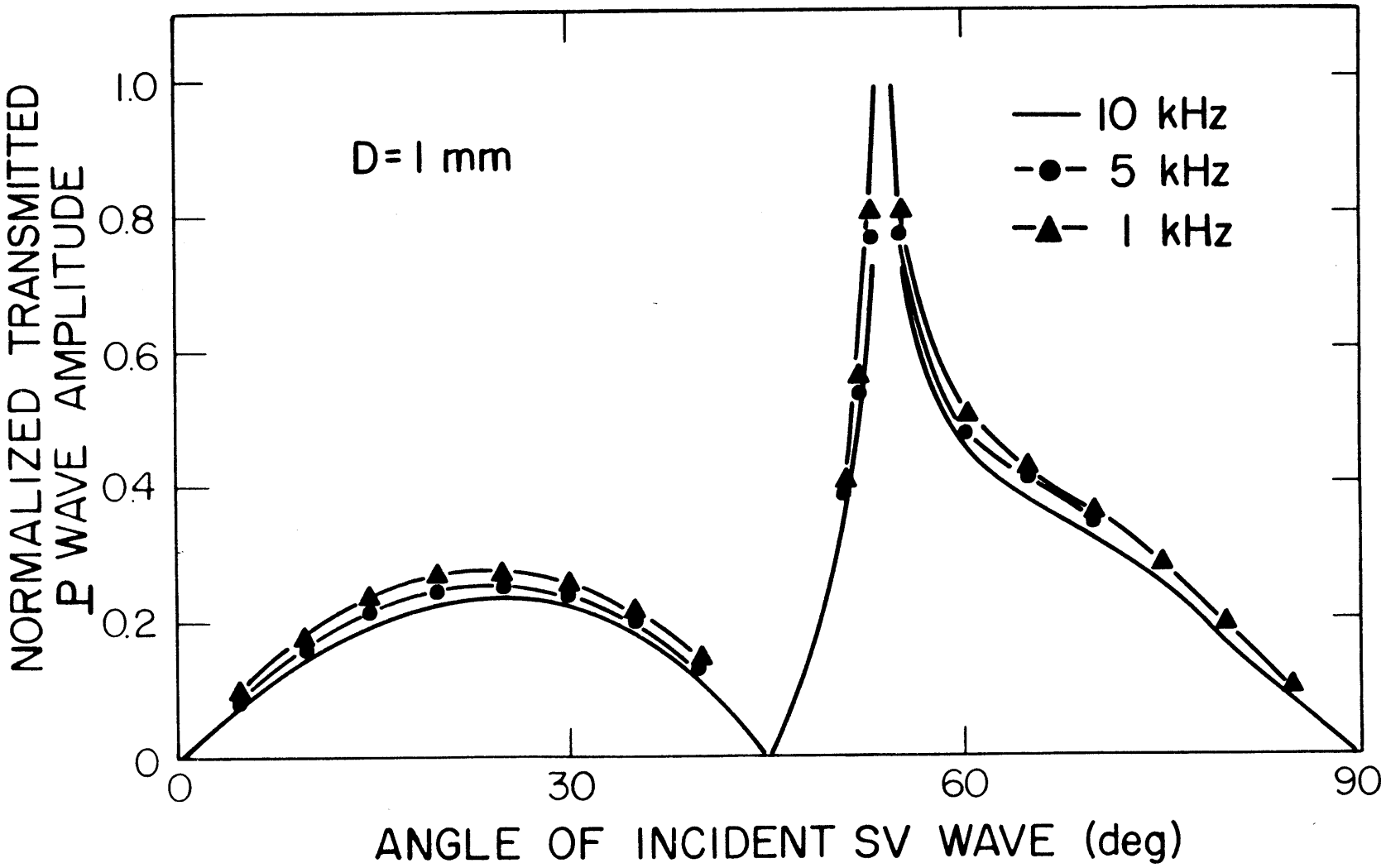
D=1 mm
10 kHz
5 kHz
1 kHz
NORMALIZED TRANSMITTED P WAVE AMPLITUDE
1.0
0.8
0.6
0.4
0.2
0
0
30
60
90
ANGLE OF INCIDENT SV WAVE (deg)

Figure 13

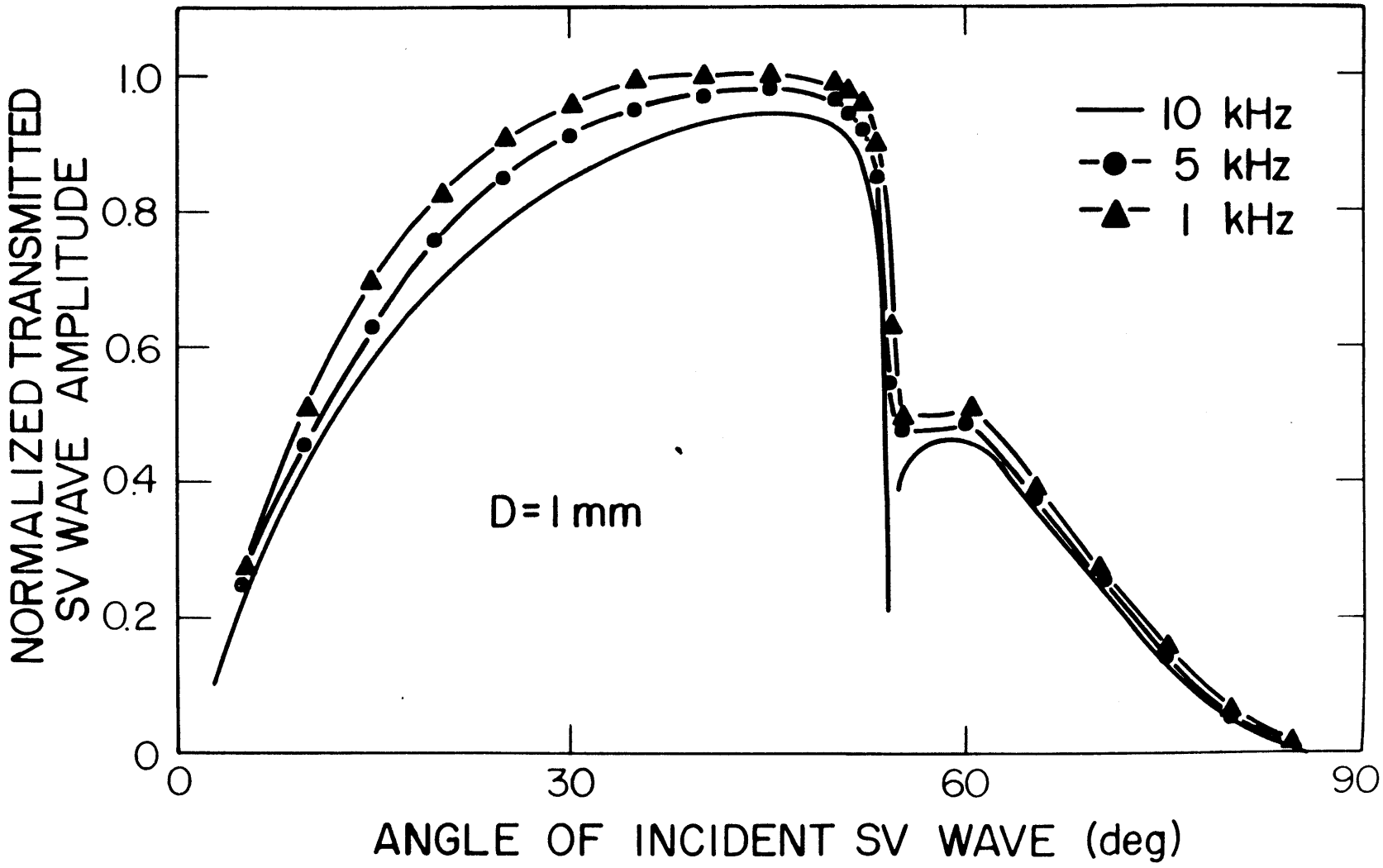
NORMALIZED TRANSMITTED
SV WAVE AMPLITUDE
1.0
0.8
0.6
0.4
0.2
0
0
30
60
90
ANGLE OF INCIDENT SV WAVE (deg)
10 kHz
5 kHz
1 kHz
D=1 mm

Figure 14

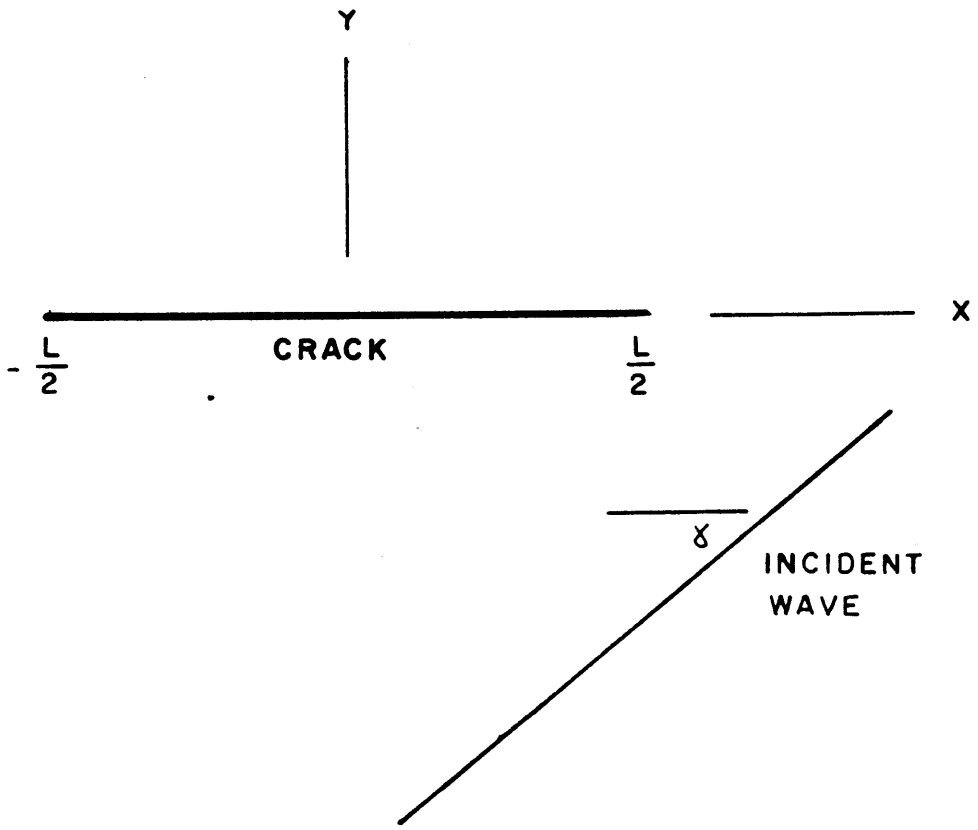

Figure 15

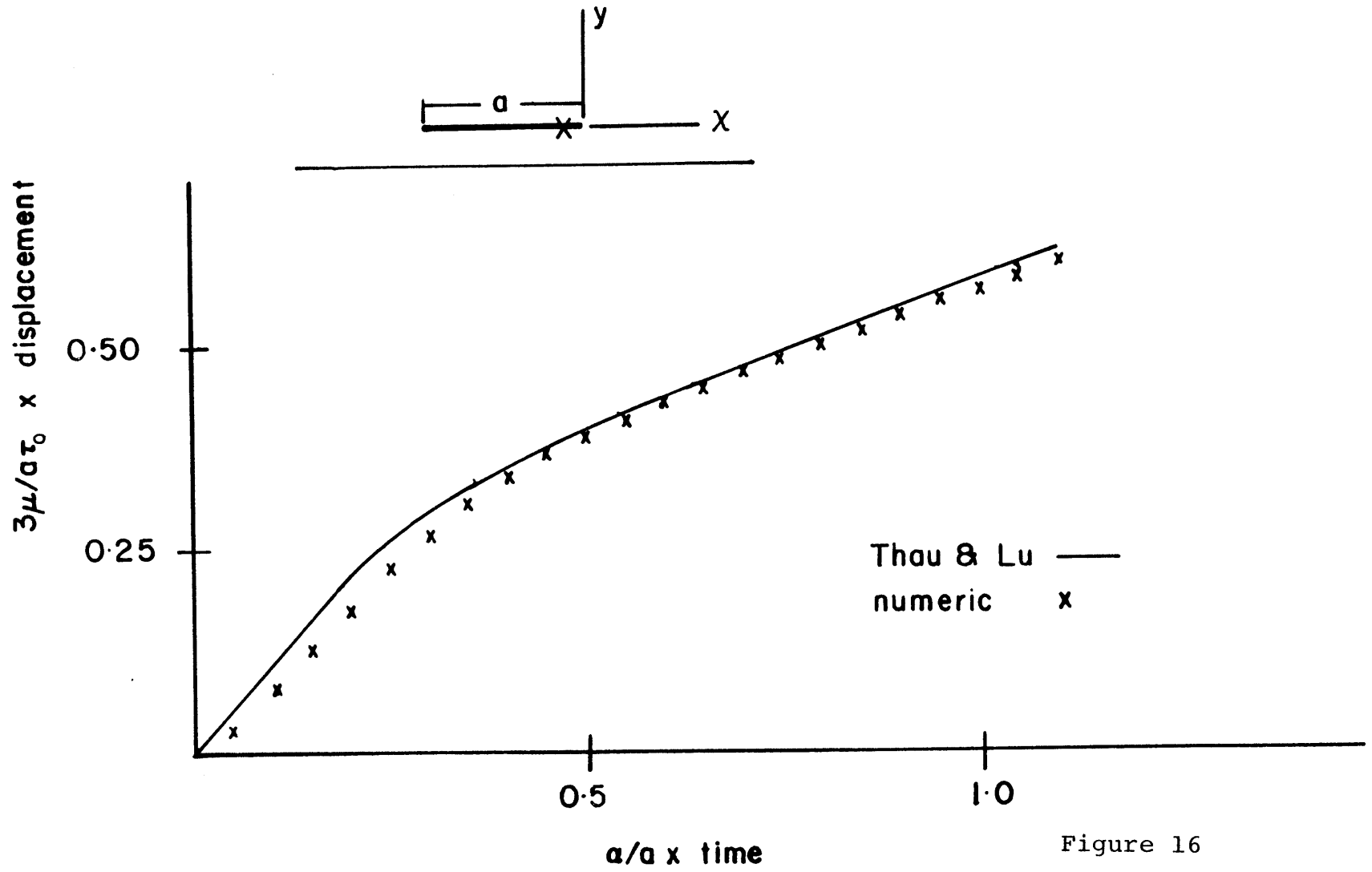
y
a
x
$3\mu/a\tau_0$ x displacement
0·50
0·25
Thau & Lu
numeric
0·5
1·0
a/a x time

Figure 16

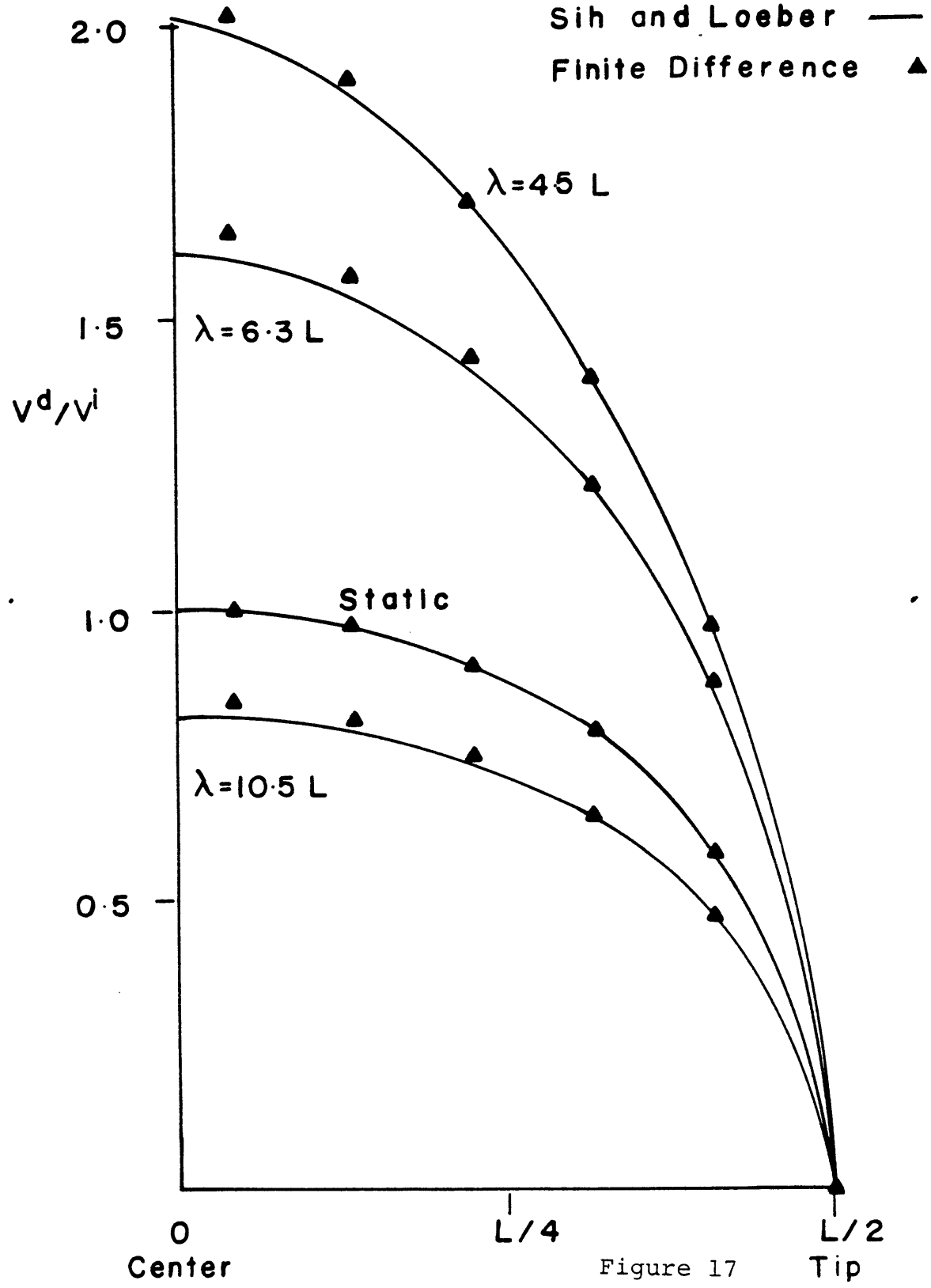
DISPLACEMENT ON CRACK SURFACE
NORMAL INCIDENCE
Sih and Loeber
Finite Difference
2·0
1·5
1·0
0·5
V^d/V^i
λ=4·5 L
λ=6·3 L
Static
λ=10·5 L
0
Center
L/4
L/2
Tip

Figure 17

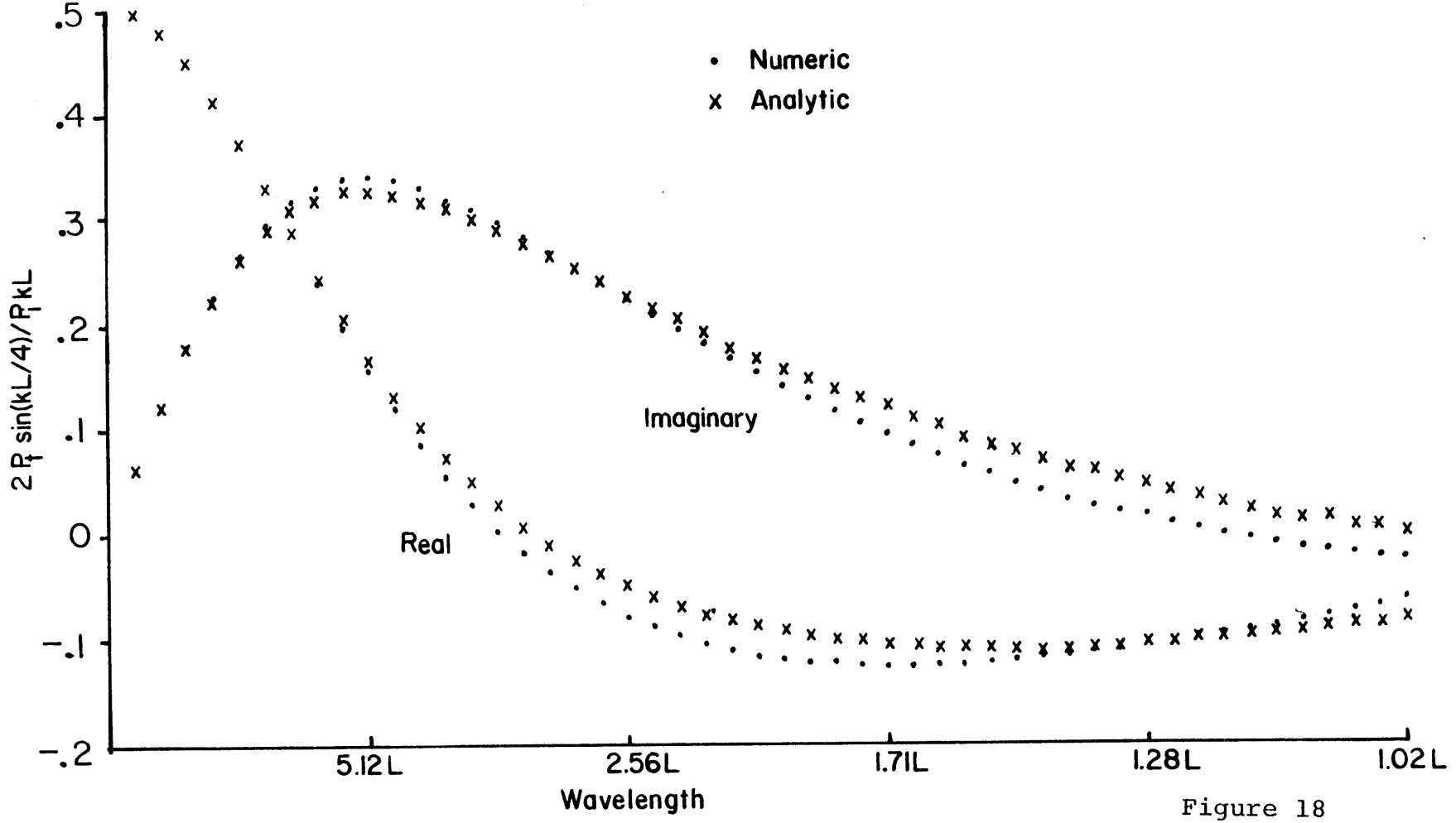
.5
.4
.3
.2
.1
0
-.1
-.2
$2P_1 \sin(kL/4)/P_1 kL$
• Numeric
x Analytic
Imaginary
Real
5.12L
2.56L
1.71L
1.28L
1.02L
Wavelength

Figure 18

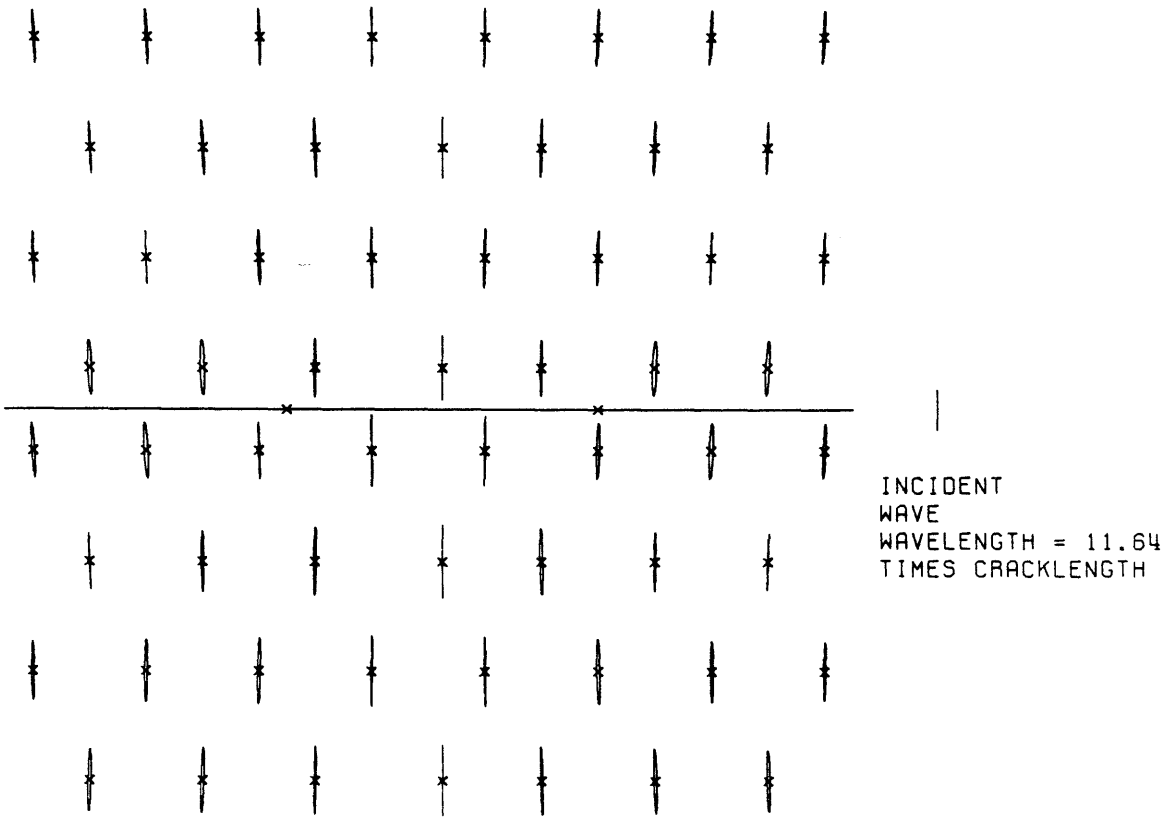

Figure 19

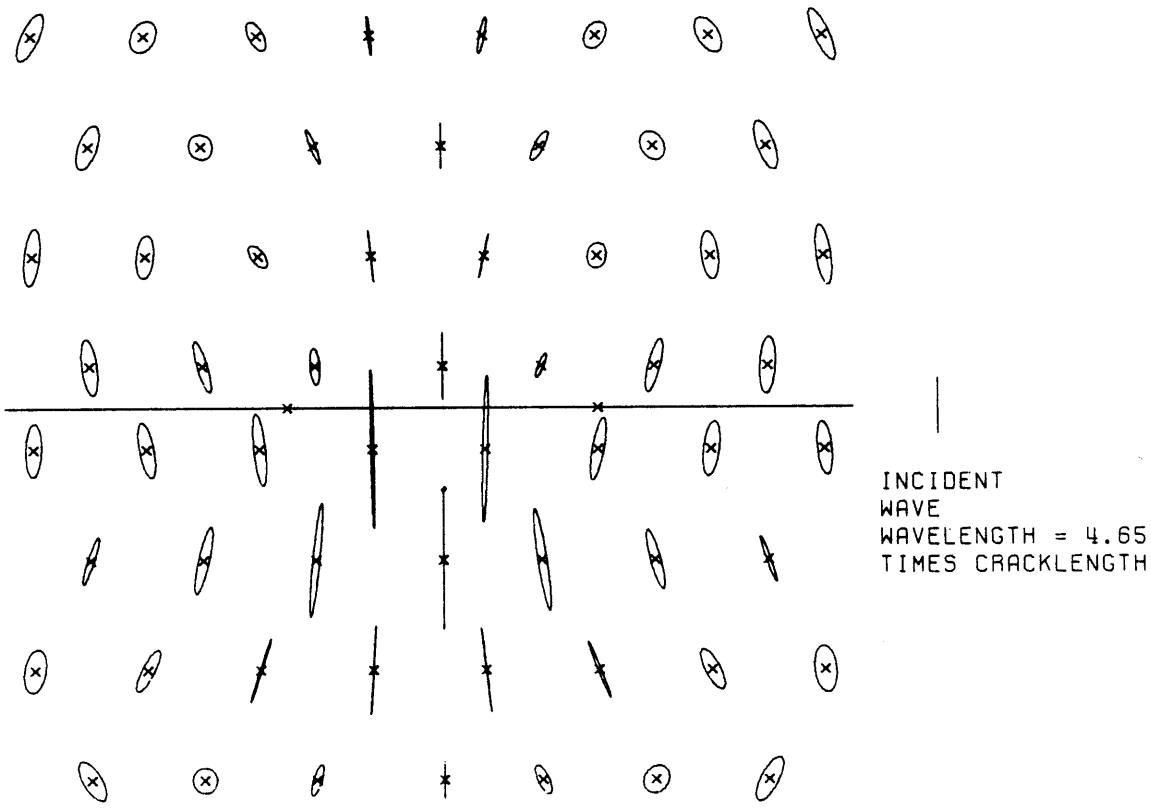

Figure 20

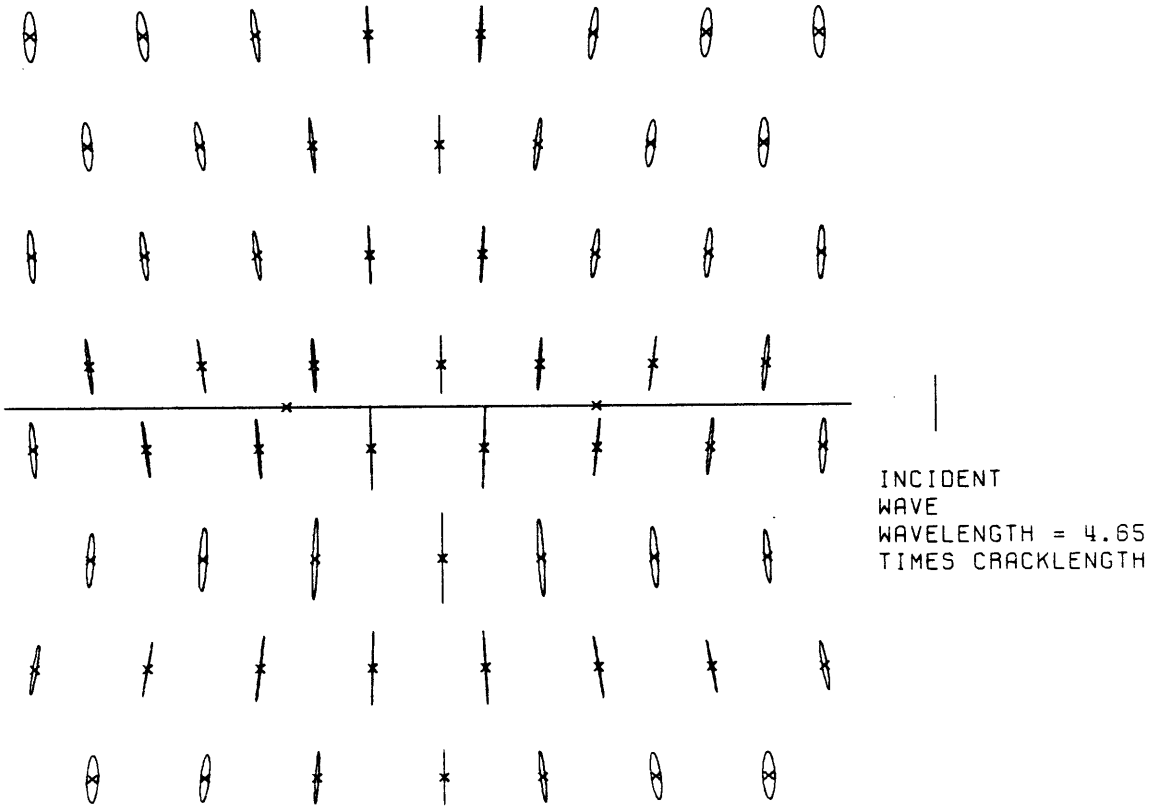

Figure 21

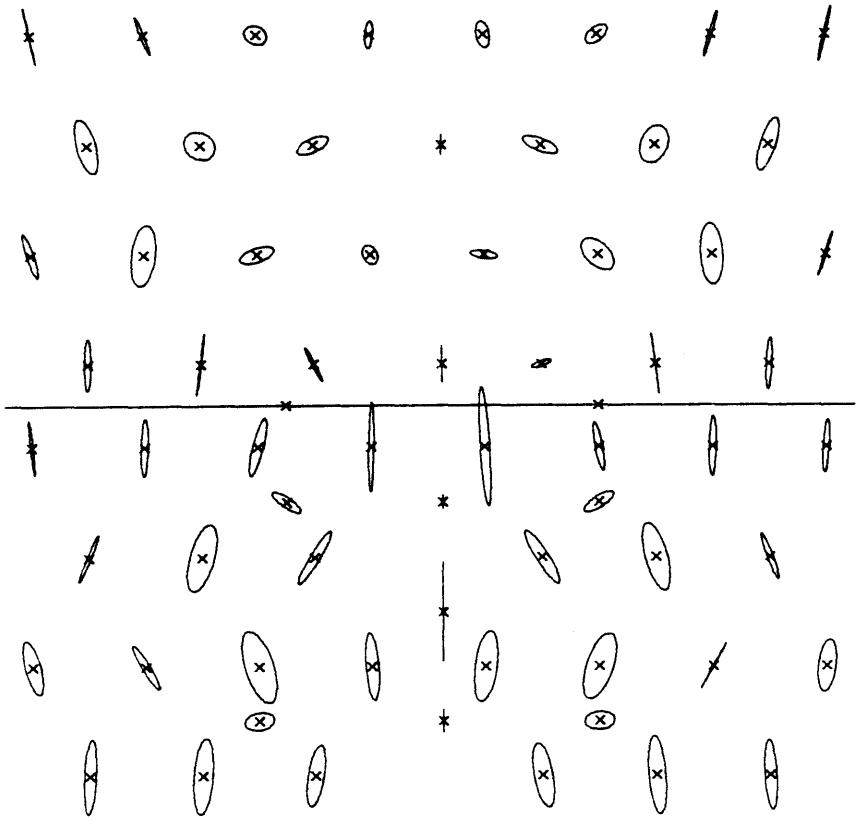

Figure 22

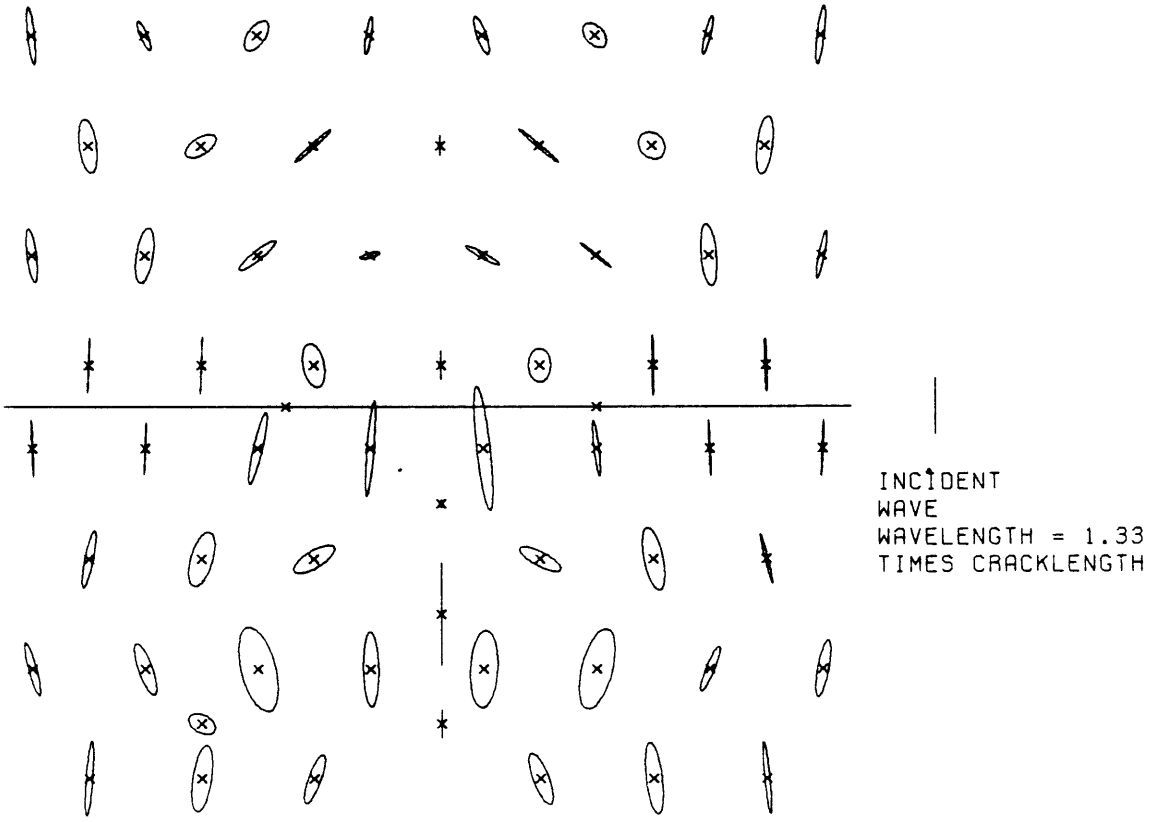

Figure 23

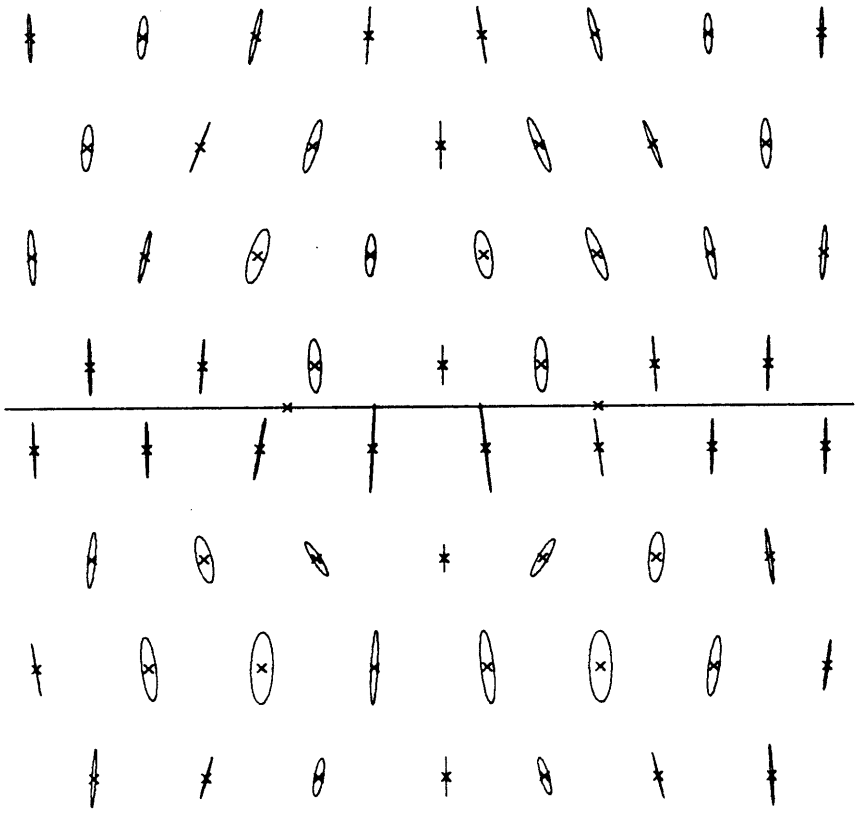

Figure 24

Figure 25

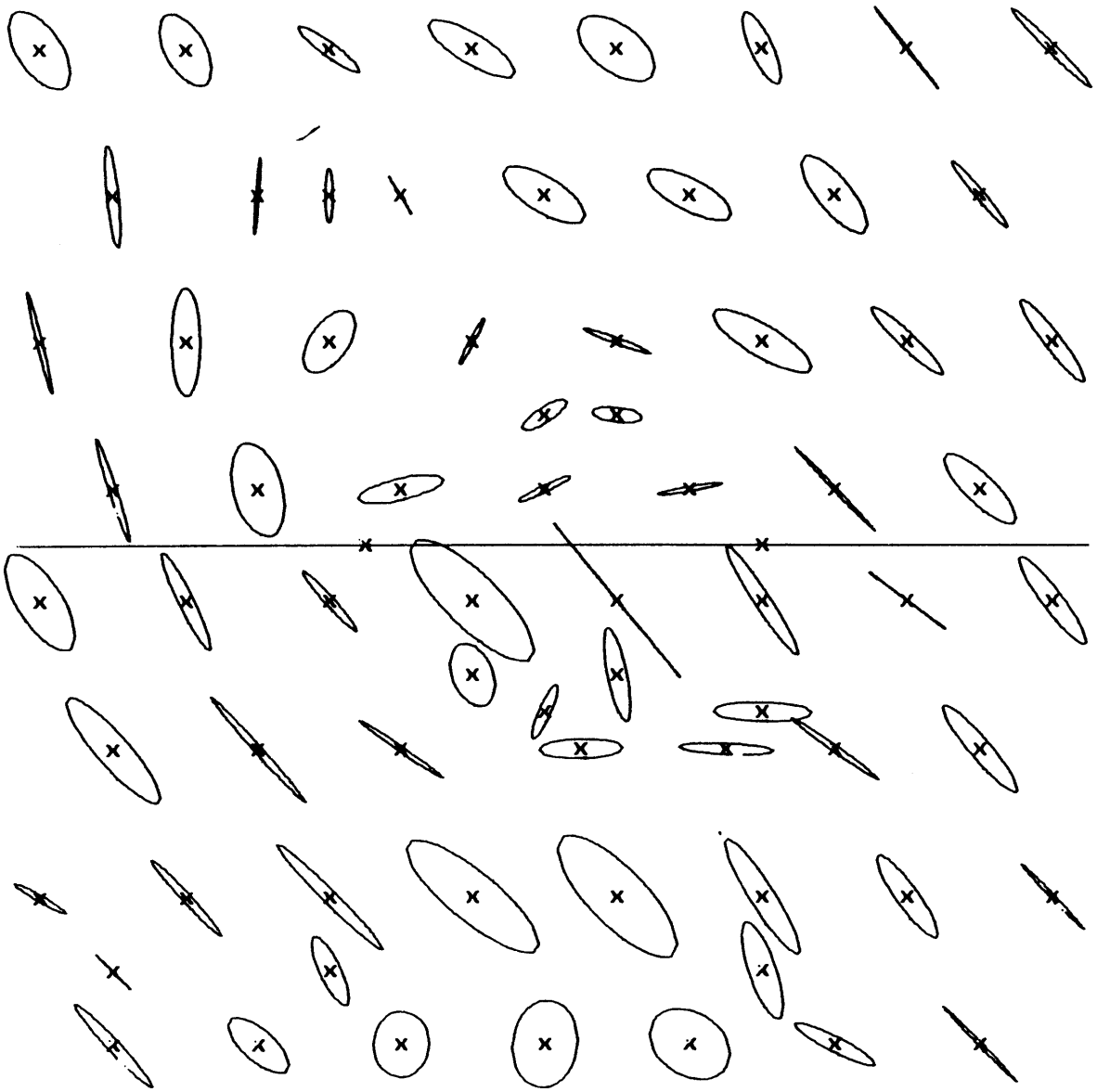

INCIDENT
WAVE
WAVELENGTH = 1.69
TIMES CRACKLENGTH

Figure 26

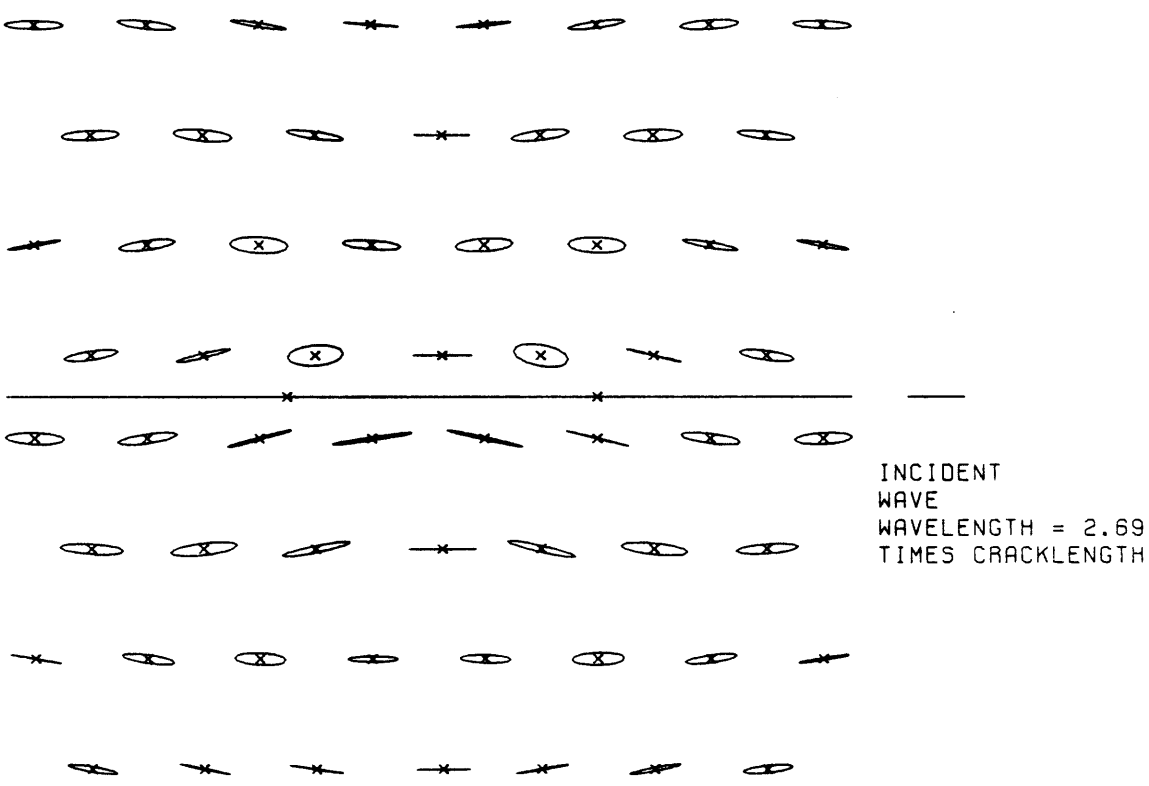

Figure 27

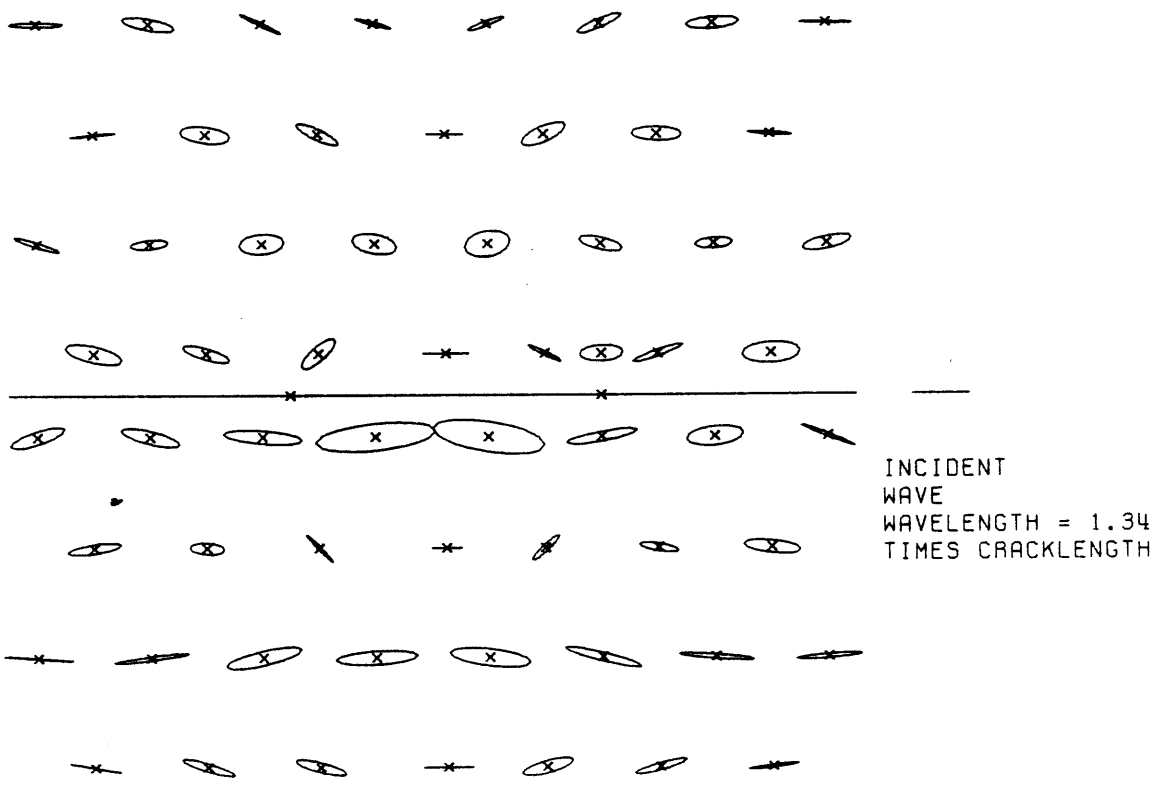

Figure 28

CHAPTER 3

PHYSICAL PROPERTIES OF ROCKS: DATA AND THEORY RELEVANT TO A HOT DRY ROCK GEOTHERMAL SYSTEM

Determination of seismic properties of a rock is often done with the intention of interpreting results to obtain other information about the rock. In Hot Dry Rock geothermal energy applications, it is desired to know the permeability of the rock, the porosity of the rock as well as to monitor the volume of rock from which heat is being extracted. To accomplish these goals using seismic techniques, a thorough knowledge of the relation between seismic and other physical properties of rocks is necessary. Unfortunately much of this knowledge does not yet exist. In other cases there is a nonunique relationship between physical properties which leads to nonuniqueness in the interpretation of seismic data.

This chapter presents a review of work on the relationship between physical properties of rocks and factors that control them. Since the most important factor influencing physical properties is the microcrack content of the rock, most discussion will center on the effects of cracks and how the crack content can be changed through application of pressure or heat. Whenever possible, that data presented will be that obtained

on samples collected at the Fenton Hill geothermal test site. The last section of this chapter contains a brief review of laboratory measurements made on Fenton Hill samples. Finally, theoretical models will be used along with laboratory data to predict velocity and attenuation under in situ conditions at Fenton Hill.

3.1 Effects of Microcracks on Elastic Properties of a Rock

It is now well established that the velocities of seismic waves in porous rock are strongly dependent on saturation conditions and quantity and shape of pores (Birch, 1961; Nur and Simmons, 1969; Kuster and Toksöz, 1974; Toksöz, Cheng and Timur, 1976; O'Connell and Budiansky, 1974; Mavko and Nur, 1978). For a dry rock containing less than one percent of its volume as pores, Kuster and Toksöz(1974) showed that the velocity can be as much as 10 percent lower than that of a rock of equivalent composition but containing no pores. The existence of microcracks in rocks has been confirmed visually using both petrographic and scanning electron microscopes (Simmons and Richter, 1976; Hadley, 1976).

3.1.1 Effects of Microcracks on Compressibility

Figure 1 shows volumetric strain vs. pressure

measured by Trice and Warren (1977) on a piece of dry granodiorite taken from a depth of 2615 meters (8581 feet) below the surface in borehole GT-2 at Fenton Hill. At pressures below 1000 bars, the volumetric strain is not a linear function of pressure as would be expected for a perfectly elastic material. The slope of the curve decreases as pressure increases which means that the rock becomes less compressible under pressure. This decrease in compressibility with increasing pressure is attributed to the closing of very narrow (small aspect ratio) cracks. Walsh (1965) studied the effects of microcracks on the compressibility of rocks and showed that the effective compressibility is equal to the compressibility of the solid material minus the change in porosity with pressure,

$$\beta_p = \beta_s - \frac{\partial c}{\partial p} \qquad (1)$$

where β_s and β_p are the compressibilities of the solid, uncracked material and the porous medium respectively and c is porosity or ratio of pore volume to total rock volume. In order to compute the change in porosity with pressure, some sort of pore model must be chosen. One model considered by Walsh (1965) is the so called penny shaped crack where pore space is

assumed to consist of very narrow, low aspect ratio, cracks. Aspect ratio is the ratio of width to length of a crack. For a material with penny shaped cracks, strain is a linear function of pressure up to the point where cracks close. The pressure at which a crack closes is given by

$$P_c = \pi\alpha E/4(1-\nu^2) \qquad (2)$$

where E is Young's modulus, ν Poisson's ratio and α the crack aspect ratio. Equation 2 shows that higher aspect ratio cracks close at higher pressures. For a granite with Young's modulus of .5Mbar and Poisson's ratio of .25, cracks that close at pressures of about 100 bars have aspect ratios on the order of 10^{-4}. The penny shaped crack model of Walsh predicts that the strain of a given material will be linear over a pressure range for which no cracks close completely and will have a change in slope at pressure P_c where a given crack or set of cracks close. In order to model a stress-strain curve as a function that has a continuous first derivative, a continuous spectrum of aspect ratios is required. Simmons, Siegfried and Feves (1974) and Siegfried and Simmons (1978) recognized this and found a relation between the porosity of cracks that close at a given pressure and the second

derivative of the stress-strain curve. Their method, called differential strain analysis, is based only in the assumption that strain is linear over any pressure range for which no cracks close completely.

Mavko and Nur (1978) considered the effects of non-elliptical cracks on the compressibility of rocks. These cracks have non-blunted tips which means that there are no stress singularities at the crack tips as is the case for the elliptical cracks considered by Walsh (1965) and others. When non-elliptical cracks are present, Mavko and Nur find that strain can be a non-linear function of pressure even at pressures where no cracks close completely. This non-linearity means that a given strain-stress curve can be modeled by considering non-elliptical cracks of only one aspect ratio. In addition, many different crack geometries can be used to match the curve which means that modelling of a stress-strain curve is a very non-unique process.

Toksöz, Cheng and Timur (1977) computed the rate of closing of an ellipsoidal crack of arbitrary aspect ratio. Their result gives equation (2) if aspect ratio is small. Using their formulation, the aspect ratio spectrum at any pressure can be computed once the spectrum at zero pressure is known. Figure 2, reproduced from Toksöz et al. (1977), shows

how the aspect ratio spectrum of a sandstone changes with pressure. A wide spectrum of aspect ratios ranging from 1 to 10^{-4} is present. As pressure increases, small aspect ratio cracks close and larger aspect ratio cracks become thinner and thus have smaller aspect ratios. Cracks with aspect ratios near 1 (spherical pores) will change very little in geometry when pressure is applied even though their volume decreases. Such cracks are very stiff and close completely only under very high pressure.

At pressures greater than 1000 bars, strain is nearly a linear function of pressure in most rocks (Figure 1) which means that most microcracks have closed. The slope of the strain-stress curve above 1000 bars gives the compressibility of the combination of the rock matrix plus pores of aspect ratio near 1. Walsh (1965) showed that the crack porosity of a rock at 0 pressure may be found by finding the zero pressure intercept of the linear (high pressure) portion of the strain curve.

3.1.2 Effects of Microcracks on Velocity of Seismic Waves in a Rock

Figure 3 shows P and S wave velocities as a function of pressure that were measured in the laboratory on a dry rock sample taken from a depth of 2615 meters

in GT-2 (Trice and Warren, 1977). The low velocity (5.1 km/sec) measured at zero pressure and gradual increase in velocity as confining pressure increases is typical of granites (Nur and Simmons, 1969). The change in velocity with increasing pressure is due to the closing of microcracks.

Figure 4 (from Toksöz, Cheng and Timur, 1977) illustrates the effects of cracks of different aspect ratios on velocity. For a material containing cracks of only one aspect ratio, P and S wave velocities as a function of crack porosity are plotted. For cracks of aspect ratio .01 it can be seen that for a porosity of 1% velocity is almost 20% lower than the velocity of the uncracked solid. A 1% porosity of cracks of aspect ratio 1 causes less than 1% change in medium velocity. Figure 4 shows that for equal porosities low aspect ratio cracks have a larger effect on the velocity of a rock than high aspect ratio cracks. Intuitively this can be understood since lower aspect ratio cracks are more compressible and thus decrease the effective modulus of a material more than will larger aspect ratio cracks. Also cracks of small aspect ratio will tend to have a smaller volume than large aspect ratio cracks which means that more narrow cracks than wider cracks will be present for a given porosity.

The effect of fluid saturation on the velocity of porous media is also shown in Figure 4. For fluid of very low viscosity, such as water, the finite bulk modulus of the fluid in cracks decreases the compressibility of the material and increases the P wave velocity. The water-filled cracks respond to shear as if the fluid were not present and there is less difference in S wave velocity between saturated and unsaturated conditions.

The results shown in Figure 4 were computed using the scattering theory of Kuster and Toksöz (1974). In this model cracks are considered as weak scatterers of elastic waves. Effective properties of a cracked material are computed by summing incident and scattered wave fields and considering the resultant field to be due to a homogeneous material with effective elastic properties. Their formulation is valid so long as the ratio of crack concentration to aspect ratio, c/α, is smaller than one. O'Connell and Budiansky (1974) and Budiansky and O'Connell (1976) formulated a theory using the self-consistent method that they claim is valid for higher crack porosity but small aspect ratios. They consider the effect of cracks on the static moduli of a rock and compute wave velocities from these moduli. Their theory reduces to that of Kuster and Toksöz to first order in c/α as do most of the theories that predict rock compressibility or

velocity of cracked material (Cheng, 1978). Cheng (1978) compared the predictions of the two theories for laboratory data on synthetic materials and found that the scattering theory gave better predictions than the self-consistent theory. The self-consistent theory gave results that were too soft, i.e., they overestimated the effects of pore space on the elastic properties of the media. Brunner (1976) pointed out this problem and presented a method to reformulate the self-consistent method.

Most theories show that to first order the most important parameter that is necessary to predict elastic properties for a dry cracked rock is the crack density parameter (Budiansky and O'Connell, 1976) which for spheroidal pores can be written as

$$\varepsilon = \frac{3}{4\pi} \frac{c_i}{\alpha_i} \tag{3}$$

where c_i is the concentration of cracks of aspect ratio α_i. Figure 4 illustrates the importance of ε. A .5% concentration of cracks of aspect ratio .01 produces the same effect as a 5% concentration of cracks of aspect ratio .1. In both cases the value of ε is .119. Hadley (1975) estimated values of ε for Westerly granite by measuring crack aspect ratios using a scanning electron microscope and used the

values to test the self-consistent and scattering theories. In view of the difficulty of trying to estimate aspect ratios for the jagged, irregular cracks observed in real rocks, her results were surprisingly good although she was not able to distinguish differences between the two theories.

Simmons and Nur (1968) compared laboratory measurements of velocities on granitic rock with borehole measurements of velocity of the same rock. They found that laboratory measurements yielded lower velocities than were measured in situ. They attributed this difference to two mechanisms: (1) the effects of fluid saturation of the rock in situ which increases rock velocity, (2) the introduction of cracks in a rock during the process of removing the sample from the borehole. Both of these effects are very important and should be kept in mind when comparing the laboratory data on GT-2 samples with in situ measurements.

3.2 Attenuation of Seismic Waves in Cracked Solids

The mechanism of attenuation in rocks has been a subject of great controversy for many years. Recently much effort has gone into laboratory experiments to measure the amount of attenuation of rocks under

different conditions of temperature and pressure. Hopefully these measurements will soon help to clarify what is the dominant attenuation mechanism under various conditions.

The decrease in amplitude due to attenuation of a seismic wave is generally written as

$$A \sim e^{-\alpha(f)x}$$

where $\alpha(f)$ is the frequency dependent attenuation coefficient and x is the travel distance. The dimensionless quantity Q is related to $\alpha(f)$ by

$$Q = \pi f/\alpha V$$

Attenuation in rocks has been found to be dependent on the wave amplitude, type of fluid filling the pores, temperature of the rock, presence of gas in the pores, amount of stress applied to the rock as well as the pore aspect ratio spectrum (Johnston, 1978; Winkler and Nur, 1979; Gordon and Davis, 1968; Knopoff, 1964a). Briefly, the following effects have been observed and reported in one or more of the following papers: Johnston (1978), Winkler and Nur (1979), Winkler, Nur and Gladwin (1979). Attenuation has been found to be independent of strain amplitude for strains

less than 10^{-6} but increases when strain amplitude is above that value. Attenuation increases as degree of saturation of the rock increases although Winkler and Nur (1979) observe a decrease in P wave attenuation as saturation increases between 95 and 100 percent. The addition of a small amount of gas to the liquid in the pores of a rock increases the attenuation of P waves and lowers the P velocities but does not affect S waves. Attenuation decreases as confining pressure increases.

Seismic attenuation is generally considered to increase linearly with frequency which means that Q is frequency independent (Knopoff, 1964a). It is difficult to produce a physical model to explain attenuation that predicts Q to be frequency independent. Frictional dissipation of energy on sliding crack surfaces has been proposed as one mechanism of attenuation and yields Q to be frequency independent (Walsh, 1966; Knopoff and MacDonald, 1960). Savage and Hasegawa (1967) point out that these frictional models are non-linear which means that superposition does not apply. They argue that the lack of the principle of superposition in the friction model of attenuation predicts results which are not observed. This argument is disputed by Gordon and Davis (1969) in reply to criticism by Savage (1969) of their con-

clusion that friction is an important mechanism (Gordon and Davis, 1968).

Relaxation mechanisms for attenuation predict frequency dependent Q with peaks in attenuation at frequencies dependent on fluid and solid elastic parameters, fluid viscosity and density as well as pore geometry and aspect ratio. Frequency independent Q can be obtained by summing relaxation mechanisms. This technique preserves linearity and the principle of superposition does apply (Zener, 1948).

Johnston, Toksöz and Timur (1979) review attenuation mechanisms and conclude that friction is the dominant attenuation mechanism at shallow depths in the earth's crust. Direct effects of fluids such as relative motion between fluid and solid (inertial flow), shear relaxation in the fluid and flow between adjacent interacting cracks (squirt flow) are also discussed briefly by Johnston et al., (1978). O'Connell and Budiansky (1977) analyzed squirt flow in detail and find that the maximum attenuation occurs at frequency

$$\omega_1 = (\kappa/\eta)\alpha^3 \qquad (4)$$

where κ is the bulk modulus of the solid and η the viscosity of the fluid. For viscous relaxation they find the characteristic frequency to be a linear

function of crack aspect ratio,

$$\omega_2 = (\mu/\eta)\alpha \tag{5}$$

where μ is the rigidity of the matrix material. For a typical case, $\kappa = 10^{11}$ gm/cm sec , $\eta = 10^{-2}$ poise, $\mu = 10^{11}$ gm/cm sec^2, $\alpha = 10^{-3}$, the shear relaxation frequency is 10^{10} rad/sec and is much higher than the squirt flow characteristic frequency which is 10^3 rad/sec. Two regimes of squirt flow are possible. In the low frequency limit, $\omega << \omega_1$ and $\omega << \omega_2$ flow between cracks is possible and pore pressure in all cracks is constant. This case is called isobaric. In the case $\omega >> \omega_1$ and $\omega << \omega_2$ there are pressure differences between cracks. In the high frequency limit, $\omega >> \omega_1$ and $\omega >> \omega_2$, shear relaxation occurs in the fluid. Since the model of O'Connell and Budiansky is formulated in a way that values of Q can be calculated from knowledge of the crack aspect ratio spectrum (porosity vs. aspect ratio) their model will be used in a later section to estimate Q at Fenton Hill.

Mavko and Nur (1979) discuss the effects of partial saturation on attenuation. In their model, fluid is allowed to move freely in pore space because of the presence of gas bubbles. Characteristic fre-

quency in this model is

$$\omega_s = \frac{2\eta}{\rho_f a^2}$$

where a is the crack thickness and ρ_f is fluid density. For crack thickness of .1 μm (Hadley, 1975) the characteristic frequency is on the order of 10^8 rad/sec. Their model, which will be discussed again later, is found to yield very high values of Q if the fluid contains less than 10% gas.

Thermoelasticity, a change in temperature that accompanies an adiabatic change in stress of a material, was proposed by Zener (1948) as an attenuation mechanism in metals. If the material is non-homogeneous the change in temperature will be non-uniform and flow of heat occurs. Mechanical energy is converted to heat and temperature increases. Savage (1966) studied the effect of cracks on thermoelasticity and found Q of about 200 for crustal rocks. Characteristic frequency in this model is

$$\omega = D/a^2$$

where D is thermal diffusivity of the rock and 2a is the crack length. For D = 10^{-2} cm^2/sec and a = 25μm

(Hadley, 1976) the characteristic frequency is 1600 rad/sec. His model predicts that attenuation increases linearly with temperature which means that thermoelasticity may be an important attenuation mechanism in cracked rocks at shallow depths in geothermal reservoirs.

The dominant attenuation mechanism in any particular rock is a function of many parameters describing the rock and conditions under which the attenuation is measured. Johnston, Toksöz and Timur (1979) argue that friction is the dominant mechanism for rocks under crustal conditions while Winkler, Nur and Gladwin (1979) argue that friction is not important and propose that fluid effects are the dominating influence. Since modeling of attenuation mechanisms is at an early stage in development and there is little data to support the current theories it is difficult to choose between the proposed mechanisms of attenuation.

3.3 Pore Pressure Effects on Mechanical Properties of Rocks

It has already been mentioned that increasing the confining pressure applied to a dry rock causes the velocity of the rock to increase and attenuation to decrease. These effects are explained by the closing of microcracks under pressure. When pore fluids are present, different results are observed.

Figure 5, from Nur and Simmons (1969), shows velocities of seismic waves measured on a granite from Casco, Maine under three conditions. In one case there is no fluid in the pores, in another the pores are saturated but the saturating fluid is open to atmospheric pressure so pore pressure is one bar. When the pore pressure equals the confining pressure, the third case, there is very little change in P or S wave velocity with pressure. This lack of change is generally considered to result because the pore pressure prevents cracks from closing (Brace, 1972). In fact, many physical properties have been found to be dependent on the difference between confining pressure and pore pressure which is known as effective pressure. Terazaghi (1923) introduced this concept in soil mechanics. Among the rock properties found to depend on effective pressure are velocity, attenuation (Johnston, 1978) and permeability (Potter, 1978).

Since pores in rock in situ are often fluid filled, laboratory data at the effective in situ pressure must be used to compare with field data. Generally confining pressure is considered to be equal to the lithostatic load, ρgz, where ρ is rock density, g is the acceleration due to gravity and z is the depth of burial. Pore pressure is often assumed to be due to a column of water of depth z and is thus some

fraction of the lithostatic load since the density of water is less than that of rock.

Simmons and Cooper (1976) used the technique of differential strain analysis (DSA) to measure porosity of rock samples obtained from GT-2. Using DSA they were able to compute the spectrum of crack porosity as a function of closure poressure (Simmons et al., 1974). They find that there are cracks with very low closure pressure, some as low as 150 bars, and argue that many of these cracks are closed in situ because of the effects of the load of the overburden. Blair et al. (1976) give the results of stress measurements made during hydraulic fracturing experiments in the GT-2 and EE-1 wellbores. Their results are listed in Table 1. Pore pressure is computed assuming that the head of water is at a depth of 610 meters. Vertical earth stress, S_1, is computed from the weight of the overburden. Table 1 shows that there is no consistent pattern of minimum stress, σ_3, with depth. Choosing some arbitrary procedure to find in situ properties from laboratory data is likely to give misleading results because stress is not isotropic and pore pressure must be taken into account. Both of these quantities are poorly constrained.

3.4 Effects of Changes in Temperature on Physical Properties of Rocks

In order to extend the life of a Hot Dry Rock geothermal system it is hoped that the size of the reservoir will increase in time through the process of thermal stress cracking so that the heat source region expands (Harlow and Pracht, 1972). While it is still not proven that thermal stress cracking will occur on a scale large enough to expand the reservoir, it is likely that the microcrack porosity of the rock will increase as heat is removed from it. The mechanisms that increase porosity as heat is removed include bulk volume changes that accompany the extraction of heat from the rock, stress introduced on a microscopic scale in the rock as a result of differences in volume thermal expansion of minerals as well as stress gradients that result from thermal gradients when heat is removed from a region near the fracture. These effects have been discussed by Nur and Simmons (1970).

One of the goals of seismic mapping of a geothermal system is to try to define the volume of rock from which heat is being extracted. While no successful experiments have been carried out in the laboratory to simulate the effects of heat extraction on physical properties of rocks under <u>in situ</u> condi-

tions, the effects of heating a rock in the laboratory have been investigated. Two regimes, fast and slow heating have been studied. Thermal gradients are kept low during slow heating so that no cracking results from the stresses induced by thermal gradients. Microcracks are introduced by the inhomogeneity in strain that occurs because of the non-uniform coefficients of thermal expansion of minerals. These cracks are called thermal cycling cracks by Simmons and Cooper (1977) who investigated the effects of heating rocks at rates of less than 1°C/min. They found that for Westerly granite crack porosity increases exponentially with temperature

$$c = 10^{-3.75+(2.24\times10^{-3})T_m} \qquad (6)$$

where T_m is the maximum temperature in degrees Celsius. The crack porosity doubles for each 140° increment in T_m. Using DSA they found that most of the cracks formed by thermal cycling are low closure pressure cracks. According to equation (2), low closure pressure cracks have low aspect ratios and are the cracks that have the greatest influence on the elastic properties of the rocks. Simmons and Cooper (1977) argue that thermal cycling cracks in granitic rock should occur near grain boundaries of quartz and other minerals.

that compose a granite. Sprunt and Brace (1974) observed thermal cycling cracks in Westerly granite using a scanning electron microscope and reported that most of the new cracks occurred around grain boundaries. Laughlin and Eddy (1977) found that samples from GT-2 contained as much as 30% quartz; Simmons and Cooper found that Westerly granite contains 22% quartz. The high quartz content would imply that there should be a larger increase in crack porosity in a thermally cycled GT-2 rock than in Westerly granite.

Johnston (1978) investigated the effect of thermal cycling on both Q and velocity of rocks. He found that thermal cycling a rock such as Westerly granite to temperatures less than 400° C caused the rock velocity to decrease while Q increased. This astonishing result is difficult to explain. Johnston argues that while heating increased the total porosity, the porosity of very small aspect ratio cracks has decreased due to widening of narrow cracks. These narrow cracks are responsible for the largest attenuation in the friction model of attenuation proposed by Johnston. It is difficult to see how the data of Simmons and Cooper (1978) support his conclusion since their data shows an

increase in porosity of low aspect ratio cracks for thermally cycled Westerly granite.

Potter (1978) reported that permeability of rock taken from GT-2 decreased as temperature increased from 20°C to the in situ temperature at the depth from which the sample was cored. He attributed this decrease to the narrowing of cracks as the rock was heated to its in situ temperature. This explanation is in disagreement with the model proposed by Johnston to explain Q data. The decrease in permeability may have been caused by the closing off of a fraction of the flow paths due to adjustments in the volume of the minerals. There could still be a widening of a large portion of the cracks which would decrease attenuation.

3.5 Permeability

In an idealized Hot Dry Rock system, water contacts the heat source as it flows through an artificially created hydrofracture as well as when it flows through the pores of the rock. Permeability is a measure of the ratio of the rate of flow of a fluid to the pressure gradient across a rock. For isotropic materials, Darcy's law gives

$$k = \frac{nQ}{A\nabla p}$$

where k is permeability, Q is flow rate, η viscosity, A cross section area and ∇P fluid pressure gradient. Permeability is strongly related to porosity but there is no simple relationship between permeability and porosity. This is because the permeability of a given set of fractures is affected by the width of the cracks, the number of pores that are interconnected as well as any anisotropy in the orientation of the pores. Large throughgoing microcracks as well as joints have a profound effect on the permeability of a given rock. Batzle (1978) found that a core sample containing one large partially sealed fracture had a permeability of six orders of magnitude larger than that of a sample of the same material without the fracture. Pratt et al. (1977) measured permeability along joints in a block of granite and found values parallel to the joints to be about 18 times those measured on small laboratory samples of the same material.

The in situ permeability of a geothermal heat source region cannot be measured directly unless fracture area and change in porosity with pressure, $\partial c/\partial \rho$, are known (LASL HDR Staff, 1978). Knowledge of these values is important to the development of a flow model of the geothermal system.

There is currently no model to relate changes in

microcrack porosity to changes in permeability. A geometric mean model relating permeability and electrical conductivity to fracture length, width, porosity and viscosity of the fluid is discussed by Batzle (1978). He considers fractures to be parallel plates and finds a relationship between permeability and the geometric properties of the plates. He finds that permeability is proportional to the square of the crack thickness. By making certain assumptions, he is able to match laboratory permeability and conductivity values as a function of confining pressure with his theory using geometrical information on cracks obtained from differential strain analysis.

Trice and Warren (1977) attempted to find a relationship between permeability and elastic properties of rocks as a function of pressure. By making assumptions about flow through a rock and crack strain vs. pressure they find that compressional modulus, ρV_p^2 , at pressure P and permeability are related to pressure as

$$\left(\frac{\rho V_p^2}{\rho_o V_{op}^2} - 1\right) \sim \left(1 - \frac{P}{P_o}\right) \tag{7}$$

$$k \sim \left(1 - \frac{P}{P_o}\right)^3 \tag{8}$$

where ρ_o and V_{op} refer to values for the uncracked matrix and P_o is a reference pressure. They plot values of k and $(\frac{\rho V_p^2}{\rho_o V_{op}^2} - 1)^3$ measured in the laboratory on Fenton Hill samples as well as on Westerly granite. Figure 6 is an example of their results for a sample from a depth of 2902 meters (9522 feet) in GT-2. The figure shows some correlation between elastic properties and permeability but further work is required to gain more insight into this relationship.

3.6 Laboratory Data on Rocks from the Fenton Hill Geothermal System

Laboratory measurements on rock samples collected from various depths in the Fenton Hill geothermal system have been made to obtain values of many physical properties under various conditions of temperature and pressure. Some of this data will now be reviewed. In addition, the P and S wave velocities as a function of pressure measured on a dry sample from 2615 meters (8581 feet) by Trice and Warren (1977) will be modeled using the technique of Cheng (1978) to find a pore aspect ratio spectrum. Once the spectrum is known, predictions of velocities under saturated conditions can be made for various values of effective pressure. In addition, values of Q for P and S waves will be computed using the technique of O'Connell and Budiansky

(1977) and the pore aspect ratio spectrum at various pressures obtained using Cheng's technique.

An extensive study of the petrography of cores obtained from GT-2 and EE-1 is contained in Laughlin and Eddy (1977). They present petrographic data on 37 samples obtained from various sections of the wellbore ranging in depth between 2070 and 2980 meters. Table 2 lists modal analysis for five samples taken from depths between 2413 and 2905 meters. This is the depth range for which seismic data will be discussed in the next chapter. Figure 7 is a generalized lithologic log of the wellbore from Blair et al. (1976).

Potter (1978) studied permeability as a function of temperature and pressure on samples from depths of 2615 and 2902 meters in GT-2. He found that permeability decreases as temperature increases up to a certain critical temperature and then increases beyond that temperature. Figure 8, from his thesis, shows permeability as a function of temperature for a sample from 2615 meters (8580 feet). The minimum permeability occurred at about 130°C which is lower than the 180°C virgin in situ temperature at 2615 meters. Potter argues that the permeability minimum represents an upper bound on the in situ permeability. He asserts that the effect of coring a sample and bringing it to the surface is a net contraction of the minerals in

the rock due to the decrease in temperature which provides a decrease in volume that is greater than the increase in volume brought about by the decrease in pressure. This net decrease in volume produces new cracks as well as causing existing cracks to widen and extend. Differences in thermal expansion and compressibility between minerals is especially important in this model since these differences will cause changes in the sizes of cracks that separate two minerals with widely differing properties. Potter finds that the permeability change with temperature measured in the laboratory shows no hysteresis as long as the temperature is maintained below the critical temperature. If temperature increases beyond the point of the permeability minimum, permanent damage occurs in the form of new cracks being introduced. Upon cooling the damaged sample, permeability is found to be higher at a given temperature than it was when the sample was being heated. Visual confirmation of the existence of new cracks in the heated sample is obtained by observing heated and unheated samples at high magnification using the scanning electron microscope.

Potter (1978) also reports that permeability increased by a factor of two to three after water at 200°C had been circulated through a sample for 120 hours.

This increase was attributed to the dissolution of quartz as hot water passed through the rock. Another mechanism to change the permeability during a period of long flow at high temperature is the formation of clays and alteration products along the flow channels. This has been observed in granites by Summers et al. (1975) who found that permeability decreased with time and in some cases flow stopped altogether.

Trice and Warren (1977) measured P and S velocities as a function of confining pressure on dry samples from depths of 2615 and 2902 meters below the surface in GT-2. They measured crack porosity by finding the zero pressure intercept of the linear, high pressure, portion of the volumetric strain vs. pressure curve (Walsh, 1965). Total connected porosity was measured using immersion techniques. Figure 1 shows the volumetric strain vs. pressure data for sample 8581 (2615 meters) and Figure 3 shows P and S wave velocities measured to six kilobars on a sample from the same depth.

3.6.1 Modeling Laboratory Velocity Data to Obtain Pore Aspect Ratio Spectrum

In order to compare laboratory data with <u>in situ</u> measurements of velocity, values of velocities in water saturated samples are needed. As discussed

earlier, the P wave velocity of a fluid saturated cracked rock is larger than the velocity of the same dry rock and is also much less pressure dependent. Using a theoretical model of elastic properties of rocks, the water saturated velocities as a function of effective pressure can be predicted from laboratory measurements on dry rocks. Theoretical modeling of laboratory measured velocities on a dry sample from 2615 meters was undertaken using the integral formulation of velocity of a two phase medium of Cheng (1978). His method follows the idea of Brunner (1976) to take account of crack interactions in a modified self-consistent fashion. Cheng uses the scattering model of Kuster and Toksöz (1974) to account for the effect of a single crack. Crack closure under pressure is computed as in Toksöz et al. (1976). Cracks are modeled as oblate spheroids.

Values of P and S wave velocities as a function of pressure to 1500 bars were taken from tables given in Trice and Warren (1977). The values used are listed in Table 3. A set of aspect ratios for cracks were chosen such that most cracks would close between 0 and 1500 bars. Values of uncracked matrix moduli are also needed. Since no values of these moduli were available, values were chosen and modified until the best fit to the data was found. The inversion scheme of Cheng

(1978) was used to invert velocity vs. pressure data to find the porosity of cracks as a function of aspect ratio that gave the best predictions of dry velocities according to his model. Once this aspect ratio spectrum was found, the velocities as a function of effective pressure could be computed for a rock saturated with water. Bulk modulus of water was chosen to be that of water at 200°C and 100 bars pressure. Figure 9 shows the laboratory velocities of the dry sample as well as the velocities computed using the crack aspect ratio spectrum that resulted from the inversion. The predicted velocities of water saturated rock are also shown. The fit to the data are very good and, as expected, velocities in the water saturated case are larger and P wave velocities are less pressure dependent than are the dry velocities. Table 4 lists the crack aspect ratio spectrum that gives the best fit to the velocity data. The values of the matrix moduli that gave the best fit are also given. These results will be useful when making comparisons with in situ measurements of velocity.

3.6.2 Prediction of Attenuation from the Pore Aspect Ratio Spectrum

Very few theoretical models of attenuation are available than can be used to predict Q values using information obtained from other measurements on a sample. The models of Johnston (1978) are formulated to predict pressure and frequency dependence of Q so that the relative importance of attenuation mechanisms can be obtained from measurements of Q under various conditions. Savage's model of thermoelastic attenuation of waves by cracks requires knowledge of crack length distribution in order to compute Q. The models of O'Connell and Budiansky (1977) and Mavko and Nur (1979) are both formulated so that Q values can be computed from the pore aspect ratio spectrum. Both of these models consider the mechanism of attenuation to be the flow of fluid in and between cracks due to change in fluid pressure as a wave passes. O'Connell and Budiansky consider the cracks to be completely saturated with fluid while Mavko and Nur consider the effects of small bubbles in the fluid that act to allow easy movement of fluid due to the high compressibility of the gas in the bubbles.

In the model of Mavko and Nur, Q can be calculated if the following quantitites are known or assumed; crack aspect ratio, α_i; porosity of each set of cracks

of a given aspect ratio, c_i; volume concentration of gas in the rock, g; rigidity of the rock matrix, μ; kinematic viscosity of the fluid, $\gamma = \eta/\rho_f$ and bubble aspect ratio, α_f. In the low frequency limit, Mavko and Nur give

$$Q = \frac{16\mu\alpha^2\alpha_f^2(1+9c_i/4\alpha_i)}{\gamma\omega g} \qquad (9)$$

where ω is angular frequency. Values of α, c_α and μ are known for sample 8581 from the results of the previous section. Unfortunately, the gas concentration and gas bubble geometry are not known and since the values of Q obtained from the above formula depend strongly on these values, Q cannot be reliably predicted from the above formula. As an example, for $\alpha=10^{-4}$, $c=4 \times 10^{-5}$, $\eta = .0014$ poise and choosing $\alpha_f = \alpha/\sqrt{g}$ the Q value obtained for $f = 10^4$ Hz is 10^7 if the liquid contains .1% gas and 10^5 for 1% gas. Both of these Q values are very high. Different relations between α and α_f will yield widely varying values for Q.

The model of O'Connell and Budiansky (1977) shows more hope of yielding well constrained values of Q. In their model, attenuation is due to the flow of fluid resulting from changes of fluid pressure that accompanies passage of a seismic wave. Two limiting

cases will be considered, saturated isolated and saturated isobaric as previously discussed. The transition frequency between the two cases is given by ω_1 in equation (4) if cracks are considered as parallel plates and fluid is incompressible. At low frequency the saturated isobaric condition applies and at high frequency cracks appear as isolated. O'Connell and Budiansky compute the complex moduli of a saturated rock where fluid flow is possible. Their self-consistent approximation yields the following nonlinear equations that must be solved to find the complex modulus.

$$\bar{\kappa}/\kappa = 1$$

$$\bar{\mu}/\mu = 1 - \frac{32}{45}\left(\frac{1-\nu'}{2-\nu'}\right)[(2-\nu')D + 3]\varepsilon$$

$$\nu' = \nu + \frac{16}{45}\left(\frac{1-\nu'^2}{2-\nu'}\right)[2(1-2\nu)c - (2-\nu')(1+3\nu)D]\varepsilon \qquad (10)$$

$$D = \frac{-id\omega_1/\omega}{1 - id\omega_1/\omega}$$

$$d = \frac{9}{16}\left(\frac{1-2\nu}{1-\nu}\right)\frac{\bar{\mu}}{\mu(1-\nu')}$$

where $\bar{\kappa}$ and $\bar{\mu}$ are effective moduli of the cracked solid, ν, κ, μ are respectively Poisson's ratio, bulk

modulus and rigidity of the matrix material and ω is angular frequency which is assumed to be much less than the frequency of shear relaxation in the fluid which is given by (5). The quantity ε is the crack density parameter which is given by (3). Equations in (10) are only valid when

$$\kappa \geq \tilde{\kappa} > \kappa\, c/\alpha \tag{11}$$

where $\tilde{\kappa}$ is the fluid bulk modulus.

When a distribution of aspect ratios are present, O'Connell and Budiansky give that the following modifications to (10) are required.

$$D = \int_0^\infty \frac{-i\omega_1(\alpha)d/\omega}{1 - i\omega_1(\alpha)d/\omega}\, \eta_1(\omega_1)d\omega_1 \tag{12}$$

where the distribution function η_1 satisfies

$$\int \eta_1(\omega_1)d\omega_1 = 1 \tag{13}$$

and

$$\text{porosity} = c = \frac{4\pi\varepsilon}{3} \int_0^\infty \alpha\eta_1(\alpha)d\alpha \tag{14}$$

For a set of cracks of discrete aspect ratios, the

distribution function, η_1, was set equal to a sum of delta functions

$$\eta_1(\omega_1) = \sum_{j=1}^{N} \frac{c_j}{c} \delta(\omega_1 - \omega_{1j}) \tag{15}$$

where c_j is the concentration of cracks of aspect ratio α_j. The equations (12) - (15) can be solved along with (10) to obtain $\bar{\mu}/\mu$ for a given crack aspect ratio spectrum. The nonlinear equations were solved using the Newton-Raphson procedure (Hildebrand, 1956). The effective Poisson's ratio of the cracked material is obtained from

$$\bar{\nu} = \frac{(1+\nu)\bar{\kappa}/\kappa - (1-2\nu)\bar{\mu}/\mu}{2(1+\nu)\bar{\kappa}/\kappa + (1-2\nu)\bar{\mu}/\mu} \tag{16}$$

and complex velocities from $\frac{\bar{V}_s}{V_s} = (\bar{G}/G)^{1/2}$

$$\frac{\bar{V}_p}{V_p} = \left(\frac{(1-\bar{\nu})(1+\nu)}{(1+\bar{\nu})(1-\nu)} \frac{\bar{\kappa}}{\kappa}\right)^{1/2} \tag{17}$$

Values of Q are computed as in Walsh (1968)

$$Q = \frac{V_R}{2V_i} \tag{18}$$

where V_R and V_i are the real and imaginary parts of the

complex velocity.

When computing values of Q using the formulation just described, cracks with aspect ratios greater than or equal to 10^{-2} were not considered. This was necessary in order for the formulation of O'Connell and Budiansky (1977) to be valid. Since the value of ε is small for high aspect ratio cracks, the effect of neglecting these cracks should be small. As an example, Figure 10 shows Q vs. frequency for a rock with only one set of cracks of aspect ratio 2.39×10^{-3} and one with aspect ratio 1.19×10^{-3}. Porosity in both cases is .001 which gives values of ε of .1 in the first case and .2 in the second. The figure shows that the attenuation changes by over an order of magnitude for a change in the value of α by a factor of 2. This change in Q is the result of the change in the value of ε as well as the change in the value of ω_1. For the smaller aspect ratio crack, ω_1 is smaller and ε larger. The value of ω_1 is on the order of 8×10^5 rad/sec for $\alpha = 1.19 \times 10^{-3}$ and is 6×10^6 rad/sec for $\alpha = 2.38 \times 10^{-3}$. The lower value of ω_1 for the smaller aspect ratio cracks is nearer the 10^3 to 20×10^3 Hz range of frequencies over which Q values will be computed for comparison with in situ measurements. Characteristic frequency of high aspect ratio cracks is very high which means that they contri-

bute little to attenuation at frequencies as high as 10 KHz.

Figure 11 shows values of Q computed using pore aspect ratio spectra obtained by inverting velocity data in the preceding section. Q values at three pressures are plotted: 0, 100 and 200 bars. Crack aspect ratio spectra at non-zero pressures were computed from the zero pressure spectrum using the technique of Toksöz et al. (1976). Pore aspect ratio spectra at 100 and 200 bars are listed in Table 5. The characteristic frequency, ω_1, for each aspect ratio is also listed. The Q values in the frequency range shown are within the range of 100 to 1000 that would be expected for virgin granitic rock. The figure clearly shows that Q is frequency dependent in the frequency range considered.

The model of O'Connell and Budiansky (1977) has been shown to give reasonable values of Q for a virgin granite. This does not mean that the mechanism proposed by them is the dominant mechanism of attenuation under in situ conditions. Many assumptions were made in the construction and use of the theory in order to compute Q. Many measurements of attenuation under varying conditions of frequency and pressure would be necessary to confirm that fluid flow is the dominant source of attenuation.

Table 1 Earth Stress Measurements in GT-2 and EE-1, (from Aamodt et al. (1976)).

Depth (meters)	Pore Pressure (bars)	Earth Stress (bars)		Effective Stress (bars)	
		s_1	s_2	σ_1	σ_2
765	15	180	147	165	132
1990	135	504	333	369	198
2930	227	753	367	526	140

Table 2 Modal Analysis of Selected Precambrian Rocks from GT-2

depth in feet	7918	8578	9519	9521	9531
depth in meters	2413	2615	2901	2902	2905
Quartz	42	29	25	32	23
Potassium Feldspar	30	21	15	29	20
Plagioclase Feldspar	24	34	38	34	37
Biotite	<1	11	13	.5	13
Others	3	5	0	4	7

Table 3 P and S wave velocities on a dry sample from depth of 2615 in GT-2 used in inversion to obtain crack aspect ratio spectra. Data is averaged from results reported in Trice and Warren (1977).

Pressure (bars)	P Velocity (km/sec)	S Velocity (km/sec)
0	5.09	3.12
50	5.24	3.18
100	5.32	3.24
200	5.50	3.33
300	5.67	3.40
500	5.95	3.50
700	6.05	3.54
1000	6.15	3.57
1500	6.24	3.60

Table 4 Results of inversion of velocity data

Aspect Ratio	Concentration
1.0	1.78×10^{-2}
.01	9.80×10^{-4}
.0022	7.95×10^{-5}
.0017	4.77×10^{-5}
.0013	4.52×10^{-5}
.0009	1.70×10^{-4}
.0005	1.08×10^{-4}
.00025	4.16×10^{-5}
.0001	2.21×10^{-5}

Matrix properties:

$$\kappa = .650 \times 10^{12} \text{ dynes/cm}^2$$
$$\mu = .360 \times 10^{12} \text{ dynes/cm}^2$$

Fluid $\kappa = 1.19 \times 10^{10}$ dynes/cm^2

Table 5. Pore Aspect Ratio spectrum used to find Q at 100 and 200 bars effective pressure.

ρ = 100 bars

Aspect Ratio	Porosity	ω_1 (radians/sec)
1.99×10^{-3}	7.17×10^{-5}	3.6×10^{6}
1.48×10^{-3}	4.17×10^{-5}	1.5×10^{6}
1.09×10^{-3}	3.77×10^{-5}	5.9×10^{5}
7.00×10^{-4}	1.32×10^{-4}	1.6×10^{5}
3.03×10^{-4}	6.57×10^{-5}	1.3×10^{4}
4.81×10^{-5}	8.00×10^{-6}	5.2×10

ρ = 200 bars

1.79×10^{-3}	6.48×10^{-5}	2.7×10^{6}
1.29×10^{-3}	3.62×10^{-5}	9.0×10^{6}
8.91×10^{-4}	3.10×10^{-5}	3.3×10^{5}
5.21×10^{-4}	9.85×10^{-5}	6.6×10^{4}
1.26×10^{-4}	2.71×10^{-5}	9.2×10^{2}

Figure Captions

Figure 1. Volumetric strain vs. pressure measured on sample from 2615 meters in GT-2. Data from Trice and Warren (1977).

Figure 2. Aspect ratio spectrum at three pressures for a sandstone. From Toksöz, Cheng and Timur (1976).

Figure 3. P and S wave velocities as a function of pressure for a dry sample from 2615 meters in GT-2. From Trice and Warren (1977).

Figure 4. Normalized velocity as a function of porosity for rock containing cracks of a single aspect ratio. P and S wave velocities are shown for dry and water saturated conditions. From Toksöz, Cheng and Timur (1976).

Figure 5. Velocity vs. confining pressure measured by Nur and Simmons (1969) on a sample of Casco granite.

Figure 6. Relationship between permeability and elastic properties as a function of pressure for sample from depth of 2902 meters in GT-2. From Trice and Warren (1977).

Figure 7. Lithologic log for GT-2 wellbore. From Blair et al. (1976).

Figure 8. Permeability vs. temperature measured by Potter (1978) on a sample from depth of 2615 meters in GT-2.

Figure 9. Velocity vs. pressure for sample from depth of 2615 meters in GT-2. Laboratory measurements of Trice and Warren (1977) are shown. Values predicted using crack aspect ratio spectrum resulting from inversion of velocity data using technique of Cheng (1978) are shown for dry and fluid saturated conditions.

Figure 10. Q vs. frequency predicted by theory of O'Connell and Budiansky (1977) for material containing cracks of one aspect ratio. Results are shown for two different aspect ratios. Porosity in each case is .001.

Figure 11. Q vs. frequency predicted by using crack aspect ratio spectrum given in Table 4 for 0 pressure and spectra in Table 5 for 100 and 200 bars pressure. Q values are those predicted by theory of O'Connell and Budiansky (1977).

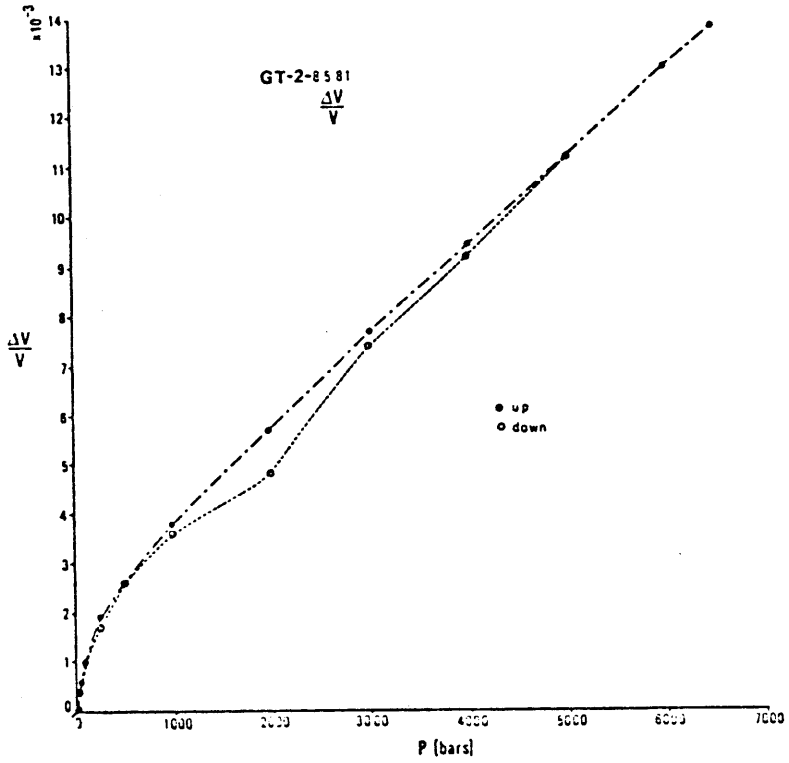

Figure 1

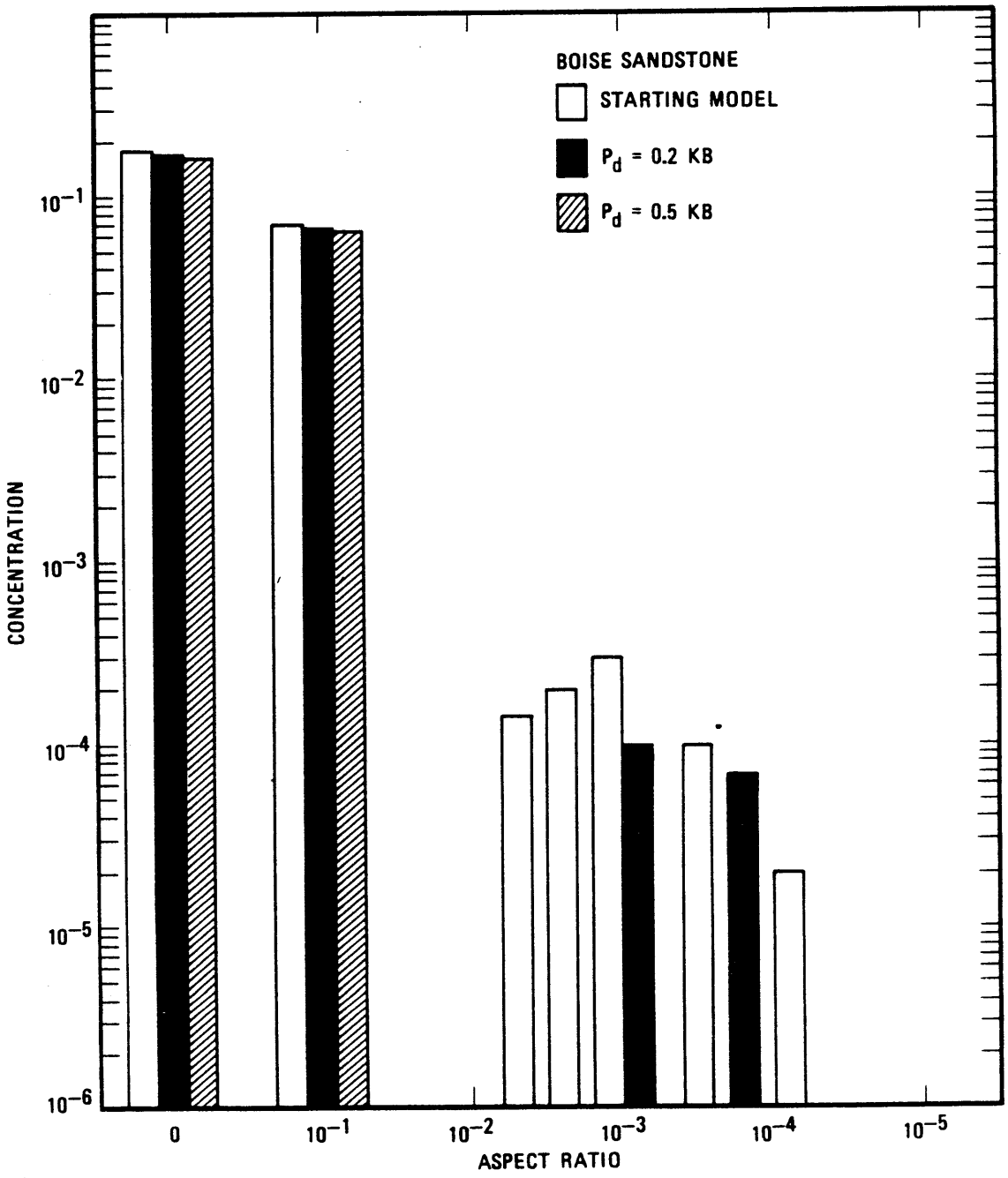
BOISE SANDSTONE
STARTING MODEL
P_d = 0.2 KB
P_d = 0.5 KB
CONCENTRATION
10^{-1}
10^{-2}
10^{-3}
10^{-4}
10^{-5}
10^{-6}
0
10^{-1}
10^{-2}
10^{-3}
10^{-4}
10^{-5}
ASPECT RATIO

Figure 2

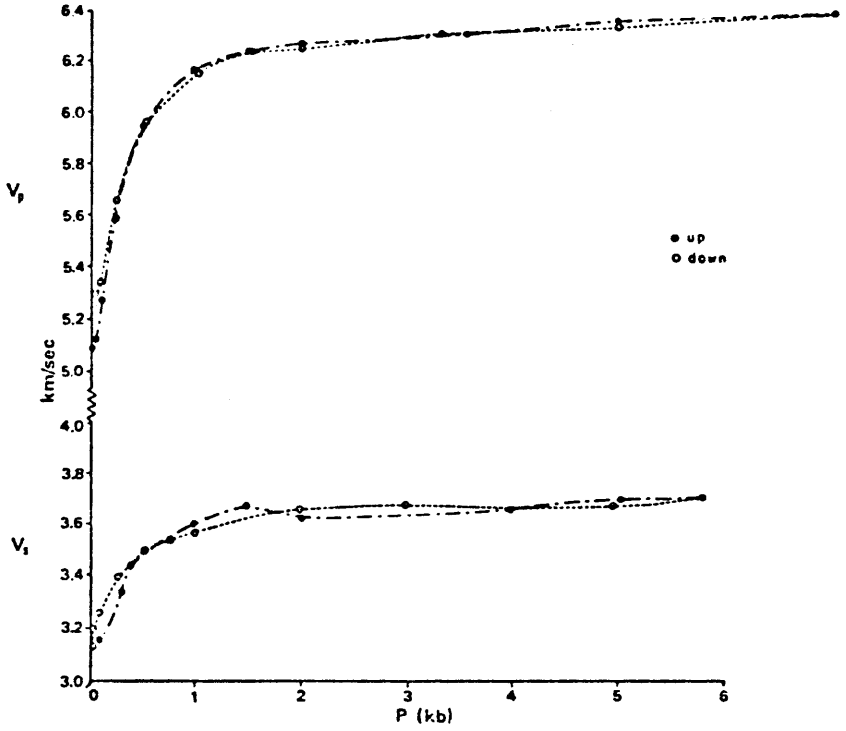
6.4
6.2
6.0
5.8
5.6
5.4
5.2
5.0
4.0
3.8
3.6
3.4
3.2
3.0
V_p
V_s
km/sec
• up
o down
0
1
2
3
4
5
6
P (kb)

Figure 3

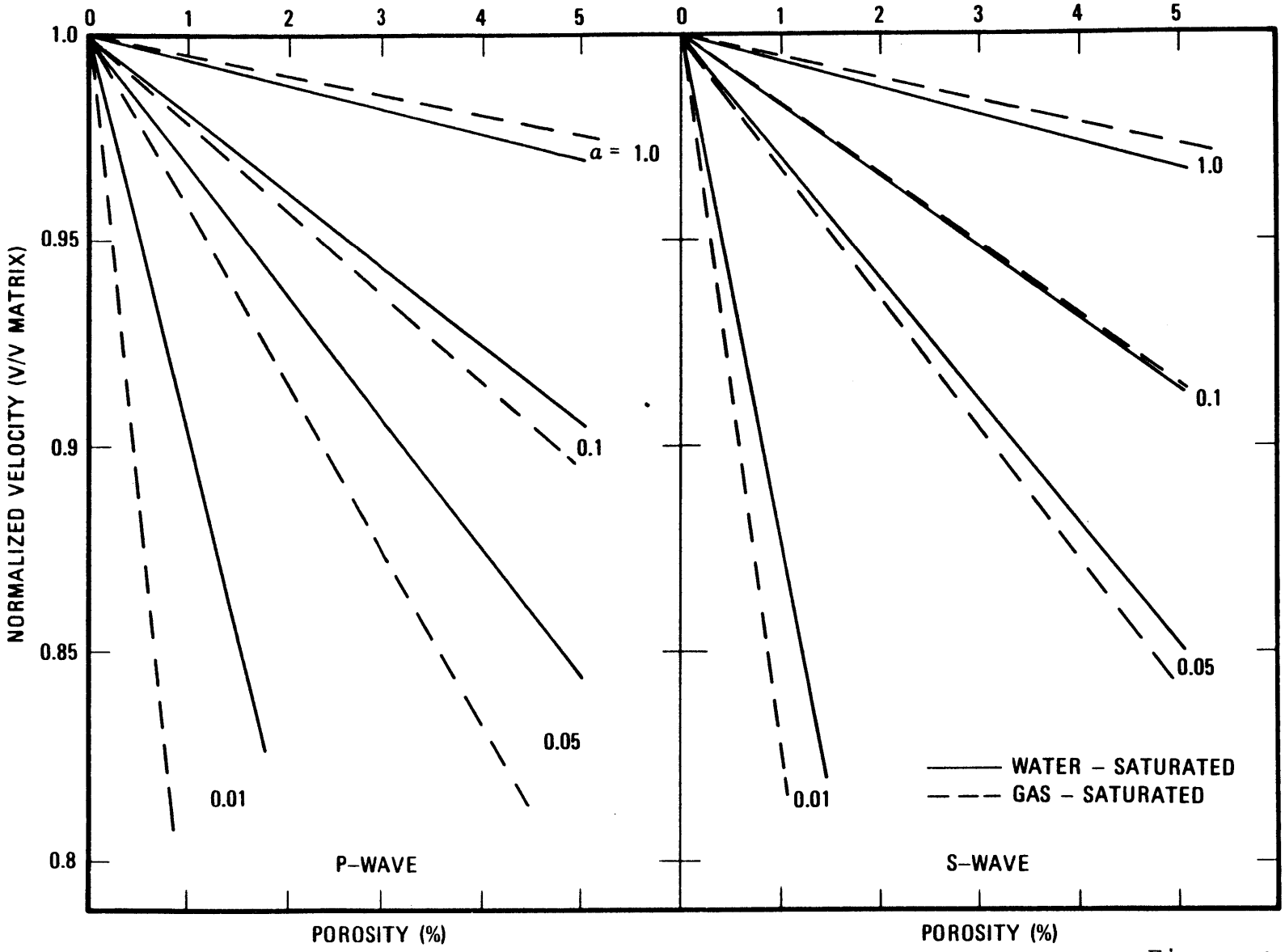
0
1
2
3
4
5
1.0
0.95
0.9
0.85
0.8
NORMALIZED VELOCITY (V/V MATRIX)
a = 1.0
0.1
0.05
0.01
P-WAVE
POROSITY (%)
1.0
0.1
0.05
0.01
S-WAVE
POROSITY (%)
WATER – SATURATED
GAS – SATURATED

Figure 4

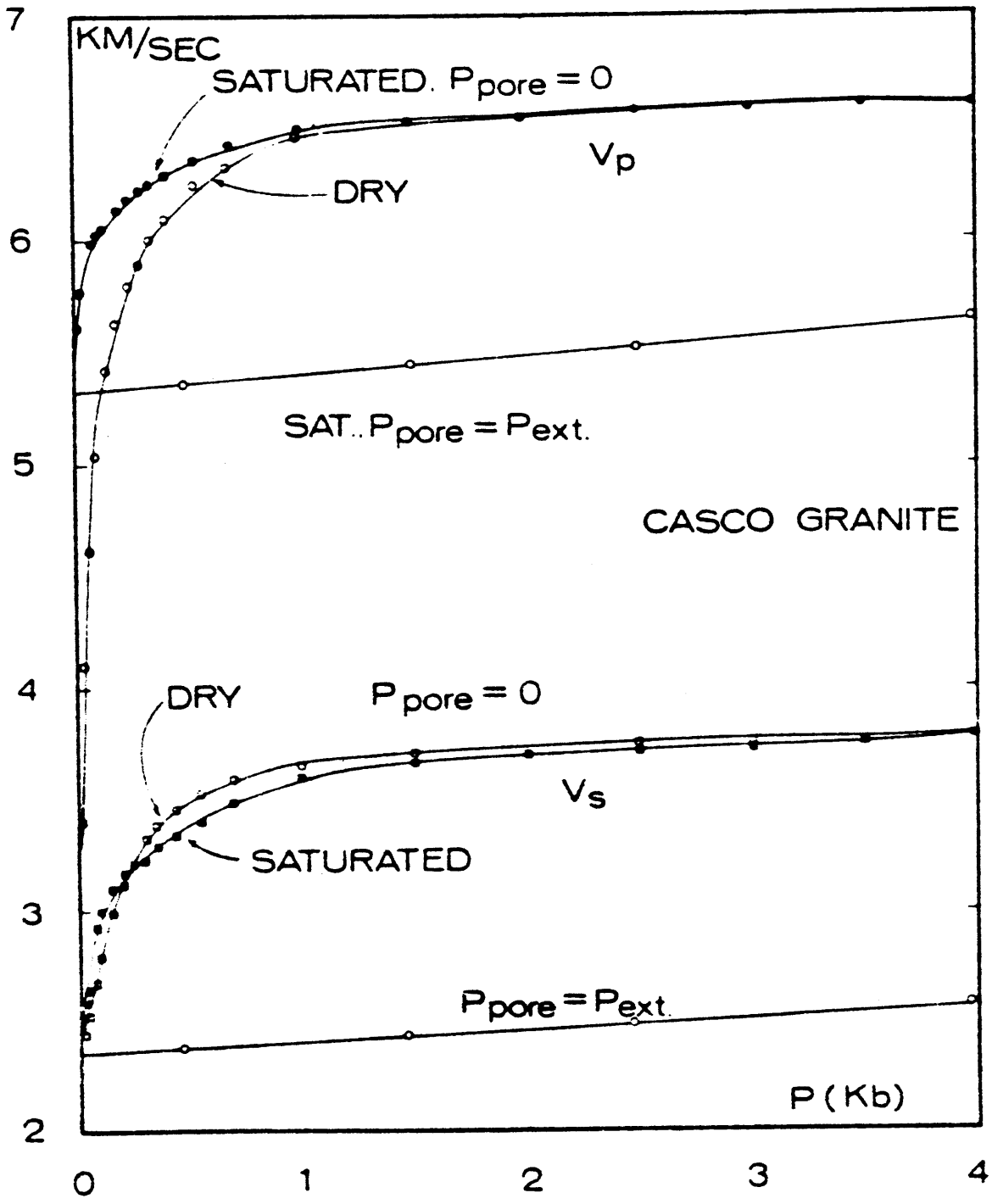
KM/SEC
SATURATED. Ppore = 0
Vp
DRY
SAT.. Ppore = Pext.
CASCO GRANITE
DRY
Ppore = 0
Vs
SATURATED
Ppore = Pext.
P (Kb)
7
6
5
4
3
2
0
1
2
3
4

Figure 5

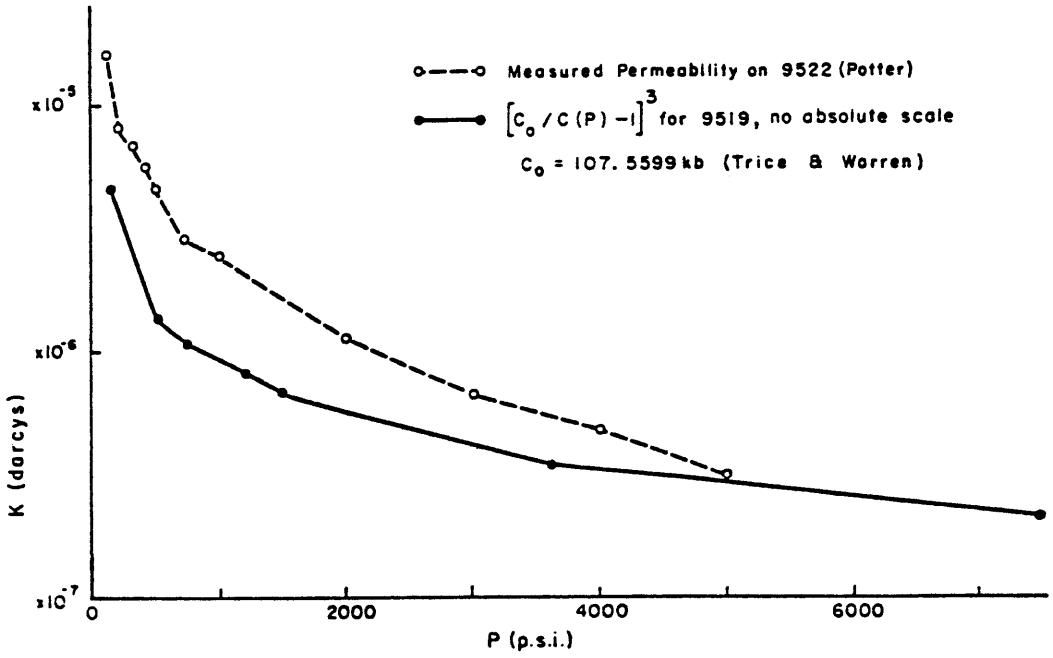
Measured Permeability on 9522 (Potter)
$\left[C_o / C(P) - 1\right]^3$ for 9519, no absolute scale
C_o = 107.5599 kb (Trice & Warren)
x10⁻⁵
x10⁻⁶
x10⁻⁷
K (darcys)
0
2000
4000
6000
P (p.s.i.)

Figure 6

LITHOLOGIC LOG OF GT-2

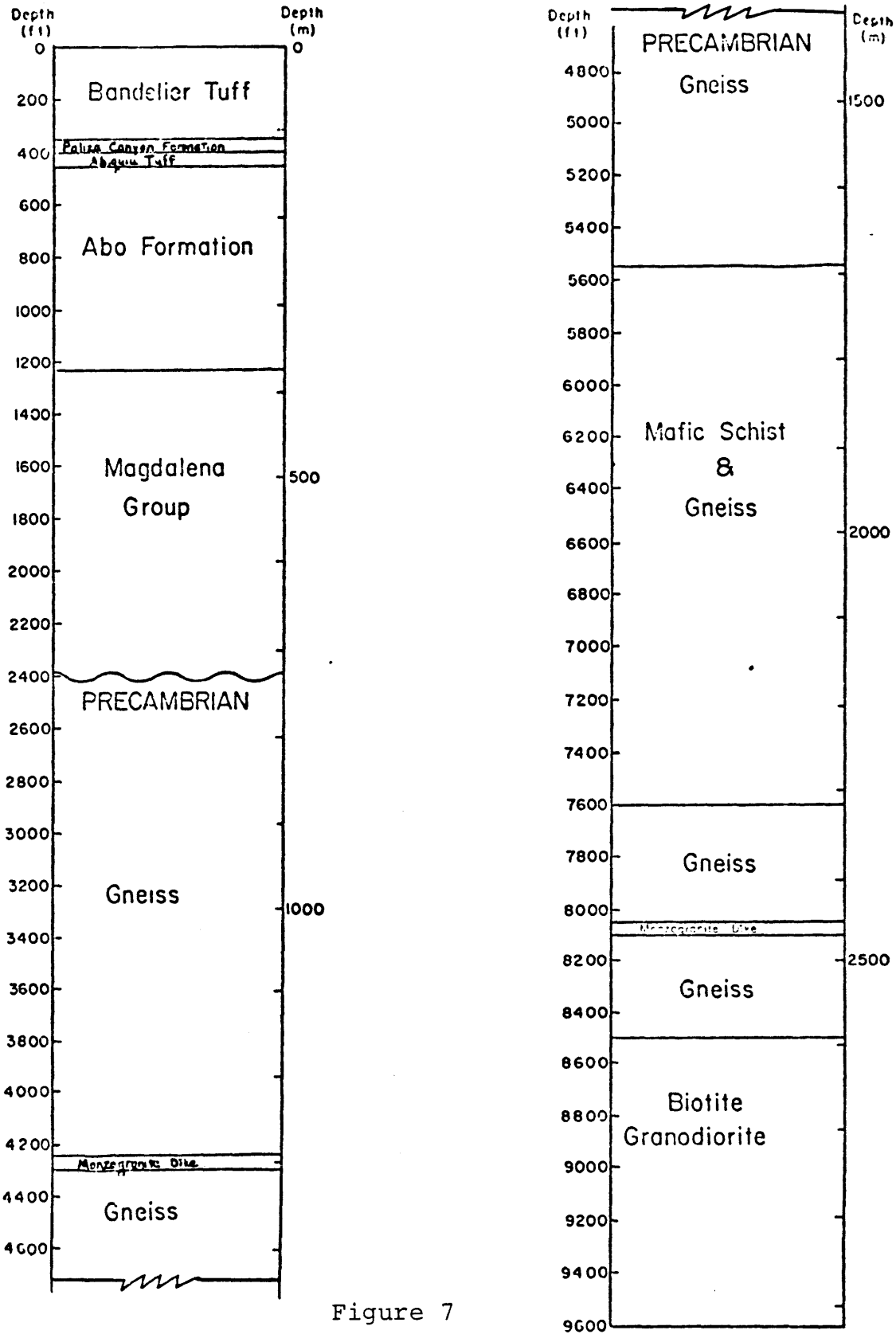

Figure 7

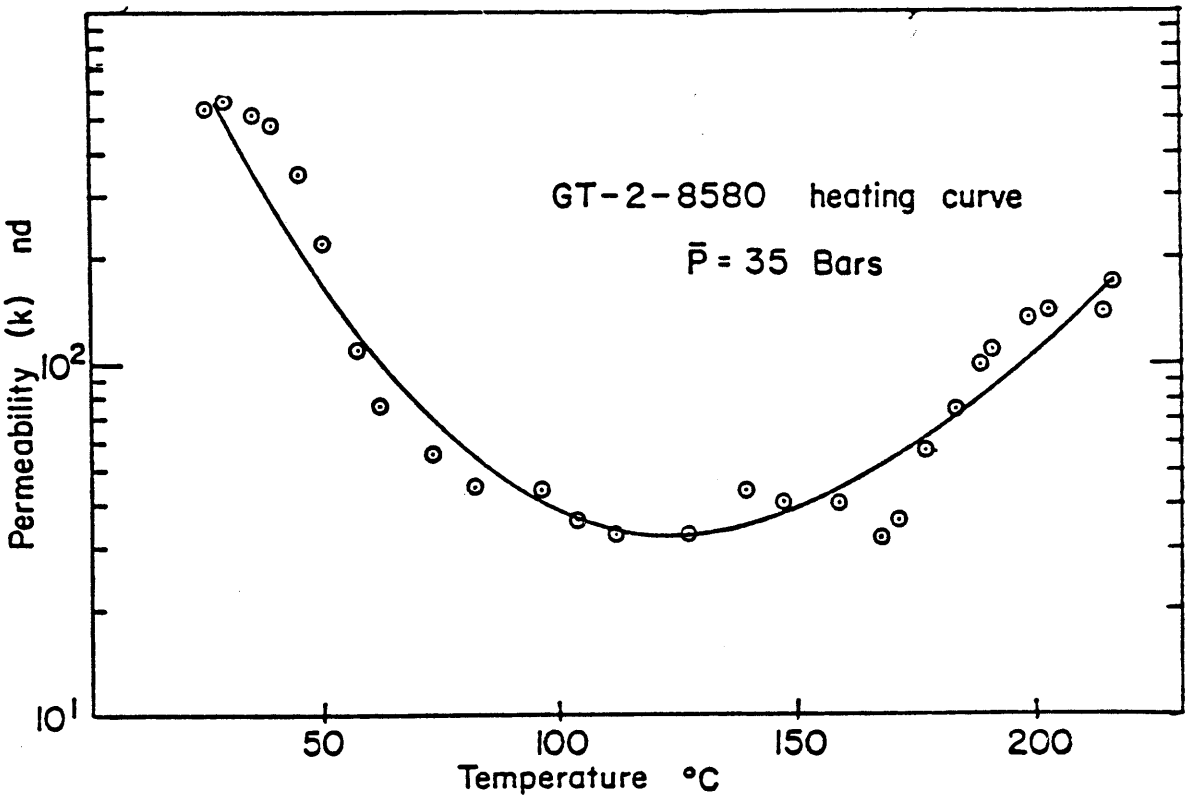
GT-2-8580 heating curve
$\bar{P}$ = 35 Bars
Permeability (k) nd
10^2
10^1
50
100
150
200
Temperature °C

Figure 8

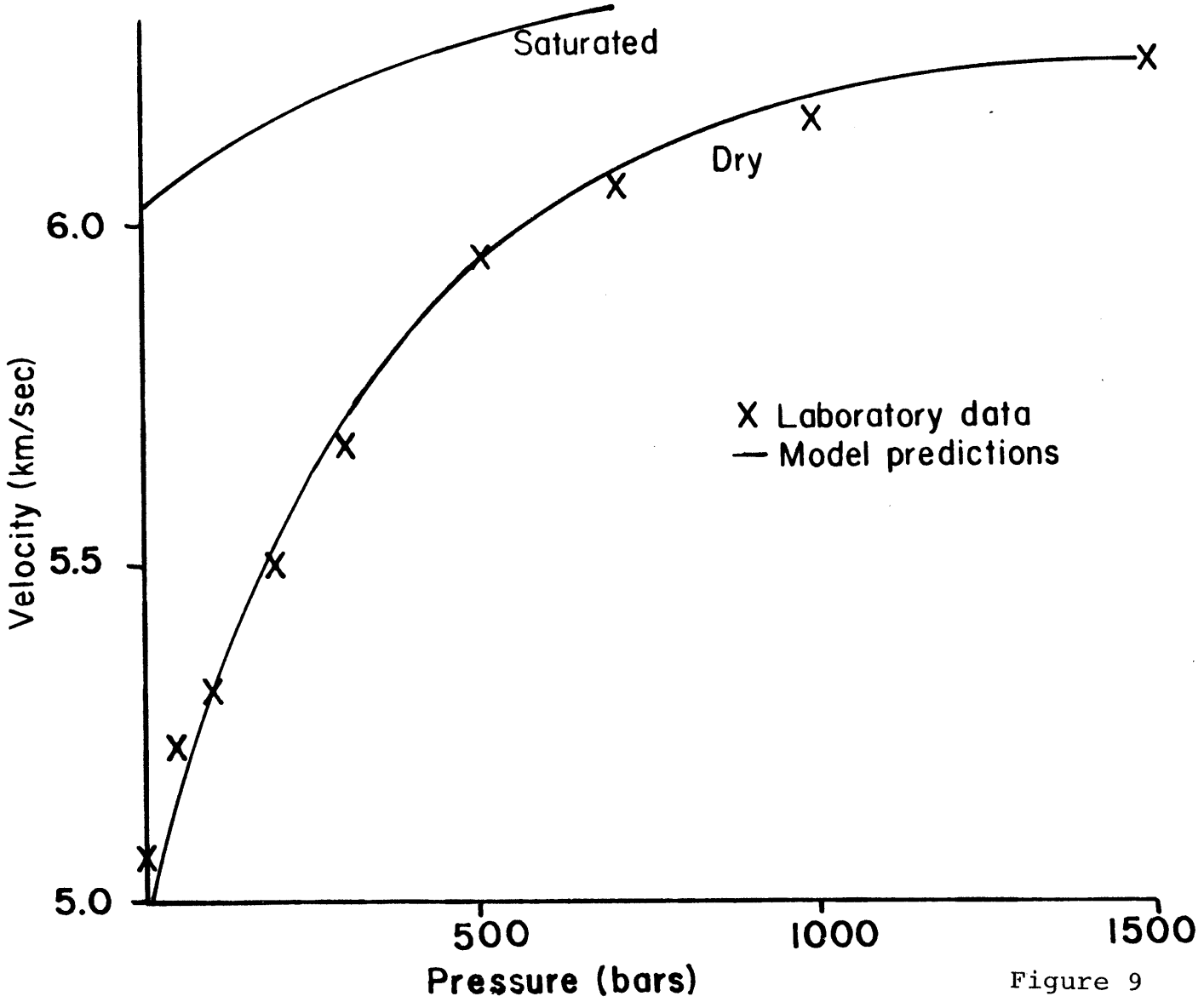
Saturated
Dry
6.0
5.5
5.0
Velocity (km/sec)
X Laboratory data
— Model predictions
500
1000
1500
Pressure (bars)

Figure 9

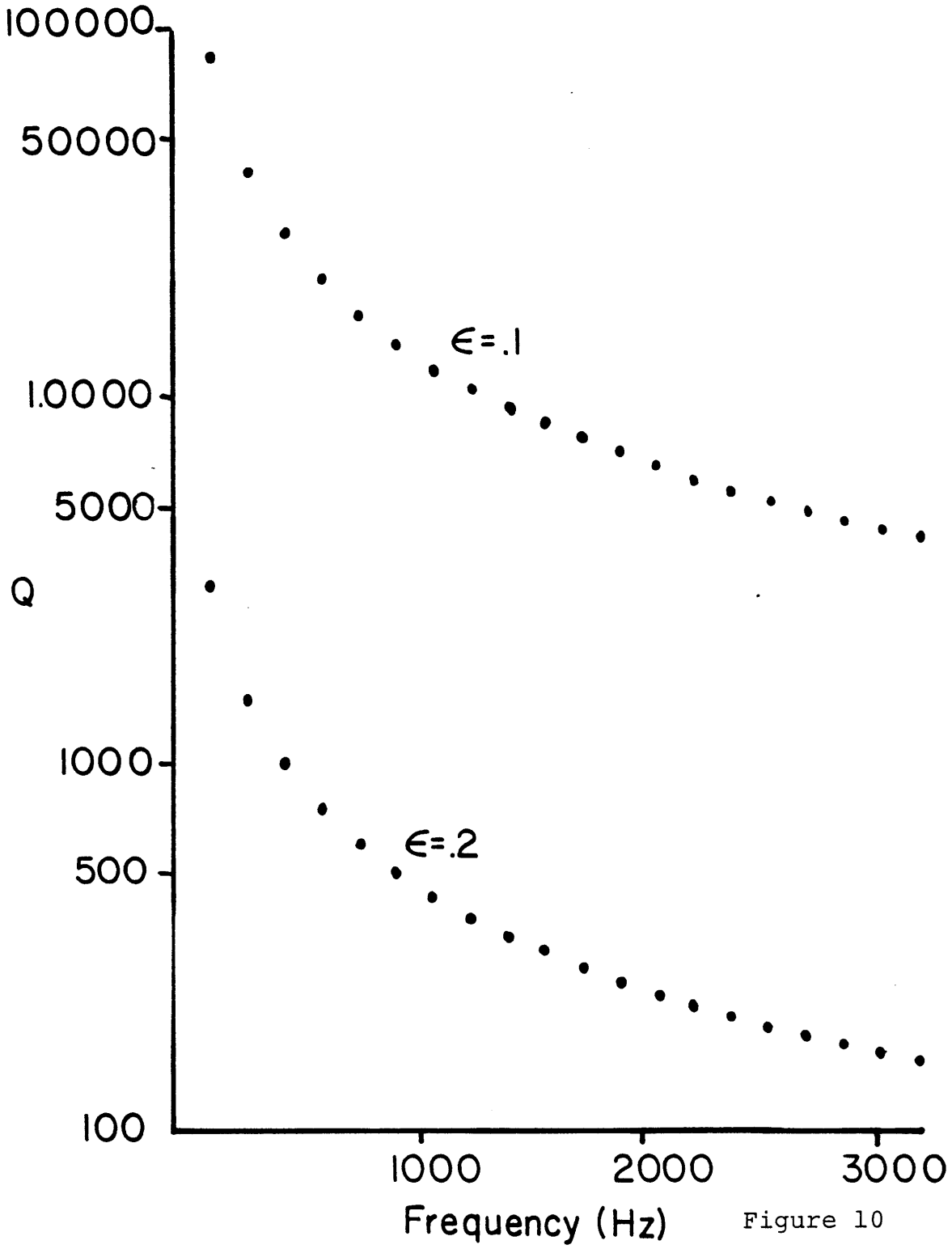
100000
50000
10000
5000
Q
1000
500
100
ϵ=.1
ϵ=.2
1000
2000
3000
Frequency (Hz)

Figure 10

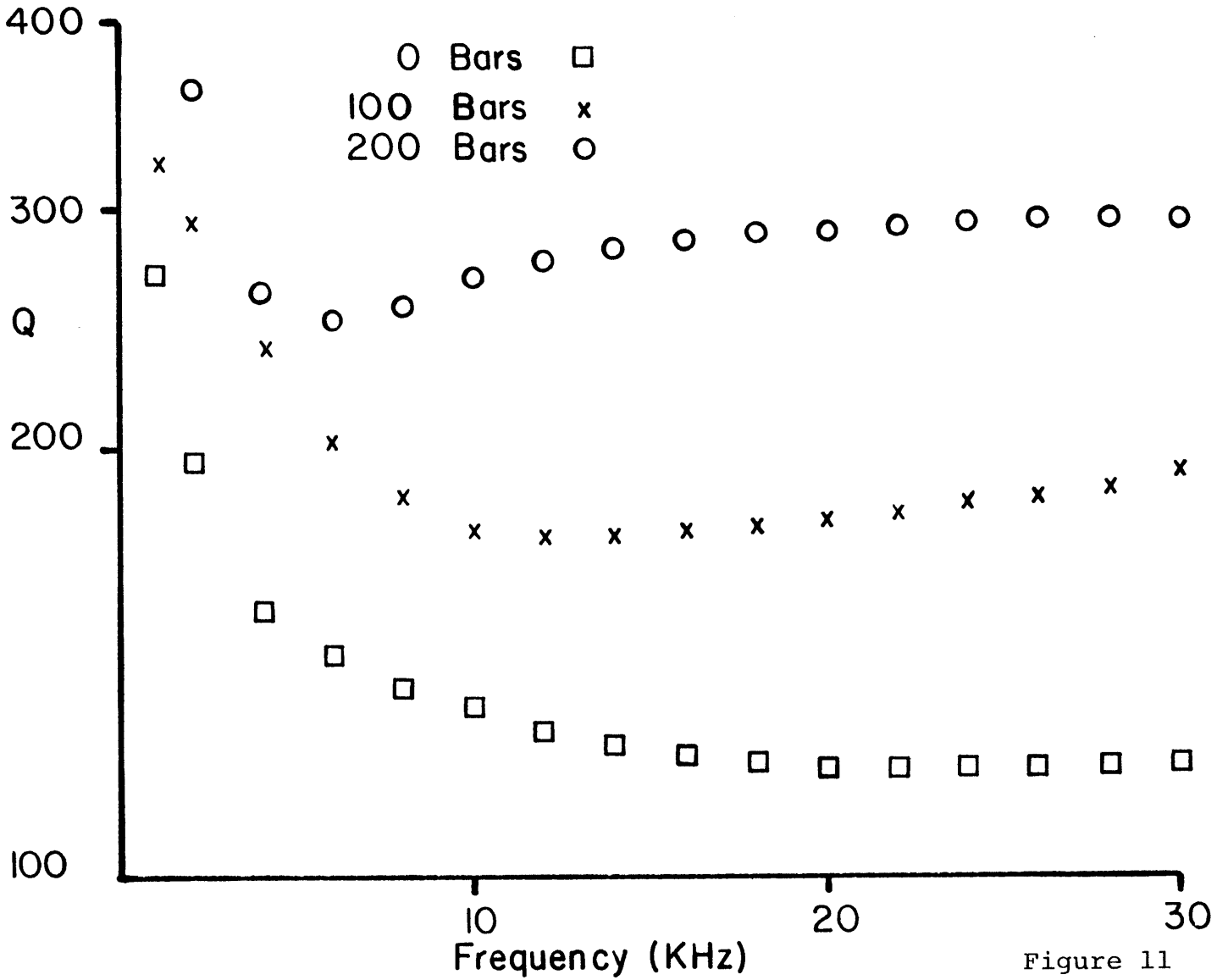
400
300
200
100
Q
0 Bars
100 Bars
200 Bars
10
20
30
Frequency (KHz)

Figure 11

CHAPTER 4

ANALYSIS OF SEISMIC DATA OBTAINED DURING DUAL WELL SEISMIC EXPERIMENTS AT THE FENTON HILL GEOTHERMAL TEST SITE

One of the major problems encountered in the development of Hot Dry Rock as an economically viable source of energy is finding the location, orientation and size of a hydraulic fracture created in the reservoir. The Los Alamos Hot Dry Rock geothermal energy group (LASL) has devoted a large effort to the problem of mapping of hydraulic fractures. Reviews of their work can be found in Blair et al. (1976) and LASL HDR staff (1978). The goal of hydraulic fracture mapping is to determine location of the fracture with sufficient accuracy to be able to drill into the fracture with a second borehole. For this reason it is desired to perform experiments using only one borehole, the one from which the fracture originates. Various techniques have been employed by LASL in an attempt to determine fracture parameters. These include seismic, electrical potential measurements and magnetic field measurements.

Seismic techniques employed to date have been both active and passive. In passive experiments, the seismic source is the noise generated by the hydraulic fracturing

process. Attempts to observe fracturing induced signals have been unsuccessful when using a surface array of geophones. Microseismic signals in the kilohertz frequency range have been observed with a three axis borehole seismometer. Seismic source for active experiments was initially chosen to be small explosives that were placed in the borehole. These explosives provided signals with frequencies in the range of 100-1000 Hertz. Signals recorded from these explosives were of very good quality even for travel distances as large as 70 meters. The advantage of using explosives was that they provided a strong source as well as their ability to function reasonably well at temperatures as high as 200°C. The disadvantages are that the explosives are dangerous to handle, particularly those that failed to fire, as well as the amount of time required to gain a small amount of seismic data: typically a maximum of six shots could be fired during a working day. It was desired to have some kind of mechanical or electrical source that could withstand high temperature and be triggered at a rate greater than six times per day. A mechanical weight dropping device was built by LASL but was found to give low quality signals. Finally Dresser Atlas Company developed a borehole piezoelectric source that could operate at high temperature and be triggered nearly continuously to provide large amounts

of seismic data. This source provided signals that are discussed in this chapter.

4.1 Dual Well Seismic Experiment

At the time that the dual well seismic experiment was conceived, it was already well established that seismic techniques could be used to find the distance between two boreholes in situ. Also, seismograms recorded in situ showed a great deal of character that was believed to have resulted from scattering off of fractures. Figure 1, from LASL HDR staff (1978), shows seismograms recorded in GT-2 when an explosive source was located in EE-1. Data is shown for two source-receiver pairs: (a) source at 2644 meters in EE-1, and receiver at 2667 meters in GT-2 and (b) source at 2415 with receiver at 2463. Depths for part b are considered to be above the region where heat is being removed from the rock by water circulation. Part a was conducted in the region where heat is being removed. In each section, seismograms are shown for two cases, pressurized and hydrostatic. In the hydrostatic, or unpressurized, case both boreholes are open at the surface and water pressure in situ is due only to the weight of the column of water in the borehole. In the pressurized case, the GT-2 wellhead was sealed off and EE-1 was pressurized to approximately 100 bars,

slightly higher than the pressure at which hydrofractures in the GT-2/EE-1 system open and extend. In Figure 1(b) there is little difference in signals recorded in the hydrostatic and pressurized case. Frequency content is very similar in both cases. In Figure 1(a) there is a profound difference in signal character between pressurized and unpressurized cases. Most of the high frequency component present in the unpressurized case has been lost when fluid is pressurized. Attempts were made to measure wave velocities using seismograms in Figure 1. The results contained a great deal of scatter so no firm conclusions about velocity could be drawn from these measurements.

4.1.1 Purpose of the Dual Well Seismic Experiment

Encouraged by the results of seismic experiments that used explosives as a seismic source it was decided to try to find some source that could provide signals at a rate greater than six per day. It was hoped that a greater amount of seismic data would aid in understanding the characteristics of the geothermal source rock.

The theory outlined in the first half of Chapter 2 shows that P and S waves in the kilohertz frequency range will produce converted waves when they impinge on a fluid layer that, if recorded, would confirm the

existence of a hydrofracture. By placing recording transducers in both the source and receiver boreholes it was hoped that reflections from the fracture and converted phases passing through the fracture could be detected. This aspect of the experiment is known as "reflection-transmission."

By choosing suitable source-receiver geometries it is possible to determine rock velocity as well as the distance between boreholes. This can be done in both pressurized and unpressurized cases so that the effect of fluid pressure on velocities can be investigated. In addition, the frequency content of recorded signals can be studied to try to determine the spatial variation of attenuation in the rock as well as to find the effects of pressurization on attenuation.

4.1.2 Design of the Experiment

Source and receivers were provided by Dresser Atlas. For the data that will be discussed in this thesis, the following source-receiver instruments were in operation. In EE-1 a cylindrical piezoelectric transmitter of diameter 9.2 cm (3-5/8 inches) provided the seismic source. Placed at a distance of 3.64 meters (12 feet) from the transmitter was a piezoelectric receiver of diameter 5.08 cm (2 inches). Transmitter and receiver are acoustically isolated so that waves traveling between

the two transducers must pass through the medium that contains them. In GT-2 the only operational transducer was a 5.08 cm diameter receiver. Peak frequency for the 9.2 cm transducer is approximately 6.5 KHz and is 12 KHz for the 5.08 cm transducer. Source and receivers are centered in their respective boreholes. Signals passing between transducer and rock must pass through water, borehole casing as well as cement used to seal casing to the surrounding rock. Borehole diameter varies between about 20 and 30 cm. Diameter decreases as depth increases. Since waves must pass through water to be measured by a recording transducer, no S waves incident on the borehole can be directly recorded. However, for S waves incident at angles other than normal to the axis of the borehole, there will be converted P waves which can travel in the water and be recorded by the receiver. This problem is discussed by White (1965).

Each experiment was done in steps. For each step, the receiver in GT-2 was held in one position and the source was moved from one position to another at a given speed. In most cases, the source was moved from a location in EE-1 that made an angle of 45° above the horizontal plane containing the stationary receiver to 45° below the plane. The source was fired at a rate of 5 times per second. Source moved in the borehole at a rate of approximately 6.1 m/min (20 feet/min).

The source thus moved about 2 cm between each firing. Signals received were transmitted by cable up to the surface where they were recorded in analog fashion on magnetic tapes. These tapes were later digitized at a rate of 82 samples/millisecond by a 5451B Hewlett Packard Fourier Analizer System. The digitized signals were sent to M.I.T. on computer type magnetic tapes.

Two complete experiments were carried out, each with an unpressurized and pressurized part. The first experiment was done on 26-27 October, 1977. The second experiment occurred on 10-12 September, 1978. The 1978 experiment was done to improve data quality using experience gained during the first experiment as well as to try to detect changes in rock properties resulting from other experiments conducted during the 11 months between the two seismic experiments. The transducers used in the second experiment were the same as those used in 1977. They had not been used in the time between experiments so presumably they functioned the same during both experiments. Most of the steps of the 1977 experiment were repeated in 1978.

During the 1977 experiment, the gain of the receiving and recording system was changed during the execution of each step to ensure that signals of sufficient amplitude for analysis were recorded. Since records of gain changes are incomplete, it is difficult to draw

any conclusions based on amplitudes of signals recorded during the first experiment. To remedy this problem in the 1978 experiment each individual step was performed once and a single gain was chosen to give the best overall signal quality for the step. The step was then repeated at that gain. Gains were different during pressurized and unpressurized parts but since differences in gains are known, amplitudes of signals can be compared.

The unpressurized part of the experiment was carried out during the first day of each experiment. On the next day, water pressure in the geothermal system was increased by approximately 100 bars and everything else was done exactly as it had been done the previous day.

Table 1 lists the steps for which data will be discussed in this thesis. Receiver location in GT-2 as well as depth range over which source moves are listed. The approximate number of seismograms recorded in GT-2 for each case, pressurized and unpressurized, are also listed for each step. Each seismogram in digitized form is 25 milliseconds in duration. The volume of data available is clearly enormous. Not all of these seismograms were analyzed for the following discussions. Limitations were placed becase of poor signal quality as well as the prohibitively large amount of computer time and storage required for working with such a large data

set.

4.1.3 In situ Conditions at the Time of the Experiment

Many different experiments to study various properties have been performed on the Fenton Hill geothermal system during the course of its development. Some of these experiments have produced irreversible changes to the rock in the region of the boreholes. Other changes induced by experiments have slow recovery rates, such as the extraction of heat from the region near the boreholes. A detailed list and discussion of experiments are found in the annual reports of the Hot Dry Rock development project (Blair et al., 1976; LASL HDR staff, 1978).

Experiments that have been done on the Fenton Hill geothermal system that could potentially alter mechanical properties of the rock that would be detected using seismic technique are hydrofracturing, fluid flow and chemical leaching. Hydrofracturing is believed to cause a single crack. If fluid filled, this crack represents an acoustic impedance contrast and its effect on seismic waves has been discussed in Chapter 2. Secondary fractures or a system of small fractures may branch off of the main hydrofracture. These fractures will have a direct effect on mechanical properties of the rock as discussed in Chapter 3. Flow of cold fluid through the

geothermal system removes heat from the rock which may be accompanied by the introduction of fractures. The introduction of new fractures by heat extraction is desired since it increases the volume of rock from which heat can be extracted, thus extending the useful life of the geothermal system. Fluid flow may also cause alteration of some of the minerals that compose the source rock, e.g., feldspars to clays. This alteration may cause changes in the physical properties of the rock.

Hydraulic fracturing has been performed from both the GT-2 and EE-1 boreholes. In September, 1975 a fracture was initiated from GT-2 at a depth of 2042 meters. Three months later a fracture was produced at 2930 meters in GT-2. EE-1 was fractured at a depth of 1965 meters in August of 1976. An impression packer placed in the borehole indicated that the fracture had an orientation of approximately N70°W. EE-1 was fractured again in October of 1976 at a depth of 2926 meters. Some of the fractures mentioned above were re-inflated at times after their initiation. In early 1977, the GT-2 hole was sealed off at 2572 m and a new section of borehole was drilled from that point. This was done in an attempt to intersect one of the fractures that originated from EE-1. If the fracture could be intersected, the impedance to fluid flow through the system would be greatly reduced

thus allowing more heat to be extracted from the rock. Although it is not clear that the new borehole intersected a hydrofracture, the impedance to fluid flow fell as low as 10 bar-sec/liter from previous values as high as 250 bar-sec/liter. This low impedance means that there must be some easy flow path for water such as through a hydraulic fracture or along some set of pre-existing joints.

Water has been pumped into the rock from GT-2 and EE-1 many times throughout the history of the Hot Dry Rock project. The circulating water has removed heat from the rock through which it flows. One month prior to the first dual well seismic experiment, an experiment was conducted where water was circulated through the EE-1/GT-2 system for 96 hours. Water temperature at the surface reached 130°C and the power extracted from the system reached a maximum of 3.2 MW (thermal). Another long term flow experiment was run in 1978, during the time between the first and second dual well seismic experiments. This experiment lasted for 75 days during which time down hole temperatures dropped as low as 66°C from the virgin in situ temperature of 185°C. This large drop in temperature along with the extraction of a large amount of heat from the rock may have produced changes in the rock properties that can be detected by the second dual well

seismic experiment.

Figure 2 shows temperature profiles of the EE-1 wellbore at various times. The uppermost curve shows the temperature profile measured after the hole was drilled and before any flow experiments had been conducted. The middle curve shows temperatures recorded after the 96 hour flow experiment in 1977 and the bottom curve shows temperatures after the 75 day experiment in 1978. The curves show that temperature has been decreasing as heat is removed from the rock. The largest decrease in temperature has occurred below a depth of 2620 meters. This depth is considered to be where major fluid flow through the rock occurs.

In an attempt to improve the flow properties of the original dual borehole system, an attempt was made in November, 1976 to remove silica by chemical leaching. During the leaching experiment, about 10^3 kg (1 ton) of silica was removed. The impedance to fluid flow between boreholes actually increased as a result of the leaching. The increase probably resulted because silica that was removed from one region of the rock was deposited in another region which plugged part of the flow path. The amount of silica removed represents less than 10^{-7}% of the weight of a block of granite of volume $10^6 m^3$. Since most granites have crack porosity on the order of .1%, removal of 10^{-7}% of the weight of the rock represents

a very small fractional increase in porosity. Even if all new porosity is in the form of cracks with aspect ratios as small as 10^{-5}, their effect on seismic velocities would be negligible.

Figure 3 (from LASL HDR staff, 1978) shows some of the features of the geothermal system at Fenton Hill as compiled from several experiments conducted by LASL. Borehole labeled GT-2B will be called GT-2 in this thesis. Dashed lines represent postulated fluid flow paths. Points where fluid enters and leaves a given wellbore are known from logging techniques such as using radioactive tracers. The top of the region most affected by fluid flow is believed to be at a depth of approximately 2620 meters which is near the gneiss-granodiorite contact (see Chapter 3, Figure 7).

4.2 Analysis of Data by LASL

Data from the dual well seismic experiment has been analyzed by workers from Los Alamos Scientific Laboratory (Albright, Aamodt, Potter and Spence, 1978). Their work to date has been mostly with data from the experiment in October, 1977. A brief account of some of their results will now be given.

Figure 4, from Albright, et al. (1978) shows the power contained in 25 msec of signal recorded at a receiver in GT-2 plotted as a function of source depth

in feet. Depth of the stationary receiver for each step is shown. Power received when system was pressurized is plotted in the left side of the figure and power for the unpressurized case is plotted on the right side of the figure. Power was obtained by squaring the signal amplitude and integrating over-time. Gain differences were corrected for (as well as they were known) and power in db computed. The power in the recorded signal is influenced by the source strength, which is considered constant throughout the experiment, radiation pattern of the source, geometric spreading of the wave as well as anelastic attenuation of the wave by the medium. Figure 3 shows that power is lower when the system is pressurized which means that attenuation is stronger. The greatest decrease in power upon pressurizing occurs in the lowest section, where the receiver is at 8850 feet (2697 meters). This region shows the greatest decrease in temperature during flow experiments (see Figure 2) and contains the points where most water leaves the EE-1 borehole and enters the rock. It should be expected that the greatest change in signal power should occur in this section since the rock has probably suffered the greatest effects of fluid circulation. There is a sudden change in power with depth in both pressurized and unpressurized cases at about 8650 feet (2636 meters).

This change in signal power with depth must be due to a change in attenuation properties of the rock and may represent the top of the region from which heat has been extracted. It is also close to a contact between a gneiss (above) and a granodiorite (see Figure 7, Chapter 2).

Albright (1978) found that signals recorded in GT-2 during the first experiment could be classified into three types which he called P, S and D. Figure 5, from his work, shows examples of each type of signal. An S type signal looks like a typical seismogram with distinct P and S waves and is recorded in regions least affected by fluid flow (see Figure 6). P type signals show a clear P arrival with no clear S arrival. For D type signal, the P arrival is emergent and often difficult to discern. There is no arrival that can be unambiguously chosen as the S wave. Albright found that the three types of waves occur in separate regions and that the type of wave observed in a given region changes on pressurizing. Figure 6 shows the types of waves recorded for various paths between the wellbores in pressurized and unpressurized cases. The type of wave observed is influenced by attenuation as well as heterogeneity of the rock through which the wave passes. These properties of the medium will be discussed throughout this chapter.

4.3 P Wave Velocity

The first step in analyzing the large number of seismograms recorded during the execution of the two dual well seismic experiments was to plot the seismograms. Figures 7 and 8 show seismograms recorded in step 16 of the first dual well seismic experiment. Figures 9 - 12 show seismograms recorded during the second experiment. Only five milliseconds of each signal is shown. Each trace begins before the direct P arrival was recorded. Source depth for some of the seismograms are given in the figures. Difference in source location between each successive seismogram shown is 2 meters. Amplitudes of each seismogram are scaled to fit on the plot so no information about relative sizes of signals can be gained from these figures. Note the difference in character between seismograms in Figures 9 and 10 for unpressurized and pressurized conditions in step 2. In Figure 9, a packet of waves is recorded at the beginning of each signal. Very little energy arrives after this packet. The S wave arrives too late to show up in this figure. In the pressurized case, Figure 10, character of the first arrival is different for each seismogram. Many wave packets are recorded in each seismogram. It is interesting that for seismograms recorded for sources with locations that differ by two meters, there is no strong

correlation of late arriving energy. This implies a strong scattering and will be discussed further in the next chapter. Figures 11 and 12, for step 16 (1978) unpressurized and pressurized respectively, show features similar to those shown in Figure 10. The predominant frequency recorded in step 16 is much lower than in step 2. The loss of high frequency content of the signals in step 16 must be due to increased scattering or attenuation since the travel distance between source and receiver is much shorter than in step 2 where high frequencies are recorded. Predominant frequencies recorded in 1977 for step 16 were much higher than in 1978 (see Figures 7 and 8) which means that significant changes occurred between the 1977 and 1978 experiments in the anelastic or scattering properties of the rock in the region of step 16.

Once seismograms had been analyzed visually, it was decided to pick first arrival times of P waves and compute medium velocity. Since the number of seismograms available for analysis was large, it was decided to develop a computer algorithm to pick first arrivals. Arrivals were defined to be the first peak in the seismogram that had sufficient amplitude that it could be distinguished from noise. The method used to pick first arrivals is outlined in Appendix B. Since many of the signals recorded had very low signal to noise

ratio, it was impossible to reliably pick first arrivals from all seismograms. The number of first arrivals used for later analysis was chosen to be the same for both pressurized and unpressurized cases for each step. For this reason the number of picks used was the smaller of the number available for each case.

4.3.1. Method of Finding Velocity

The method for finding the velocity of the rock between the EE-1 and GT-2 wellbores is to fit hyperbolae to the first arrival time data by a least squares method for each section of the wellbore. By doing this, rock velocity and wellbore spacing may be found. Throughout this section it will be assumed that the velocity of the rock is isotropic, i.e. the velocity is independent of the direction of propagation of the wave.

Since the speed at which the seismic source is moving along the EE-1 wellbore is known, seismograms can be matched to given source locations in the wellbore. The first arrival data can then be plotted as a function of position, x, of the source along the borehole from some origin position, x_o. If v is the velocity of P waves in the rock and t the travel time from source to receiver, the relation between x, t and v is

$$v^2 t^2 = (x-x_o)^2 + d^2 \qquad (1)$$

where d is the travel distance between source and receiver when the moving source is at its closest point to the stationary receiver.

Travel times, t_i, as a function of position, x_i, along the wellbore are fit to find v, x_o and d so that equation (1) gives a curve which best satisfies the data. For each section of wellbore data is available for the unpressurized and pressurized cases. Primary interest is in finding what effects pressurizing the rock system has on the rock properties. In order to get constraints on this, hyperbolae will be simultaneously fit to the pressurized and unpressurized data for each section of wellbore. A different velocity will be found for each case. The origin position x_o will also be different for each case. The value of d , the travel distance between source and receiver at their closest approach, is the same for both pressurized and unpressurized cases. There are two effects which may case d to be different for the two states; 1) the receiver is not in the same location for each experiment and 2) pressurizing introduced strains which result in a significantly shorter travel path. It will be assumed that the receiver position is nearly the same during the pressurized and unpressurized experiments.

Since the linear compressibility of granite is on the order of 10^{-6}/bar (Birch, 1966), a stress of 100 bars applied across a block of granite 20 meters across would cause a strain of 10^{-2}% or a change in length of less than .1 cm. For this reason any change in length of the travel path for waves brought about by pressurizing the medium will be ignored.

In order to use (1) to find a least squares fit to the data, the equation must be linearized so that the usual linear least squares formalism is applicable. The procedure will be to first assign initial values to model parameters which include velocities, wellbore spacing, d, and source location at its closest approach to the receiver, x_o. Using these values predicted travel times will be computed which will then be compared with the real travel times. Perturbations to the model parameters will be made in order to minimize the difference between the actual arrival times and those predicted by the model. To linearize equation (1) begin by re-writing with travel time t as a variable that is dependent on the model parameters;

$$t = \frac{1}{v}\sqrt{(x-x_o)^2 + d^2} \qquad (2)$$

Equation (2) will be used to calculate travel time, t, from the model parameters, v, x_o and d for each value

of x. In order to improve the predictions of the model small variations into the model parameters are introduced and their effect on the predictions are computed. Since the changes in the model are considered to be small only the first order effects on the travel time predictions are computed. To do this t in equation (2) is expanded in a Taylor Series about v, x_o and d and only terms that are linear in their variations are kept.

$$t = \frac{1}{v}\sqrt{(x-x_o)^2 + d^2} - \frac{1}{v^2}\sqrt{(x-x_o)^2 + d^2}\,\Delta v - \frac{(x-x_o)\,\Delta x_o}{v\sqrt{(x-x_o)^2 + d^2}} + \frac{d\Delta d}{v\sqrt{(x-x_o)^2 + d^2}} \tag{3}$$

Equation (3) is used for each set of data in pressurized and unpressurized cases to write a system of equations for perturbations in the unknowns Δv_p pressurized velocity, Δv_u unpressurized velocity, Δx_{op} pressurized Δx_o, Δx_{ou} unpressurized Δx_o and d the minimum distance between source and receiver. For each arrival time t_i of the pressurized case and t_j in the unpressurized case we can write an equation of the form (3).

$$t_i - \frac{1}{v_p}\sqrt{(x_i-x_{op})^2 + d^2} = -\frac{1}{v_p}\sqrt{(x_i-x_{op})^2 + d^2}\,\Delta v_p - \frac{(x_i-x_{op})\;\Delta x_{op}}{v_p\sqrt{(x_i-x_{op})^2 + d^2}} + \frac{d\Delta d}{v_p\sqrt{(x_i-x_{op})^2 + d^2}} \quad i=1,2\ldots N \tag{4}$$

$$t_j - \frac{1}{v_u}\sqrt{(x_j-x_{ou})^2 + d^2} = -\frac{1}{v_u^2}\sqrt{(x_j-x_{ou})^2 + d^2}\,\Delta v_u$$

$$- \frac{(x_j-x_{ou})\ \Delta x_{ou}}{v_u\sqrt{(x_j-x_{ou})^2 + d^2}} + \frac{d\Delta d}{v_u\sqrt{(x_j-x_{ou})^2 + d^2}} \qquad j = 1,2\ldots M \tag{5}$$

The left hand sides of equations 4 and 5 are the differences between model predictions of travel times and actual arrival times. The right hand sides of the equations give the changes in model travel times as a function of changes in the model. If there are N data points for the pressurized case and M for the unpressurized, there are a total of M + N equations with 5 unknowns. This overdetermined system is solved using the normal least squares procedure. The system is written in matrix form

$$Y = AX \tag{6}$$

where Y is an (M+N) by 1 matrix composed of the differences between actual arrival times and the times predicted by the model, A is a (M+N) by 5 matrix of coefficients computed from the starting model and X is a 5 by 1 matrix which is the solution matrix or perturbation to the initial model. The least squares solution of (6) is

$$X = (A^T A)^{-1} A^T Y \tag{7}$$

The solution given by equation (7) is valid in the case that the matrix A^TA has a non-zero determinant. In many cases of interest it is found that the matrix A^TA is nearly singular. In this case the damped least squares inverse is used (see Appendix C). The damped least squares solution of equation (6) is

$$X = (A^TA + \varepsilon^2 I)^{-1} A^TY \qquad (8)$$

where ε is called the damping parameter.

The fit of the computed model to the data is not the best possible fit when damped least squares technique is employed. The best fit is found for $\varepsilon^2=0$ which is the least squares fit. When A^TA is nearly singular, error in the data can cause widely varying model predictions. Use of damped least squares helps to stabilize the solution so that the model is less affected by error in the data. The value of ε^2 is picked as a trade off between the resolution or uniqueness of the model and the effects of data errors on the computed model parameters. Resolution is defined in Appendix C as

$$R = (A^TA + \varepsilon^2 I)^{-1} A^TA \qquad (9)$$

If $\varepsilon^2=0$ then R=I and the model is unique. The covariance

matrix is defined as

$$C = \sigma^2 (A^T A + \varepsilon^2 I)^{-1} A^T A (A^T A + \varepsilon^2 I)^{-1} \quad (10)$$

where σ^2 is the variance of the data. The diagonal elements of C give the error in the computed model parameters. If there is no known value for σ^2, it can be estimated from (Draper and Smith, 1969)

$$\sigma^2 = \frac{1}{f} \sum_i (\Delta y_i)^2 \quad (11)$$

where Δy_i is the difference between model prediction of the travel time and the actual travel time and f is the number of degrees of freedom in A which equals the number of rows minus the number of columns of A. Increasing ε results in smaller estimates of model error but worse resolution.

The equation relating travel time to velocity and source location was linearized to facilitate inversion. The assumption made in linearizing the equation was that the perturbations to the initial model are small and thus that terms of order greater than one in model perturbations could be neglected. This assumption means that the starting model should be close to the final model. It also means that iteration of the inversion scheme is possible to allow the solution to converge to

some desired accuracy. Six iterations were used in all cases to be discussed.

4.3.2 Results of Velocity Determination

Arrival time data from four steps of the first dual well seismic experiment and three steps from the second experiment were inverted to find seismic velocity. For each step in each experiment, the receiver was in a location that was different from the other steps. Table 2 lists for each step of the first experiment the receiver depth in GT-2 and the depth range for the source over which good quality first arrivals were found. Table 3 gives the same information for the second experiment. Depths in the holes are measured from a reference at 2651.8 meters (8700 ft) above mean sea level. This ensures that depths in both boreholes are given with respect to a common horizontal plane. Results of the 1977 experiment will be discussed first.

Table 2 lists the velocities obtained by inverting data obtained during the first experiment. In addition the table contains values of minimum source receiver spacing, the source depth at which that minimum spacing occurred and the total number of first arrival times for each condition, pressurized and unpressurized, used in the inversion. A parameter describing how well the

predicted hyperbola fits the data is also given. This parameter is computed from (11)

$$\sigma^2 = \frac{\sum_{k=1}^{N} (t_{pk} - t_k)^2}{N} \qquad (12)$$

where t_{pk} is the predicted time in milliseconds for the k^{th} arrival, t_k is the actual time of the k^{th} arrival and N is the number of arrival times used. If undamped least squares inversion were used, $\varepsilon^2 = 0$, then σ^2 would be a minimum for all choices of models. Since damped least squares was used, σ^2 is not a minimum value.

Figures 13-20 show plots of the first arrival time data for each step in both pressurized and unpressurized cases. Every other data point is represented in each figure. Triangles represent measured arrival times and the line is the least squares fit to the data. Note that data is obtained from different source depth ranges for pressurized and unpressurized cases. This was necessary in order to obtain a usable number of good quality first arrivals for the inversion.

The agreement between predicted travel times and measured travel time is remarkably good. The velocity computed for the pressurized case in each of steps 2, 30 and 16 is less than the velocity computed for the unpressurized cases. Only in step 7 do the pressurized and unpressurized velocities appear to be equal.

The value of σ (equation 12, Table 2) is always larger for the pressurized case than the unpressurized case. Since first arrivals for pressurized seismograms were often more difficult to pick than the corresponding first arrivals of the unpressurized seismograms more error in the arrival time for the pressurized case may be expected. Another explanation for why the fit to the unpressurized data is better than the fit to the pressurized data may be that the rock is more heterogeneous when pressurized than when unpressurized. Scale of heterogeneity must be on the order of a few meters or less to cause variations that can be detected during one step of the experiment. Cause of heterogeneity may be fluid pressure entering microcracks in some regions more than others. Since a single velocity was used to fit all data for a single, pressurized or unpressurized, case for each step, rock heterogeneity will result in a misfit between theory and data. If there are regions of heterogeneity in the rock then arrival time data will depart from a hyperbola. The model fit to the data will provide an average value of the rock velocity for paths between source and receiver as the source moves along EE-1. To investigate this further, Figures 21-24 show the difference between pressurized and unpressurized arrival times as a function of depth of the source in EE-1. The differences in steps 2 and 7 are fairly

smooth functions of depth which indicate that if heterogeneity is introduced into the rock in these regions when the system is pressurized it is larger than the 20 meter size of the region being examined in these steps. Differences for steps 30 and 16 show much more variation with position of source along the EE-1 wellbore. The amplitude of the difference in step 30 is the largest of all four steps. Waves traveling from source to receiver for this step cross the gneiss-granodiorite boundary that may be a weak zone where microcracks are easily permeated by water which causes a change in velocity when water pressure is increased. The velocities found for step 30 are the lowest of all four steps which means that rock in this region must contain more open microcracks than rock in other regions. Travel time differences between pressurized and unpressurized cases for step 16 (Figure 24) show strong variations with source position. Characteristic length of this variation is about 3 meters. This variation must be caused by increase in porosity of the rock during removal of heat from this region. Rock in this region shows the greatest change in temperature from the virgin in situ temperature (see Figure 2).

Table 3 lists results found from analysis of first arrivals of the 1978 dual well seismic experiment. Figures 25 through 30 show arrival times for each step

as well as fits to the data. Velocities measured from the 1978 data are lower than velocities found from the 1977 data. This result was expected because of the large drop in in situ temperature that occurred during the 75 day flow experiment. This drop in temperature should have had some effect on the microcrack content of the rock and thus on seismic velocities. This will be discussed in more detail in the next chapter. The differences in velocities between pressurized and unpressurized cases are smaller for the second experiment than they were during the first experiment. This result is surprising and may be due to the aspect ratios of cracks introduced by the removal of heat. If the cracks that are introduced close at pressures greater than a few hundred bars, a change of pore pressure of 100 bars, that changes minimum effective stress from 200 to 100 bars (see Table 1, Chapter 3), will have little effect on seismic velocity. The amount and aspect ratios of cracks necessary to explain the velocities measured during the second experiment will be discussed in greater detail in the next chapter. The very small difference in seismic velocity between pressurized and unpressurized cases found for step 2 is probably a result of the different locations of the data sets used in the inversion. The pressurized data begins at a depth of 2556 meters which is 15 meters above

the beginning of the unpressurized data. The additional distance of the pressurized data away from the heat extraction region causes waves to be less affected by new fractures resulting in a larger velocity than would be obtained if the data were recorded for lower source depths.

The values of σ in Table 3 for the 1978 experiment are smaller than values found from inversion of data from the 1977 experiment. This may be due to the higher signal to noise ratio of seismograms recorded in 1978 which allowed more accurate picking of P wave arrival times. Another explanation is that the 75 day flow test extracted heat uniformly from the rock between the GT-2 and EE-1 boreholes and actually reduced heterogeneity in the rock that was present at the time of the 1977 seismic experiment.

Travel time differences between pressurized and unpressurized cases are plotted vs. source depth for steps 2, 11, and 16 in Figures 31-33. The differences are smaller than the differences found for 1977 data. Steps 2 and 11 show fairly regular patterns with depth. Data for step 16, Figure 33, shows some variation with depth. Length scale of the heterogeneity appears to be about 3 meters as was found for the 1977 experiment (Figure 24).

4.4 Spectral Analysis of Seismograms

If the spectrum of the source of a seismic signal is known, information about scattering and attenuation properties of a medium can be gained by analyzing the spectral content of the signal after it has propagated some distance through the medium. While it appears that the amount of attenuation of waves is a very sensitive indicator of the microcracks as well as fluid in the rock, measurement of attenuation is very difficult and results often show a great deal of scatter. The scatter in results is usually attributed to scattering of waves as they pass through the medium. It is very difficult to separate the effect of scattering from attenuation. Aki (1973) applied the random medium theory of Chernov (1960) to teleseismic P waves recorded at the Montana LASA. He successfully explained amplitude and phase variations recorded across the array for .5 Hz waves but found that scattering for 1 Hz waves was too strong for the assumptions made by Chernov to be valid. Aki and Chouet (1975) studied amplitude decay of coda waves from local earthquakes to model attenuation and scattering effects on waves in the frequency range of 1-24 Hz. In their model, coda waves are assumed to be waves that are singly scattered by heterogeneities. Because of the scattering model, radiation pattern at the source does not enter into their analysis.

Chouet, Aki and Tsujiura (1978) and Rautian and Khalturin (1978) used coda waves to simultaneously determine earthquake source spectrum as well as medium characteristics.

In this section, spectral characteristics of signals recorded during the second dual well seismic experiment will be discussed. Data from the first experiment was not analyzed in detail because of the many gain changes that occurred during the execution of the first experiment and the lack of reliable records of times and magnitudes of the gain changes. This lack of records would make it difficult to reliably compare amplitudes between different sets of data. The second reason for not analyzing data from the first experiment is the large amount of computer time required to process the data.

It was found that the spectra of individual signals were often quite different from one another even though their source locations were very close together. This was expected because the seismograms themselves appear to be very different (see e.g. Figures 11 and 12). This means that the signals are composed of a great deal of noise or that the medium through which the waves travel is strongly heterogeneous. In order to try to find some consistency in signal spectra, it was decided to average the spectra of a large number of signals and compare these averages among the data sets. If noise

in the signal is considered to be signal generated, e.g. due to scattering, then the amplitude of the noise is proportional to the amplitude of the signal. In this case, Patton (1978) showed that the appropriate averaging process is to average the logarithms of signal amplitudes. The procedure used was to window a section of each seismogram, taper the ends of the windowed signal, perform a digital fast Fourier transform and average log amplitudes of the spectra of all the signals. Amplitude was found by exponentiation of the logarithmic average. Window length was chosen to be .85 milliseconds. Sections of each seismogram were windowed beginning .06 msec before the P arrival time. Averages of the log of spectral amplitudes of seismograms were computed for successive time windows along the seismogram. In this way, average amplitudes as a function of time are found. Rather than using all seismograms for all steps, only 900 seismograms for each case of each step were used. The seismograms used began with the seismogram with the shallowest source depth for each case as listed in Table 3. Spectral amplitudes will be discussed by separating data into two sets. The first set contains only direct P waves and secondly the decay of the amplitude of the signals with time will be considered.

4.4.1 Direct P Waves

In this section, average of amplitudes of the first windowed section of each seismogram will be discussed. Waves in the first .79 milliseconds after the first arrival will be considered as direct P waves. Figures 34-36 show amplitude spectra averaged as discussed above for the first .85 milliseconds of signal beginning .06 milliseconds before the fist P arrival for steps 2, 11 and 16. Average spectra for unpressurized signals are drawn with a solid line and pressurized spectra are dashed lines. Amplitudes have been corrected for differences in gain of the recording system so all plots are referenced to a common gain. The figures show that the amplitudes of the pressurized signals are lower than amplitudes of unpressurized signals. Table 4 lists spectral amplitudes at selected frequencies. If it is assumed that source strength is the same for both pressurized and unpressurized cases, the lower amplitude of the pressurized signal means that either Q is lower or scattering is stronger when the fluid is pressurized. Lower values of Q are expected because the effective pressure is lower when the system is pressurized. First arrivals may have lower amplitude when the system is pressurized if waves have passed through a fluid filled crack as discussed in Chapter 2.

The change in amplitude of a body wave due to attenuation and geometric spreading can be written as

$$A \sim \frac{1}{x} e^{-\frac{\pi f x}{Qv}} \qquad (13)$$

where x is travel distance, v wave velocity, f frequency and Q seismic quality factor. If velocity is considered to remain constant for the pressurized and unpressurized cases, the ratio of the signal amplitude of the two cases can be written as a function of the difference in inverse Q's

$$\ln\frac{A_{up}}{A_p} = \frac{\pi f x}{v} \left(\frac{1}{Q_p} - \frac{1}{Q_{up}}\right) \qquad (14)$$

where subscript up stands for unpressurized and p for pressurized cases. Values of differences in inverse Q's for three frequencies 8, 12 and 15 Khz are given in Table 5a. Velocities used to compute values given in the table were the average value of the velocities for pressurized and unpressurized cases for each step. Travel distance, x, in equation (14) was chosen as the average of the maximum and minimum source-receiver distance for each step.

It is impossible to compute absolute values of Q from values given in Table 5a. If Q is known in one case, say pressurized, then the value of Q in the other

may be found. To find absolute values of Q it would be necessary to have some information on the amplitude of waves as a function of travel distance. Since source-receiver distance changes as the source moves in the borehole, one might expect to obtain the distance dependence of amplitude by computing amplitudes for various source locations. Unfortunately this procedure is complicated by the lack of knowledge of source radiation pattern which modulates the amplitude of the signal as a function of angle between the borehole and the direction of wave propagation. Another problem is that the differences between maximum and minimum travel distances are too small to produce a significant change in amplitude.

Although it is impossible to find absolute values of Q from data in Table 5a, it is possible to place an upper bound on values of Q in the pressurized case by assuming that Q_{up} is infinite. The values of Q_p obtained in this manner are listed in Table 5b. Values of Q_p are very low for steps 11 and 16 which may mean that signal amplitude was decreased by scattering or passing through a fracture rather than by anelastic attenuation.

Amplitudes of waves for different steps can also be compared to find differences in inverse Q as a function of depth. Since signals recorded in step 2

are of much higher amplitude than signals in steps 11 and 16, even though travel distance is greater in step 2, it may be useful to compare steps 11 and 16 to step 2. From (13)

$$\ln \frac{x_2 A_2}{x_s A_s} = \frac{\pi f}{V} \left(\frac{x_s}{Q_s} - \frac{x_2}{Q_2}\right) \tag{15}$$

where subscript 2 stands for data from step 2 and s stands for either of steps 11 or 16. Velocity has been chosen to be the average of the velocities for the two steps being compared. Table 6 gives values of $\frac{x_s}{Q_s} - \frac{x_2}{Q_2}$ for steps 11 and 16. For frequency of 8 KHz in the unpressurized case, the difference is less than zero. Since $x_2 > x_s$ for s = 11, 16 the negative value of the differences are compatible with physically possible values of Q_{up} for steps 11 and 16. Since Q must be positive, the negative values of the differences can be used to place upper bounds on pressurized Q_2 since from (15)

$$\frac{x_s}{Q_s} = \frac{V}{\pi f} \ln \frac{x_2 A_2}{x_s A_s} + \frac{x_2}{Q_2} > 0 \tag{16}$$

For x_2 equal to 28.1 meters, equation (16) gives that for 8 KHz, Q_{2up} must be less than 122 for Q_{16up} to be non-negative and less than 234 for Q_{16up} to be non-negative. A value of 122 for Q_{2up} is slightly lower

than the value predicted in Chapter 3 for the virgin rock at 0 pressure based on the model of O'Connell and Budiansky (1977). It should be expected that Q will be somewhat lower than that of the virgin rock because of the experimental activity that has taken place.

4.4.2 Amplitude Spectra for Consecutive Time Windows

Using the first part of each seismogram, some bounds on the values of Q have been found but there is no way to find actual values of Q unless source amplitude or decay of amplitude with distance are known. It is possible to investigate the decay with time in amplitude of the recorded signal. This is the procedure used by Aki and Chouet (1973), Chouet et al. (1978) and Rautian and Khalturin (1978) in studies of coda waves. When coda waves are studied, time dependence of the amplitude of a seismograph trace is assumed to be of the form

$$A(t) \sim \frac{1}{t} e^{-\frac{\pi f t}{Q}} \qquad (17)$$

Equation (17) follows from (13) if x is replaced by vt, the total distance covered by a wave that travels from source to receiver along some indirect path that includes scattering. For singly scattered waves

the point of scattering of a wave recorded at time t is at some point on an ellipsoid with major axis of length vt and whose foci are at the source and receiver. Equation (17) is only valid after some time t where source and receiver spacing is small compared to the length of the major axis of the ellipse (Sato, 1977a). Time required for this to hold is approximately two times the S wave travel time. It will be assumed in this section that equation (17) is valid for all times and the consequences of this assumption will be investigated.

Figures 37-39 show values of natural logarithm of the product of amplitude times time for various frequencies for steps 2, 11 and 16. Amplitudes are obtained from spectral analysis of windowed seismograms as discussed above. Each window has a length of .85 milliseconds. Time is chosen as the time at the middle of the window on the seismogram that has the earliest P wave arrival time.

Values of log amplitude times time (lnAt) are remarkably close to being linear functions of time in steps 11 and 16. The linear character begins nearly at the first arrival and persists until signal amplitude decreases to the noise level that existed before waves arrived. This early start of linearity is unexpected and is not in agreement with single scattering

theories (Sato, 1977a).

Decay of lnAt with time shown in Figure 37 for step 2 is quite different from that found for steps 11 and 16. In the pressurized case, the first four points for each frequency decrease nearly linearly with time. Amplitude of lnAt jumps abruptly at 8 milliseconds after which there is again a linear decrease with time up until about 16.5 milliseconds where there is again a jump. The increase in lnAt at 8 msec can be attributed to the S wave arrival. The lack of a jump in Figures 38 and 39 at the S wave arrival time means that direct S waves in steps 11 and 16 have been severely scattered or attenuated. Since S waves have smaller wavelength than P waves of the same frequency it should be expected that S waves will be more severely scattered than P waves. It was found in Chapter 2 that SH waves should be reflected by a water filled fracture. Relative amount of attenuation of P to S waves is more difficult to quantify but S wave attenuation is probably not strong enough to completely obscure the S wave arrival. The jump in the value of lnAt at 16.5 msec for step 2 in the pressurized case cannot be attributed to any phase arrival that is visible on seismogram traces. Travel time of 16.5 milliseconds is about the time required for a ray to travel from its source down to a depth of

2630 meters and back up to the receiver. Figure 3 shows that 2630 meters is about the depth of the gneiss-granodiorite contact which is believed to be the top of the region most affected by fluid flow and heat extraction. Figure 2 shows that the top of the temperature anomaly due to heat extraction is at about 2630 meters. The top of the geothermal system near the gneiss-granodiorite boundary may coincide with the top of one or many hydrofractures which act to scatter waves in all directions. In the next section an attempt will be made to locate the tops of such fractures by stacking seismograms recorded during the pressurized part of step 2.

Time dependence of lnAt for unpressurized step 2 data is almost an exponential decrease in time with a large jump in amplitude at the S wave arrival time. This data will be discussed in more detail in the next chapter.

From equation (17) the slope of lnAt vs t is proportional to frequency divided by Q. Table 7 gives the values of Q at various frequencies determined from the slope of the lines in Figures 37-39. No values are given for unpressurized step 2 and values given for pressurized step 2 are those obtained from the slopes of lines at times prior to the S wave arrival. Values of Q given in Table 7 are much

larger than values that were expected from first arrival amplitudes. The smaller values of Q required by first arrival amplitudes may mean that first arrivals have been attenuated by passing through one or more fluid filled fractures that later arrivals do not pass through. Another explanation is that later arriving scattered waves travel mainly outside of the altered, highly attenuating rock near the boreholes. As waves travel away from the immediate vicinity of the boreholes, fluid pressure must decrease, temperature approaches virgin in situ values and attenuation decreases. Outside the region of fluid flow, the effective stress may be increased when the geothermal system is pressurized since fluid pressure acts as an added confining pressure to the rock where pore pressure is not increased. These ideans will be quantified in the next chapter.

4.5 Stacking of Seismograms

In the previous section it was found that values of lnAt decreased linearly with time for most of the data analyzed. Data from step 2 showed deviation from linearity which is not yet completely understood. The jump in the value of lnAt that occurs at 8 msec in the pressurized case is due to the S wave arrival. The jump in amplitude at 16.5 msec cannot be attributed to any late arriving phase that is visible on

individual seismograms. Figure 40 shows parts of siesmograms recorded during the pressurized part of step 2. Every tenth seismogram beginning from a depth of 2580 meters is shown. Difference in source location between successive seismograms is approximately 20 cm. Five milliseconds of each seismogram is plotted beginning 14 msec after the source fired. There is no increase in signal amplitude on seismograms in Figure 40 at 16.5 milliseconds. In order to further investigate the increase in amplitude of lnAt it was decided to stack a large number of signals to search for a coherent arrival to explain the jump at 16.5 msec. Only pressurized case of step 2 is discussed in this section.

If signals are completely uncorrelated, the ratio of amplitudes of stacked to unstacked seismograms should be $1/\sqrt{N}$ where N is the number of seismograms stacked. Since differences between two adjacent source locations is 2 cm and wavelength of 15 KHz is approximately 40 cm for P waves and 23 cm for S waves, all of the seismograms used are not statistically independent. If it is assumed that source locations for two signals must differ at least by one half wavelength for seismograms to be considered as statistically independent samples, then ratio of stacked to unstacked seismograms

should be at least $\sqrt{10/N}$ for P waves and $\sqrt{5.75/N}$ for S waves if signals are uncorrelated. For 450 stacked seismograms, the ratios are .15 for P waves and .11 for S waves.

A set of possible scattering points for P to P and S to S scattering were chosen such that the travel time from source to potential scattering point and then to the receiver fell in the interval 14 to 18 msec. Only points below the region of step 2 and between the GT-2 and EE-1 wellbores were used. For P to P scattering, the points were in the region of the gneiss-granodiorite contact. For S to S scattering points were above the contact. For a given potential scattering location, travel time for the P (or S) wave from each source location to the scattering point and then back to the receiver was computed. Time for each seismogram was shifted so that waves scattering from the given point would all fall at the same time and seismograms were stacked. Total number of points for which stacking was done was 336 for P to P scattering and 364 for S to S scattering. Scattering points were chosen to be at the edges of squares with sides of length one meter. Only points in the plane of the two wellbores were considered. Five milliseconds of record for each

seismogram were stacked. Time of stacking was 13 to 18 msec into the record for source depth of 2574 meters. Time intervals of other seismograms were shifted by an amount equal to the difference in travel time between the source at 2574 meters and the scattering point and the source location of a given seismogram and the stacking point. Total number of seismograms used was 450.

Amplitudes of stacked seismograms for S to S stacking were a maximum of .12 times the amplitude of individual unstacked seismograms in the time range for which stacking was done. Small sections of increased amplitude do occur on the stacked seismogram but the magnitude of these events are too small to be associated with the 16.5 msec arrival in Figure 37.

When seismograms are stacked for scattering points appropriate to P to P scattering, the maximum amplitudes of the resultant stacked seismograms are as large as .2 times the amplitudes of the unstacked seismograms. These stacked seismograms show coherent phase arrivals but the ratio of stacked to unstacked seismogram amplitude is too small for the arrivals to have any significance.

4.6 Summary

A great deal of data has been obtained from the

seismograms recorded during the two dual well seismic experiments. Values of P wave velocity have been measured to very high accuracy. It was found that P wave velocity decreases when fluid pressure in the geothermal system is artificially increased by 100 bars. This decrease in velocity is consistent with the concept of effective pressure discussed in Chapter 3. The size of the decrease in velocity will be further discussed in the next chapter. P wave velocity was found to be lower during the 1978 experiment than during the 1977 experiment in both pressurized and unpressurized cases. This lower velocity is due to the introduction of microcracks during the 75 day fluid flow and heat extraction experiment performed during the time between the two dual well seismic experiments. The low velocities in the unpressurized case mean that the cracks do not close up completely when fluid pressure is lowered.

In order to measure magnitude of Q using direct P waves, more information about source amplitude or change in signal amplitude with distance is needed. Since this information is not available, only values of differences of inverse Q's between two data sets can be obtained. These values enable bounds on Q to be placed for some cases. Upper bounds for Q in the pressurized case of the 1978 experiment are listed

in Table 5b. These values were obtained by assuming that Q is infinity in the unpressurized case. Values given in Table 5b are very low for steps 11 and 16 and may indicate that wave amplitude in the pressurized case has been decreased by passing through one or more fluid filled fractures.

Values of the log of spectral amplitude times time have been found to decrease linearly with time in steps 11 and 16 of the second experiment. The slopes of the lines can be measured to find values of Q. The values of Q obtained in this way are too large to be consistent with first arrival data and may be due to high Q rock that surrounds the region that has been affected by heat extraction. Jumps in the value of lnAt at 8 and 16.5 msec have been found in step 2 pressurized data. The jump at 8 msec is due to the arrival of the S wave from the source. The jump at 16.5 msec is unexplained. Individual seismograms show no arrivals that can be associated with the 16.5 msec jump. Stacking of seismograms in an attempt to improve signal to noise and enhance a late arrival showed that late arrivals could be found, but none were of sufficient amplitude to be a coherent arrival from a distinct scatterer.

Step	Receiver depth	Source depth range beginning	end	Approximate Number of Seismograms Available
2	2586	2554	2612	2850
7	2634	2612	2652	1970
16	2697	2683	2709	1280
30	2612	2634	2587	2310
2a	2586	2554	2612	2850
11a	2669	2652	2683	1530
16a	2697	2683	2709	2310

Table 1. Source and receiver locations for dual well seismic experiment.

a refers to 1978 experiment.

	Step	Data begins at depth	Data ends at depth	Center depth	Minimum spacing (meters)	Velocity (km/sec)	σ (msec)	Number of First arrivals
Unpressurized	2	2577.1	2597.2	2586.2	28.5	5.95	.012	1100
	30	2625.8	2596.5	2610.6	24.6	5.83	.015	1500
	7	2615.5	2637.7	2631.9	22.1	5.93	.011	1100
	16	2682.9	2707.3	2695.3	15.8	5.89	.016	1200
Pressurized	2	2571.0	2592.9	2581.4	28.5	5.88	.013	1100
	30	2623.1	2593.1	2605.7	24.6	5.71	.020	1500
	7	2612.2	2634.3	2628.0	22.1	5.82	.014	1100
	16	2685.3	2708.4	2690.5	15.8	5.78	.018	1200

Table 2. Results of least squares fit to first arrival data obtained from October, 1977 dual well seismic experiment.

Depths in meters below 2651.8 above mean sea level.

	Step	Data begins at depth	Data ends at depth	Center depth	Wellbore spacing (meters)	Velocity (km/sec)	σ (msec)	Number of first arrivals
Unpressurized	2	2571	2606	2589	28.1	5.89	.008	1800
	11	2656	2671	2671	17.9	5.69	.008	800
	16	2690	2707	2699	15.1	5.52	.013	900
Pressurized	2	2556	2591	2584	28.1	5.87	.011	1800
	11	2652	2668	2666	17.9	5.61	.008	800
	16	2687	2705	2694	15.1	5.48	.016	900

Table 3. Results of least squares fits to first arrival data obtained from September, 1978 dual well seismic experiment.

	Step	Travel distance (meters)	Amplitude 8 KHz	12 KHz	15 KHz
Unpressurized	2	28.1	10.3	49.0	77.1
	11	17.9	43.8	18.6	6.82
	16	15.1	32.3	28.4	7.05
Pressurized	2	28.1	8.0	16.7	43.1
	11	17.9	5.7	3.22	1.02
	16	15.1	4.26	1.80	.71

Table 4. Averages of first arrival amplitudes of 900 signals at selected frequencies. Amplitudes are corrected for differences in recorder gain between sections.

Step	8 KHz	12 KHz	15 KHz
2	.0019	.0054	.0023
11	.0224	.0128	.0111
16	.0267	.0265	.0161

Table 5a. Values of $\frac{1}{Q_p} - \frac{1}{Q_{up}}$ for various frequencies.

Step	8 KHz	12 KHz	15 KHz
2	526	185	435
11	45	78	90
16	37	38	62

Table 5b. Maximum values of Q_p obtained by choosing Q_{up} to be infinity in Table 5a.

	Step	8 KHz	12 KHz	15 KHz
Unpressurized	11	- 0.23	0.22	0.35
	16	- 0.12	0.18	0.37
Pressurized	11	0.18	0.32	0.51
	16	0.29	0.43	0.58

Table 6. Values of $\frac{x_s}{Q_s} - \frac{x_2}{Q_2}$ for steps 11 and 16.

	Frequency Step	8 KHz	12 KHz	15 KHz
Unpressurized	2			
	11	220	224	
	16	109	140	166
Pressurized	2	132	377	224
	11	165	188	217
	16	63	117	126

Table 7. Values of Q obtained from slope of lnAt vs. t plotted in Figures 37-39.

Figure Captions

Figure 1. Seismic records recorded using explosive source in EE-1 and 3-axis geophone package in GT-2. Figure a is for source at 2644 m., receiver at 2667 m. Source depth for Figure b is 2415 m., receiver depth is 2463. From LASL HDR staff (1978).

Figure 2. Temperature logs recorded in EE-1 borehole at time after hole was drilled but before flow experiments were undertaken; (a) after 96 hour flow experiment in 1977, (b) and (c) after 75 day flow experiment in 1978. Data from LASL.

Figure 3. Model of EE-1/GT-2 system as obtained from geophysical logs. From LASL HDR staff (1978).

Figure 4. Power contained in seismograms as a function of source depth. Location of receiver in GT-2 for each step is given. From Albright et al. (1978).

Figure 5. Examples of P, S and D type waveforms. From Albright (1978).

Figure 6. Type of waveform recorded traveling between wellbores for pressurized and unpressurized cases. From Albright

(1978).

Figure 7. Seismograms recorded during 1977 dual well seismic experiment, unpressurized step 16. Source depth for each seismogram is given in meters.

Figure 8. Seismograms recorded during 1977 experiment, pressurized step 16.

Figure 9 - Figure 12. Seismograms recorded during 1978 experiment. Source depth is given in meters. Step and case, unpressurized or pressurized, is given at the top of each figure.

Figure 13 - Figure 20. P wave arrival times vs. source depth and theoretical fit to data for 1977 experiment. Triangles represent arrival times measured on seismograms. Only every other data point is shown. Solid line is fit to arrival time data using model parameters given in Table 2. Step and case are given at the top of each figure.

Figure 21- Figure 24. Differences in arrival times between pressurized and unpressurized cases. Step and case are listed at the top of each figure. Figures show results for seismograms recorded during 1977 experiment.

Figure 25 - Figure 30. See Figures 13-20. Data for 1978 experiment. Model parameters given in Table 3.

Figure 31 - Figure 33. See Figures 21-24. Data for 1978 experiment.

Figure 34 - Figure 36. Amplitude spectra obtained by averaging logs of amplitudes of 900 windowed signals for each step of 1978 experiment. Window for each seismogram began .06 msec before first arrival and is .85 msec in length. Solid line shows unpressurized spectra, dashed lines are spectra of pressurized signals. Effects of different gains have been corrected for. Step number is given at the top of each figure.

Figure 37 - Figure 39. Values of lnAt for various frequencies as a function of time measured from source origin time. Amplitudes obtained from averaging log spectra of 900 windowed seismograms for each case. Step number is given at the top of each figure. Part a is for unpressurized, b for pressurized.

Figure 40. Seismograms recorded in pressurized part of step 2. Each trace begins 14 msec after source fired. Source depth for top seismogram is 2580 m. Source depth for each successive seismogram is 20 cm

lower than the one above it. No phase arrival is observed at 16.5 msec.

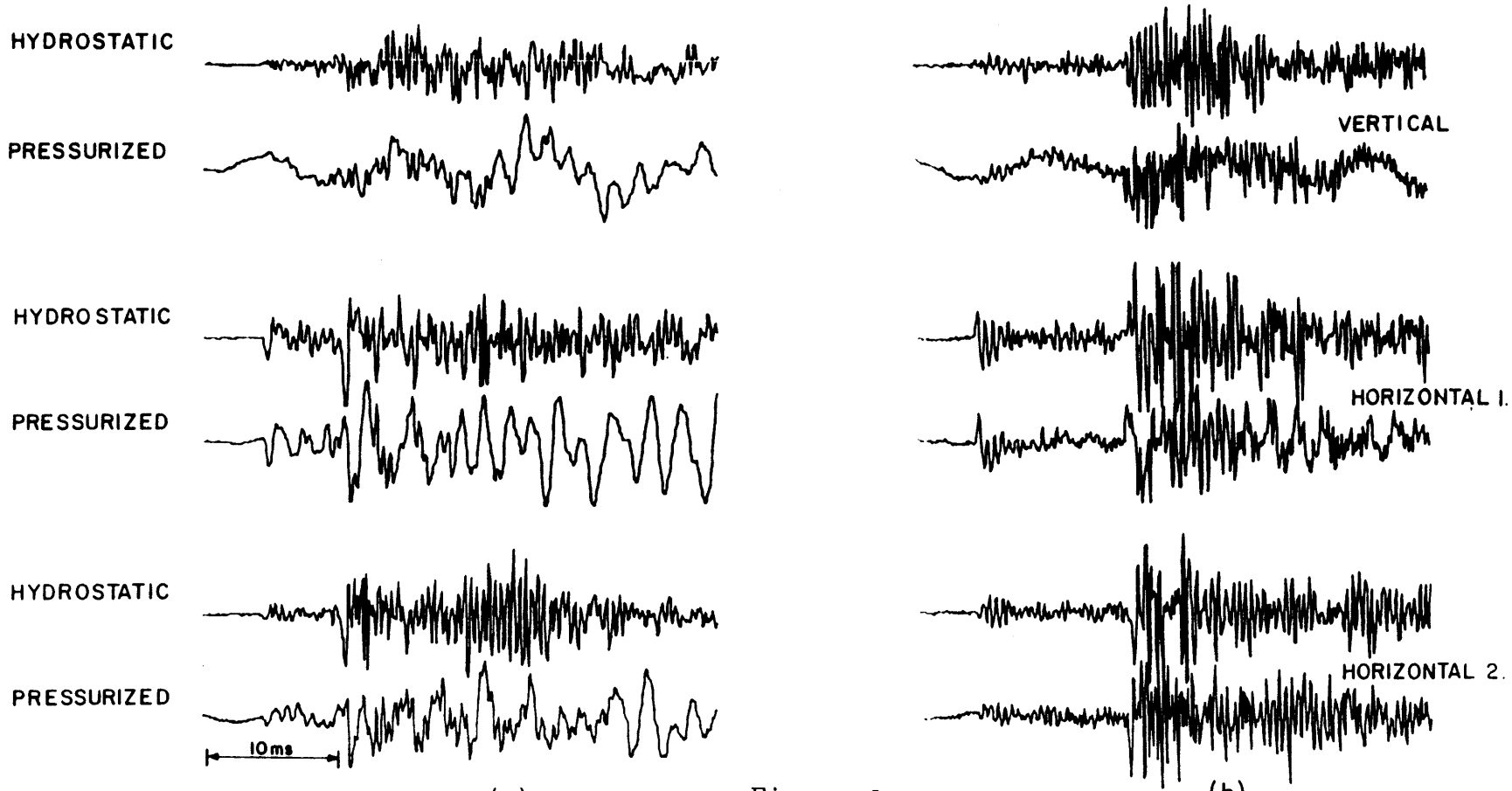
HYDROSTATIC
PRESSURIZED
HYDROSTATIC
PRESSURIZED
HYDROSTATIC
PRESSURIZED
10ms
VERTICAL
HORIZONTAL 1.
HORIZONTAL 2.
(a)
(b)

Figure 1

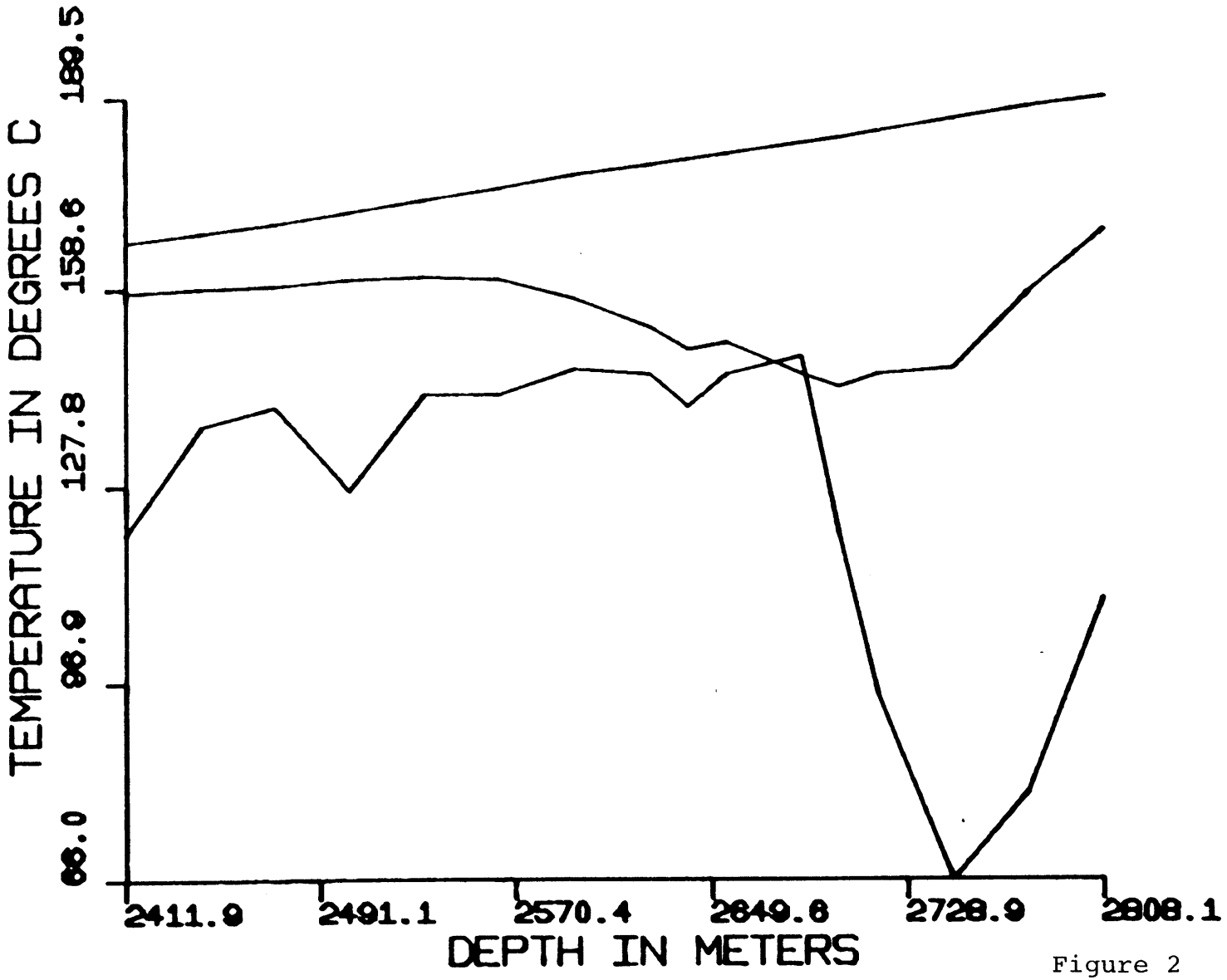
TEMPERATURE IN DEGREES C
189.5
158.6
127.8
96.9
66.0
2411.9
2491.1
2570.4
2649.6
2728.9
2808.1
DEPTH IN METERS

Figure 2

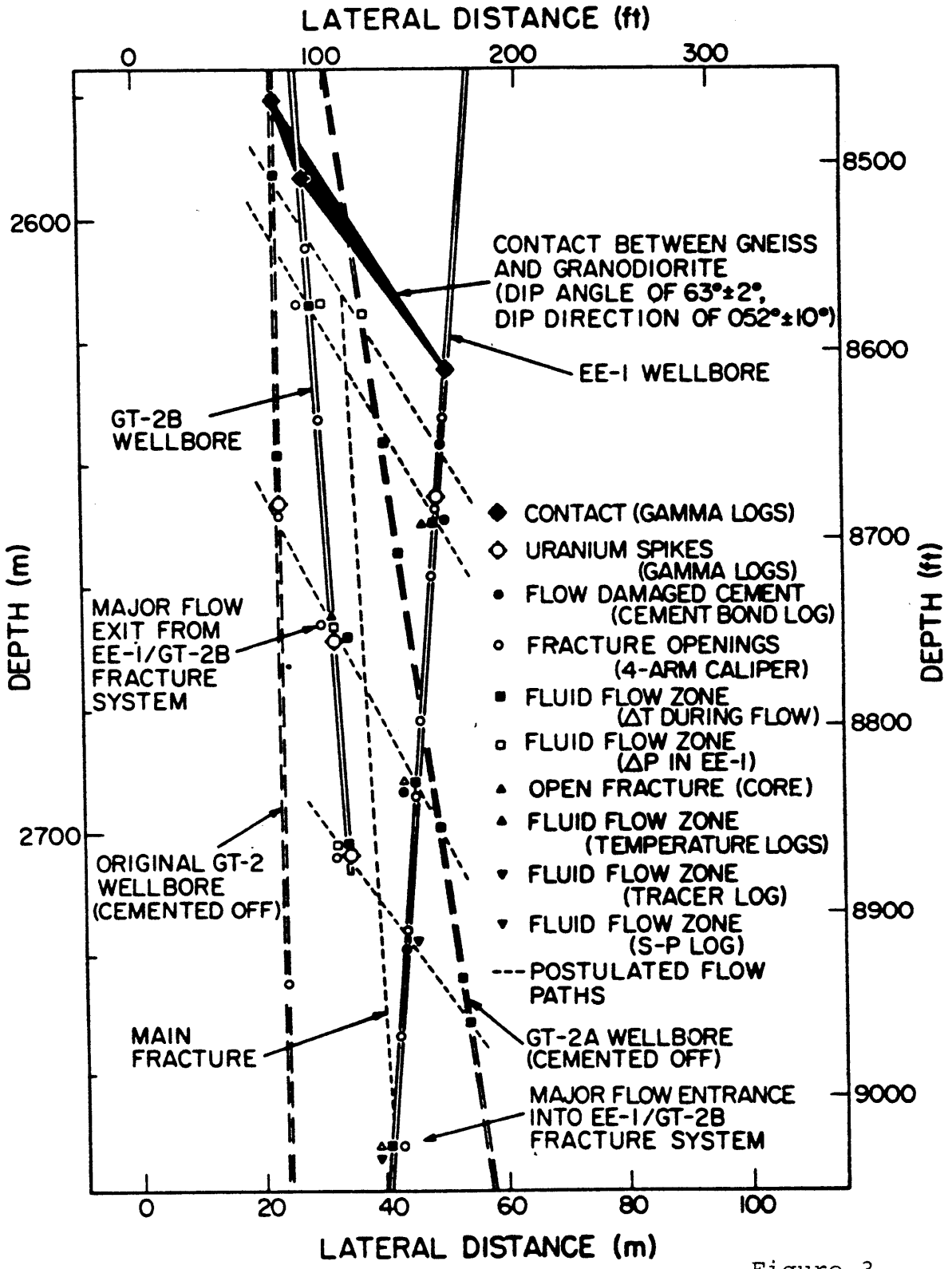
LATERAL DISTANCE (ft)
0
100
200
300
2600
2700
8500
8600
8700
8800
8900
9000
DEPTH (m)
DEPTH (ft)
CONTACT BETWEEN GNEISS AND GRANODIORITE (DIP ANGLE OF 63°±2°, DIP DIRECTION OF 052°±10°)
EE-1 WELLBORE
GT-2B WELLBORE
MAJOR FLOW EXIT FROM EE-1/GT-2B FRACTURE SYSTEM
ORIGINAL GT-2 WELLBORE (CEMENTED OFF)
MAIN FRACTURE
GT-2A WELLBORE (CEMENTED OFF)
MAJOR FLOW ENTRANCE INTO EE-1/GT-2B FRACTURE SYSTEM
CONTACT (GAMMA LOGS)
URANIUM SPIKES (GAMMA LOGS)
FLOW DAMAGED CEMENT (CEMENT BOND LOG)
FRACTURE OPENINGS (4-ARM CALIPER)
FLUID FLOW ZONE (ΔT DURING FLOW)
FLUID FLOW ZONE (ΔP IN EE-1)
OPEN FRACTURE (CORE)
FLUID FLOW ZONE (TEMPERATURE LOGS)
FLUID FLOW ZONE (TRACER LOG)
FLUID FLOW ZONE (S-P LOG)
POSTULATED FLOW PATHS
0
20
40
60
80
100
LATERAL DISTANCE (m)

Figure 3

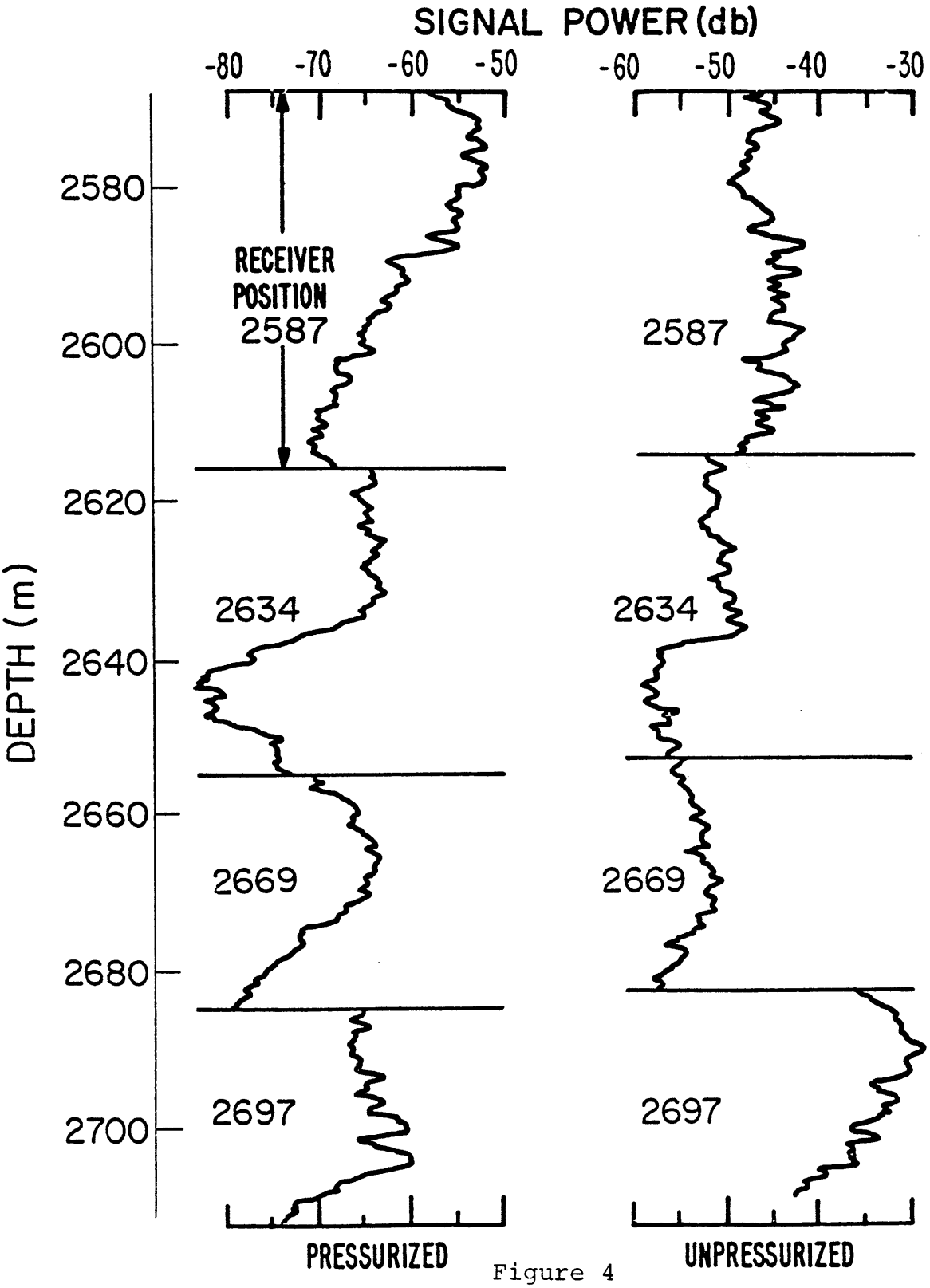
SIGNAL POWER (db)
-80
-70
-60
-50
-60
-50
-40
-30
DEPTH (m)
2580
2600
2620
2640
2660
2680
2700
RECEIVER POSITION
2587
2587
2634
2634
2669
2669
2697
2697
PRESSURIZED
UNPRESSURIZED

Figure 4

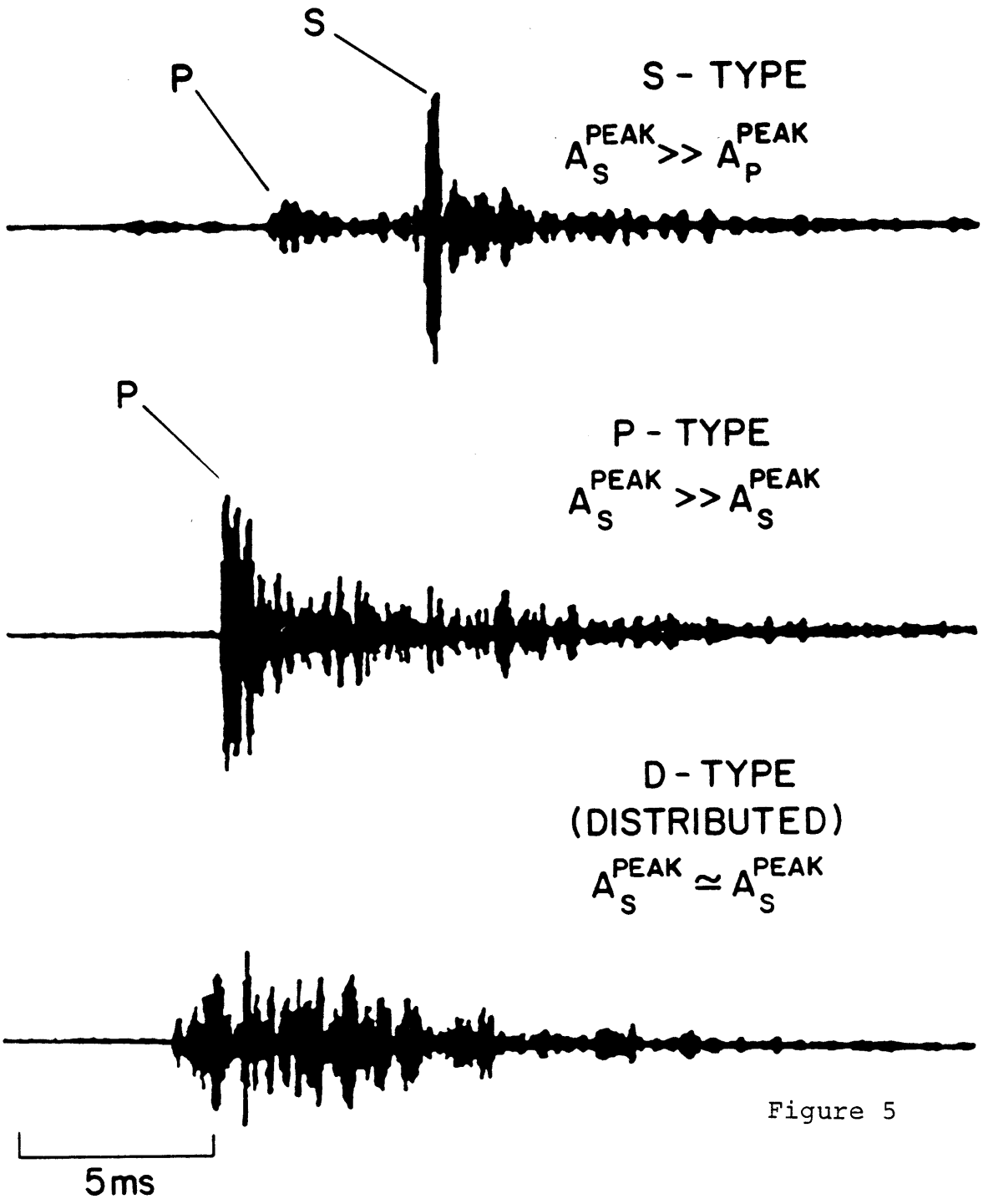
S
P
S - TYPE
$A_S^{PEAK} >> A_P^{PEAK}$
P
P - TYPE
$A_S^{PEAK} >> A_S^{PEAK}$
D - TYPE
(DISTRIBUTED)
$A_S^{PEAK} \simeq A_S^{PEAK}$
5ms

Figure 5

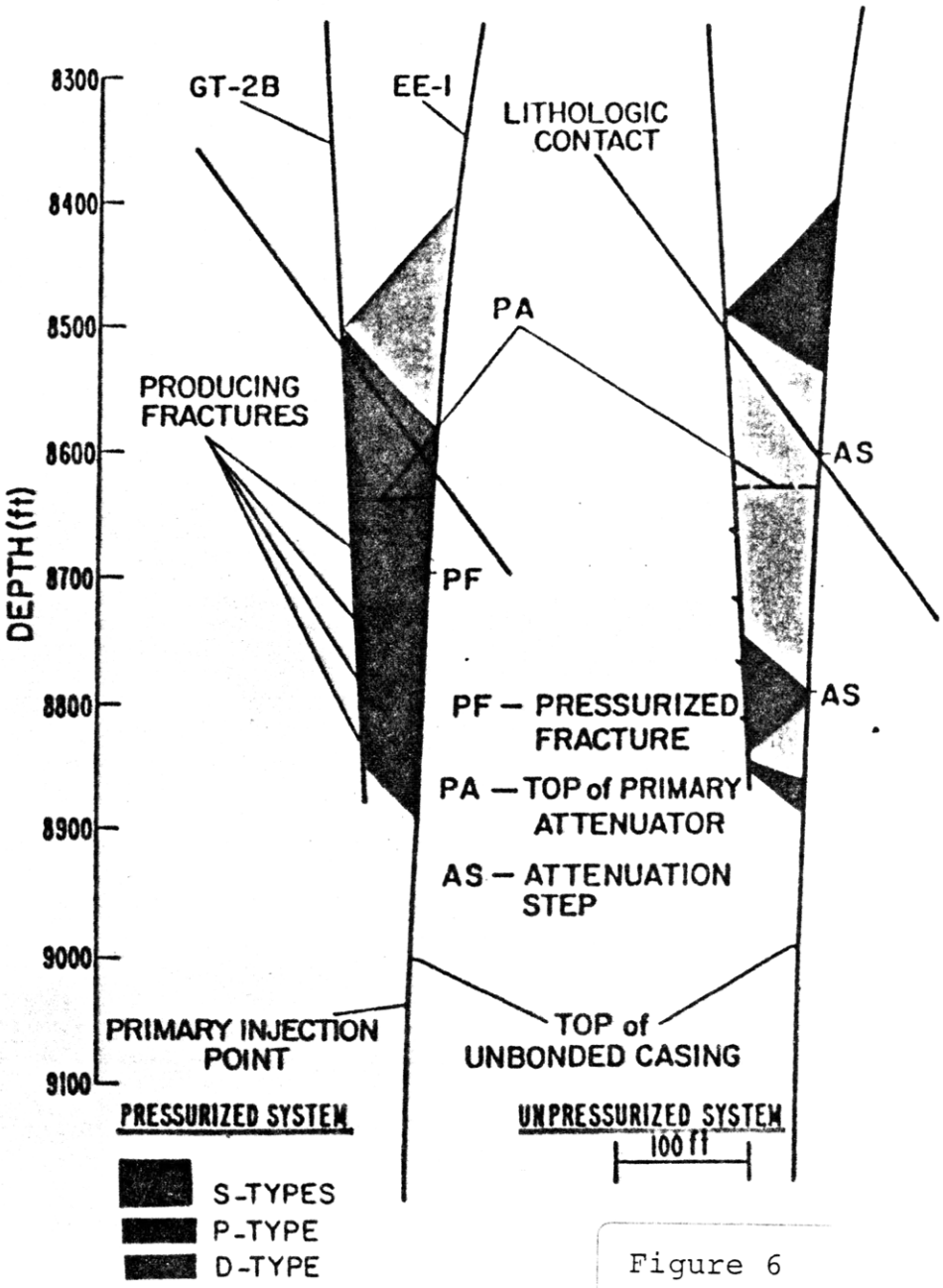
8300
8400
8500
8600
8700
8800
8900
9000
9100
DEPTH (ft)
GT-2B
EE-I
LITHOLOGIC CONTACT
PA
PRODUCING FRACTURES
AS
PF
AS
PF — PRESSURIZED FRACTURE
PA — TOP of PRIMARY ATTENUATOR
AS — ATTENUATION STEP
PRIMARY INJECTION POINT
TOP of UNBONDED CASING
PRESSURIZED SYSTEM
UNPRESSURIZED SYSTEM
100 ft
S-TYPES
P-TYPE
D-TYPE

Figure 6

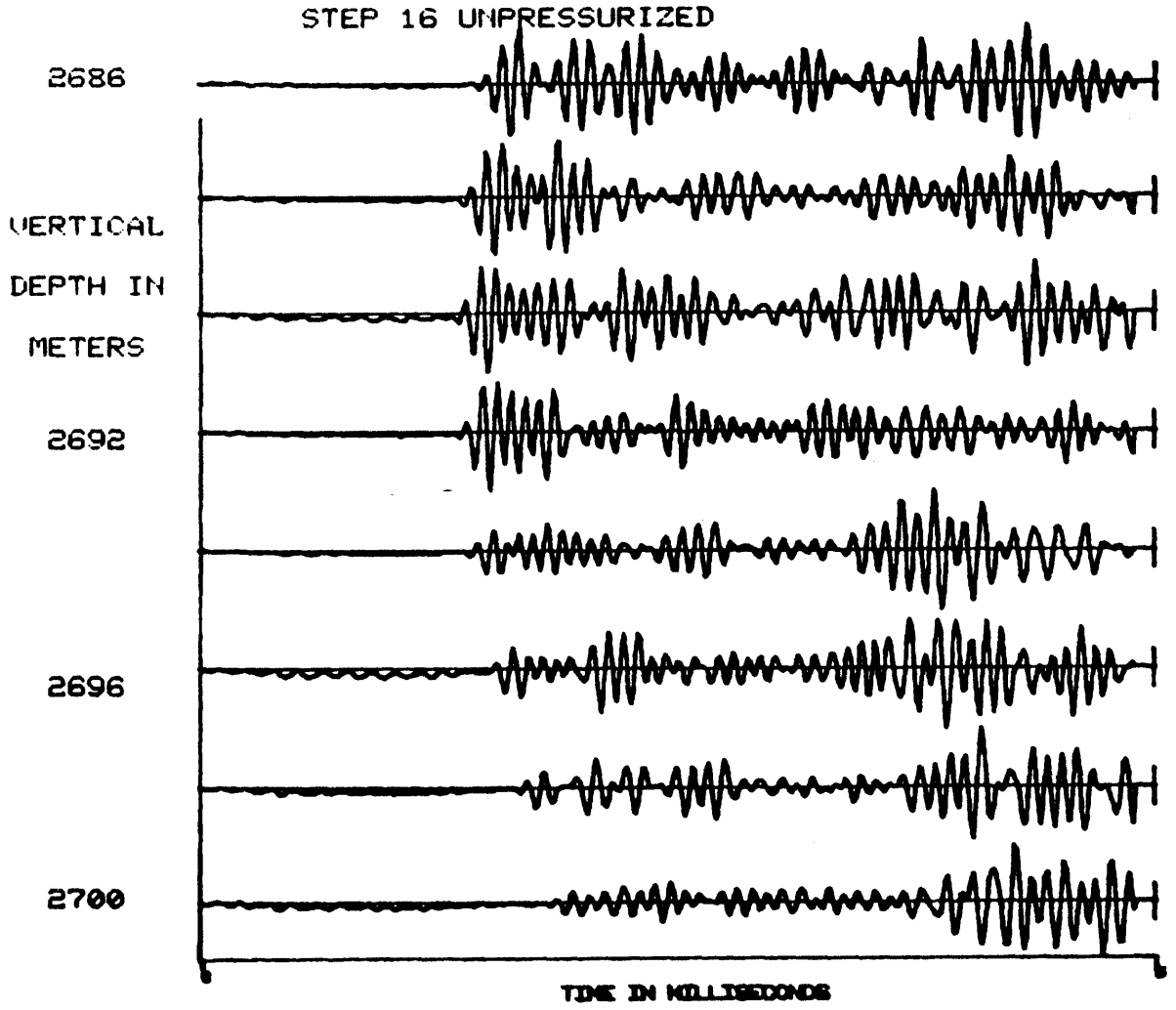
STEP 16 UNPRESSURIZED
2686
VERTICAL
DEPTH IN
METERS
2692
2696
2700
TIME IN MILLISECONDS

Figure 7

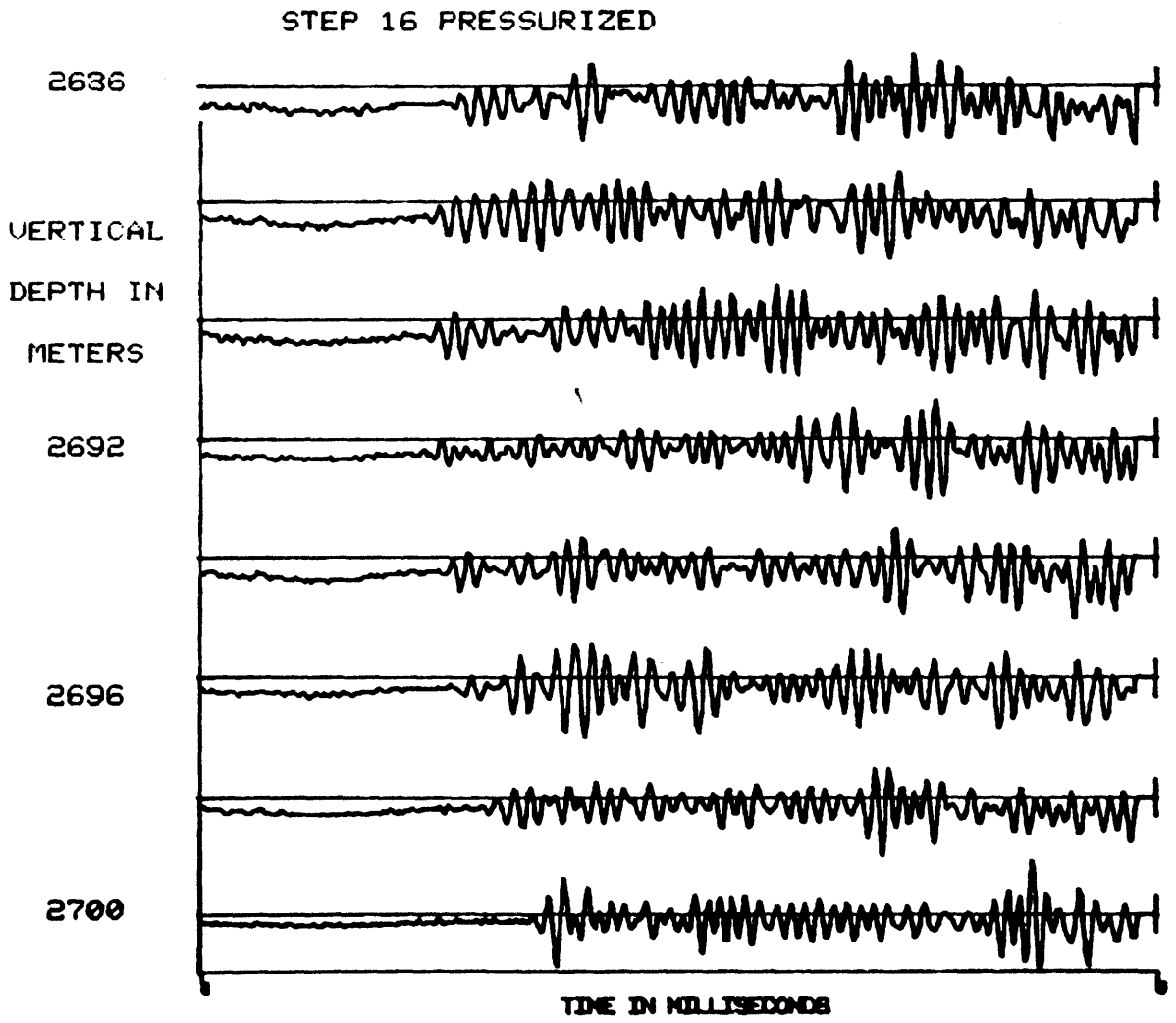
STEP 16 PRESSURIZED
2636
VERTICAL
DEPTH IN
METERS
2692
2696
2700
TIME IN MILLISECONDS

Figure 8

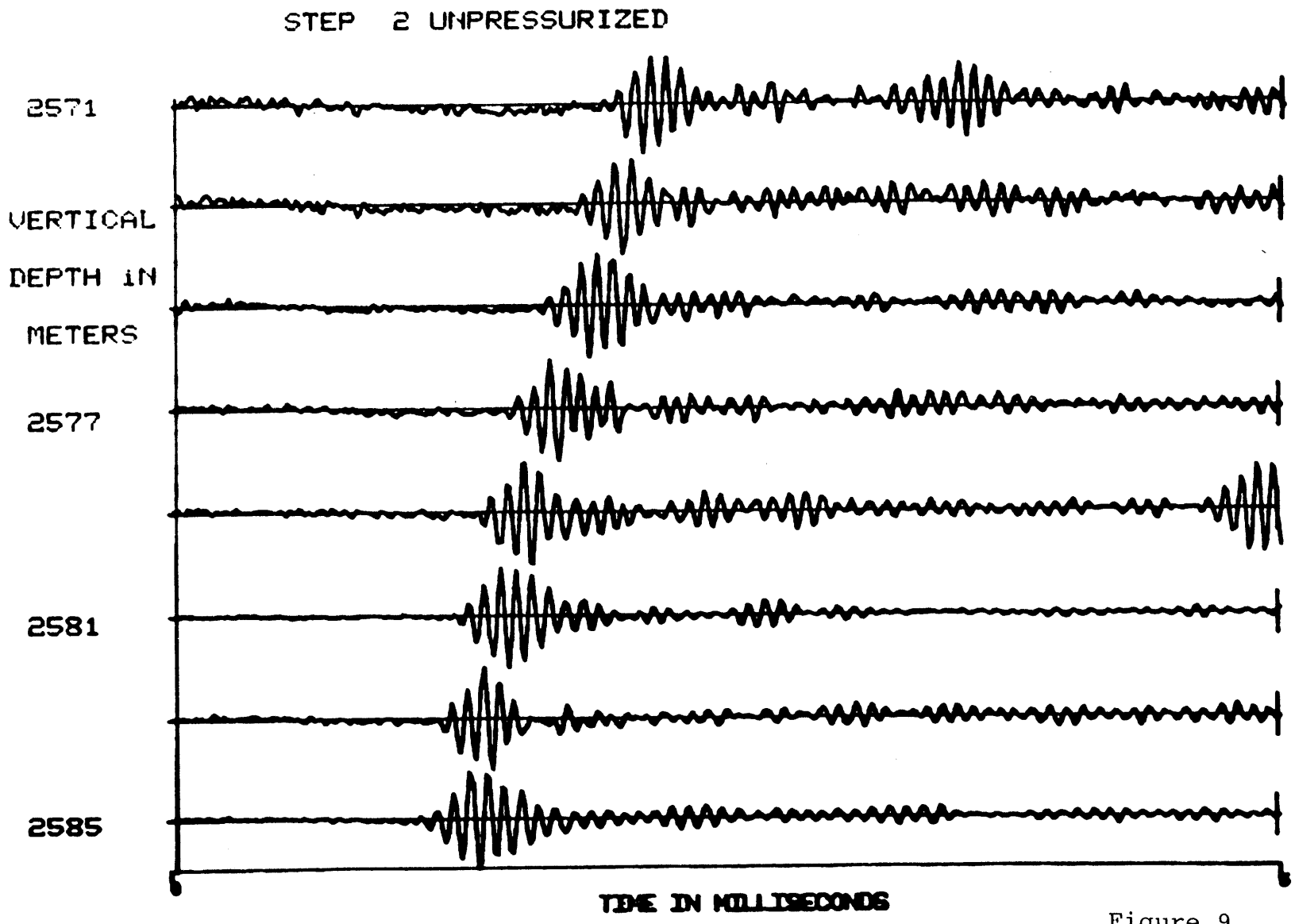
STEP 2 UNPRESSURIZED
2571
VERTICAL
DEPTH IN
METERS
2577
2581
2585
TIME IN MILLISECONDS

Figure 9

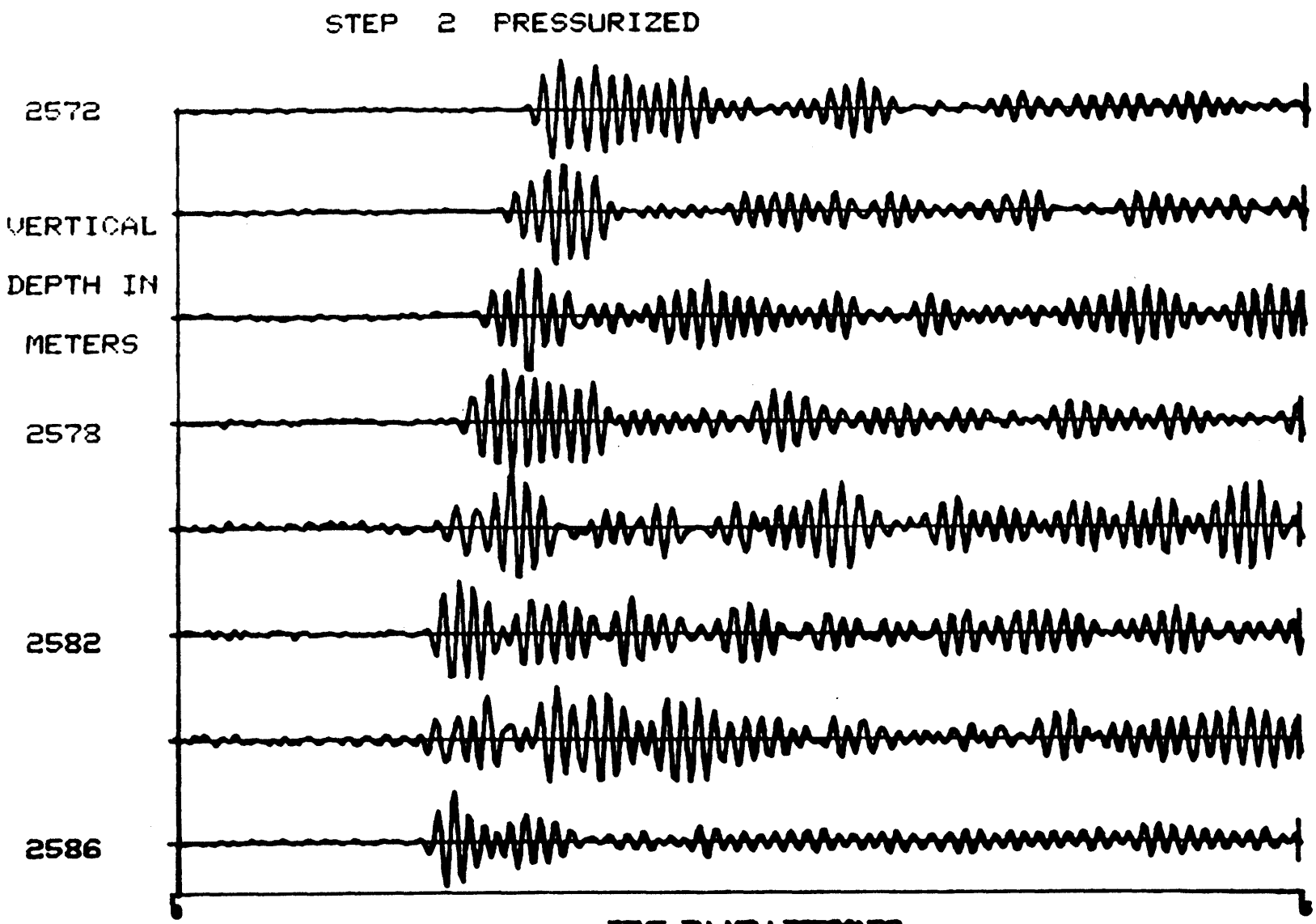
STEP 2 PRESSURIZED
2572
VERTICAL
DEPTH IN
METERS
2578
2582
2586
TIME IN MILLISECONDS

Figure 10

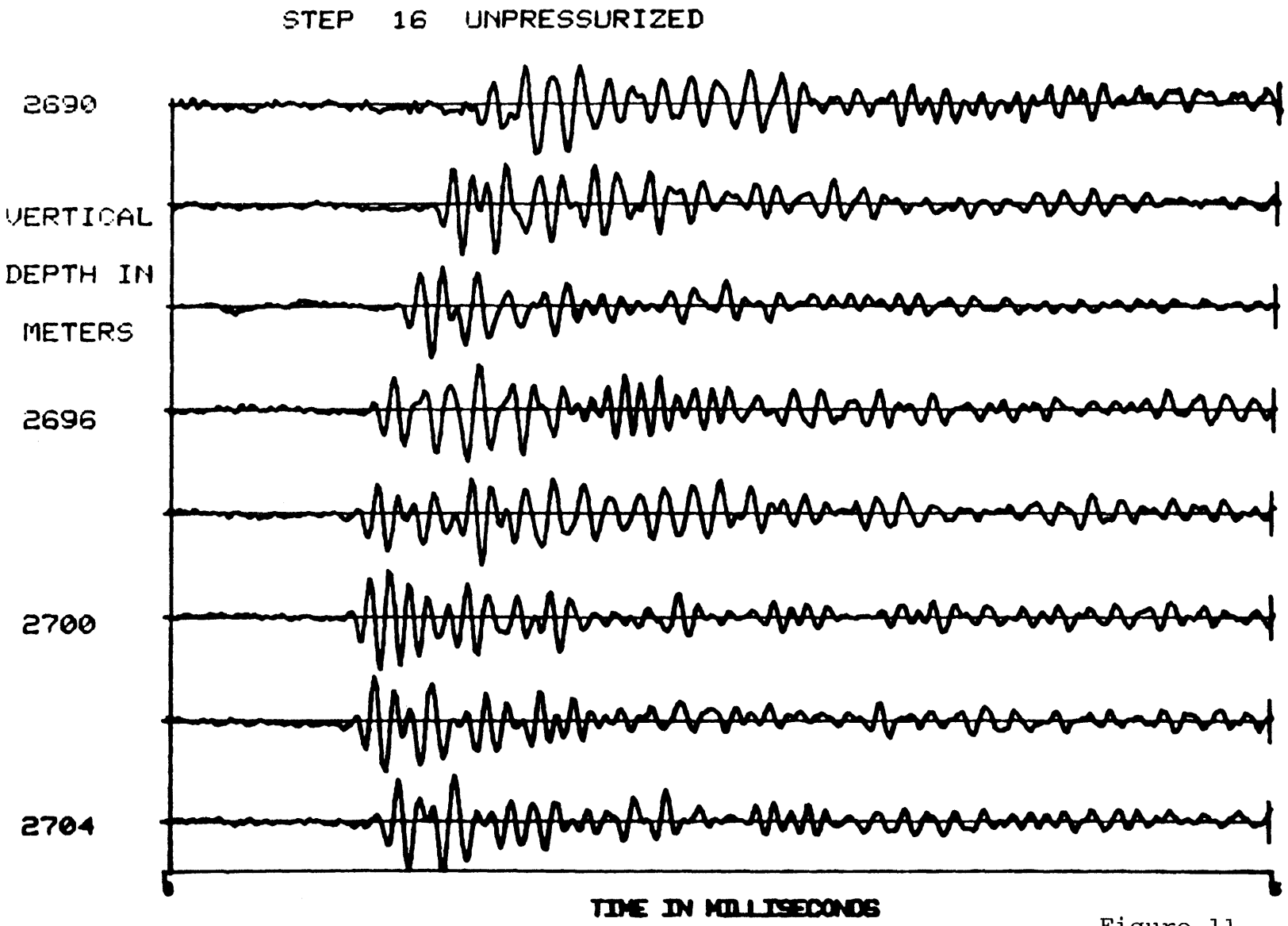
STEP 16 UNPRESSURIZED
2690
VERTICAL
DEPTH IN
METERS
2696
2700
2704
TIME IN MILLISECONDS

Figure 11

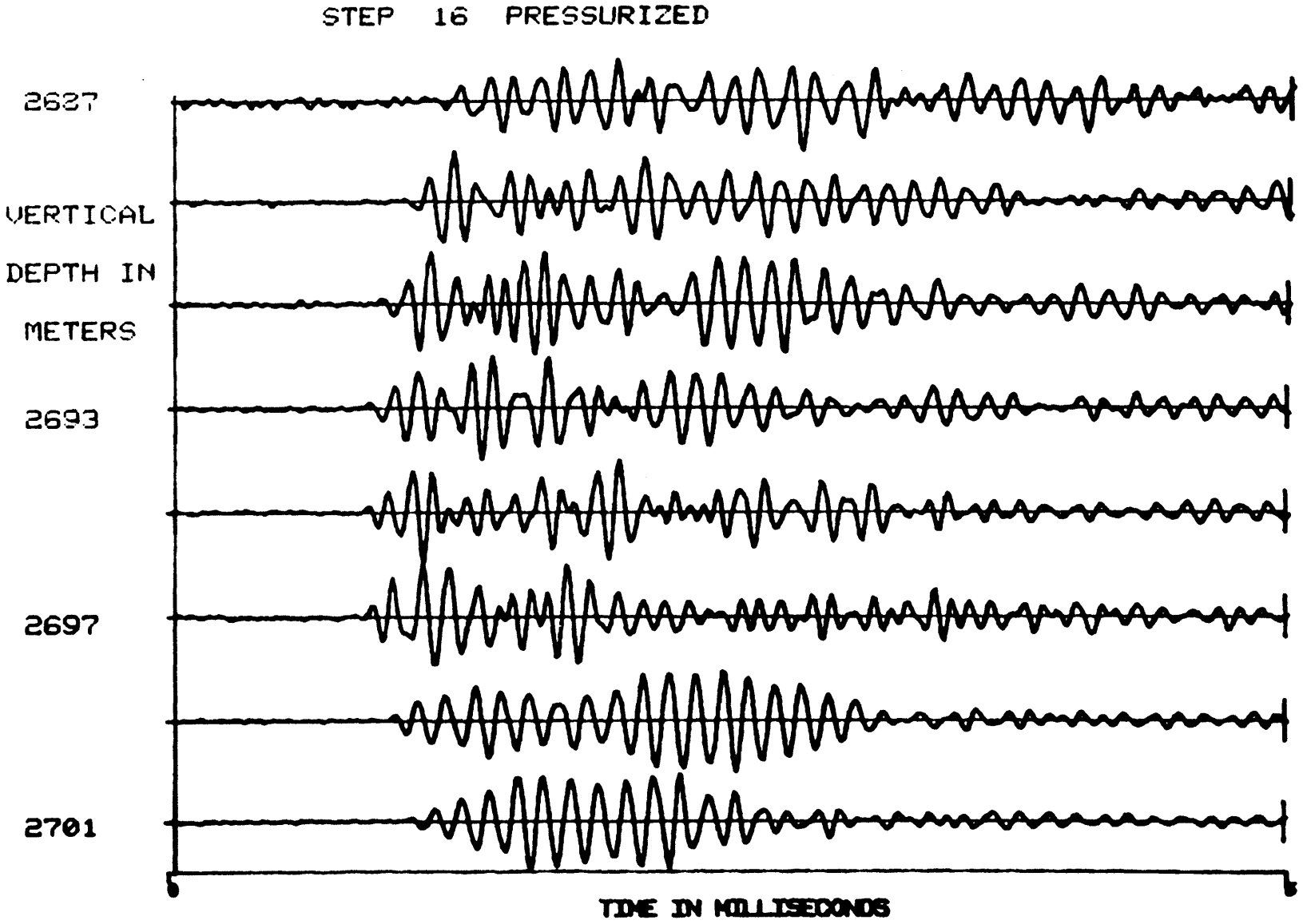
STEP 16 PRESSURIZED
2687
VERTICAL
DEPTH IN
METERS
2693
2697
2701
TIME IN MILLISECONDS

Figure 12

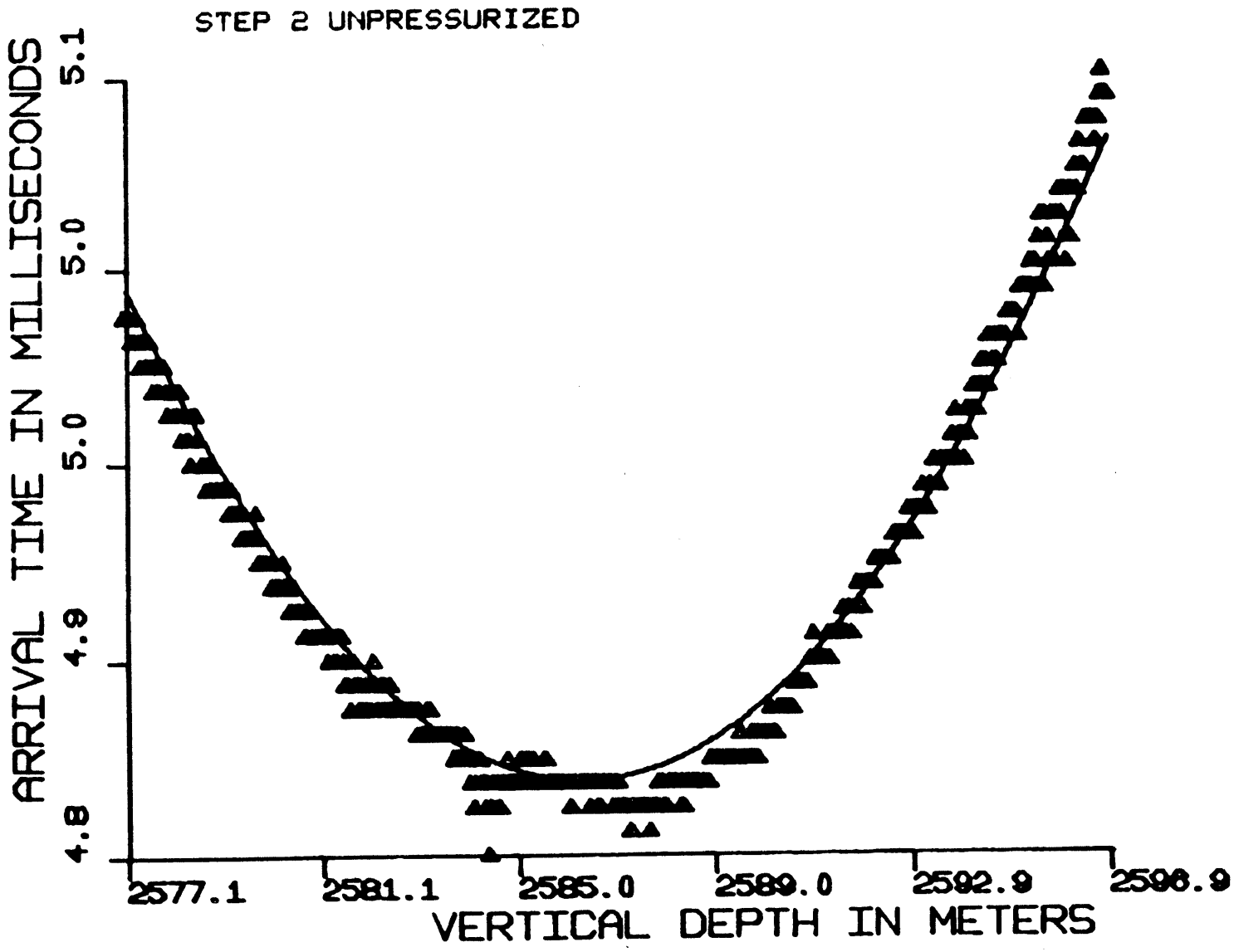
STEP 2 UNPRESSURIZED
ARRIVAL TIME IN MILLISECONDS
5.1
5.0
5.0
4.9
4.8
2577.1
2581.1
2585.0
2589.0
2592.9
2596.9
VERTICAL DEPTH IN METERS

Figure 13

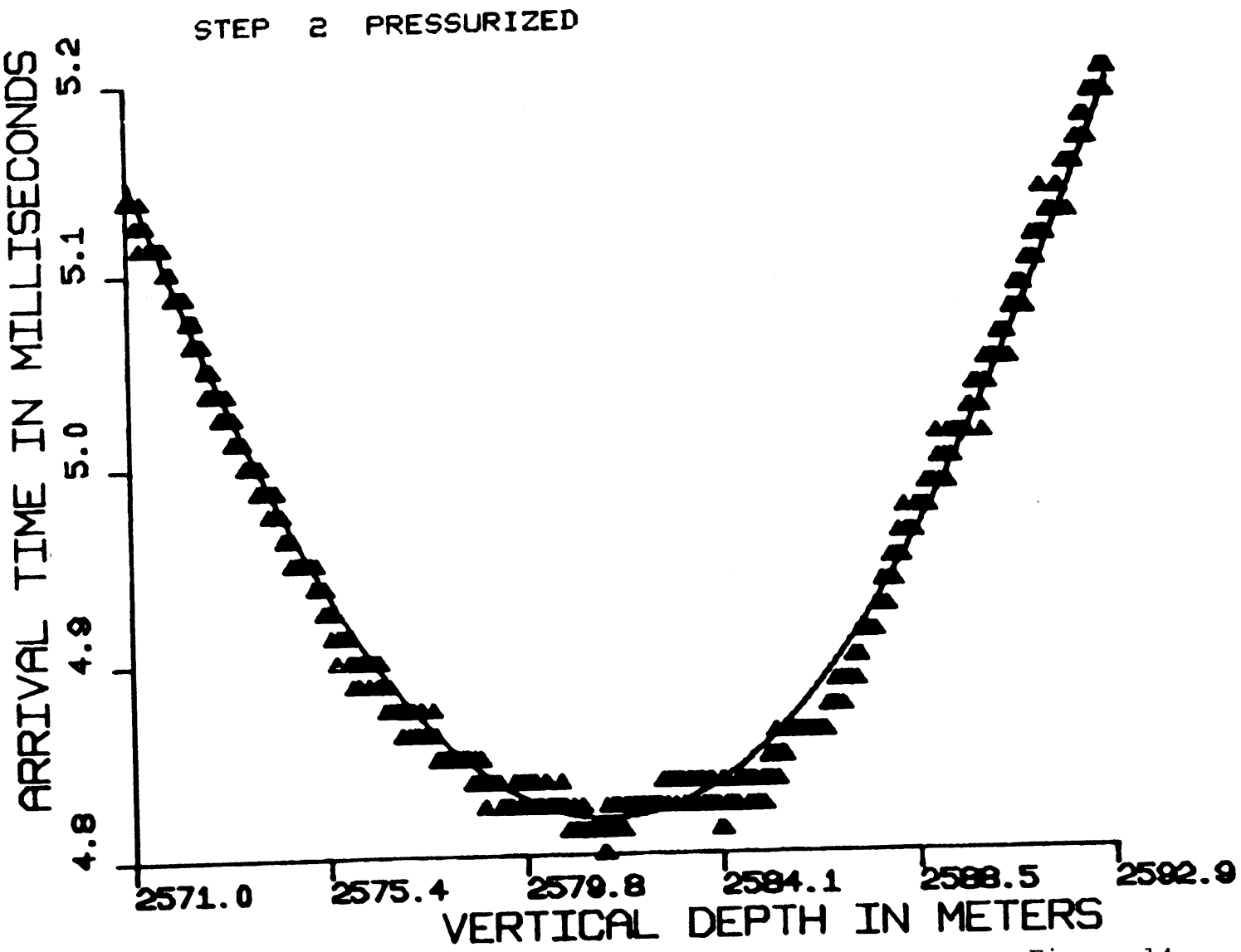
STEP 2 PRESSURIZED
ARRIVAL TIME IN MILLISECONDS
5.2
5.1
5.0
4.9
4.8
2571.0
2575.4
2579.8
2584.1
2588.5
2592.9
VERTICAL DEPTH IN METERS

Figure 14

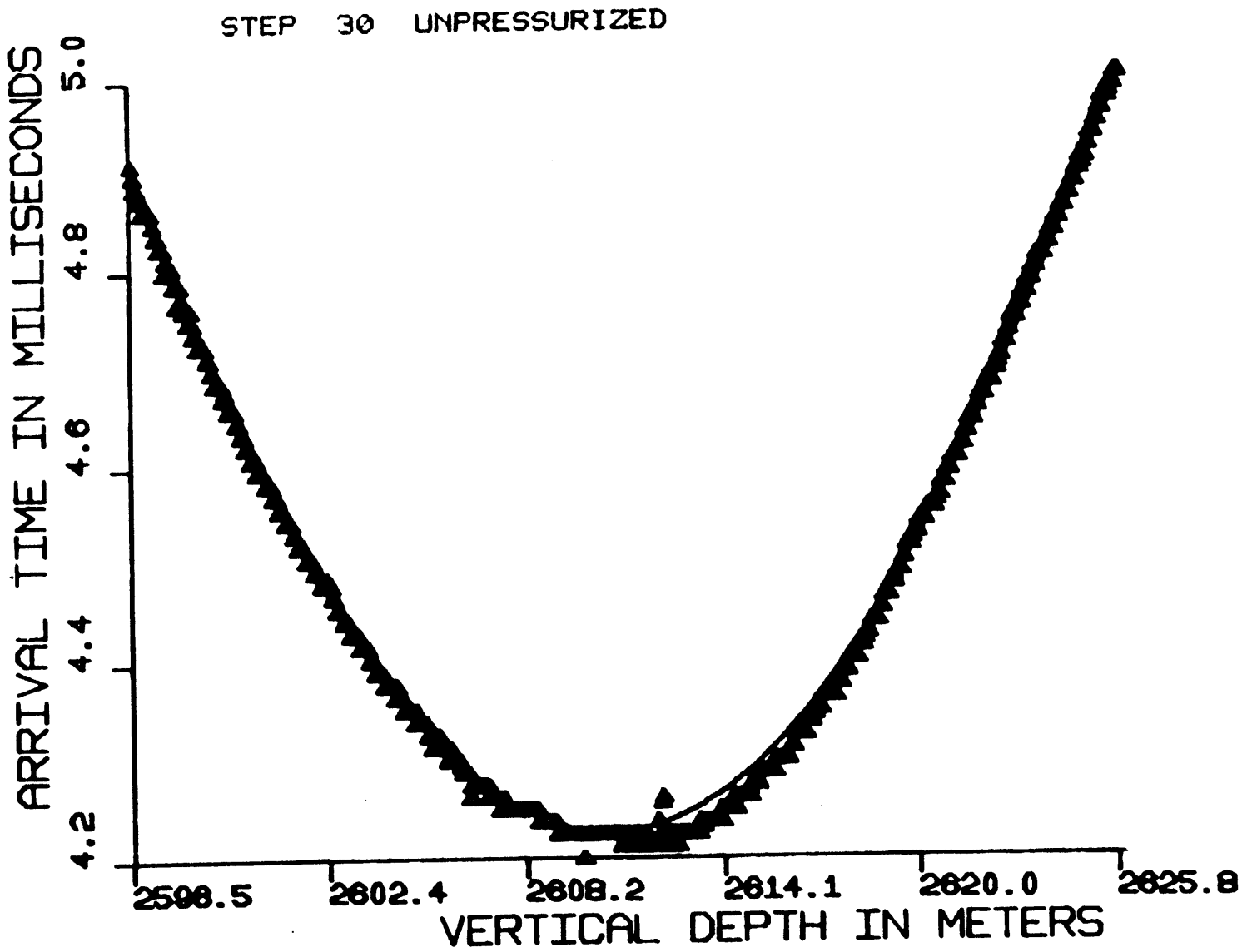
STEP 30 UNPRESSURIZED
ARRIVAL TIME IN MILLISECONDS
5.0
4.8
4.6
4.4
4.2
2596.5
2602.4
2608.2
2614.1
2620.0
2625.8
VERTICAL DEPTH IN METERS

Figure 15

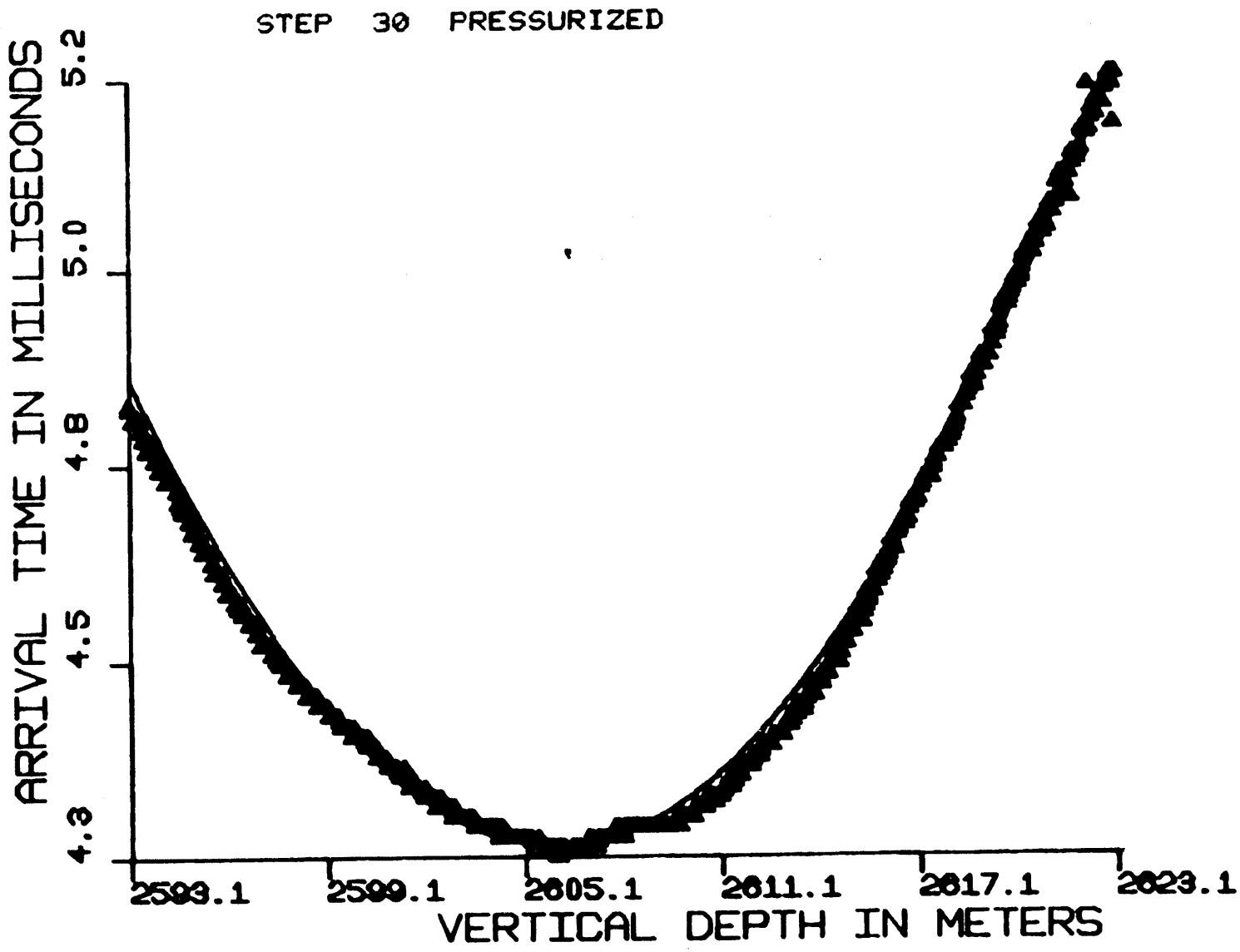
STEP 30 PRESSURIZED
ARRIVAL TIME IN MILLISECONDS
5.2
5.0
4.8
4.5
4.3
2593.1
2599.1
2605.1
2611.1
2617.1
2623.1
VERTICAL DEPTH IN METERS

Figure 16

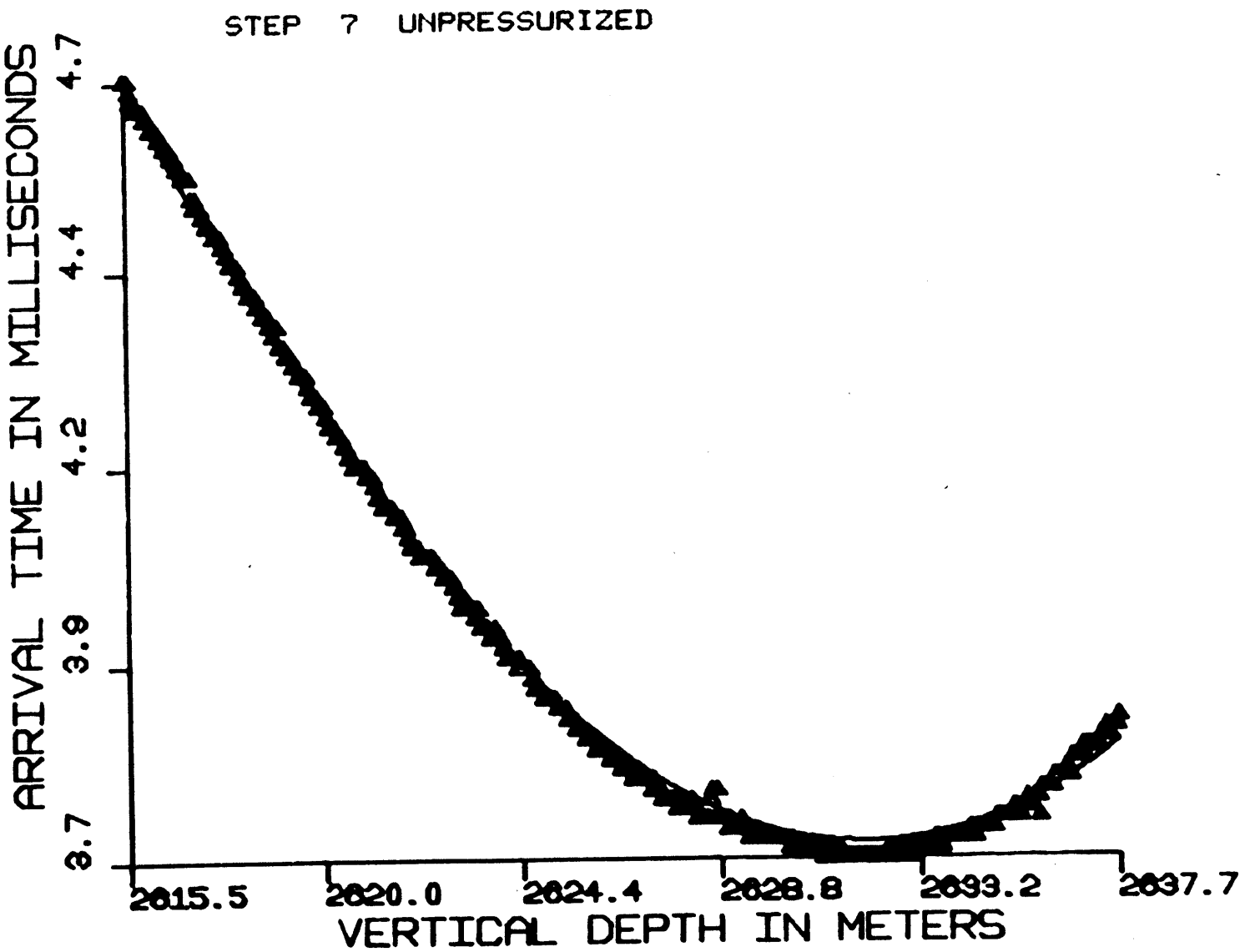
STEP 7 UNPRESSURIZED
ARRIVAL TIME IN MILLISECONDS
4.7
4.4
4.2
3.9
3.7
2015.5
2020.0
2024.4
2028.8
2033.2
2037.7
VERTICAL DEPTH IN METERS

Figure 17

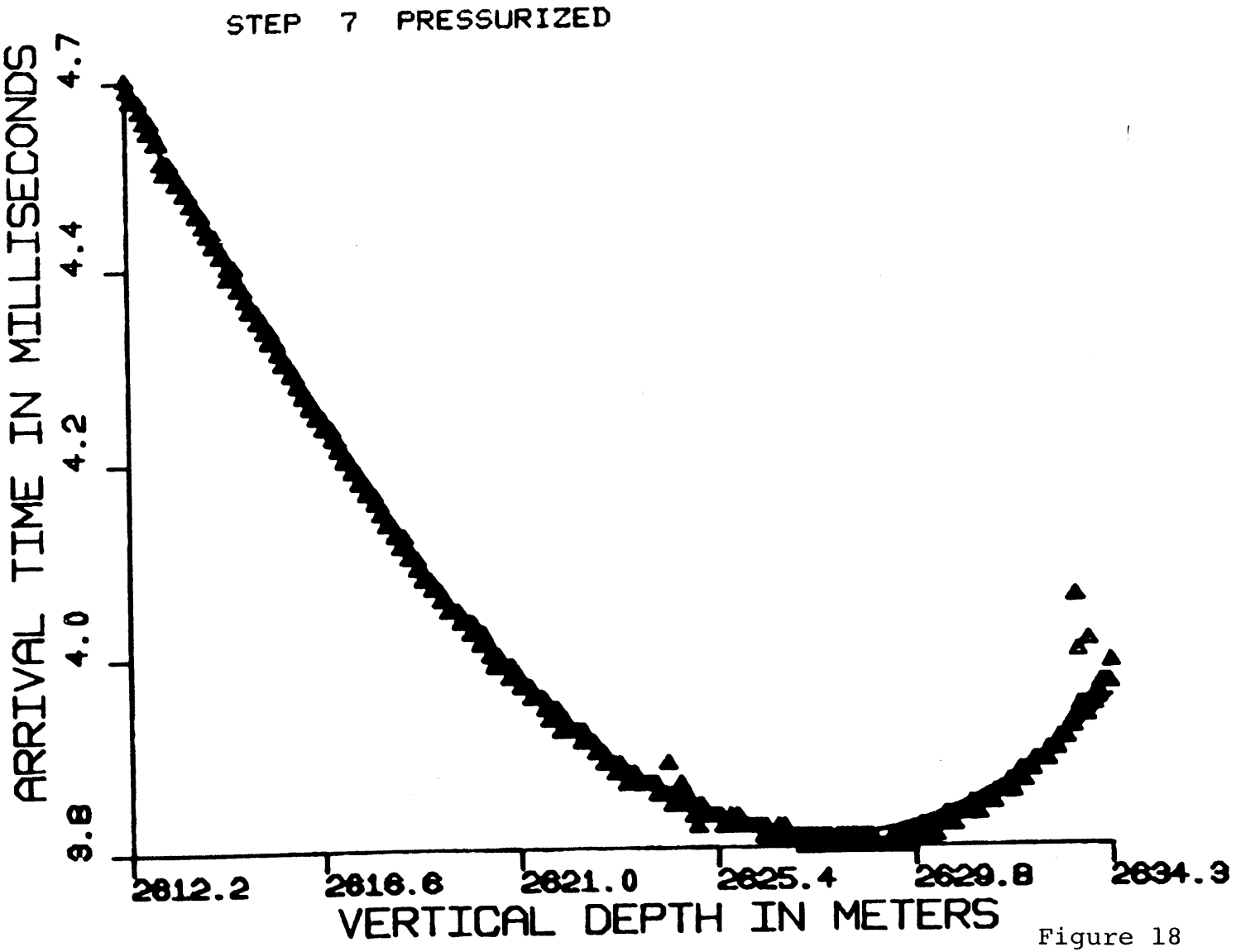
STEP 7 PRESSURIZED
ARRIVAL TIME IN MILLISECONDS
4.7
4.4
4.2
4.0
3.8
2612.2
2616.6
2621.0
2625.4
2629.8
2634.3
VERTICAL DEPTH IN METERS

Figure 18

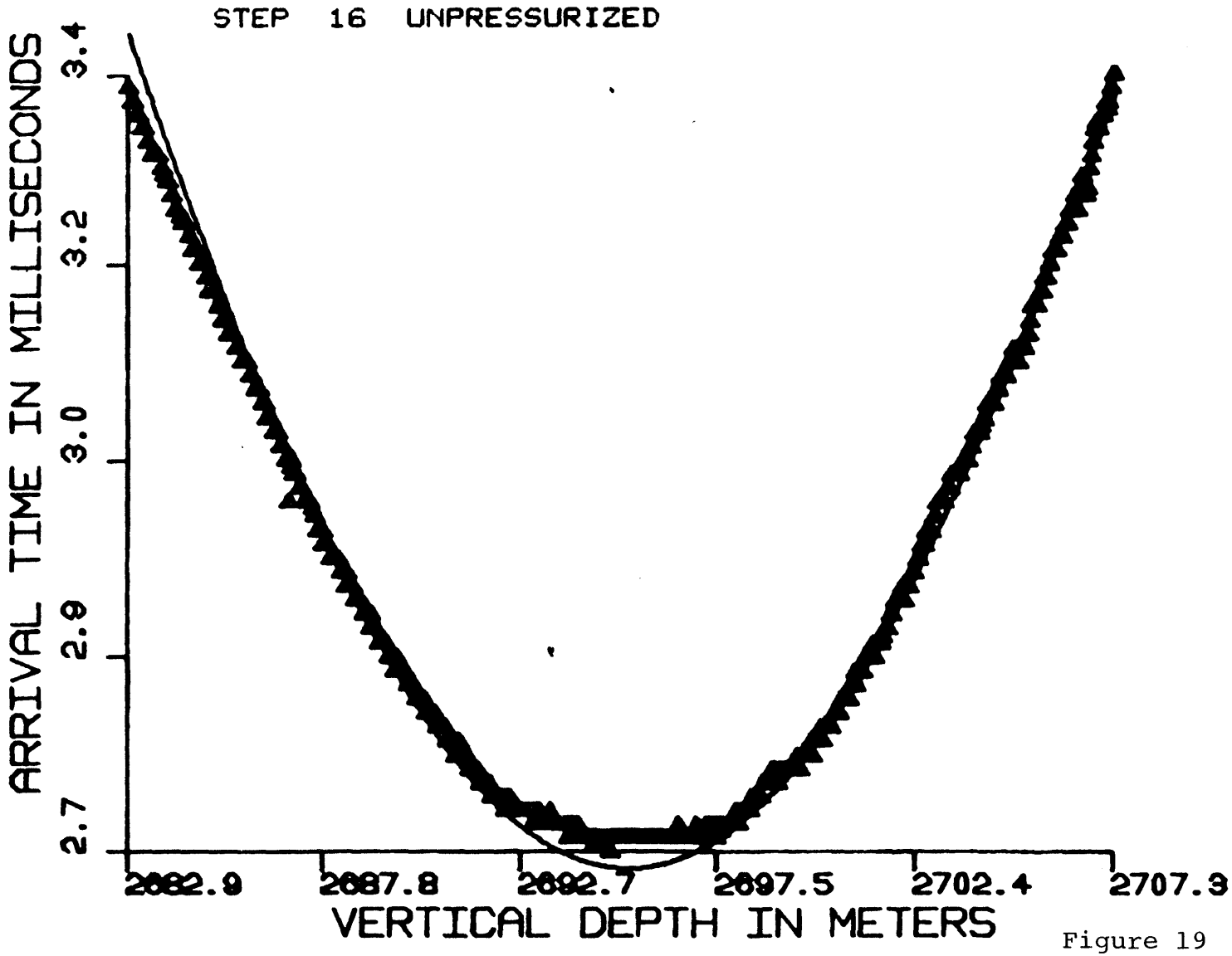
STEP 16 UNPRESSURIZED
ARRIVAL TIME IN MILLISECONDS
3.4
3.2
3.0
2.9
2.7
2682.9
2687.8
2692.7
2697.5
2702.4
2707.3
VERTICAL DEPTH IN METERS

Figure 19

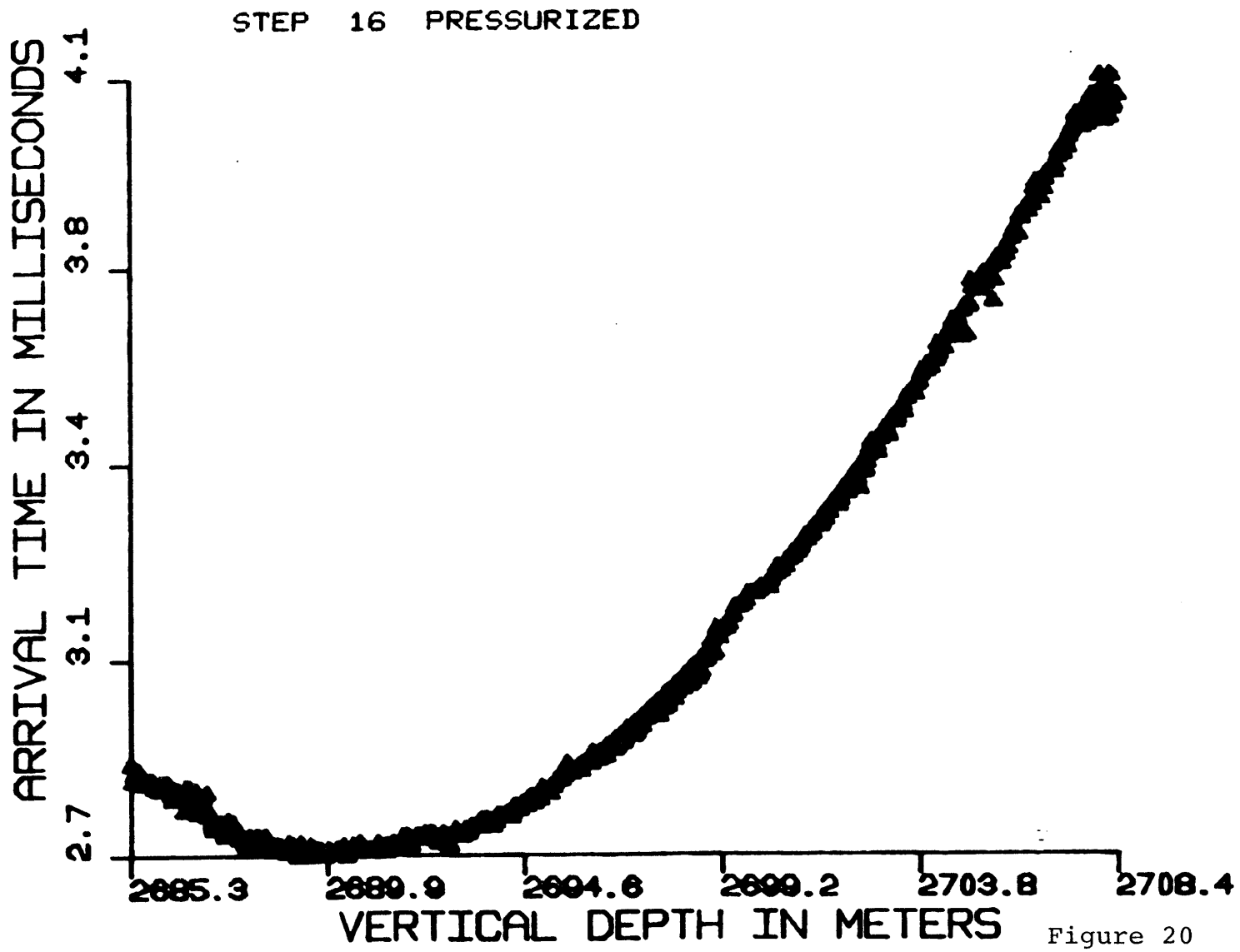
STEP 16 PRESSURIZED
ARRIVAL TIME IN MILLISECONDS
2.7
3.1
3.4
3.8
4.1
2685.3
2689.9
2694.6
2699.2
2703.8
2708.4
VERTICAL DEPTH IN METERS

Figure 20

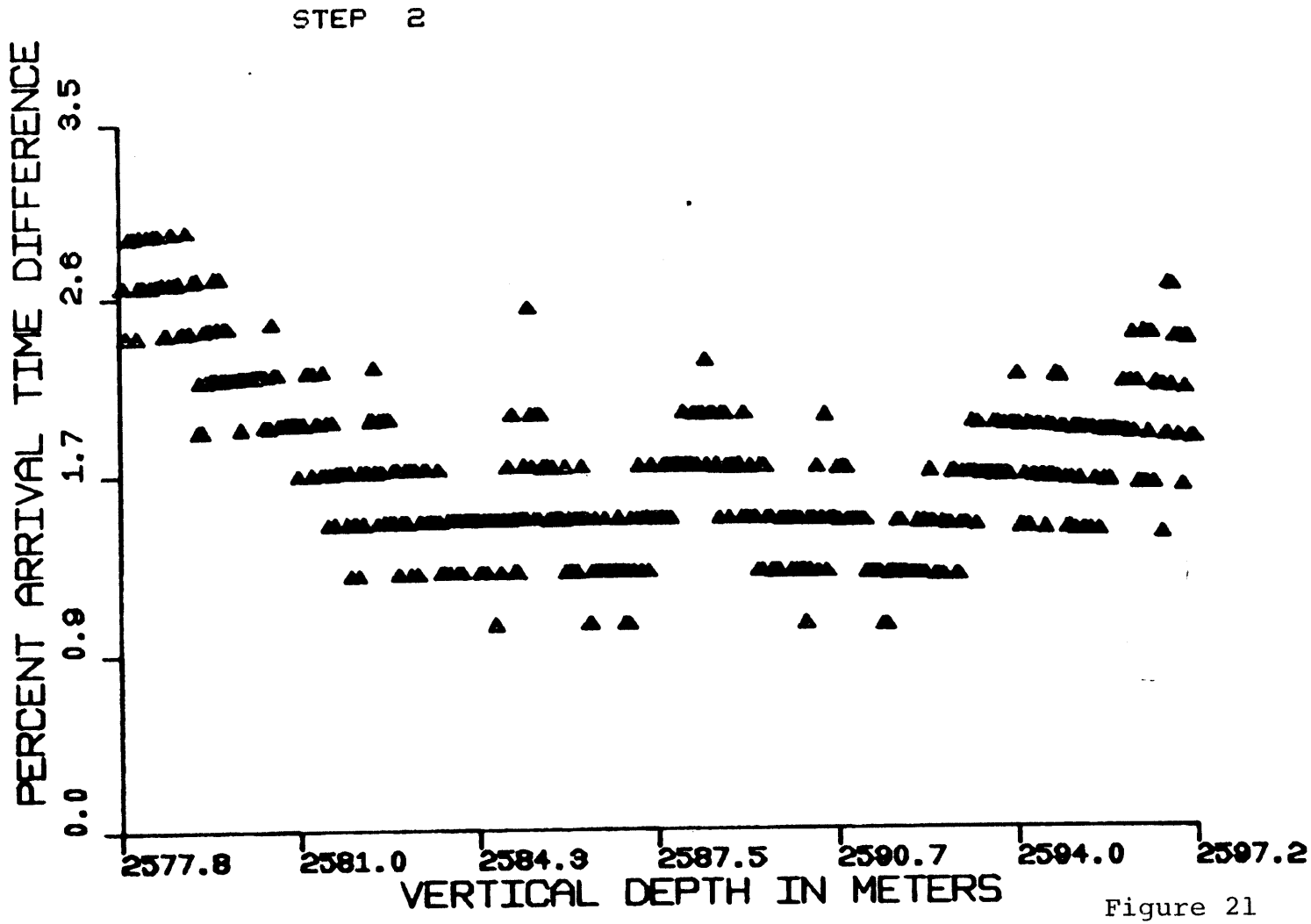
STEP 2
PERCENT ARRIVAL TIME DIFFERENCE
0.0
0.9
1.7
2.6
3.5
2577.8
2581.0
2584.3
2587.5
2590.7
2594.0
2597.2
VERTICAL DEPTH IN METERS

Figure 21

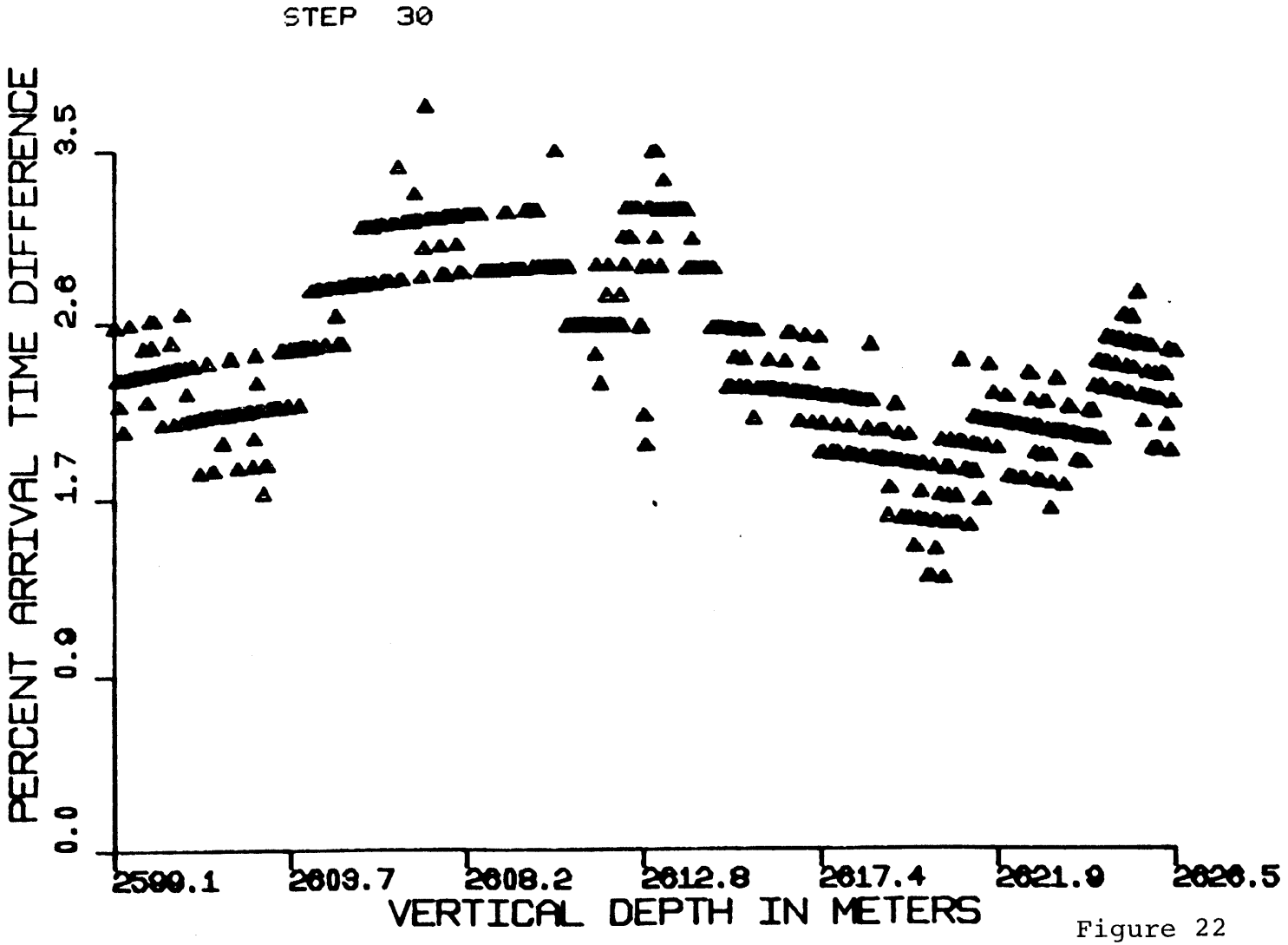
STEP 30
PERCENT ARRIVAL TIME DIFFERENCE
0.0
0.9
1.7
2.6
3.5
2599.1
2603.7
2608.2
2612.8
2617.4
2621.9
2626.5
VERTICAL DEPTH IN METERS

Figure 22

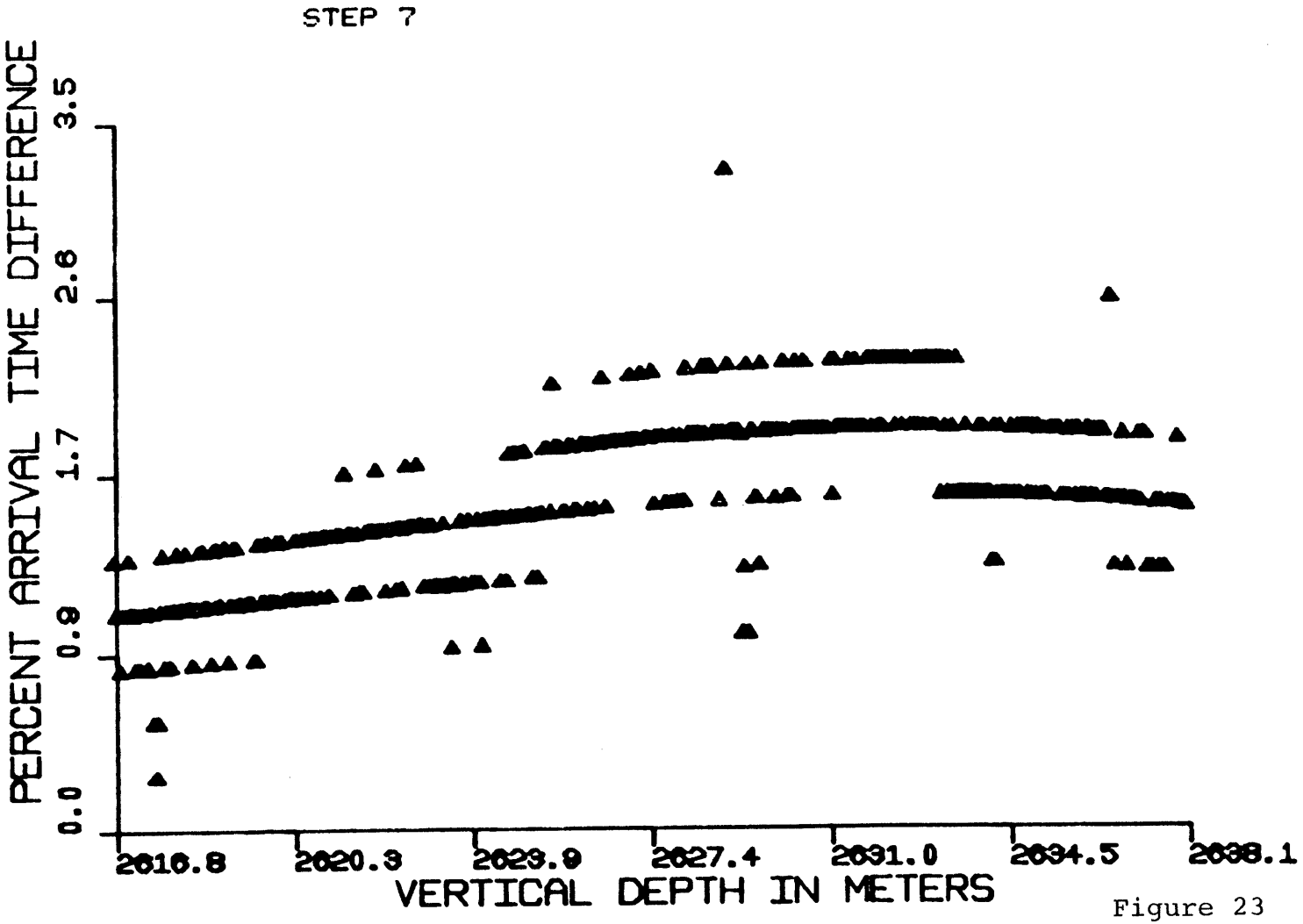
STEP 7
PERCENT ARRIVAL TIME DIFFERENCE
0.0
0.9
1.7
2.6
3.5
2016.8
2020.3
2023.9
2027.4
2031.0
2034.5
2038.1
VERTICAL DEPTH IN METERS

Figure 23

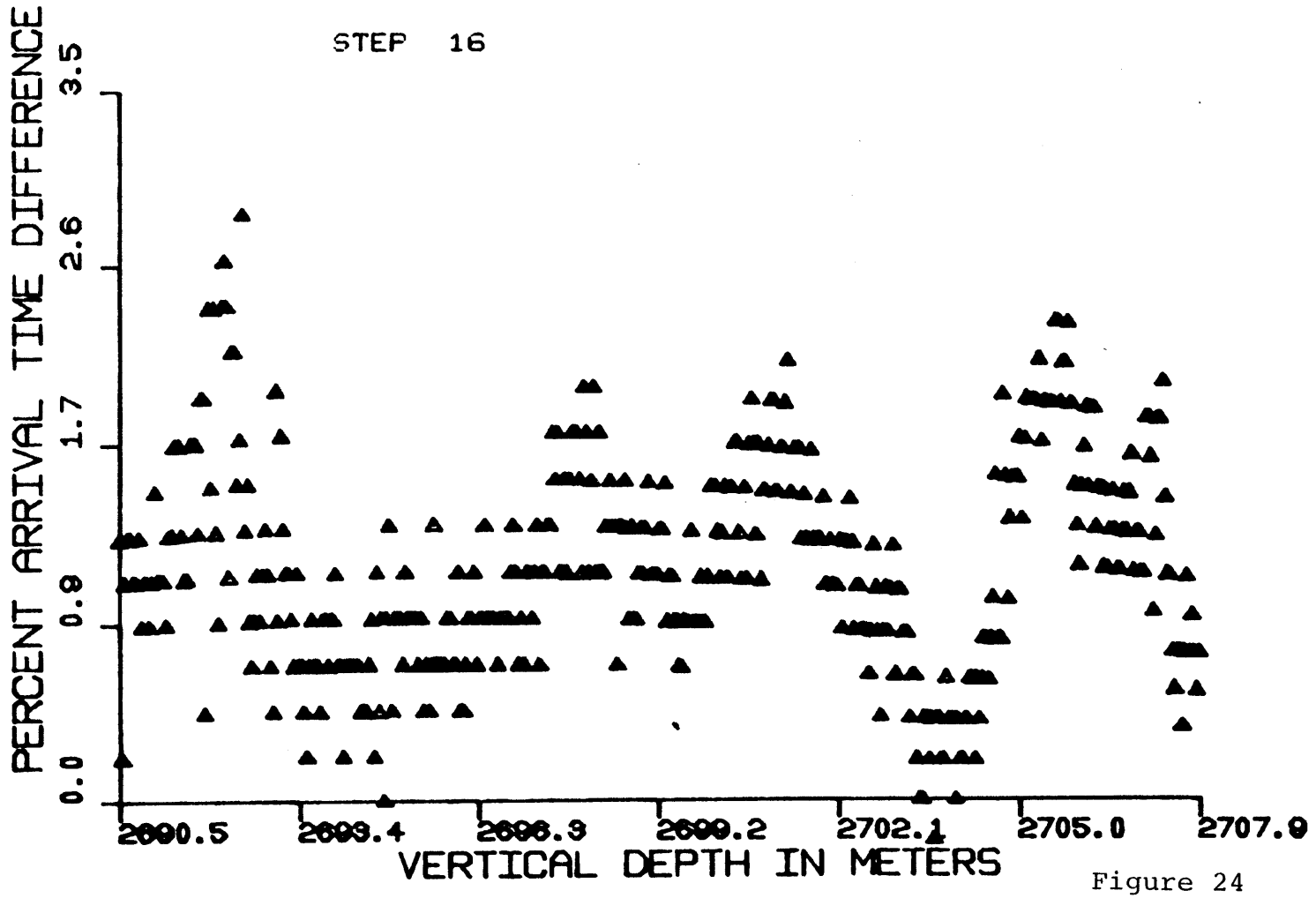
STEP 16
PERCENT ARRIVAL TIME DIFFERENCE
0.0
0.9
1.7
2.6
3.5
2690.5
2693.4
2696.3
2699.2
2702.1
2705.0
2707.9
VERTICAL DEPTH IN METERS

Figure 24

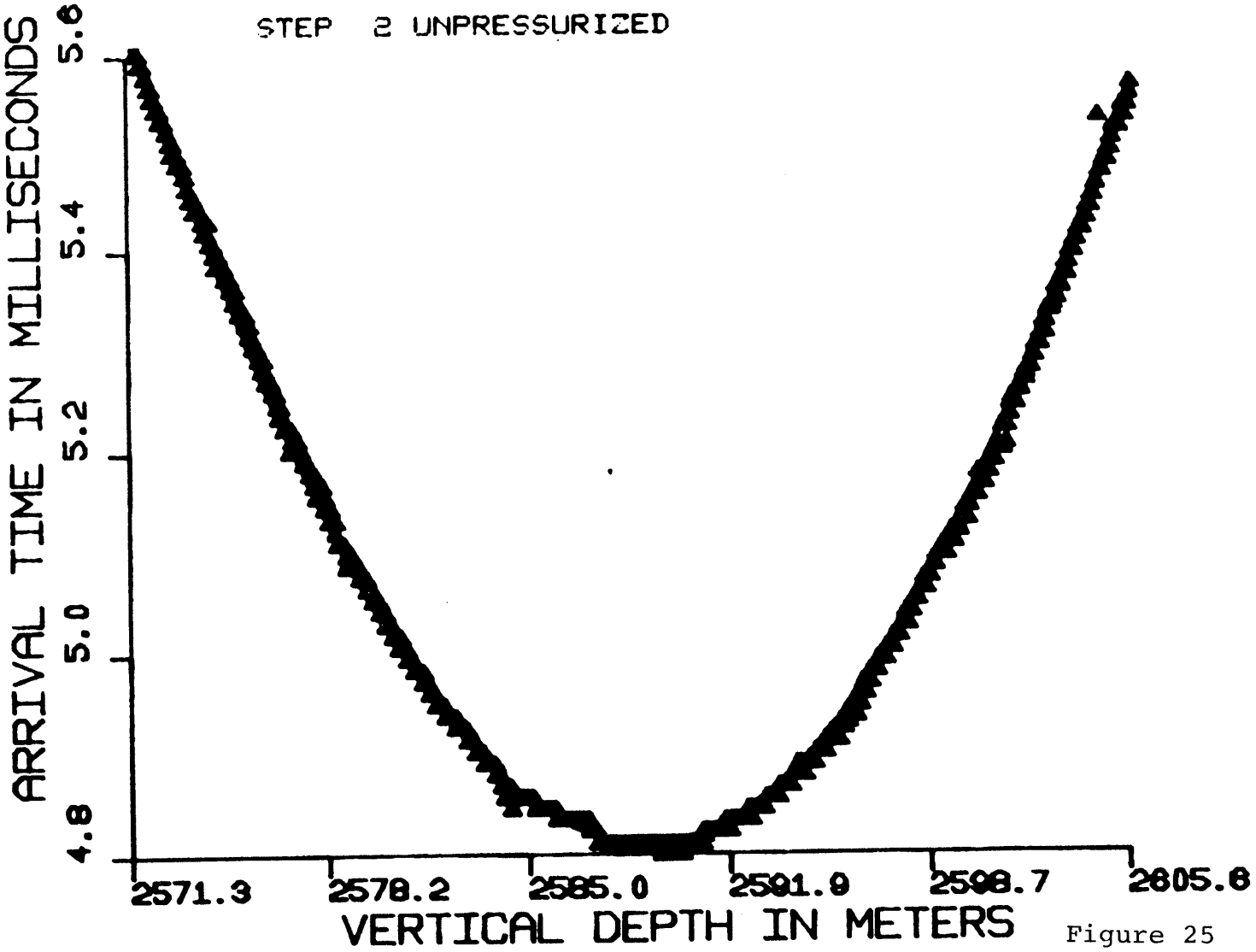
STEP 2 UNPRESSURIZED
ARRIVAL TIME IN MILLISECONDS
5.6
5.4
5.2
5.0
4.8
2571.3
2578.2
2585.0
2591.9
2598.7
2605.6
VERTICAL DEPTH IN METERS

Figure 25

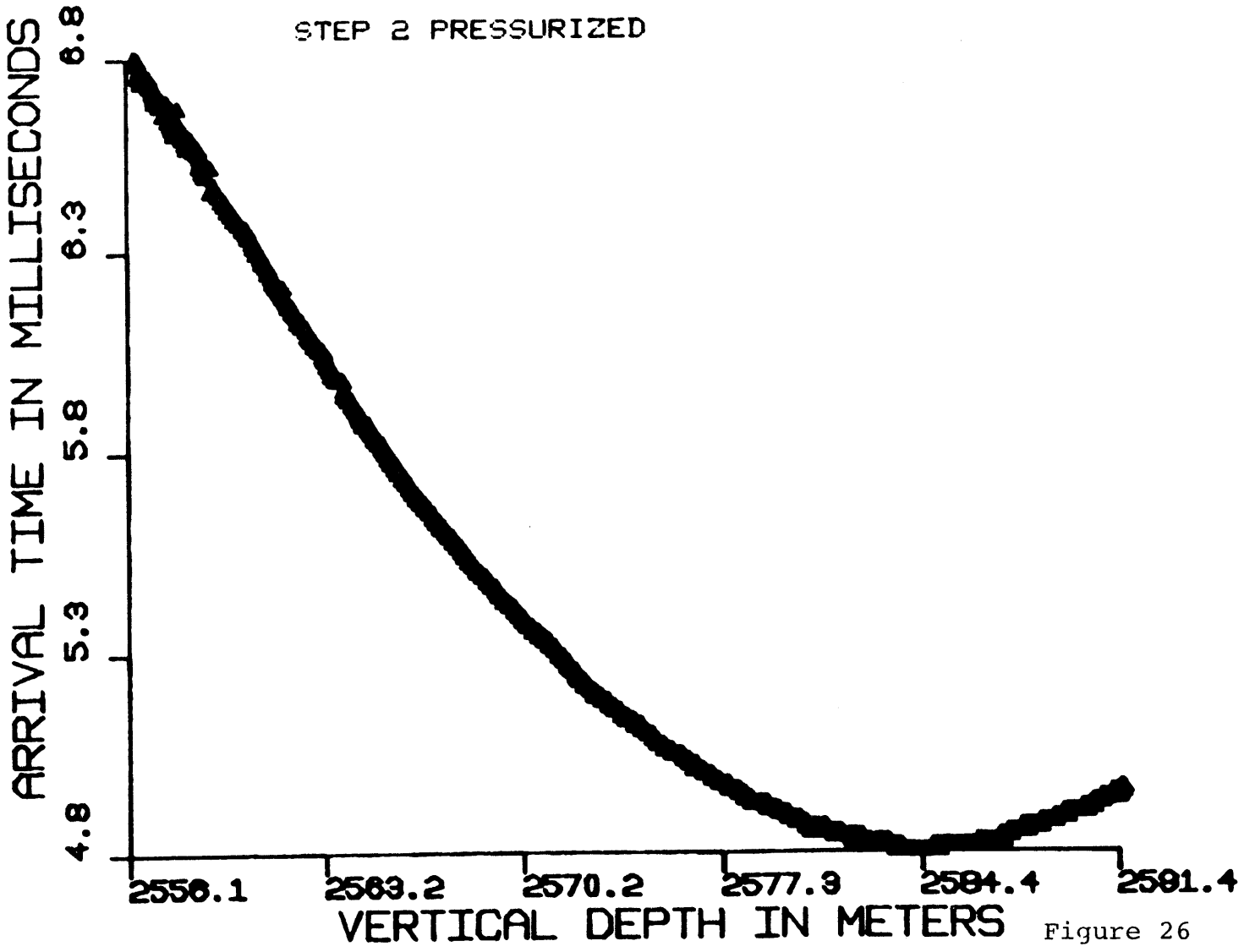
STEP 2 PRESSURIZED
ARRIVAL TIME IN MILLISECONDS
6.8
6.3
5.8
5.3
4.8
2556.1
2563.2
2570.2
2577.3
2584.4
2591.4
VERTICAL DEPTH IN METERS

Figure 26

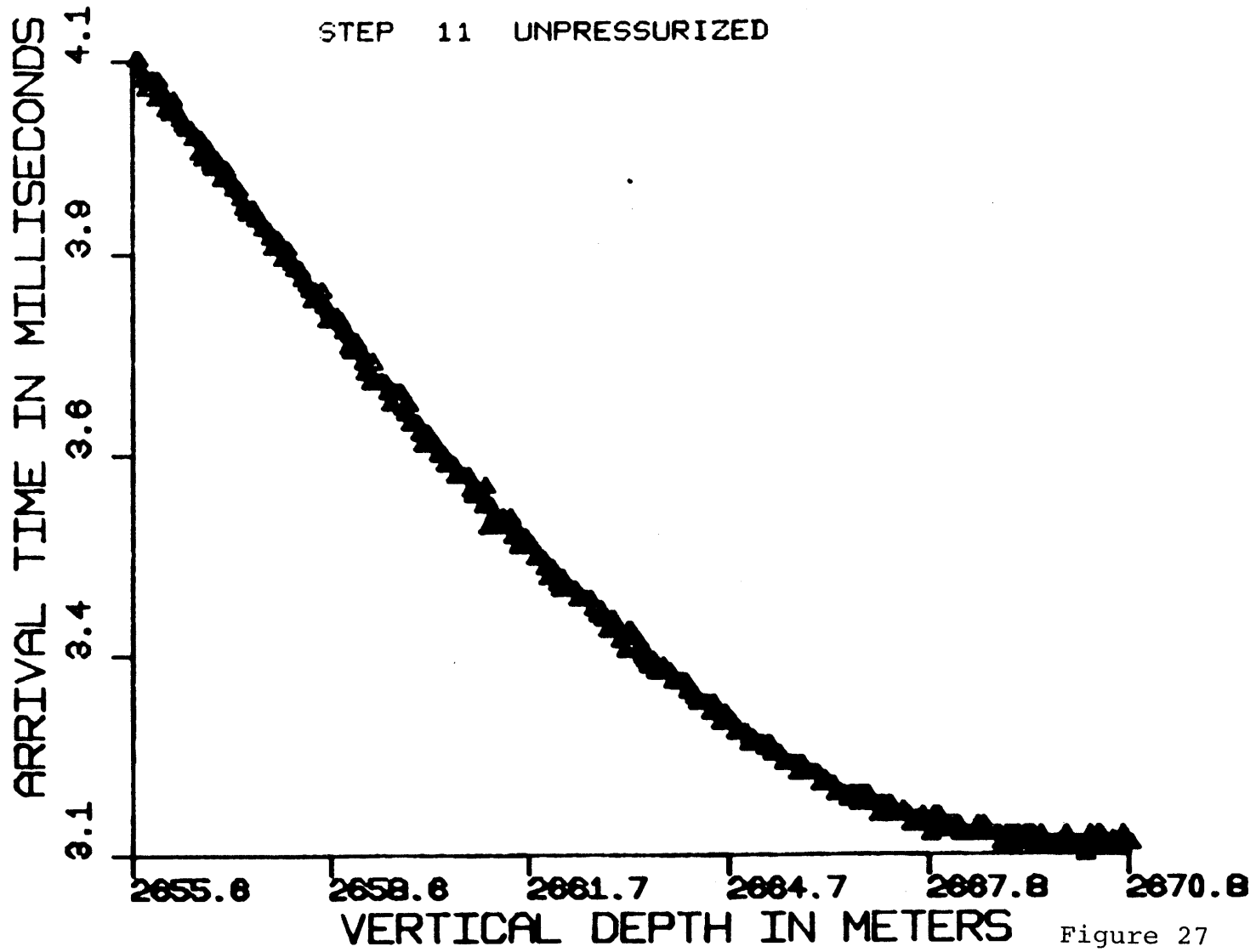
STEP 11 UNPRESSURIZED
ARRIVAL TIME IN MILLISECONDS
4.1
3.9
3.6
3.4
3.1
2655.6
2658.6
2661.7
2664.7
2667.8
2670.8
VERTICAL DEPTH IN METERS

Figure 27

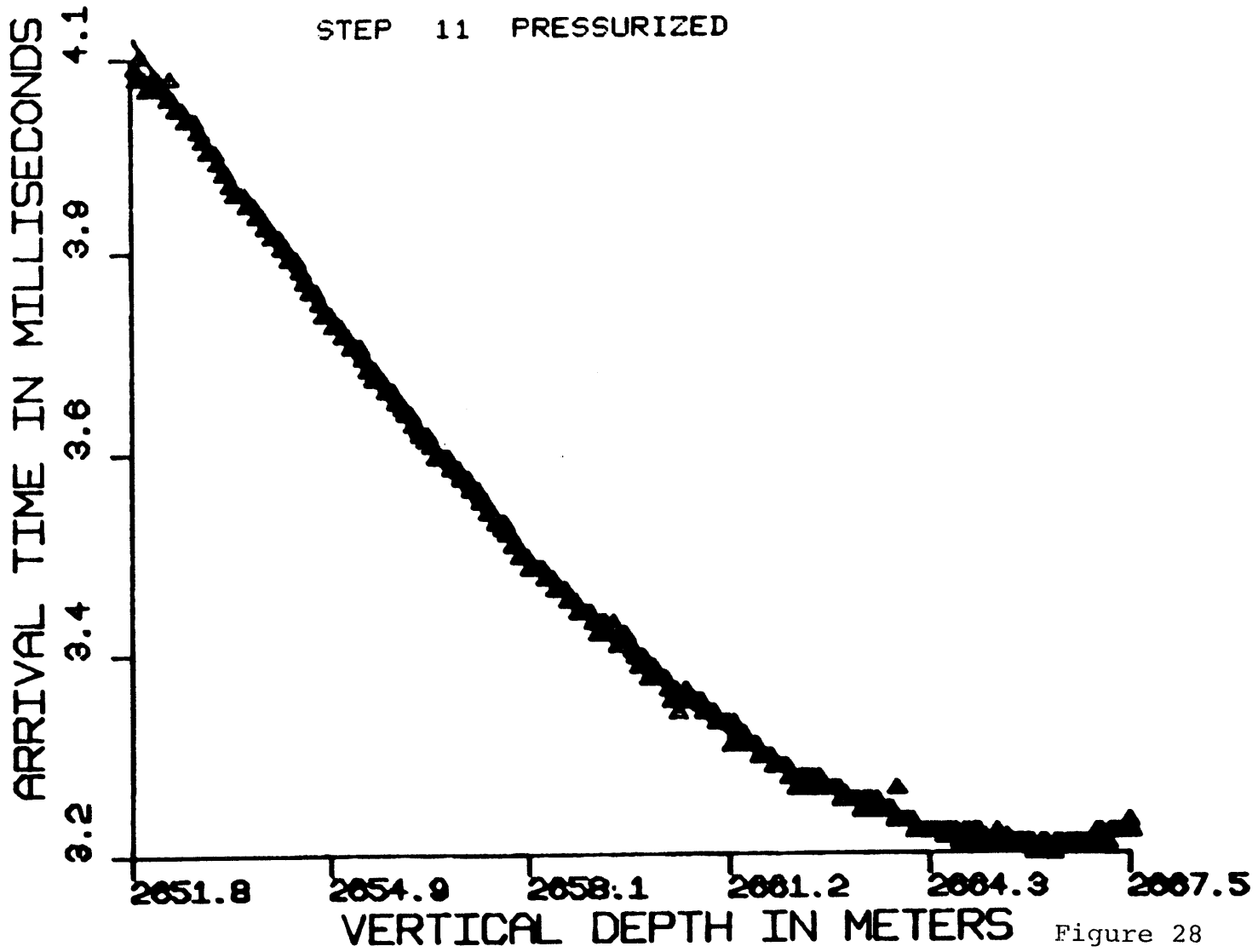
STEP 11 PRESSURIZED
ARRIVAL TIME IN MILLISECONDS
4.1
3.8
3.6
3.4
3.2
2651.8
2654.9
2658.1
2661.2
2664.3
2667.5
VERTICAL DEPTH IN METERS

Figure 28

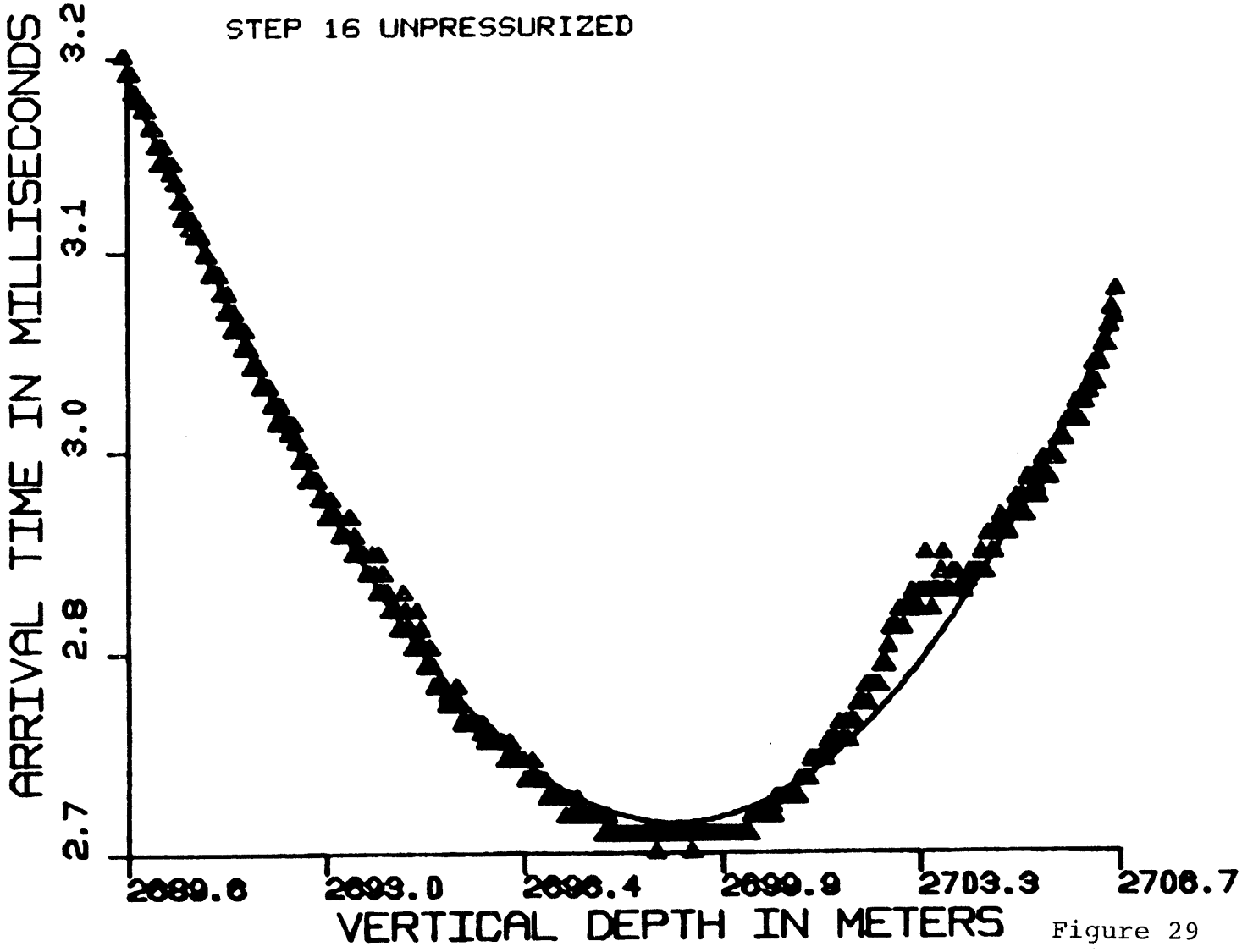
STEP 16 UNPRESSURIZED
ARRIVAL TIME IN MILLISECONDS
3.2
3.1
3.0
2.8
2.7
2689.6
2693.0
2696.4
2699.9
2703.3
2706.7
VERTICAL DEPTH IN METERS

Figure 29

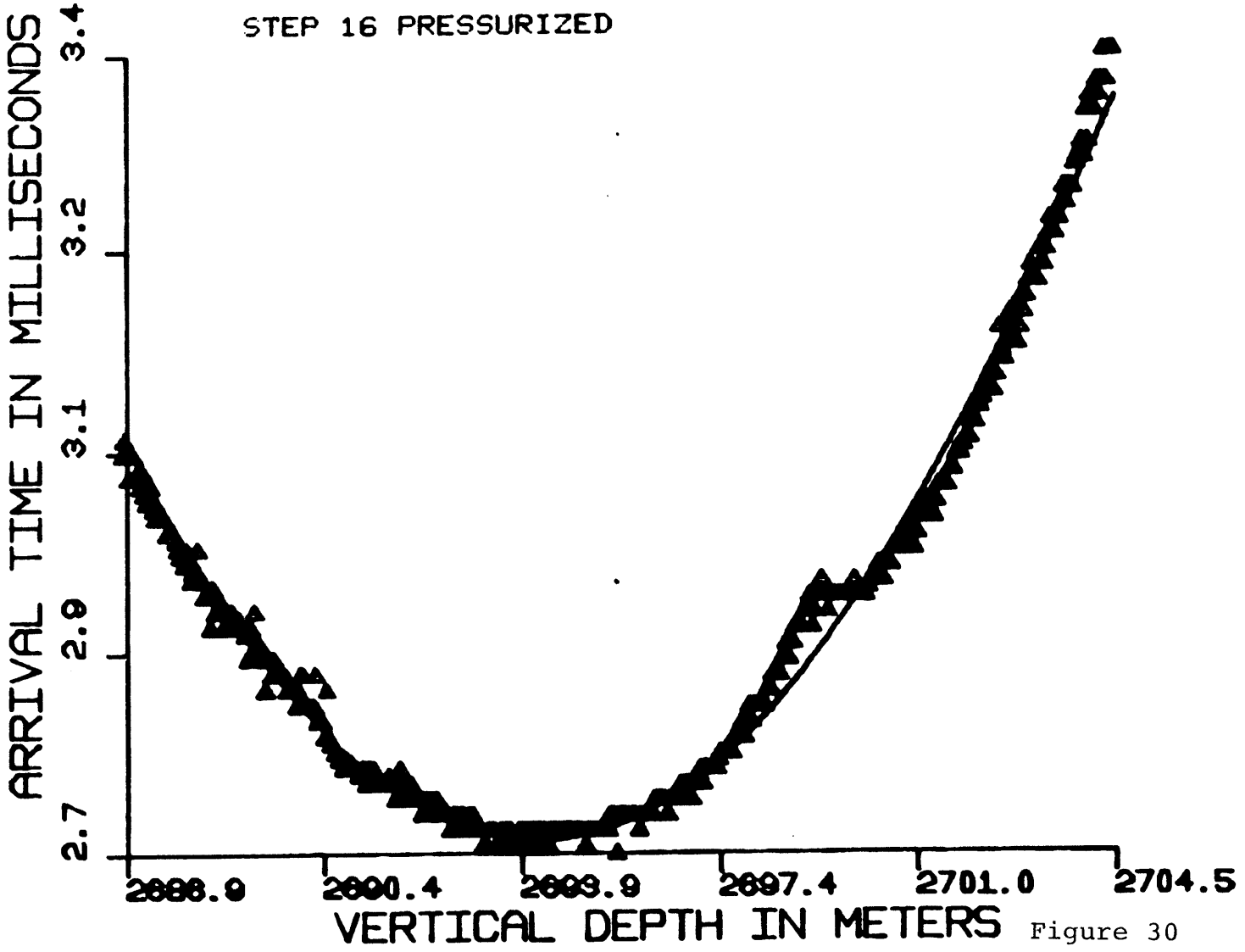
STEP 16 PRESSURIZED
ARRIVAL TIME IN MILLISECONDS
3.4
3.2
3.1
2.9
2.7
2694.9
2700.4
2703.9
2697.4
2701.0
2704.5
VERTICAL DEPTH IN METERS

Figure 30

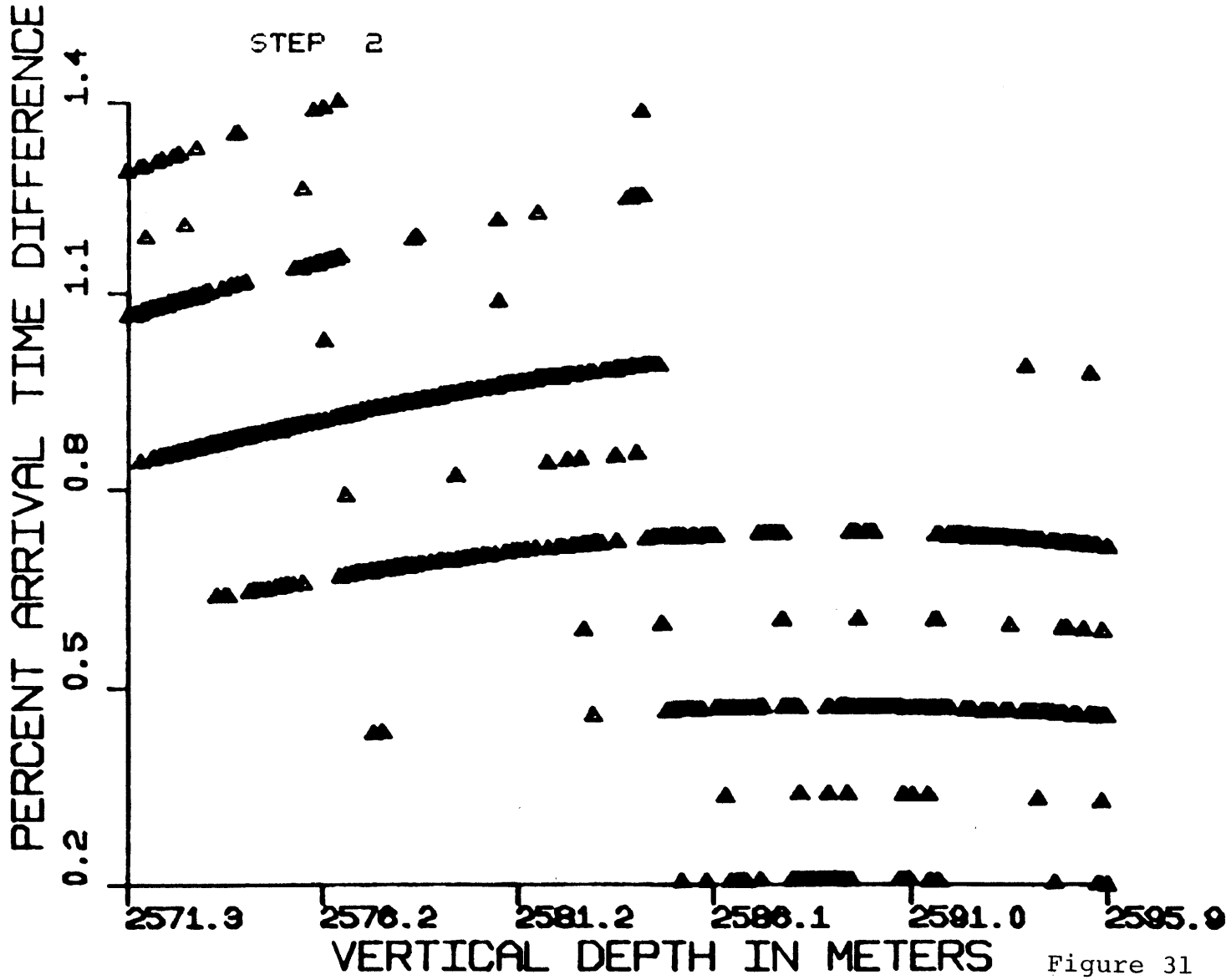
STEP 2
PERCENT ARRIVAL TIME DIFFERENCE
0.2
0.5
0.8
1.1
1.4
2571.3
2576.2
2581.2
2586.1
2591.0
2595.9
VERTICAL DEPTH IN METERS

Figure 31

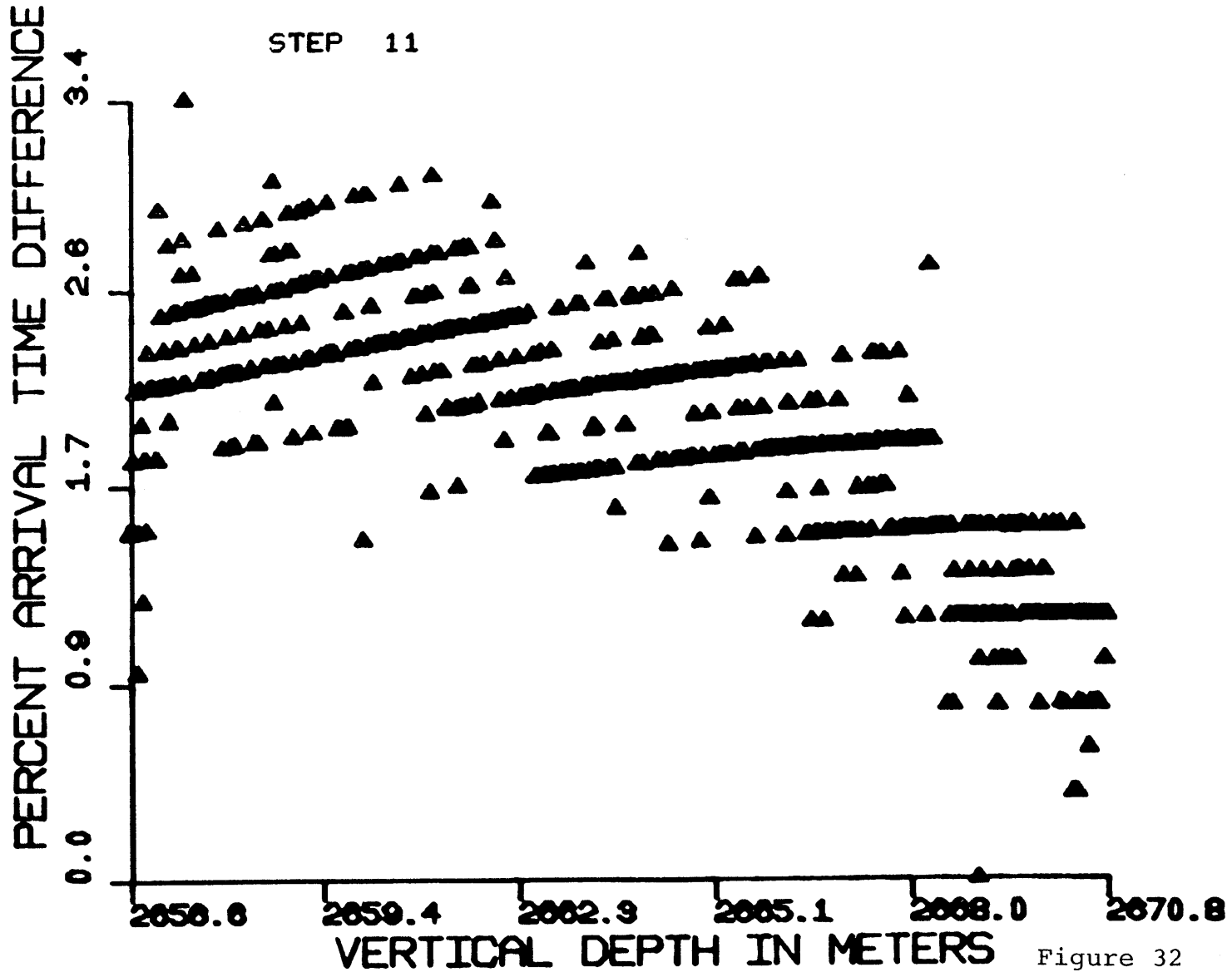
STEP 11
PERCENT ARRIVAL TIME DIFFERENCE
0.0
0.9
1.7
2.6
3.4
2656.8
2659.4
2662.9
2665.1
2668.0
2670.8
VERTICAL DEPTH IN METERS

Figure 32

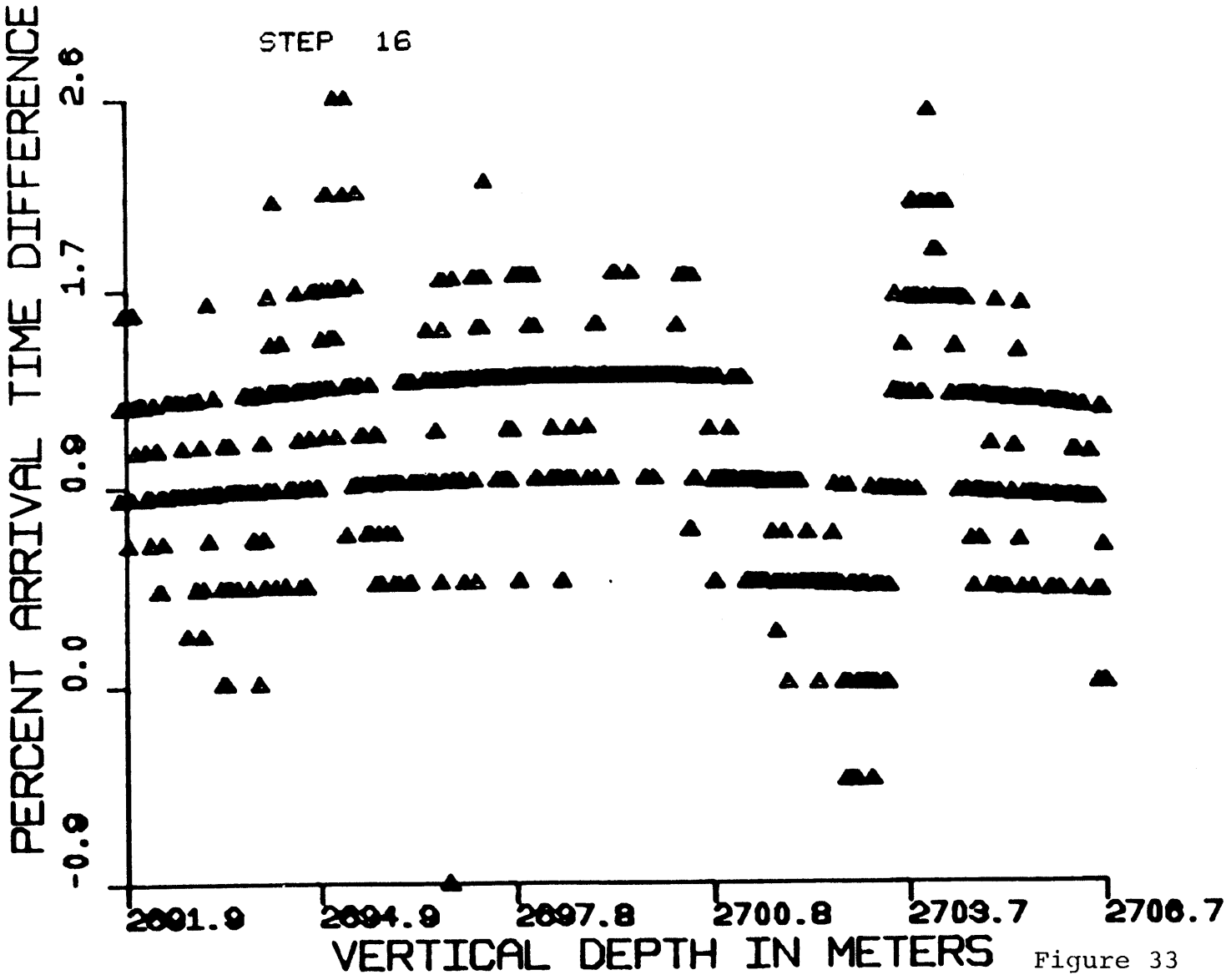
STEP 16
PERCENT ARRIVAL TIME DIFFERENCE
2.6
1.7
0.9
0.0
-0.9
2691.9
2694.9
2697.8
2700.8
2703.7
2706.7
VERTICAL DEPTH IN METERS

Figure 33

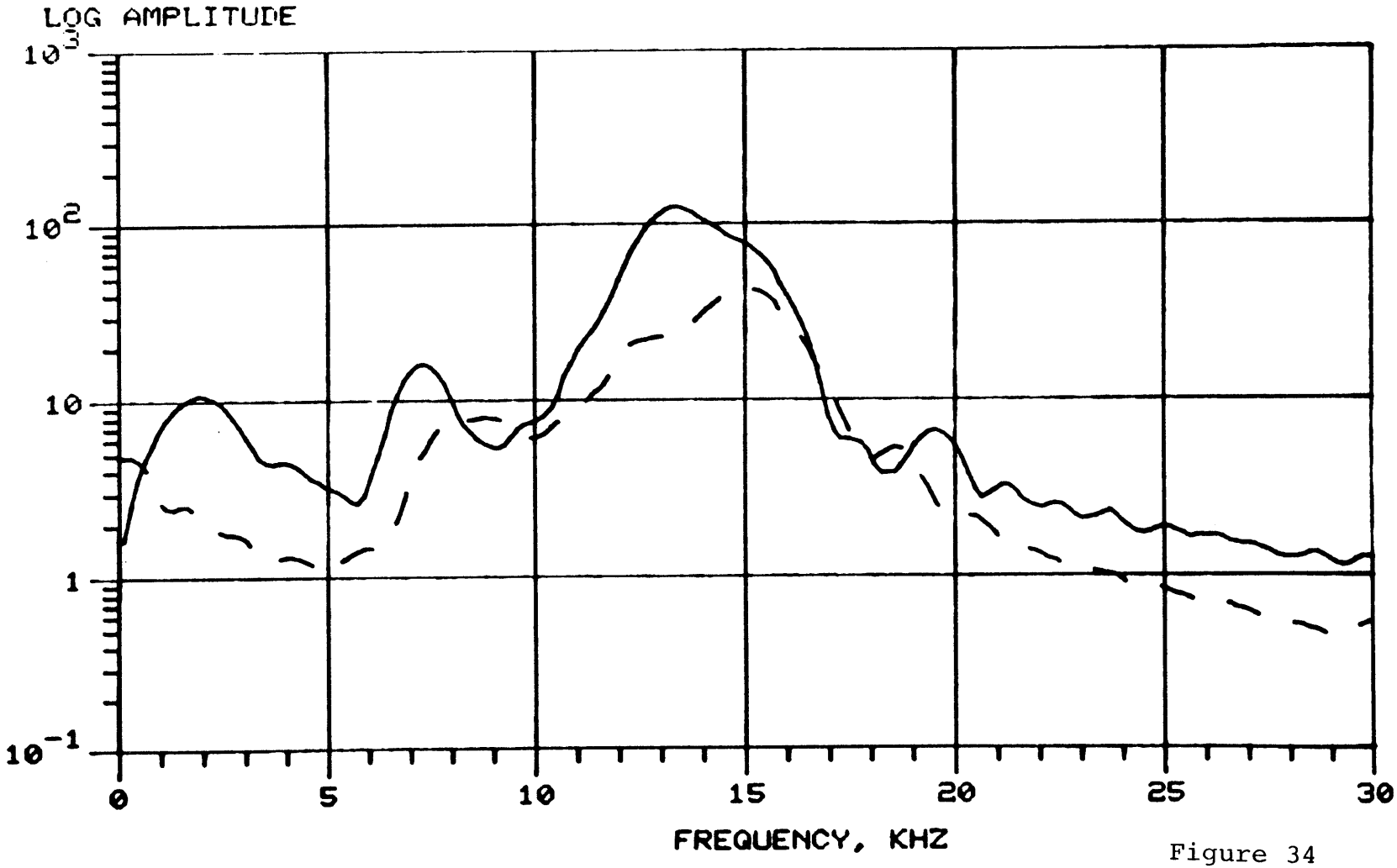

Figure 34

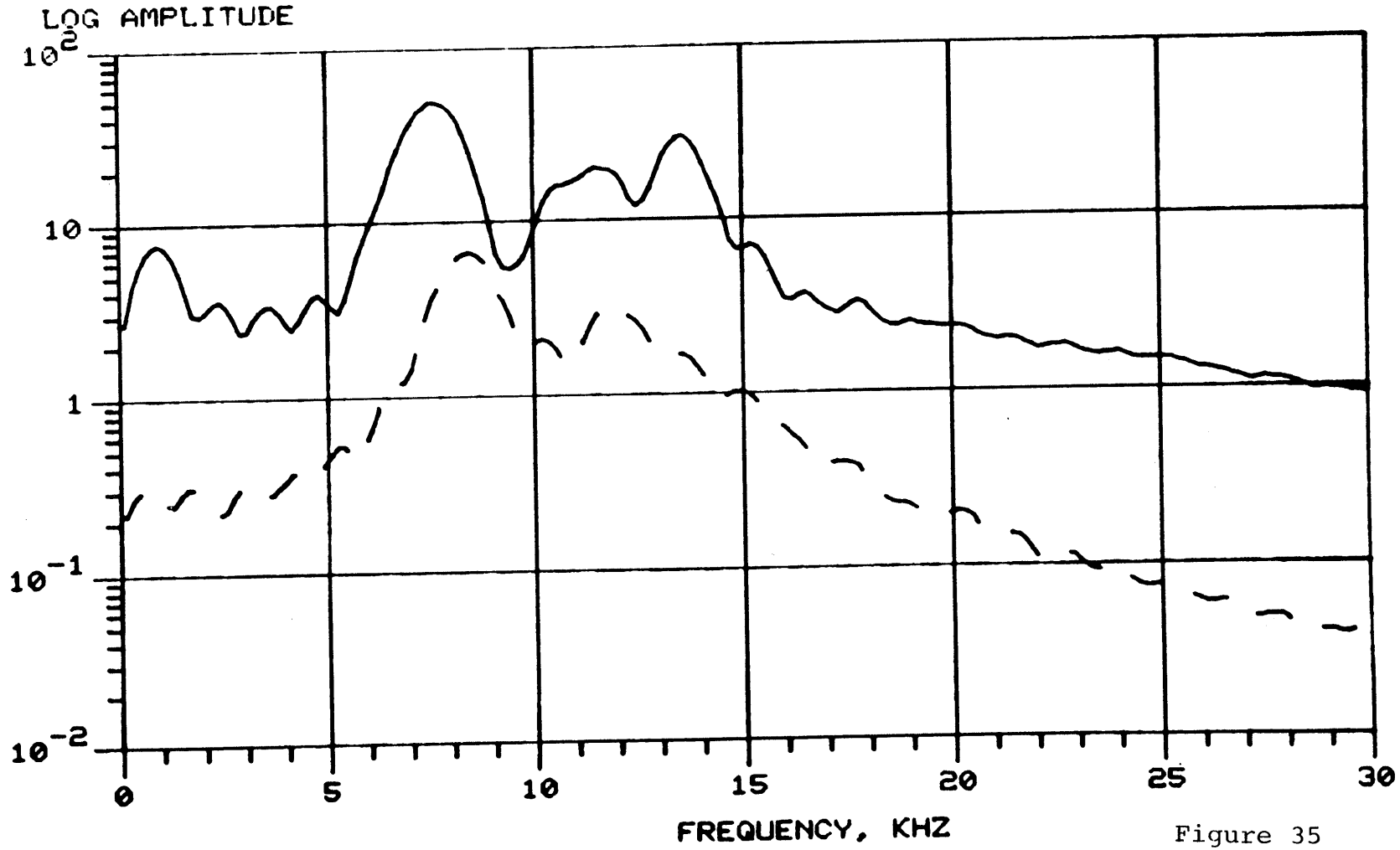

Figure 35

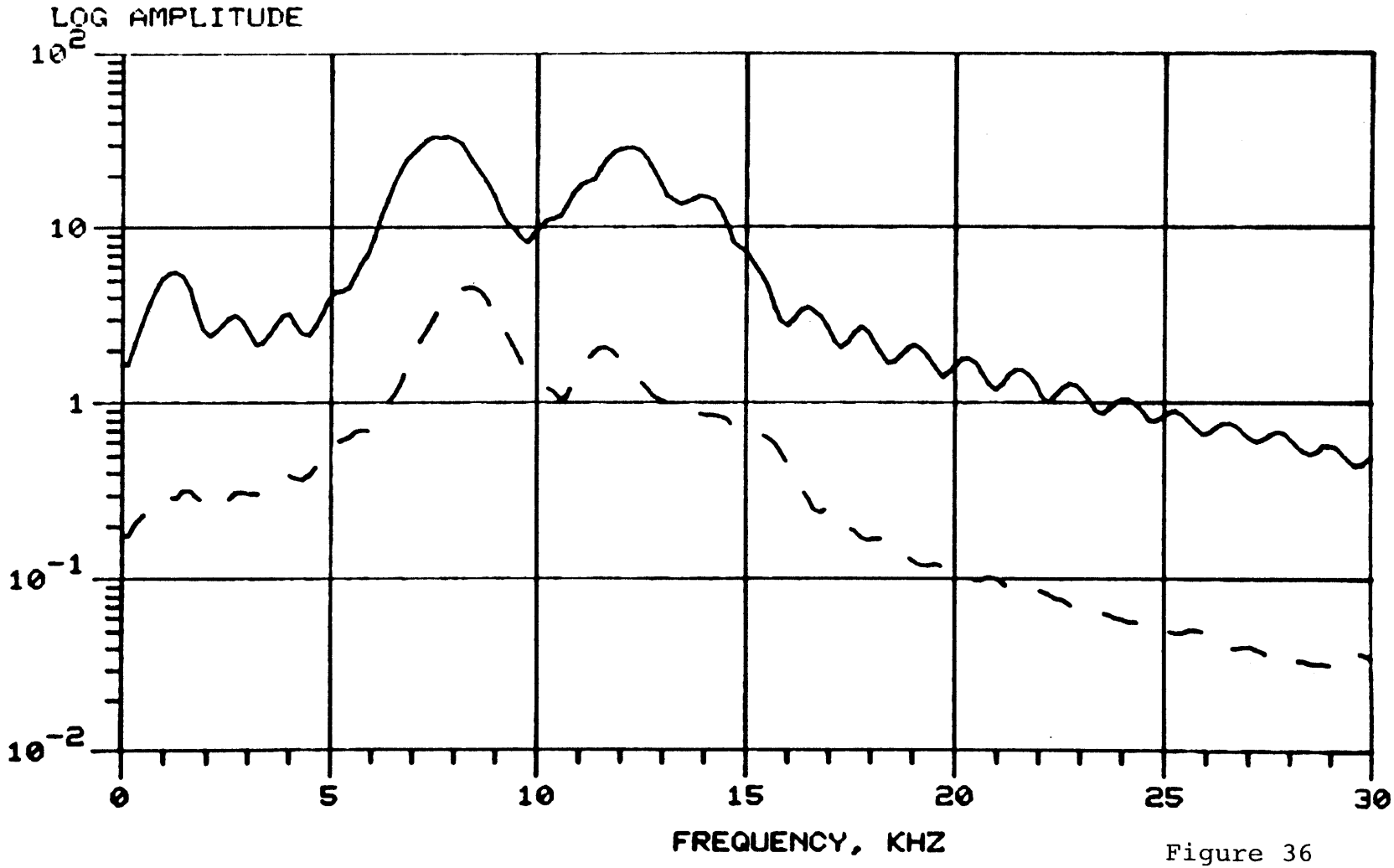

Figure 36

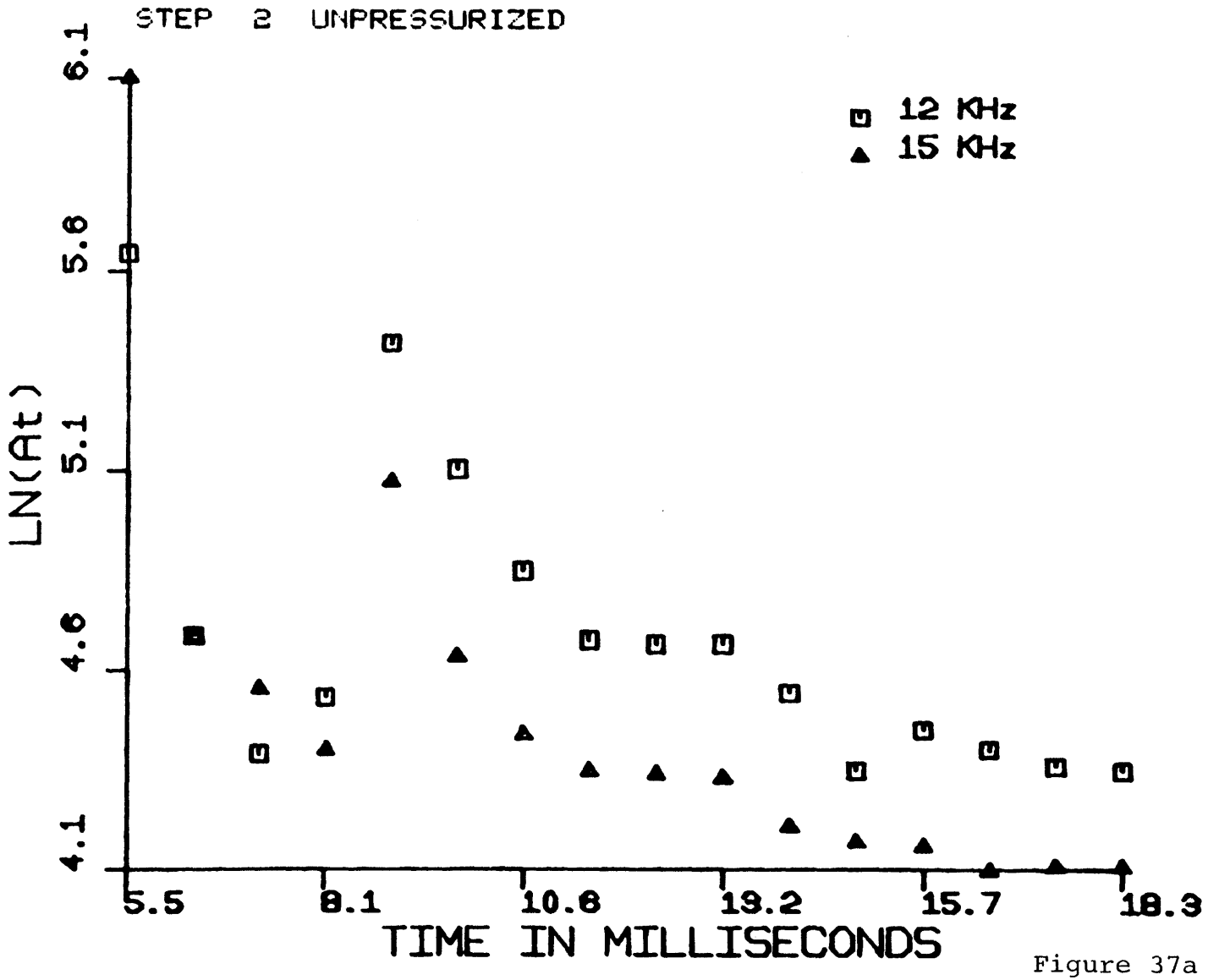
STEP 2 UNPRESSURIZED
12 KHz
15 KHz
LN(At)
6.1
5.6
5.1
4.6
4.1
5.5
8.1
10.6
13.2
15.7
18.3
TIME IN MILLISECONDS

Figure 37a

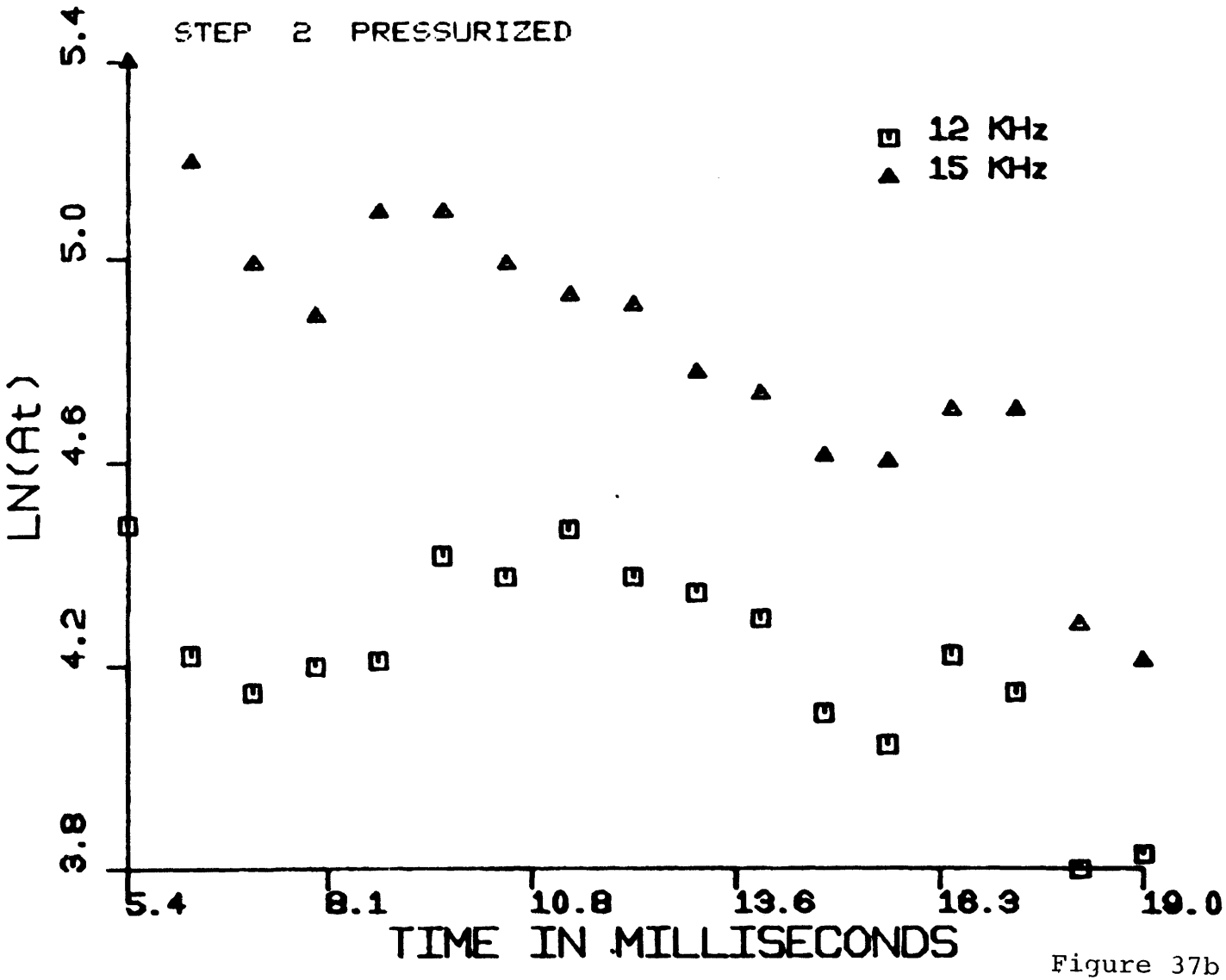
STEP 2 PRESSURIZED
12 KHz
15 KHz
LN(At)
5.4
5.0
4.6
4.2
3.8
5.4
8.1
10.8
13.6
16.3
19.0
TIME IN MILLISECONDS

Figure 37b

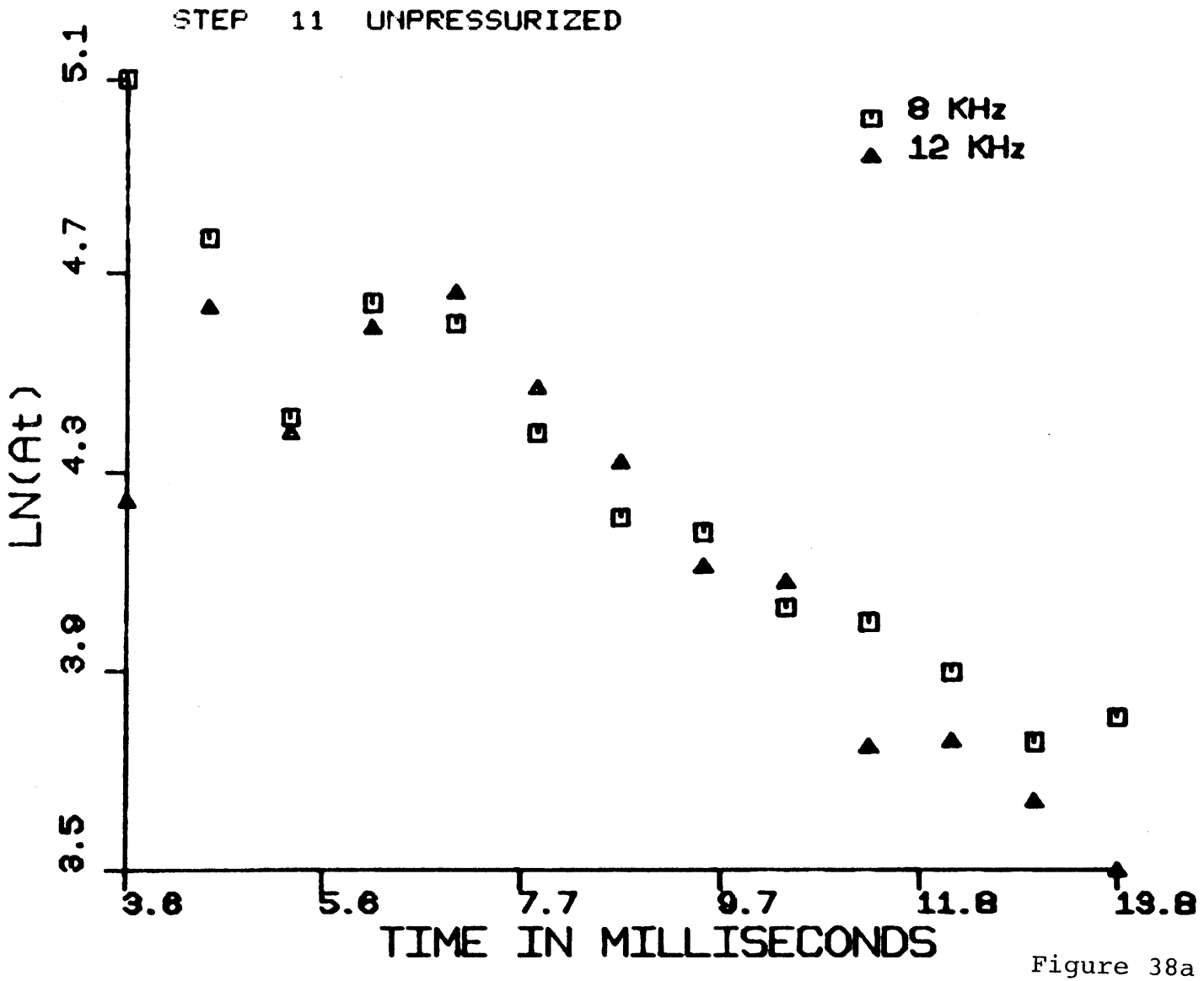
STEP 11 UNPRESSURIZED
8 KHz
12 KHz
LN(At)
5.1
4.7
4.3
3.9
3.5
3.6
5.6
7.7
9.7
11.8
13.8
TIME IN MILLISECONDS

Figure 38a

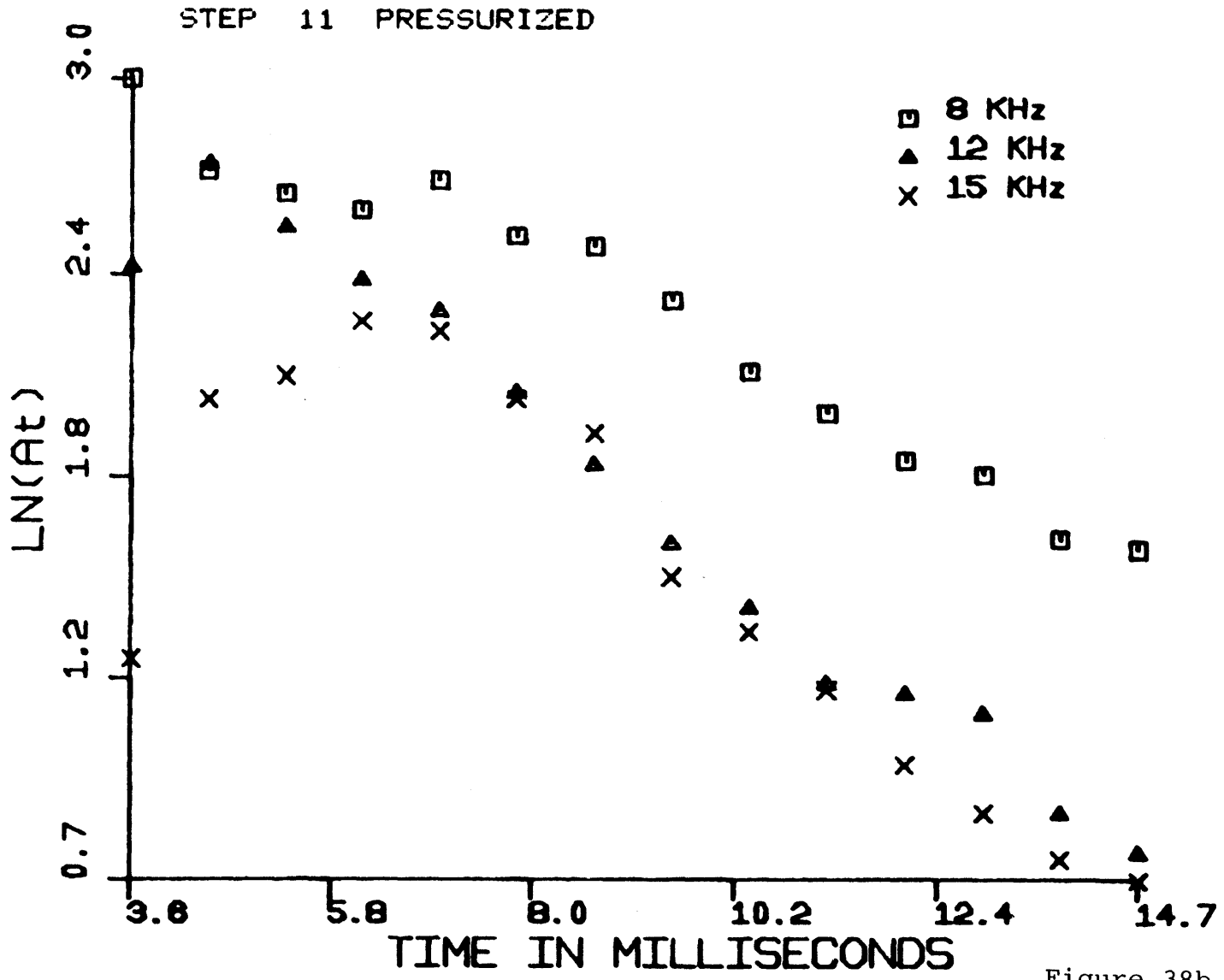
STEP 11 PRESSURIZED
8 KHz
12 KHz
15 KHz
LN(At)
3.0
2.4
1.8
1.2
0.7
3.6
5.8
8.0
10.2
12.4
14.7
TIME IN MILLISECONDS

Figure 38b

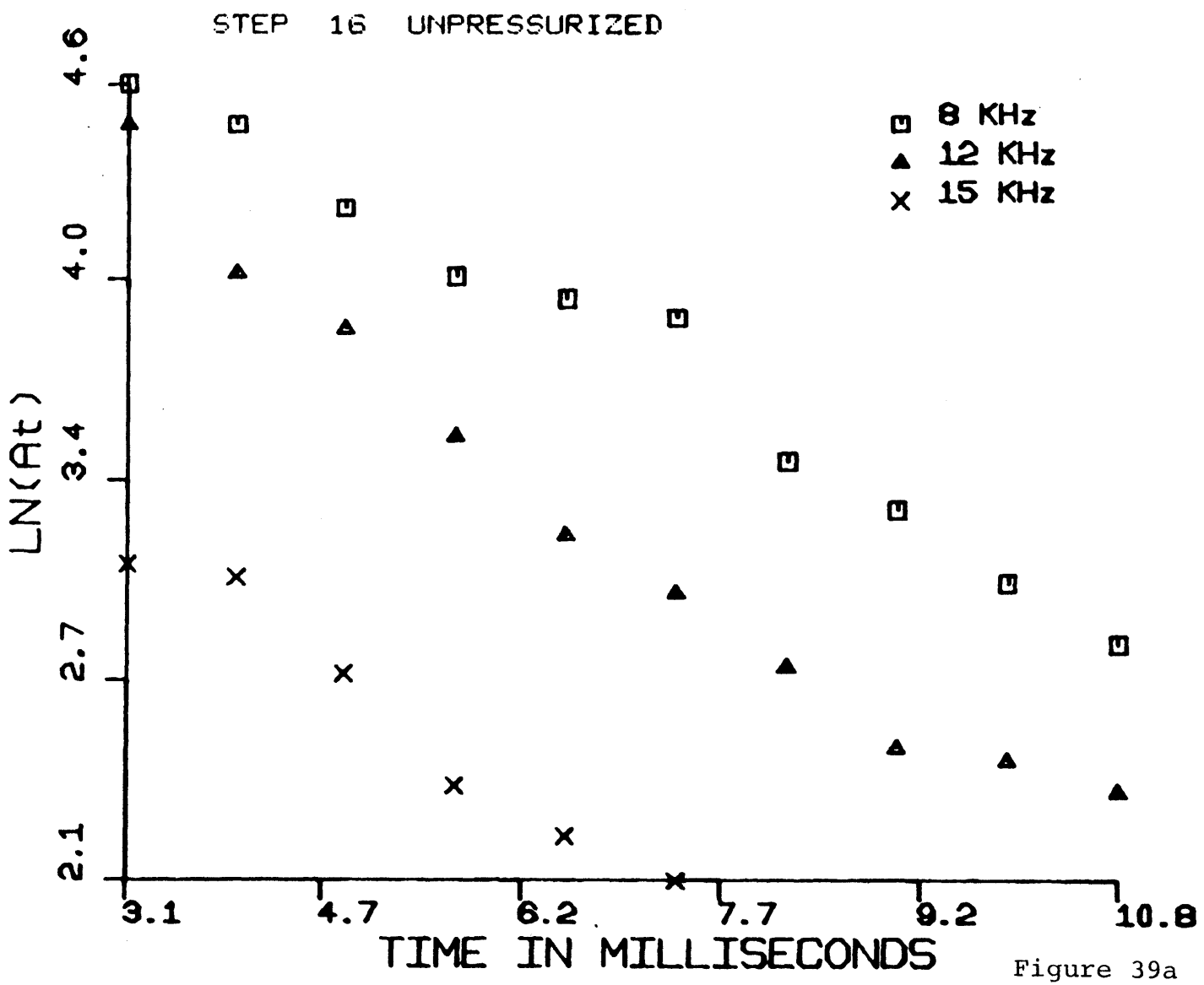
STEP 16 UNPRESSURIZED
8 KHz
12 KHz
15 KHz
LN(At)
4.6
4.0
3.4
2.7
2.1
3.1
4.7
6.2
7.7
9.2
10.8
TIME IN MILLISECONDS

Figure 39a

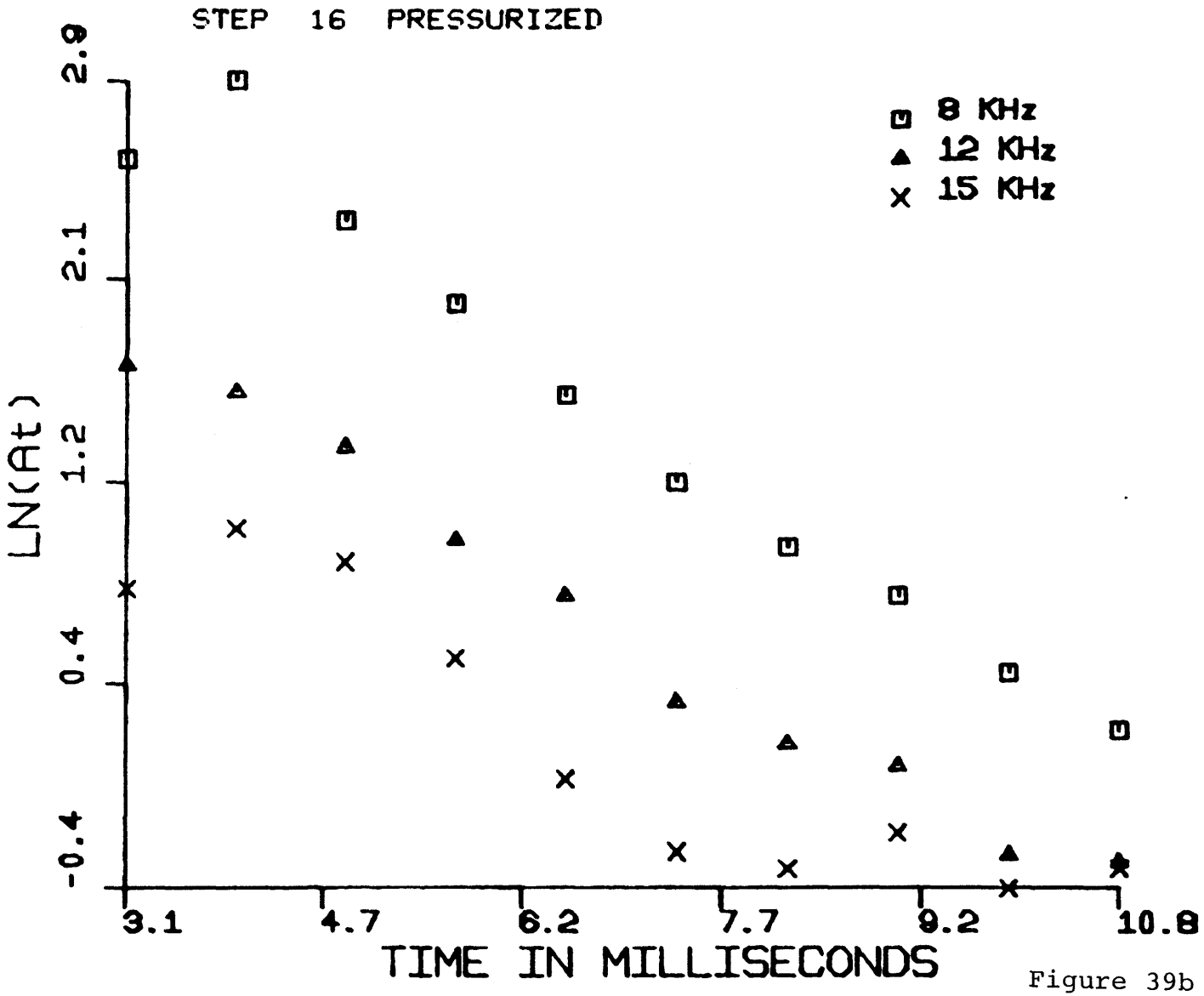
STEP 16 PRESSURIZED
8 KHz
12 KHz
15 KHz
LN(At)
2.9
2.1
1.2
0.4
-0.4
3.1
4.7
6.2
7.7
9.2
10.8
TIME IN MILLISECONDS

Figure 39b

number 4

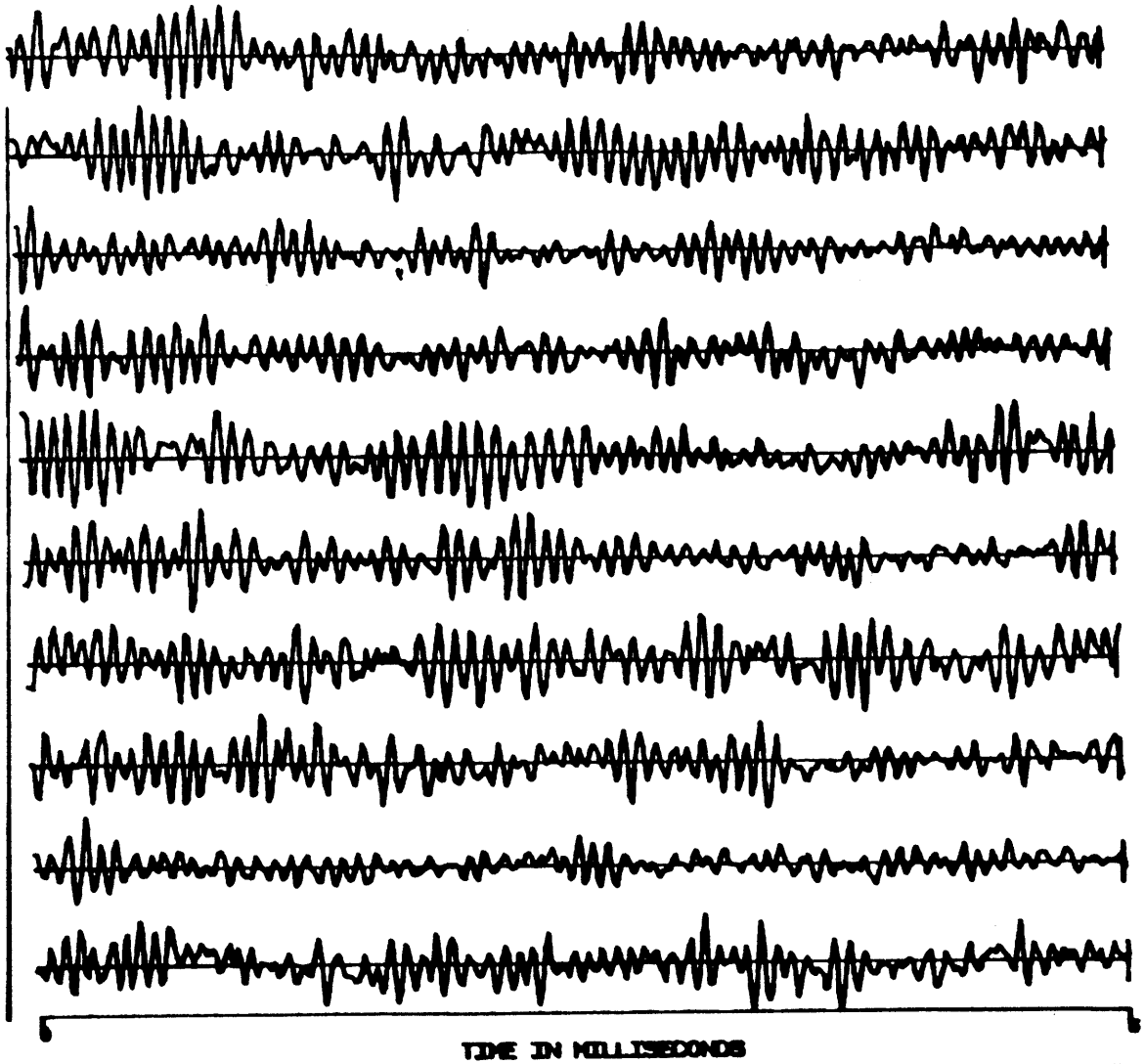

Figure 40

CHAPTER 5

DISCUSSION AND CONCLUSION

The model of a Hot Dry Rock geothermal system was originally conceived to be a single large fracture connecting two boreholes that are drilled into otherwise impermeable rock. In the preceding chapter it was found that this simplified model is not easily supported by seismic data collected at Fenton Hill. Our observations, in fact, indicated heterogeneities of various scale lengths. Lack of coherence of waveforms between seismograms for closely spaced sources provides evidence of a great deal of scattering of waves by small scale heterogeneity. Travel time differences between pressurized and unpressurized conditions in step 16 show that scale of heterogeneity is approximately three meters. Differences in average P wave velocities measured in 1977 and 1978 show that microcrack porosity of rock in the reservoir has increased. Changes in velocity when fluid pressure in the reservoir is altered means that water can permeate the microcrack porosity. Thus there is a wide range of heterogeneity in the Fenton Hill reservoir. In this chapter we will discuss quantitative limits on the strength, location and size of heterogeneity that

is consistent with seismic data.

In the first section of this chapter, heterogeneity on the scale of wavelength of waves will be discussed. The single isotropic scattering model of Sato (1977a,b) will be used to model the time dependence of the envelope of seismograms recorded in unpressurized step 2. Scattering in steps 11 and 16 is very strong and will be modeled using a diffusion approach to energy propagation.

In the second section the velocity measurements made from 1978 data will be modeled to find pore aspect ratio spectra using the technique of Cheng (1978). In this section the rock is considered to be homogeneous on the scale of the wavelength of waves and only the effects of microcracks are considered to be important. In addition, the effects of changes in temperature on seismic velocity will be discussed.

The original concept of the geothermal system as a single fracture is discussed in the third section. Results of previous seismic experiments are given along with their interpretation in terms of the existence of a single fracture. Beginning with the original seismic experiments made at Fenton Hill, we will outline the evolution of the model of the reservoir from a single elliptical crack to a complex heterogeneous

structure as data accumulated. Finally, arguments for the existence of a system of fractures with thicknesses as large as 4 mm and vertical extent of as much as 200 meters will be given.

In the final section a summary of results of this thesis will be given and new experiments proposed that would help resolve some of the uncertainty in current models of the geothermal reservoir.

5.1 Scattering

When an elastic medium contains a number of heterogeneities that have characteristic sizes comparable to the wavelength of a wave, a deterministic solution for wave propagation is usually not available. In such a case, one may resort to a statistical approach, for example, by making appropriate assumptions about the scattering cross sections for given heterogeneities, the time dependence of the envelope of the motion at one point can be estimated. In this section, Sato's (1977a,b) predictions of the time dependence of seismogram envelope, made using a weak single scattering approximation, will be discussed. Data presented in Chapter 4 for step 2 unpressurized case will be modeled using Sato's (1977b) theory. Data for step 2 pressurized case and steps 11 and 16 cannot be explained with Sato's theory because of stronger

scattering in these cases. A diffusion model of wave propagation (Dainty and Toksöz, 1977) will be investigated and shown to provide a reasonable explanation for the data in the case of strong scattering.

5.1.1 Single Scattering

When scattering from heterogeneities is weak, the effects of multiple scattering may be ignored when modeling wave propagation through the medium. This leads to the "single scattering approximation" which has been used successfully by seismologists to determine statistical properties of the distribution of heterogeneity in a medium (Aki, 1973; Chouet, 1976). Sato (1977a,b) used the single scattering approximation to predict the time dependence of the envelope of energy that propagates through a heterogeneous medium. He considers the density of scatterers, n, to be the same everywhere in the medium but is different for each mode of scattering, P to P, P to S, S to P, and S to S. Sato assumes that the size of the heterogeneity is small compared to the distance between source and receiver. Scattering is isotropic in Sato's model and scattering cross section is given by σ. Time dependence of energy density of direct and scattered waves, in a narrow frequency band around ω, from a point source located at r = 0 is given by

$$E_s(r,t/\omega) = W_o^p n^{pp}\sigma^{pp}(\omega)k(\beta)\theta(\beta-1)+W_o^s n^{ss}\sigma^{ss}(\omega)k(\tfrac{\beta}{\gamma})\theta(\tfrac{\beta}{\gamma}-1)$$

$$+ W_o^s n^{sp}\sigma^{sp}(\omega)k_c(\beta)\theta(\beta-1) + W_o^p n^{ps}\sigma^{ps}(\omega)\gamma k_c(\beta)\theta(\beta-1) \qquad (1)$$

where

$$k(x) = \frac{1}{x}\ln\frac{x+1}{x-1} \quad \text{for } x > 1$$

$$\theta(x) = \begin{cases} 1 & \text{for } x \geq 0 \\ 0 & \text{for } x < 0 \end{cases}$$

$$k_c(x) = \begin{cases} \frac{1}{2x}\ln\frac{\gamma+x}{\gamma-x} & \text{for } 1 < x < \gamma \\ \frac{1}{2x}\ln\frac{(x+1)(x+\gamma)}{(x-1)(x-\gamma)} & \text{for } x > \gamma \end{cases}$$

$$\beta = \frac{V^p t}{r}$$

$$\gamma = \frac{V^p}{V^s}$$

V^p and V^s are P and S wave velocities of the medium, and W_o^p and W_o^s are the energies of the P and S waves at the source.

Anelastic attenuation of waves has not been accounted for in equation (1). For a rough estimate of the effects

of attenuation on time dependence of energy density, assume that Q is the same for P and S waves. Then the right hand side of (1) can be multiplied by $\exp(-\omega t/Q)$ to account for the effects of attenuation.

Equation (1) predicts that the energy density has a logarithmic singularity at the P and S wave arrival times. For times large compared to S wave travel time, $k(x)$ and $k_c(x)$ in (1) become proportional to $1/t^2$ which means that energy density decreases as $\frac{1}{t^2} e^{-\omega t/Q}$ when the effects of attenuation are included. The time dependence of the envelope of a seismogram at times large compared to the S wave travel time is thus predicted by Sato's (1977b) model to be

$$A \sim \frac{1}{t} e^{-\frac{\omega t}{2Q}} \qquad (2)$$

To test the applicability of Sato's model to data obtained at Fenton Hill, it was decided to try to match time dependence of seismogram envelope predicted by equation (1) with spectral amplitude vs. time obtained from windowed seismograms for the unpressurized part of step 2. Unpressurized step 2 was chosen because seismograms recorded for different source locations show greater coherence than is found for other steps, suggesting a weaker scattering. To determine the time dependence of seismogram envelope given by equation (1),

the four coefficients, $W_o^p n^{pp} \sigma^{pp}$, $W_o^s n^{ss} \sigma^{ss}$, $W_o^s n^{sp} \sigma^{sp}$, and $W_o^p n^{ps} \sigma^{ps}$ must be chosen as well as the value of Q. Each coefficient is related to the source strength, W_o, as well as the mean free path for P or S waves. Unknowns must be positive quantities. Using the least squares technique, some of the coefficients became negative so it was decided to use the linear programming method which allows the signs of coefficients to be specified. When using linear programming we attempt to find a range of models that fit the data to within some specified confidence limit.

Spectral amplitudes at 8, 12 and 15 KHz were analyzed. The direct P arrival was excluded from the data because of the singularity of the envelope predicted by equation (1) at the time of the arrival which is not possible in reality. Using spectral amplitudes obtained from windowed seismograms for unpressurized step 2 ranges for coefficients and Q in equation (1) were found that resulted in model predictions that fell within confidence limits of the data. No model could be found for 8 KHz that fit data within acceptable bounds. It is interesting that for frequencies of 12 KHz and 15 KHz the values of $W_o^s n^{sp} \sigma^{sp}$ and $W_o^p n^{ps} \sigma^{ps}$ were zero for both upper and lower bounds. This means that no wave conversions take place upon scattering. Ranges of Q obtained from the linear pro-

gramming are 430-500 for 12 KHz and 275-350 for 15 KHz which are slightly higher than Q's obtained for step 2 pressurized case by fitting a straight line to time dependence of lnAt (see Table 4-7).

An attempt was made to model step 2 pressurized data using the same technique as was used for unpressurized data. No models could be found that reasonably fit the data. Seismograms recorded for pressurized step 2 show much more variability with the change in source location than do unpressurized step 2 seismograms indicating a stronger scattering for the former case than for the latter.

5.1.2 Multiple Scattering

As shown in the preceding section, time dependence of the spectral amplitude of seismograms for unpressurized case of step 2 can be explained by Sato's (1977b) model of single isotropic scattering without mode conversions. The observed linear time dependence at early times of lnAt for seismograms recorded in step 2 pressurized and steps 11 and 16, however, are not explained by the single scattering theory. Seismograms plotted in Figures 7, 8 and 10-12 of Chapter 4 show that energy arriving after the first arrival cannot be correlated between seismograms that have source locations that differ by two meters. It is even difficult to

correlate late arriving energy of signals whose sources differ by only 20 cm as shown in Figure 40 of Chapter 4. This lack of coherency of late arriving signals at a common receiver from sources that are very close together in space means that the medium through which waves travel is strongly heterogeneous and effects of multiple scattering must be taken into account to properly model the data. To explain the time dependence of the envelope of seismograms for waves passing through strongly heterogeneous media, Dainty and Toksoz (1977) consider that seismic energy propagates through a diffusion process. From the conservation of energy, they arrive at a modified diffusion equation for E, the seismic energy per unit volume at angular frequency ω

$$\frac{\partial E}{\partial t} = \frac{C\lambda}{3} \nabla^2 E - \frac{\omega}{Q} E \qquad (3)$$

where λ is the average distance that energy travels before it is scattered (mean free path), and C is wave velocity. The last term in equation (3) represents the loss of energy due to anelasticity. The solution to (3) for a point source in time and space is given (e.g., Aki and Chouet, 1975) as

$$E(r,t,\omega) = \frac{W(\omega)}{(4\pi Dt)^{3/2}} \exp\left(-\frac{r^2}{4Dt}\right) \exp\left(-\frac{\omega t}{Q}\right) \qquad (4)$$

where D is the diffusivity which is equal to $C\lambda/3$, and $W(\omega)$ is the source energy. If diffusivity or time is very large, the term $\exp(-r^2/4Dt)$ is unimportant and equation (4) implies that seismogram amplitude varies as $\exp(-\frac{\omega t}{2Q})/t^{3/4}$ which means that $\ln At^{3/4}$ is a linear function of t. In Chapter 4 it was found that lnAt was nearly a linear function of time for all cases except for step 2 unpressurized. Since $\ln At^{3/4}$ is very similar to lnAt, (4) may be used to fit data to find Q and D. From equation (4) time dependence of $\ln At^{3/4}$ is

$$\ln At^{3/4} = -(\frac{r^2}{8t})\ \frac{1}{D} - (\frac{\omega t}{2})\ \frac{1}{Q} + B \qquad (5)$$

where B is an additive term that depends on source strength as well as diffusivity. Equation (5) can be solved for D and Q using the least squares method. Examination of the covariance matrix (see section 5.3.1) showed that the errors in the predicted values of D are so large (often two to three times the predicted value of D) that no reasonable constraints could be placed on diffusivity. The errors in Q, on the other hand, are less than 10% of the predicted value in all cases. With only one exception, the Q resulting from the diffusion model, listed in Table 1, is larger but within a factor of two of the Q found in Chapter 4

(Table 4-7) from the slope of lnAt. The only exception is unpressurized step 16 at 8KHz where diffusion model gave a slightly lower Q. Larger Q should be expected when using (5) since Q in the single scattering model may be considered to include energy loss due to scattering.

No attempt was made to model step 2 pressurized data using (5) because the jumps in amplitude that occur at the S wave arrival time as well as at 16.5 msec are not consistent with the diffusion model.

5.2 Microcracks

In Chapter 3 the models of Cheng (1978) and O'Connell and Budiansky (1977) were used to predict velocity and attenuation under water-saturated conditions for virgin core samples obtained from GT-2. Figure 3-9 shows velocity as a function of pressure for dry and saturated rock and Figure 3-11 shows the corresponding Q. In situ P wave velocity found during dual well seismic experiments was always lower than the minimum velocity of water-saturated virgin core samples (Figure 3-9) which means that there are more microcracks present now in rock in situ than were present when cores were sampled in 1975. Increased microcrack content is due to the hydrofracturing and heat extraction that have been performed since the boreholes were drilled. In

this section porosity spectra of microcracks will be found using velocities measured in situ. A spectrum of microcracks will be found for rock in each step of the 1978 seismic experiment as well as for step 16 of the 1977 experiment. Knowledge of microcrack spectrum will aid in modeling fluid flow through the reservoir.

Before going into details of the pore spectrum study, we shall describe one of the most important results obtained from the monitoring of in situ seismic velocities, namely, the strong correlation between the decrease in velocity and cooling. Temperature profiles measured in EE-1 are shown in Figure 4-2. The minimum in situ temperature reached after EE-1 was drilled but before the time that the 1977 seismic experiment was performed is shown by the middle curve in Figure 4-2. The lower curve in the figure represents the minimum temperature reached before the 1978 seismic experiment. Figure 1 shows P wave velocity for pressurized case plotted against difference between the temperature at the time of the seismic measurement and the virgin in situ temperature. For zero temperature difference velocity predicted for fluid saturated virgin core samples at 100 bars effective stress, as shown previously in Figure 3-9, is plotted. P wave velocity shows a linear decrease with temperature difference. Least squares fit gives

the slope of the line to be 1.07 (km/sec)/100°C. Johnston (1978) measured P wave velocity on thermally cycled Westerly granite and found that velocity decreases approximately linearly with maximum temperature reached during cycling. He found change of velocity with maximum temperature to be approximately .35 (km/sec)/100°C which is less than the change in velocity with temperature difference found for our data. Velocities on thermally cycled Westerly granite were always measured at room temperature so some of the microcracks introduced by the temperature increases were closed when temperature decreased. Since temperature in situ at Fenton Hill remains low for a long time after a flow experiment, seismic measurements were made when rock was in a thermally stressed state. Thus microcracks induced by temperature changes have not closed resulting in very low velocity. An important conclusion from Figure 1 is that seismic velocity may be used to map the temperature decreased due to heat extraction.

Velocity for pressurized condition differs from unpressurized one because pore pressure is higher and the effective pressure is lower. If the effective pressure is known for each case, the pore aspect ratio spectrum for the unpressurized case can be found from that for the pressurized case by using Cheng's (1978)

technique for computing the closure of cracks under pressure.

For the unpressurized case of each step it will be assumed that effective stress is 200 bars which is slightly higher than the minimum effective stress at 2930 meters found by hydrofracturing experiments (see Table 3-1). When the geothermal system is pressurized, fluid pressure in the pores of the rock can be determined from (LASL HDR staff, 1978)

$$\nabla \cdot \frac{\rho k}{\eta} \nabla P = \frac{d\rho\theta}{dP} \frac{\partial P}{\partial t} \qquad (5)$$

where P is fluid pressure, η fluid viscosity, ρ fluid density, θ porosity, and k the permeability tensor. If ρ, k and η are considered to be independent of location and ρ is independent of pressure, equation (5) is a diffusion equation where diffusivity is given by

$$D = k/(\eta \frac{\partial \theta}{\partial P}) \qquad (6)$$

From measurements made during flow experiments in 1976, LASL HDR staff (1978) estimate the value of scalar k to be 2×10^{-17} m^2 (20 μDarcys) and for $\frac{\partial \theta}{\partial P}$ they find 2×10^{-7} /bar. For viscosity of .0014 poise, (6) gives the diffusivity to be 714 cm^2/sec. If fluid pressure in EE-1 is maintained constant for a given length of

time, the fluid pressure in the pores of the rock will be approximately one half the pressure in EE-1 at a distance x from EE-1 which is given by

$$x = \sqrt{Dt} \qquad (7)$$

Choosing t to be one hour (3.6×10^3 seconds) equation (7) gives that at a distance of 16 meters from the pressure source, the fluid pressure will be half of the pressure at the source. For step 16 the distance between boreholes was found to be 15.1 meters (Table 4-3). If fluid pressure increase in EE-1 due to pressurizing is 100 bars, fluid pressure in rock surrounding GT-2 should have increased by 50 bars after one hour. After two hours, fluid pressure increase in rock near GT-2 due to pressure increase in EE-1 will be greater than 50 bars. Since fluid was pumped into EE-1 for at least two hours prior to the execution of step 16, it will be assumed that fluid pressure between the boreholes in the region of step 16 has increased by 100 bars which means that effective pressure in step 16 is 100 bars during the pressurized part of this step. Pore pressure in the region of step 11 will be assumed to be the same as in step 16 since the two steps are located fairly close together. In step 2, distance between boreholes is 28.1 meters. Time required for pore

pressure to reach 50 bars at a point 28 meters from a 100 bar source of pressure is about 3 hours. Because of the large borehole separation in step 2 it will be assumed that average pore pressure in step 2 changes by only 50 bars when EE-1 is pressurized. Effective pressure for step 2 will be taken as 150 bars for the pressurized case.

Beginning with the pore aspect ratio spectrum found in section 3.6.1 for virgin core samples, porosity of cracks with a given aspect ratio was increased until velocities predicted by the model at two pressures agreed with those measured in situ. Pore aspect ratio spectrum determined by this method is very non-unique since there are nine aspect ratios for which porosities may be chosen and only two measurements of velocity to fit.

The difference between velocities in pressurized and unpressurized cases in 1978 was small which implies that new porosity must be in the form of cracks with aspect ratio on the order of 10^{-3}. Lower aspect ratio cracks cause large pressure dependence of velocity at low pressures.

Listed in Table 2 are crack aspect ratio spectra consistent with the measured velocities for steps 2, 11 and 16. Table 2d shows results for step 16 of the 1977 experiment. Microcrack porosity found for each case is

listed in Table 3 along with the porosity of the virgin rock at 100 and 200 bars effective pressure. Microcrack porosity is taken to be the sume of the porosities of all cracks except those of aspect ratio 1. Microcrack porosity in step 16 (1978) is about four times the porosity of cracks in virgin rock under the same effective pressure. Microcrack porosity in step 11 is approximately three times that of the virgin rock and in step 2 it is about twice that of the virgin rock.

Now that pore aspect ratio spectrum is known, the crack compressibility, $\partial\theta/\partial P$, can be found by using Cheng's (1978) formula. According to Cheng (personal communication), a reliable estimation of $\partial\theta/\partial P$ requires the aspect ratio spectrum obtained from the data on pressure dependence of both velocity and linear strain. If only velocity data were used, the estimated model is too stiff, or $|\frac{\partial\theta}{\partial P}|$ is underestimated. Since the aspect ratio spectra were obtained from velocity data alone in this thesis, the computed values of $|\frac{\partial\theta}{\partial P}|$ should be considered as lower bounds. They are listed in Table 4 for various in situ pressures for steps 2, 11 and 16 of the 1978 experiment, step 16 of the 1977 experiment, and the virgin GT-2 rock discussed in Chapter 3.

If microcrack compressibilities in Table 4 are used to compute fluid pressure diffusivity in equation (5) the resulting diffusivity is too low to be consistent with flow measurements. This means that flow cannot be occurring only through the microcracks. Some part of the flow must be along larger fractures whose volumes are not affected by pressure changes at the low pressures at which flow experiments were conducted. If a hydrofracture or joint is held open by some mechanism other than fluid pressure, e.g., debris or asperities along the fracture surfaces, flow may occur along the fracture and compressibility of the fracture in flow experiments may be extremely low.

Using the pore aspect ratio spectra obtained from velocity measurements, Q was calculated for each step using the model of O'Connell and Budiansky (1977) which was discussed in Chapter 3. The resulting predictions of Q, which are listed in Table 5, are much lower than values found by using scattering models in Section 5.1. Higher Q determined from scattering models refer to late arriving waves that may have traveled outside of the highly attenuating region between the boreholes. From observations of direct P waves only $1/Q_p - 1/Q_{up}$ can be computed. With the

exception of step 2, differences in reciprocal Q's obtained for direct P waves between pressurized and unpressurized cases, listed in Table 5a of Chapter 4, are larger than the corresponding values listed in Table 5 computed using O'Connell and Budiansky (1977). This difference is most likely due to the scattering of direct P waves unaccounted for in the model of O'Connell and Budiansky.

5.3 Modeling the Seismic Response of the Fenton Hill Geothermal System

The unique ability to control fluid pressure in the Fenton Hill reservoir enables comparisons to be made of in situ seismic measurements at selected effective pressures with corresponding laboratory measurements and theoretical models. Furthermore, body wave propagation can be studied without contamination from surface waves because the measurements were made at depths. In Chapter 4 seismograms were studied to gain information about the seismic response of the Fenton Hill geothermal reservoir. Throughout the history of the Hot Dry Rock geothermal energy project, many methods to define the characteristics of the fractures in the reservoir have been proposed and tested. In this section a historical overview of seismic studies will be presented and the evolution of the model of the reservoir as more infor-

mation has been gained will be developed.

When the Hot Dry Rock concept was first proposed (Harlow and Pracht, 1972) a geothermal reservoir in impermeable Precambrian crystalline rock was envisioned. Impermeable rock was desired so that water losses due to flow out of the reservoir could be minimized. It was hoped that through use of the hydrofracturing technique a fracture with a diameter of approximately 1 km could be created. In order to define orientation and size of the hydrofracture a seismic diffraction experiment using surface source and receivers was proposed. As an aid in designing and interpreting diffraction experiments, the diffraction of P and S waves by finite empty and fluid-filled cracks was studied. Results of this theoretical study are presented in Chapter 2. Although diffraction effects due to a shallow magma reservoir in Kilauea Iki, Hawaii, have been observed and interpreted using results in Chapter 2 (Fehler and Aki, 1978) no diffraction experiment has been attempted at Fenton Hill. The reason for this is that the Bandalier Tuff that is the surface rock in the region of Fenton Hill is highly attenuating so that a very large seismic source would be needed, with a strict requirement of repeatability for calculating differential seismograms between pressurized and unpressurized cases.

During hydraulic fracturing experiments in a shallow borehole called GT-1, surface geophones were set up to observe fracturing induced seismic signals. Seismic noise with a period of about .1 second that gradually increased as water was pumped into the fracture was recorded (Potter and Dennis, 1974). This noise is probably generated by the vibration of the water-filled fracture caused by pressure increases due to pumping. Period of such noise should increase as the diameter of the crack increases. Seismic noise, with frequency of 7 Hz, was observed using a downhole 3-axis geophone placed in EE-1 while pressuring GT-2. Particle motion of this noise was consistently elliptical with the major axis of the ellipse oriented along a NW-SE direction. The noise observed during hydrofracturing has characteristics that are similar to those of volcanic tremor observed in Hawaii and on other volcanoes. Aki, Fehler and Das (1977) proposed that volcanic tremor is due to excess pressure of fluid in a magma that causes narrow channels along the magma flow path to open and close. They found that such a process resulted in a spectrum of seismic radiation that has a peak at a frequency which is determined by the size of the channel. If the crack is empty, the particle motion near the channel is predicted by their model to be elliptical with major axis perpendicular to the

crack plane. When fluid is present inside the fracture, the finite bulk modulus of the fluid decreases the amplitude of particle motion perpendicular to the crack and the major axis of the particle motion ellipse may become parallel to the crack plane if crack stiffness factor, defined in Chapter 2 to be bulk modulus of the fluid divided by the product of the crack aspect ratio times rigidity of the solid, is sufficiently large. The orientation of the particle motion ellipse observed when pumping into GT-2 thus means that the hydrofracture plane trends in either a NW-SE direction or NE-SW direction depending on the crack stiffness factor. It is generally believed that the plane of a hydrofracture will be oriented perpendicular to the direction of the minimum principal stress. The proximity of Fenton Hill to the Rio Grande rift zone suggests that the regional tectonic stress should have a minimum in the NW-SE direction. Fault plane solutions obtained for earthquakes in North Central New Mexico agree with a NW-SE direction of minimum stress (Olson, 1978). The local stress field near Fenton Hill is, on the other hand, most directly influenced by the presence of the Valles Caldera. Ring fractures and topography near Fenton Hill suggest the minimum principal stress in the NE-SW direction. Thus the current knowledge of in situ principal stress orientation is not sufficient to distinguish between the

two fracture orientations that are consistent with the particle motion of low frequency seismic noise. A televiewer placed in EE-1 after hydrofracturing indicated a NW-SE trending fracture.

Using borehole geophones during hydraulic fracturing experiments microearthquakes were recorded that are believed to be due to the fracturing of rock as the crack expands. Frequency range of the recorded signals is a few hundred to a few thousand Hertz. Unlike the longer period continuous noise just described, these signals appear to be due to discrete events. P and S wave arrivals could be determined in many of the signals. Since only one seismic receiver could be operated at a time, a unique location for each seismic event cannot be determined. Using difference between P and S wave arrival times the distance separating the source and receiver can be determined. Polarization of direct P waves gives two possible directions to the event (Albright, 1976). If source mechanism is known a unique direction can be determined. By careful selection between the two directions LASL HDR staff (1978) found that all events recorded at common receiver depth could be made to fall along a line which is interpreted to be the plane of the hydrofracture. Orientations of the lines vary a bit with depth but generally trend in a NW direction which means that minimum compressive

stress, S_3, is SW-NE and is probably due to the proximity to the Valles Caldera. To clarify the uncertainty in source location, Aki (1977) studied P and S wave polarization of the signals from the microseismic events and concluded that if direction of S_3 is SW-NE the events must be dip slip normal faults located as far as 40 meters from the pressurized well. If S_3 is SE-NW he argues that the events are strike slip along vertical planes and fall very close to the pressurized well. For NW minimum compressive stress the fracture must trend NE. Aki's analysis presents an opposing view to the LASL interpretation that the microseismic events fall along the fracture and thus define the orientation and extent of the fracture. Aki's conclusion is based on the assumption that the microseismic events are shear-slips which share the common S_3 axis with the main hydrofracture, a mechanism attributed to decrease of effective normal stress by increased pore pressure along fault plane by Lockner and Byerlee (1977) and Hill (1977). At the time that hydrofracturing was performed, permeability of the reservoir rock was near the virgin in situ permeability which is approximately 400 times less than that estimated by modeling flow through the reservoir in 1976. Such low permeability means that fluid pressure does not penetrate into the pores at a very rapid rate since diffusivity in equation (6) is

very small. If pore pressure is not increased around the hydrofracture, the mechanism suggested by Lockner and Byerlee (1977) may not be operating in this case.

Microseismicity and low frequency noise recorded during hydrofracturing experiments were interpreted in terms of a single fracture created in the reservoir. In order to further define the properties of this single fracture, the shear shadowing experiments were proposed. The purpose of these experiments was to observe the different character of seismic signals traveling between boreholes under unpressurized and pressurized conditions. As found in Chapter 2, S waves of a certain polarization cannot be transmitted through a water layer imbedded between two elastic half spaces so they are in effect shadowed by the fracture. In an initial attempt at a shear shadowing experiment a three axis geophone package was placed in GT-2 and explosive sources were detonated in EE-1. Four receiver locations were occupied at different times in GT-2. For each receiver location, three shots were fired in EE-1 with the reservoir in an unpressurized state. The receiver was left in place while explosives were reloaded, positioned in EE-1 at the point where they had been previously fired and the wellbore pressurized to 100 bars. The sources were then re-fired. Seismograms obtained for two source receiver locations in pressurized and unpres-

surized conditions are shown in Figure 4-1. It was found that for source and receiver locations in the depth range of 2600 to 2700 meters the high frequency (3 KHz) waves present in seismograms when system was unpressurized were nearly wiped out upon pressurization. Waves of frequency less than 1 KHz were amplified by pressurizing. Amplification of long period waves may be due to reverberation of seismic waves traveling back and forth between parallel fractures. Amplification of long periods and the disappearance of high frequencies when the system was pressurized, as well as the complex waveforms recorded during the shear shadowing experiment suggested that a system of "multiple fractures" with lateral extent of at least 100 meters is present in the geothermal reservoir.

Another observation made from data collected during the shear shadowing experiment was the appearance of a strong arrival, when the system is pressurized, on seismograms recorded for source and receiver depths at about 2450 meters, which is above the temperature anomaly that is considered to be the top of the heat extraction region. Aki (1977) found that the particle motion of the late arrival was that of an S wave which he interpreted to be the result of a P wave scattered to an S wave at a depth of 2530 m or an S wave scattered to an S wave at 2500 meters.

If the wave is scattered off of the top of a crack, the S wave polarization can be used to determine the crack orientation. Aki (1977) found that the S wave polarization requires a NW-SE trend for the main fracture but that a single fracture is not sufficient to explain the amplitude of the late arrival. Thus either multiple cracks are required or some other scattering source is responsible for the late arrival.

The shear shadowing experiment showed that in order to explain details of the observed waveforms a complex system of fractures was required. Further definition of the detailed structure of the fracture system was desired. The Dresser Atlas seismic equipment with higher frequency range (8-18 KHz) provided the ability to gain large amounts of high-quality seismic data for detailed analysis. The original goal of the dual well seismic experiment was to define the extent of the fractured region by the use of waves converted at the fracture and shadowing of S waves by the fracture. In Chapter 4, we found that the fracture was too complex for these short waves to allow recording of clear converted waves. Scattering due to small scale inhomogeneity was the dominant factor. Analysis of data obtained during the two dual well seismic experiments suggests the existence of a wide range of scale of heterogeneity. Using results

obtained in this thesis, the complex structure of the heterogeneity will now be discussed.

The pattern of P, S and D type waves distinguished by Albright (1978) and shown in Figures 4-5 and 4-6 show that some characteristics of wave polarization persist over large regions in the reservoir. The complete absence of S type waves when the reservoir is pressurized may be explained by the existence of one or more fractures through which S waves are poorly transmitted. The absence of S type waves below the Gneiss-Granodiorite contact in the unpressurized case indicates that fractures are open even when the fluid in the boreholes is not pressurized.

Other evidence for a large fracture in the reservoir can be found by comparing Q's in Table 4-7 with the amplitudes of direct P wave arrival listed in Table 4-4 and amplitude spectra shown in Figures 4-37, 4-38, and 4-39. In step 2, the amplitude spectrum peaked at 12 KHz. Amplitude at 8 KHz was so low that it dropped to noise level very soon after the P wave arrival. In step 16 as well as pressurized step 11 the amplitude spectrum was peaked at 8 KHz and decreased considerably at 15 KHz. Low amplitude of 15 KHz compared to 8 KHz in the deeper steps could be explained if Q of the medium between two boreholes is very low at 15 KHz. Another explanation for loss

of high frequencies is that they are poorly transmitted through a fracture. Table 4-7 shows that Q at 15 KHz is higher than Q at either 8 or 12 KHz in step 16 and pressurized step 11 so the loss of high frequency is due to a fracture. To investigate the loss of high frequency signal we will assume that Q of direct P waves is the same as that determined using later arrivals in Chapter 4 and a comparison will be made between the first arrival amplitudes for steps 11 and 16 predicted using Q's given in Table 4-7 and actual amplitudes listed in Table 4-4. In order to remove the effect of the source strength, ratios of amplitudes between a given step and step 2 will be compared in a manner similar to that used to construct Table 4-6 (see equation 4-15). Measured values of $q = \frac{x_s}{Q_s} - \frac{x_2}{Q_2}$ (Table 4-6) found by comparing first arrival amplitudes of step s with step 2 will be compared with q computed using distances x_s given in Table 4-3 and values of Q in Table 4-7. Q for step 2 unpressurized will be taken as 465 at 12 KHz and 315 at 15 KHz which are averages of the bounds found using Sato's model. The ratio of predicted to measured first arrival amplitude, A_p/A_m, is found from

$$\frac{A_p}{A_m} = \exp\left\{\frac{\pi f}{V}(q_m - q_p)\right\} \qquad (8)$$

where subscript m refers to quantity measured directly from first arrival amplitude and p is predicted from tables of Q and x. If first arrival amplitude is decreased only through inelastic attenuation and if Q of direct P waves is the same as that of scattered waves, A_p/A_m should be unity. The ratio differs dramatically from unity as is shown in Table 6. If the very low Q's given in Table 5, found using the O'Connell and Budiansky (1977) model, are used in (8) the large values of A_p/A_m in Table 6 are reduced by as much as a factor of six but still show the features apparent in Table 6. Because of the uncertainty of the applicability of the model of O'Connell and Budiansky to our data we will not pursue a fracture model based on values of Q in Table 5. The most conspicuous feature of the ratios in Table 6 is that they increase dramatically with increasing frequency which means that high frequency component of first arrivals have been severely diminished by some mechanism other than anelastic attenuation. The decrease in amplitude of high frequencies can be reasonably explained by the existence of multiple fractures between the wellbores that have vertical extent of at least as large as 75 meters, the vertical distance covered in steps 11 and 16. Transmission coefficient for P waves incident on a fracture with thickness of a few millimeters shows frequency dependence

over a frequency range of 10-20 KHz, although transmission through fractures less than 1 mm in thickness is nearly frequency independent in the same range. Table 7 lists the amplitude of the transmitted P wave when a P wave of amplitude one is incident at various angles on a fluid layer. Amplitudes are obtained using the method described in Chapter 2. Amplitudes of transmitted waves for frequencies 8, 12 and 15 KHz are given. Examination of the table shows that amplitude of a 15 KHz wave may be as little as one half the amplitude of an 8 KHz wave after passing through a water layer. If a 15 KHz wave passes through four fluid layers, each with a thickness of 4 mm, at an angle of 60° from the plane of the layer the amplitude of the wave will be decreased by a factor of $(.31)^{-4}$ or 108 which is nearly equal to the decrease in amplitude of direct P wave at 15 KHz observed in step 16 pressurized case. If four fractures of thickness 2 mm are present the factor of 20 decrease in amplitude observed in unpressurized step 16 can be explained. To explain decrease in amplitude at 8 and 12 KHz only two or three fractures of thickness 4 mm are required in the pressurized case. Since large uncertainties must be assigned to ratios given in Table 6 it is not unreasonable that there is some variation in the number of

cracks required to fit the data. Nevertheless, the number of fractures required is fairly well constrained to be between two and four. Fracture thickness is approximately 4 mm in the pressurized case and 2 mm in the unpressurized case. The existence of multiple fractures is also consistent with the observed amplification of 3 KHz waves during the shear shadowing experiment where explosive sources were used. This amplification must be due to reverberation of waves between the fractures. Multiple fractures were also required by Aki (1977) to explain amplitude of the late S arrival observed at 2600 meters. The inability to discern S waves in seismograms recorded in GT-2 is consistent with this model because amplitudes of S waves traveling through a water-filled fracture with thickness of 2-4 mm are so severely decreased that they probably could not be observed after passing through multiple fractures. If fracture thickness is less than one millimeter, Figure 2-14 shows that the transmitted SV wave amplitude becomes large for angles less than the critical angle. S type waves were observed in the lower part of unpressurized step 16 in 1977 beginning at a depth where the incident angle of waves on a vertical fracture is less than critical. The appearance of S waves means that the fracture thickness in the unpressurized part of step 16

in 1977 was less than 1 mm. In the 1977 experiment, seismograms recorded in step 16 contained much more high frequency than in 1978 (compare Figure 4-7 with 4-11 and 4-8 with 4-12) which means that fractures were less than 1 mm in width at the time of the first experiment. Fracture width estimated from flow experiments prior to 1977 seismic measurement is .2 mm.

It has now been established that much of the seismic data obtained at Fenton Hill can be explained by the existence of two to four water-filled fractures with thickness of approximately 4 mm when boreholes are pressurized and 2 mm when no external fluid pressure is applied. These fractures extend over depth ranges that include at least the regions in steps 11 and 16 and probably extend up to the gneiss-granodiorite contact which makes the vertical extent of the fractures as much as 200 meters. Seismic data also gives evidence of smaller scale heterogeneity in the reservoir. Small scale heterogeneities act as scattering sources and are responsible for the lack of coherence between seismograms. Successful application of diffusion model of energy propagation to data in steps 11 and 16 showed that these regions are dominated by strong scattering. Differences in direct P wave arrival times between pressurized and unpressurized cases showed that the scale of the

heterogeneity in step 16 is on the order of three meters and that velocity inside the small heterogeneities is at least 3% less when the system is pressurized. Velocity variations in the heterogeneities are brought about by the change in pore pressure in the microcracks. Heterogeneities thus must represent regions of increased microcrack porosity or permeability. Extremely small scale heterogeneity in the form of microcracks are present throughout the geothermal reservoir and causes seismic velocities to be much lower than would be predicted by measurements in core samples removed at the time the boreholes were drilled.

5.4 Conclusions and Suggestions for Further Work

In this thesis we have studied theoretical problems and analyzed data in an attempt to define the mechanical properties of a Hot Dry Rock geothermal system. In the preceding section the evolution of the conceptual model of a Hot Dry Rock system from a single large fracture to a system of large multiple fractures and smaller scale heterogeneity was developed. The major accomplishments made and conclusions about the Fenton Hill geothermal system are:

(1) A Hot Dry Rock geothermal system provides an excellent field laboratory for study of seismic properties of rock. Because of the

abilities to control fluid pressure, obtain core for laboratory studies and introduce new microcracks through heat extraction we have a unique opportunity to compare seismic field measurements with laboratory measurements and theoretical formulations of rock properties.

(2) High frequency seismic waves (8-15 KHz) have been successfully used to probe the detailed structure of the reservoir.

(3) Velocity decrease due to introduction of microcracks during heat extraction has been observed. Velocity variations with fluid pressure changes have also been observed. We find that velocity decreases almost linearly with change in temperature from the virgin *in situ* temperature. Rate of change of velocity with temperature is 1.07 (km/sec)/100°C. Thus velocity may be used to effectively monitor changes in temperature in the reservoir.

(4) Using methods developed by Cheng (1978) to model laboratory measurements of velocity, the *in situ* microcrack spectra have been estimated from field velocity measurements. Microcrack porosity is estimated to be as much as four times the virgin microcrack

porosity. Changes in porosity with pressure were computed and found to be approximately one order of magnitude larger than were found from flow experiments indicating that some flow occurs along a path whose channel capacity is little affected by pressure. Those paths are called self-propped fractures since they are open even when outside fluid pressure is not applied.

(5) Spectral analysis of windowed seismograms revealed that logarithm of spectral amplitude times the time t measured from source origin time decreased nearly linearly with t, when the amplitudes were averaged over many seismograms. Spectral amplitudes of individual seismograms showed no consistent pattern.

(6) Envelopes of spectral amplitude in unpressurized step 2 were modeled using Sato's (1977b) single isotropic scattering model and Q of approximately 465 at 12 KHz was found. At 15 KHz, Q was found to be about 315. Diffusion model of energy propagation adequately explains energy propagation in the highly fractured region of steps 11 and 16. Values of Q were also estimated for

these regions. Diffusion coefficients were poorly constrained.

(7) Average spectral amplitudes of pressurized step 2 seismograms decreased as time increased from source firing except for two jumps. The first jump in amplitude is due to the arrival of the S wave. The second jump is probably due to some reflection off the top of the region from which heat is being extracted. The arrival of scattered waves is not apparent in individual seismograms and was not successfully amplified by phase shifting and stacking of seismograms.

(8) Differences in travel times between pressurized and unpressurized cases were found to be smooth functions of seismic source location at steps 2 and 11 in 1978 and steps 2 and 7 in 1977. Differences in travel times in step 30 in 1977 and step 16 both years showed variation with source depth with a characteristic length of approximately 3 meters. This indicates the existence of heterogeneity that has scale of 3 meters in these regions. Velocity variation in the heterogeneity due to pressurizing the reservoir is approximately 3%.

(9) Diffraction of P and S waves by finite empty and fluid-filled (zero viscosity) cracks has been studied. Only waves with wavelength on the order of the crack length were considered.

(10) Transmission and reflection of P and S waves incident on a fluid layer imbedded between two elastic half spaces have been studied as a function of elastic properties of fluid and solid, fluid viscosity as well as fluid layer thickness.

(11) Frequency dependence of the attenuation of direct P waves was compared to that of later arriving scattered waves and interpreted in terms of the number and thickness of large fractures present in the geothermal reservoir. Attenuation of scattered waves is due to the anelastic properties of the medium while direct P waves lose energy to anelasticity as well as reflection by the fractures. It was found that at the time of the 1978 experiment two to four fractures, each with thickness of 4 mm in the pressurized case and 2 mm in the unpressurized case, are required to explain the observed low amplitude of high frequency waves. Higher frequencies observed in 1977 mean that

fractures were less than 1 mm thick at that time. Vertical extent of the fractures may be as much as 200 m. Orientation of the fracture is either NW-SE or NE-SW as determined from seismic noise generated during hydrofracturing as well as microseismic events. S wave scattered off the top of the fracture implies a NE-SW fracture direction while a televiewer placed in the borehole indicated a NW-SE direction.

Clarification of the mechanical properties of the geothermal system could be obtained through further seismic experimentation. In particular I propose the following

(1) Repeat of the dual well seismic experiment using lower frequency source. Lower frequencies are less affected by fine scale structure of the medium and may provide a clearer image of the gross structure of the reservoir.

(2) Collection of three component seismic data at two or more receiver locations so that type of waves may be determined and propagating wavefronts reconstructed.

(3) Detailed laboratory studies on core samples removed from various depths in the reservoir. Measurements of static strain and velocity

as a function of effective pressure could be made to check the in situ measurements as well as find pore aspect ratio spectra of cracks.

(4) Careful and extensive dual well seismic measurements made in a new reservoir location before hydrofracturing. This is important so that the effects of fracturing and heat extraction on seismograms can be easily and accurately determined.

(5) Use of two or more stations to record microseismic signals generated by hydrofracturing. This would eliminate the present uncertainty in location of seismic sources.

(6) Perform a diffraction experiment using surface sources and receivers as well as borehole receivers. Use of long period (.1 sec) waves may provide information on the total reservoir in three dimensions, as the long period seismology provides information on the gross features of earthquake fault motion.

Step	Frequency	Q_{up}	Q_p
11	8	267	192
11	12	255	241
11	15		276
16	8	88	77
16	12	295	169

Table 1. Q found by using diffusion model to predict seismogram envelope.

Table 2a. Crack aspect ratio spectra for rock in region of step 2.

Pressurized: effective pressure = 150 bars

Aspect Ratio	Concentration
1.0	1.78×10^{-2}
.0096	1.94×10^{-3}
.0017	1.27×10^{-4}
.0012	7.29×10^{-5}
.0008	5.82×10^{-5}
.0005	2.78×10^{-4}
.0001	5.12×10^{-5}

Unpressurized: effective pressure = 200 bars

Aspect Ratio	Concentration
1.0	1.78×10^{-2}
.0095	1.89×10^{-3}
.0016	1.17×10^{-4}
.0011	6.54×10^{-5}
.0007	4.94×10^{-5}
.0004	2.24×10^{-4}

Table 2b. Crack aspect ratio spectra for rock in region of step 11

Pressurized: effective pressure = 100 bars

Aspect Ratio	Concentration
1.0	1.78×10^{-2}
.0096	2.88×10^{-3}
.0018	2.79×10^{-4}
.0013	2.61×10^{-4}
.0009	4.62×10^{-4}
.0005	2.97×10^{-4}
.0007	1.30×10^{-5}

Unpressurized: effective pressure = 200 bars

Aspect Ratio	Concentration
1.0	1.78×10^{-2}
.0093	2.79×10^{-3}
.0014	2.29×10^{-4}
.0010	1.96×10^{-4}
.0007	3.27×10^{-4}
.0003	1.50×10^{-4}

Table 2c. Crack aspect ratio for rock in region of step 16.

Pressurized: effective pressure = 100 bars

Aspect Ratio	Concentration
1.0	1.78×10^{-2}
.0095	3.82×10^{-3}
.0017	4.41×10^{-4}
.0012	2.82×10^{-4}
.0009	7.02×10^{-4}
.0004	1.98×10^{-4}

Unpressurized: effective pressure = 200 bars

Aspect Ratio	Concentration
1.0	1.78×10^{-2}
.0092	3.69×10^{-3}
.0014	3.55×10^{-4}
.0009	2.03×10^{-4}
.0007	5.02×10^{-4}
.0001	6.29×10^{-5}

Table 2d. Crack aspect ratio spectrum for rock in region of step 16 during 1977 experiment.

Pressurized: effective pressure = 100 bars

Aspect Ratio	Concentration
1.0	1.78×10^{-2}
.0096	2.88×10^{-4}
.0018	3.15×10^{-4}
.0013	2.98×10^{-4}
.0010	5.29×10^{-4}
.0006	4.02×10^{-4}
.0001	3.22×10^{-5}

Unpressurized: effective pressure = 200 bars

Aspect Ratio	Concentration
1.0	1.78×10^{-1}
.0093	2.78×10^{-4}
.0015	2.64×10^{-4}
.0010	2.34×10^{-4}
.0007	3.98×10^{-4}
.0003	2.48×10^{-4}

Table 3. Microcrack porosity as determined from velocity measurements.

Case	Effective Pressure (bars)	Microcrack Porosity (%)
Virgin rock	100	.131
Virgin rock	200	.120
Step 2 pressurized	150	.253
step 2 unpressurized	200	.235
step 11 pressurized	100	.419
step 11 unpressurized	200	.369
step 16 pressurized	100	.544
step 16 unpressurized	200	.481
step 16 (1977) pressurized	100	.186
step 16 (1977) unpressurized	200	.142

Pressure (bars)	Step 2	Step 11	Step 16	Step 16 (1977)	Virgin
50	5.2×10^{-6}	8.0×10^{-6}	1.0×10^{-5}	7.6×10^{-6}	1.8×10^{-6}
100	3.6×10^{-6}	5.6×10^{-6}	8.0×10^{-6}	5.2×10^{-6}	1.6×10^{-6}
200	2.6×10^{-6}	4.6×10^{-6}	6.6×10^{-6}	4.0×10^{-6}	8.0×10^{-7}
300	2.0×10^{-6}	4.6×10^{-6}	4.0×10^{-6}	4.0×10^{-6}	8.0×10^{-7}

Table 4. Microcrack compressibility ($\partial\theta/\partial P$) in $bars^{-1}$ found using pore aspect ratio spectrum for each step and Cheng's (1978) crack closure model.

Table 5. Q calculated using pore aspect ratio spectra given in Table 2 in model of O'Connell and Budiansky (1977).

Step	Frequency (KHz)	Q_{up}	Q_p	$\frac{1}{Q_p} - \frac{1}{Q_{up}}$
2	8	118	82	.004
2	12	129	90	.003
2	15	134	95	.003
11	8	40	33	.005
11	12	40	32	.006
11	15	41	31	.008
16	8	28	25	.004
16	12	29	23	.009
16	15	30	23	.010

	Step	8 KHz	12 KHz	15 KHz
Unpressurized	11		4.0	
	16		2.4	21.3
Pressurized	11	3.4	7.5	96
	16	3.2	12.2	133

Table 6. Ratios of first arrival amplitude predicted from measurements of Q on scattered waves to actual first arrival amplitudes.

		Layer thickness in millimeters				
	Frequency	1	2	3	4	5
Angle = 45°	15	.54	.40	.30	.24	.20
	12	.57	.45	.36	.29	.24
	8	.60	.53	.45	.38	.33
Angle = 60°	15	.69	.51	.38	.31	.25
	12	.72	.57	.45	.37	.31
	8	.77	.67	.57	.49	.42
Angle = 75°	15	.80	.59	.45	.35	.29
	12	.85	.67	.52	.42	.36
	8	.90	.79	.67	.57	.49

Table 7. Transmitted P wave amplitude normalized by incident wave amplitude when P wave is incident on a water layer.

Figure Caption

Figure 1. P wave velocity measured in the pressurized case for each step vs. change in temperature from the virgin *in situ* temperature. Data for both 1977 and 1978 experiments are plotted.

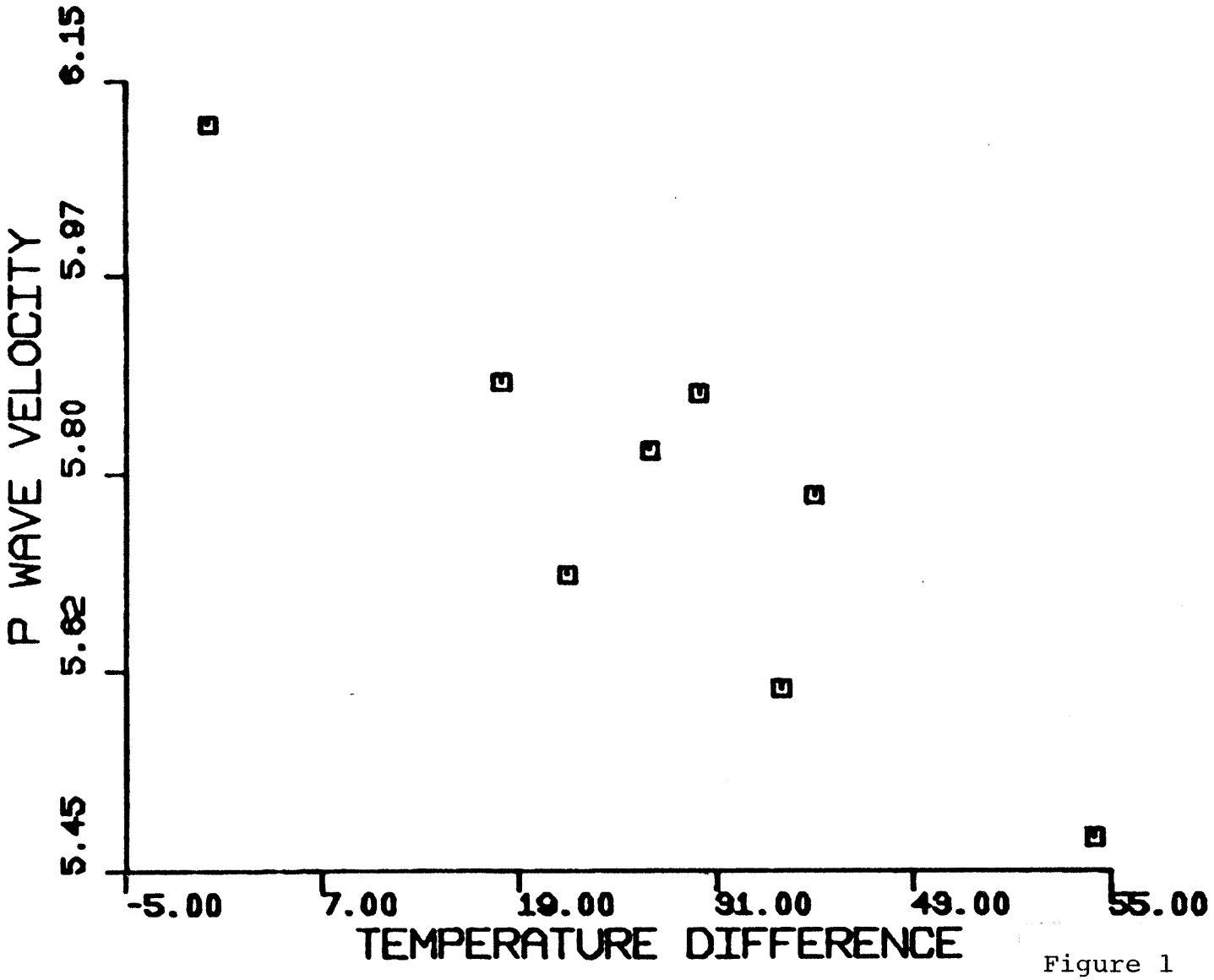
P WAVE VELOCITY
6.15
5.97
5.80
5.62
5.45
-5.00
7.00
19.00
31.00
43.00
55.00
TEMPERATURE DIFFERENCE

Figure 1

REFERENCES

Abo-Zena, Anas, Dispersion function computations for unlimited frequency values, preprint, 1978.

Achenbach, J.D. and A.K. Gautesen, Geometrical theory of diffraction for three-D elastodynamics, J. Acoust.Soc. Am., 61, 413-421, 1977.

Achenbach, J.D., A. Gautesen and H. McMaken, Diffraction of point-source signals by a circular crack, Bull. Seism. Soc. Am., 66, 1501-1523, 1978.

Aki, K., Scattering of P waves under the Montana LASA, J. Geophys. Res., 78, 1334-1346, 1973.

Aki, K., Defining the fractures of the Fenton Hill Hot Dry Rock System, LASL group G-3 internal report #43, 43 pp., 1977.

Aki, K. and B. Chouet, Origin of coda waves: source attenuation and scattering effects, J. Geophys. Res., 80, 3322-3342, 1975.

Aki, K., M. Fehler and S. Das, Source mechanism of volcanic tremor: fluid-driven crack models and their application to the 1963 Kilauea eruption, J. Volcan. Geotherm. Res., 2, 259-287, 1977.

Albright, J.N., Preliminary seismic mapping of the main fracture in GT-2 (abstract), EOS, Trans. Am. Geophys. Union, 57, 349, 1976.

Albright, J.N., Toward characterizing the acoustic response of the Fenton Hill reservoir, LASL group

G-3 internal report #31, 13 pp., 1978.

Albright, J., R. Aamodt, R. Potter and R. Spence, Acoustic methods for detecting water-filled fractures using commercial logging tools, preprint, 1978.

Ang, D.D. and Knopoff, L., Diffraction of scalar elastic waves by a finite crack, Proc. Nat. Acad. Sci., 51, 593-598, 1964a.

Ang, D.D. and Knopoff, L., Diffraction of vector elastic waves by a finite crack, Proc. Nat. Acad. Sci., 52, 1075-1081, 1964b.

Batzle, M., Fracturing and sealing in geothermal systems, Ph.D. thesis, M.I.T., Cambridge, Mass., 1978.

Birch, F., The velocity of compressional waves in rocks to 10 kilobars, Part 2, J. Geophys. Res., 66, 2199-2224, 1961.

Birch, F., Compressibility: elastic constants; in Handbook of Physical Constants, S.P. Clark, ed; Geol. Soc. Am. Mon. 97, 97-173, 1966.

Biswas, Arabinda, The transmission of waves through a layered Voight solid sandwiched between isotropic homogeneous elastic media of some nature, Pageoph. 66, 25-29, 1967.

Blair, A.G., J. Tester and J. Mortensen, ed., LASL Hot Dry Rock Geothermal Project, July 1, 1975 - June 30, 1976, Los Alamos Scientific Laboratory, Los

Alamos, New Mexico, 1976.

Borcherdt, Roger D., Energy and plane waves in linear viscoelastic media, J. Geophys. Res., 78, 2442-2453, 1973.

Brace, W., Pore pressure in geophysics, Flow and Fracture of Rocks, Geophys. Mon. No. 16, John Wiley and Sons, New York, pp. 265-274, 1972.

Brekhovskikh, Leonid M., Waves in Layered Media, Academic Press, New York, 1960.

Bruner, W.M., Comments on "Seismic velocities in dry and saturated cracked solids" by Richard J. O'Connell and Bernard Budiansky, J. Geophys. Res., 81, 2573-2576, 1976.

Budiansky, B. and R. O'Connell, Elastic moduli of dry and saturated cracked solids, Int. J. Solids and Structures, 12, 81-97, 1976.

Burridge, R., The numerical solution of certain integral equations with non-integrable kernals arising in the theory of crack propagation and elastic wave diffraction, Phil. Trans. Roy. Soc. London, 265, 353-372, 1969.

Cheng, C.H., Seismic velocities in porous rocks: direct and inverse problems, Ph.D. thesis, M.I.T., Cambridge, Mass., 1978.

Chernov, L.A., Wave Propagation in a Random Medium, McGraw-Hill, New York, 1960.

Chouet, B., Source scattering and attenuation effects on high frequency seismic waves, Ph.D. thesis, M.I.T., Cambridge, Mass., 1976.

Chouet, B., K. Aki and M. Tsujiura, Regional variation of the scaling law of earthquake source spectra, Bull. Seis. Soc. Am., 68, 49-79, 1978.

Cummings, R.G., G. Morris, J. Tester and R. Bivins, Mining earth's heat: Hot Dry Rock geothermal energy, Technology Review, 81, 58-78, 1979.

Dainty, A. and M.N. Toksöz , Elastic wave propagation in a highly scattering medium - a diffusion approach, J. Geophys., 43, 375-388, 1977.

Das, S. and K. Aki , A numerical study of two-dimensional spontaneous rupture propagation, Geophys. J. Roy. Astr. Soc., 50, 643-668, 1977.

Draper, N. and H. Smith, Applied Regression Analysis, John Wiley and Sons, New York, 1966.

Dunkin, J.W., Computation of modal solutions in layered elastic media at high frequencies, Bull. Seis. Soc. Am., 55, 335-358, 1965.

Ewing, M., W. Jardetzky and F. Press, Elastic Waves in Layered Media, McGraw-Hill, New York, 1957.

Fehler, M. and K. Aki, Numerical study of diffraction of plane elastic waves by a finite crack with application to location of a magma lens, Bull. Seis. Soc. Am., 68, 573-598, 1978.

Gordon, R. and L. Davis, Velocity and attenuation of seismic waves in imperfectly elastic rock, J. Geophys. Res., 73, 3917-3935, 1968.

Gordon, R. and L. Davis, Reply, J. Geophys. Res., 74, 729-730, 1969.

Hadley, K., Dilatancy, Further studies in crystalline rock, Ph.D. thesis, M.I.T., Cambridge, Mass., 1975.

Hadley, K., Comparison of calculated and observed crack densities and seismic velocities in Westerly granite, J. Geophys. Res., 81, 3484-3494, 1976.

Harlow, F. and W. Pracht, A theoretical study of geothermal energy extraction, J. Geophys. Res., 77, 7038-7048, 1972.

Haskell, N.A., The dispersion of surface waves in multilayered media, Bull. Seis. Soc. Am., 43, 17-34, 1953.

Hildebrand, F., Introduction to Numerical Analysis, McGraw-Hill, New York, 1956.

Hill, D., A model for earthquake swarms, J. Geophys. Res., 82, 1347-1352, 1977.

Johnston, D.H., The attenuation of seismic waves in dry and saturated rocks, Ph.D. thesis, M.I.T., Cambridge, Mass., 1978.

Johnston, D.H., M.N. Toksöz and A. Timur, Attenuation of seismic waves in dry and saturated rocks: II.

Mechanisms, Geophysics, 44, 691-711, 1979.

Knopoff, L., A matrix method for elastic wave problems, Bull. Seis. Soc. Am., 54, 431-438, 1964.

Knopoff, L., Q, Rev. Geophys., 2, 625-660, 1964a.

Knopoff, L. and G. MacDonald, Attenuation of small amplitude stress waves in solids, Rev. Mod. Physics, 30, 1178-1192, 1960.

Kuster, G. and M. Toksöz, Velocity and attenuation of seismic waves in two-phase media: Part 1. Theoretical formulations, Geophysics, 39, 587-618, 1974.

LASL HDR Staff, Hot Dry Rock Geothermal energy development project, annual report Fiscal year 1977, Los Alamos Scientific Laboratory, Los Alamos, New Mexico, 1978.

Laughlin, W. and A. Eddy, Petrography and geochemistry of precambrian rock from GT-2 and EE-1, Los Alamos Scientific Laboratory Informal Report, LA-6930-MS, 1977.

Lockner, D. and J. Byerlee, Hydrofracture in Weber sandstone at high confining pressure and differential stress, J. Geophys. Res., 82, 2018-2026, 1977.

Loeber, J.F. and G.C. Sih , Diffraction of antiplane shear waves by a finite crack, J. Acoust. Soc. Am., 44, 90-98, 1968.

Loeber, J.F. and G.C. Sih , Wave propagation in an elastic solid with a line of discontinuity or finite crack, Q. Appl. Math., 27, 193-213, 1969.

Madariaga, R., Dynamics of an expanding circular fault, Bull. Seis. Soc. Am., 66, 639-666, 1976.

Mavko, G.L. and A. Nur, The effect of nonelliptical cracks on the compressibility of rocks, J. Geophys. Res., 83, 4459-4468, 1978.

Mavko, G.M. and A. Nur, Wave attenuation in partially saturated rocks, Geophysics, in press, 1979.

Nur, A. and G. Simmons, The effect of saturation on velocity of low porosity rocks, Earth and Plan. Sci. Lett., 7, 183-193, 1969.

Nur, A. and G. Simmons, The origin of small cracks in igneous rocks, Int. J. Rock Mech. Min. Sci., 7, 307-314, 1970.

O'Connell, R. and B. Budiansky, Seismic velocities in dry and saturated cracked solids, J. Geophys. Res., 79, 5412-5426, 1974.

O'Connell, R.J. and B. Budiansky, Viscoelastic properties of fluid-saturated cracked solids, J. Geophys. Res., 82, 5719-5735, 1977.

Olson, K., Regional seismicity of the Northern Rio Grande Rift and Jemez Mountains, in Memories from APSMAGS Workshop, R.W. Ward, ed., 1978.

Patton, Howard J., Source and propagation effects of

Rayleigh waves from central Asian earthquakes, Ph.D. thesis, M.I.T., Cambridge, Mass., 1978.

Pettitt, R.A., Environmental monitoring for the Hot Dry Rock geothermal energy development project Annual report for the period July 1975 - June 1976, Los Alamos Scientific Laboratory status report, LA-6504-SR, 1976.

Pettitt, R.A., Testing, planning and redrilling of geothermal test hole GT-2, phases IV and V, Los Alamos Scientific Laboratory Progress Report, LA-7586-PR, 1978.

Potter, J., Experimental permeability studies at elevated temperature and pressure of granitic rock, M.S. thesis, University of New Mexico, Albuquerque, N.M., 1978.

Potter, R.M. and B. Dennis, Seismic and fluid pressure response from a series of hydraulic fractures in granite (abstract), EOS, Trans. Am. Geophys. Union, 55, 431, 1974.

Pratt, H.R., H.S. Swolfs, R. Lingle and R. Nielsen, In situ and laboratory measurements of velocity and permeability, in The Earth's Crust: Its Nature and Physical Properties, Geophys. Monogr. Ser., Vol. 20, edited by J. Heacock, A.G.U., Washington, D.C., 215-231, 1977.

Rautian, T., and V. Khalturin, The use of the coda

for determination of earthquake source spectrum, Bull. Seis. Soc. Am., 68, 923-948, 1978.

Sato, H., Energy propagation including scattering effects single isotropic scattering approximation, J. Phys. Earth, 25, 27-41, 1977a.

Sato, H., Single isotropic scattering model including wave conversions. Simple theoretical model of the short period body wave propagation, J. Phys. Earth, 25, 163-176, 1977b.

Savage, J., Thermoelastic attenuation of elastic waves by cracks, J. Geophys. Res., 71, 3929-3938, 1966.

Savage, J.C., Comments on paper by R.B. Gordon and L.A. Davis, "Velocity and attenuation of seismic waves in imperfectly elastic rock," J. Geophys. Res., 74, 726-728, 1969.

Savage, J. and H. Hasegawa, Evidence for a linear attenuation mechanism, Geophysics, 32, 1003-1014, 1967.

Shaw, R.P. and R. Bugl, Transmission of plane waves through layered linear viscoelastic media, J. Acoust. Soc. Am., 46, 649-654, 1968.

Siegfried, R. and G. Simmons, Characterization of oriented cracks with differential strain analysis, J. Geophys. Res., 83, 1269-1278, 1978.

Simmons, G. and H. Cooper, DSA of the microcracks in GT-2 core: interpretation and implications,

contract report to Los Alamos Scientific Laboratory, 1976.

Simmons, G. and H. Cooper, Thermal cycling cracks in three igneous rocks, submitted to J. Geophys. Res., 1977.

Simmons, G. and A. Nur, Granites: relation of properties in situ to laboratory measurements, Science, 162, 789-791, 1968.

Simmons, G. and D. Richter, Microcracks in rocks, in The Physics and Chemistry of Minerals and Rocks, R. Sterns, ed., Wiley, New York, 1976.

Simmons, G., R. Siegfried and M. Feves, Differential strain analysis: a new method for examining cracks in rocks, J. Geophys. Res., 79, 4383-4385, 1974.

Sommerfeld, A., Optics, Academic Press, New York, 1949.

Sprunt, E. and W. Brace, Some permanent structural changes in rocks due to pressure and temperature, Proc. 3rd Congress International Society of Rock Mechanics, Themes 1-2, Vol. II, p. 524-529, 1974.

Summers, R., K. Winkler and J. Byerlee, Permeability changes during fluid flow through hot granite (abstract), EOS, Trans.Am. Geophys. Union, 56, 1060, 1975.

Terzaghi, K., Die Berechnung der Durchassigkeitsziffer

des Tones aus dem Verlauf der hydrodynamischen Spannungsercheinungen, Sitzungsber. Akad. Wis. Wien Math. - Naturviss.kl., Abt 2A, 132, 105, 1923.

Thau, S.A. and T. Lu , Diffraction of transient horizontal shear waves by a finite crack and a finite rigid ribbon, Int. J. Engng. Sci., 8, 857-874, 1970.

Thau, S.A. and T. Lu , Transient stress intensity factors for a finite crack in an elastic solid caused by a dilatational wave, Int. J. Solids Structures, 7, 731-750, 1971.

Thomson, W.T., Transmission of elastic waves through a stratified solid medium, J. Appl. Phys., 21, 89-93, 1950.

Toksöz, M.N., C.H. Cheng and A. Timur, Velocities of seismic waves in porous rocks, Geophysics, 41, 621-645, 1976.

Trice, R. and N. Warren, Preliminary study on the correlation of acoustic velocity and permeability in two granodiorites from the LASL Fenton Hill deep borehole, GT-2, near the Valles Caldera, New Mexico, Los Alamos Scientific Laboratory Report LA-6851-MS, 1977.

Walsh, J.B., The effects of cracks on the compressibility of rock, J. Geophys. Res., 70, 381-389,1965.

Walsh, J., Seismic wave attenuation in rock due to friction, J. Geophys. Res., 71, 2591-2599, 1966.

Walsh, J.B., Attenuation in partially melted material, J. Geophys. Res., 73, 2209-2216, 1968.

White, J.E., Seismic waves; radiation, transmission and attenuation, McGraw-Hill, New York, 302 pp., 1965.

Winkler, K. and A. Nur, Pore fluids and seismic attenuation in rocks, preprint, 1979.

Winkler, K., A. Nur and M. Gladwin, Friction and seismic attenuation in rocks, Nature, 277, 528-531, 1979.

Zener, Clarence, Elasticity and Anelasticity of Metals, Univ. of Chicago Press, Chicago, Ill., 1948.

Appendix A Finite Difference Method

Rather than trying to solve a second order differential equation by a finite difference method to obtain the solution of the wave equation in two dimensions for a crack problem Madariaga (1976) solves an equivalent system of first order equations. The procedure developed by Madariaga gives solutions for stress and particle velocities. There are two advantages with this approach when solving crack problems: (1) boundary conditions are given in terms of stress and displacement which are easily adapted to the numerical scheme, and (2) numerical integration of velocities yields a displacement function which is very smooth - also velocities are essential for computation of far-field radiation.

The set of first order equations that is equivalent to the equation of motion in two dimensions with no body forces is:

$$\begin{aligned}
\dot{\tau}_{yy} &= \lambda\left(\frac{\partial \dot{u}}{\partial x} + \frac{\partial \dot{v}}{\partial y}\right) + 2\mu\frac{\partial \dot{v}}{\partial y} \\
\dot{\tau}_{xx} &= \lambda\left(\frac{\partial \dot{u}}{\partial x} + \frac{\partial \dot{v}}{\partial y}\right) + 2\mu\frac{\partial \dot{u}}{\partial x} \\
\dot{\tau}_{xy} &= \mu\left(\frac{\partial \dot{u}}{\partial y} + \frac{\partial \dot{v}}{\partial x}\right) \qquad \text{(A1)} \\
p\ddot{u} &= \frac{\partial}{\partial x}\tau_{xx} + \frac{\partial}{\partial y}\tau_{xy} \\
p\ddot{v} &= \frac{\partial}{\partial x}\tau_{xy} + \frac{\partial}{\partial y}\tau_{yy}
\end{aligned}$$

where λ, μ are Lame's constants.

We solve the above equation by a finite difference method using a staggered grid method. Velocities are defined at times $k\Delta t$ and stresses at times $(k + 1/2)\Delta t$. The cell whose corner is

at $n\Delta x$, $m\Delta y$ is arranged so that $\dot{u}$ is defined at position $n\Delta x$, $m\Delta y$, $\dot{v}$ at $(n + 1/2)\Delta x$, $(m + 1/2)\Delta y$; τ_{xx} and τ_{yy} at position $(n + 1/2)\Delta x$, $m\Delta y$ and τ_{xy} is defined at position $n\Delta x, (m + 1/2)\Delta y$. This arrangement is shown in Figure 1.

Define $\dot{u}(n,m,k)$ to be the particle velocity in the x-direction at position $n\Delta x$, $m\Delta y$ and time $k\Delta t$. Derivatives are replaced by the following central difference operations.

$$\frac{\partial}{\partial t}\dot{u}(n,m,k+1/2) \rightarrow \frac{1}{\Delta t}\{\dot{u}(n,m,k+1)-\dot{u}(n,m,k)\}$$

$$\frac{\partial}{\partial x}\dot{u}(n+\tfrac{1}{2},m,k) \rightarrow \frac{1}{\Delta x}\{\dot{u}(n+1,m,k)-\dot{u}(n,m,k)\} \equiv \frac{1}{\Delta x}\delta_x\dot{u}(n+\tfrac{1}{2},m,k) \qquad (A2)$$

$$\frac{\partial}{\partial y}\tau_{xy}(n,m+1,k+\tfrac{1}{2}) \rightarrow \frac{1}{\Delta y}\{\tau_{xy}(n,m+\tfrac{3}{2},k+\tfrac{1}{2})-\tau_{xy}(n,m+\tfrac{1}{2},k+\tfrac{1}{2})\} \equiv \frac{1}{\Delta y}\delta_y\tau_{xy}(n,m+1,k+\tfrac{1}{2})$$

Defining $H \equiv \frac{\Delta t}{\Delta x} = \frac{\Delta t}{\Delta y}$ as the time-space ratio of the grid, the numerical equivalent of (A1) is

$$\rho\dot{u}(n,m,k+1) = \rho\dot{u}(n,m,k)+H\{\delta_x\tau_{xx}(n,m,k+\tfrac{1}{2})+\delta_y\tau_{xy}(n,m,k+\tfrac{1}{2})\}$$

$$\rho\dot{v}(n+\tfrac{1}{2},m+\tfrac{1}{2},k+1) = \rho\dot{v}(n+\tfrac{1}{2},m+\tfrac{1}{2},k)+H\{\delta_x\tau_{xy}(n+\tfrac{1}{2},m+\tfrac{1}{2},k+\tfrac{1}{2})+\delta_y\tau_{yy}(n+\tfrac{1}{2},m+\tfrac{1}{2},k+\tfrac{1}{2})\}$$

$$\tau_{yy}(n+\tfrac{1}{2},m,k+\tfrac{1}{2}) = \tau_{yy}(n+\tfrac{1}{2},m,k-\tfrac{1}{2})+\lambda H\delta_x\dot{u}(n+\tfrac{1}{2},m,k)+(\lambda+2\mu)H\delta_y\dot{v}(n+\tfrac{1}{2},m,k)$$

$$\tau_{xx}(n+\tfrac{1}{2},m,k+\tfrac{1}{2}) = \tau_{xx}(n+\tfrac{1}{2},m,k-\tfrac{1}{2})+\lambda H\delta_y\dot{v}(n+\tfrac{1}{2},m,k)+(\lambda+2\mu)H\delta_x\dot{u}(n+\tfrac{1}{2},m,k)$$

$$\tau_{xy}(n,m+\tfrac{1}{2},k+\tfrac{1}{2}) = \tau_{xy}(n,m+\tfrac{1}{2},k-\tfrac{1}{2})+\mu H\{\delta_y\dot{u}(n,m+\tfrac{1}{2},k)+\delta_x\dot{v}(n,m+\tfrac{1}{2},k)\}$$

Stability and dispersion of the numerical solution have been discussed by Madariaga and reference is made to his paper. He finds the condition for stability is

$$H \leq 1/\sqrt{2}\alpha$$

which is the usual result for a two-dimensional wave equation. Study of the dispersion relation shows that the continuum dispersion relation w = kc, k = wave number, is obtained for wavelengths where there are at least 5 cells per wavelength. Waves are dispersive for higher frequencies.

Various tests of the validity of this leap-frog finite difference scheme have been made by Madariaga and in the course of the present study. Some of these tests have been discussed in the text.

Special considerations are necessary to satisfy the boundary condition for a fluid filled crack because this condition involves displacement and not velocity. Since v^d is antisymmetric when solving the problem defined by equation (1) we may write (2-51) as

$$\dot{\tau}_{yy}(n+\tfrac{1}{2},0,k) = \frac{\kappa}{d}\Delta\dot{v}^d(n+\tfrac{1}{2},0,k) = \frac{2\kappa}{d}\dot{v}^d(n+\tfrac{1}{2},0,k)$$

This can be re-written using (A2) as

$$\tau_{yy}(n+\tfrac{1}{2},0,k+\tfrac{1}{2}) = \tau_{yy}(n+\tfrac{1}{2},0,k-\tfrac{1}{2}) + \frac{2\kappa}{d}\Delta t\ \dot{v}^d(n+\tfrac{1}{2},0,k)$$

This gives a procedure for applying the boundary condition for a fluid filled crack. There is a slight error introduced by this procedure since $\dot{v}^d$ is computed at $y = \frac{1}{2}\Delta y$, not y=0. This error is considered to be negligible since there was little difference between analytic and numeric computations for the problem of P wave normally incident in a fluid layer as is discussed in the text.

Figure Caption

Figure 1. The finite difference grid used to obtain the numerical solution to the diffraction problem in Chapter 2. The grid is staggered in time so that stresses are defined at times $(k + \frac{1}{2})\Delta t$ and particle velocities are defined at $k\Delta t$.

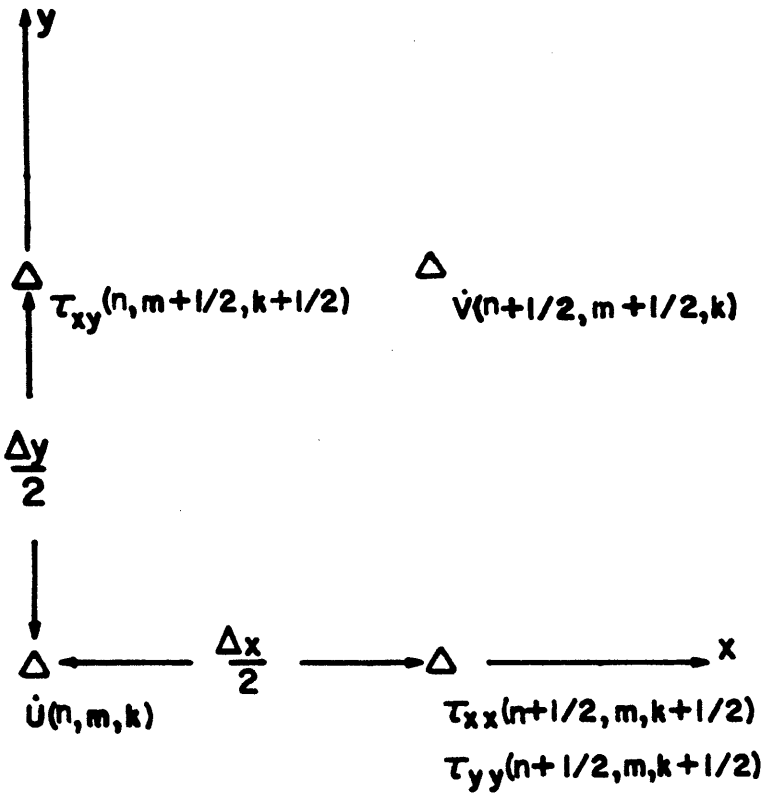

STRESS AT TIME $(K+1/2)\Delta T$

VELOCITY AT TIME $K\Delta T$

Figure 1

Appendix B

Method of picking arrival times

First arrival times for P waves were picked with a computer program designed specifically to work for the type of data obtained in the dual well seismic experiment. Computer picking of arrival times was possible because most of the first arrivals were of the same frequency throughout the experiment. Rather than trying to measure the first arrival time of the P wave at the point where there is an obvious break in the signal from noise to a coherent signal, I chose to pick the time of the first minima in the seismic signal. This should introduce at most a 1/2 period error in arrival time which will be consistent throughout the experiment provided that the character of the first wave pocket does not change a great deal. Since the frequency of the signal is approximately 12 KHz, a 1/2 cycle error in origin time amounts to an error of about .04 milliseconds out of a total travel time of greater than 2.5 milliseconds.

The first arrival will be defined as the first minimum in the seismic signal on the trace. This will also be referred to as the first minimum. The peak or maximum that follows the first minimum (by about .04 milliseconds) will be called the first

maximum.

A brief description of the algorithm used to pick first arrival time on seismograms recorded in GT-2 will now be given. The actual program evolved through a "learning process". Modifications were made to an original program as problems arose. The program contains a number of parameters which can be adjusted for various sets of data.

First, we need to define acceptable standards for a point to be a first arrival and then write a computer program to check points in a signal to see if they meet the standards defined. Definition of a first arrival consists of the following:

(1) The point must be a relative minimum point of the signal - i.e. amplitude of the signal both forwards and backwards in time from the first arrival must be larger in value than the first arrival.

(2) The first arrival must fall at a point in time greater than some predetermined time. This predetermined time is the same for all data for one step of the experiment. The time was chosen by visual inspection of the seismic traces.

(3) The frequency of the first arrival must be greater than about 10 KHz. This frequency was varied for different sets of data.

(4) Signal to noise level of the first arrival must be

of a certain level. Signal to noise was checked in two ways; (a) compute the standard deviation of five sets of data each consisting of 6 consecutive points (period of most first arrivals) using points of the signal that occur before the first P arrival. Each set of six points began with a relative minimum point. The average value of the standard deviation of these five sets of data was computed. The standard deviations of the first arrival and the next five points must exceed the value of the average standard deviation of the five sets of data by a given factor. In addition, the standard deviation of sets of points beginning with the three relative minima after the first arrival must exceed the average value of the original five sets of data. (b) The amplitude of the first maximum after the first arrival must be greater than a weighting factor times the amplitude of the first maximum of the preceding seismograms in the same step. (5) The change of arrival times from seismogram to seismogram was checked. The first arrival time was not allowed to vary by more than about .04 milliseconds from one seismogram to the next seismogram. Since the speed of the seismic source was about 20 feet/min and the time between successive seismograms 400 milliseconds, the difference in source positions is less than 4 cm (.133 feet). It seems reasonable to assume that a

difference in source location of this size would not effect the travel time by greater than .04 milliseconds.

Each seismogram is checked for a point that satisfies the above criteria. If no point is found, the requirements are modified slightly and the signal is checked again. If no arrival is found after a sequence of modifications to the criteria for a first arrival, a no reading code is signalled and the next seismogram is processed. There were typically less than 5 no reading codes triggered for each 1000 seismograms examined. Parameters were defined to indicate how severely the initial first arrival criteria had to be modified before a first arrival was found. Most arrivals were picked with little modification of the original criteria.

The first arrivals for each step were plotted as a function of position along the wellbore in order to visually inspect the data. Once this plot was made, the overall quality of the first arrival picks could be judged. Usually the plot consisted of regions where arrivals read on successive seismograms fell very close to each other as well as regions where arrival times varied drastically from seismogram to seismogram. This large variation was considered to be the result of bad first arrival picks due to poor quality of the seismograms. Data from these regions

were omitted from further analysis unless minor adjustments in the criteria to pick first arrivals could be made and the seismograms successfully reprocessed. The data that is inverted for velocity and plotted in Chapter 4 represents the data that was considered to be of sufficiently good quality to justify further analysis. This data contained a few picks of arrival times that were significantly different from the seismogram preceding or following the "bad pick." In these cases, less than 10 out of 1000, the bad picks were changed to follow the trend of the other data.

As a final check on the arrival times chosen by the program, a few of the times were checked against plots of the seismograms. The arrival times could be picked visually to within about ±.04 milliseconds. The error in the position of the first minimum chosen by the computer algorithm is .01 milliseconds provided the correct minimum is chosen. The arrivals chosen by computer agreed well with those found from the plots of the seismograms.

Appendix C

Damped Least Squares Inversion

It is often found that the matrix A^TA in equation 7, Chapter 4 is singular or nearly singular. To investigate the case, begin by rewriting (6), Chapter 4, as

$$A^TY = (A^TA)x \qquad (1)$$

The matrix A^TY is an (M+N) by 1 matrix which will be called D. This matrix is composed of linear combinations of the data. Matrix A^TA is an (N+M) by (M+N) square matrix which will be renamed B. If B is non-singular a set of (M+N) independent vectors of length (N+M) can be found that satisfy

$$BQ_k = \lambda_k Q_k \qquad k=1,2....M+N \qquad (2)$$

The Q_k are called the eigenvectors of B and the λ_k are the associated eigenvalues. Since the Q_k are linearly independent they span the (M+N) dimensional vector space which means that any M+N vector can be written as a linear combination of the Q_k's. In particular X and D can be written as linear sums of the Q_k's.

$$X = \sum_k \alpha_k Q_k$$

$$D = \sum_k \beta_k Q_k \qquad (3)$$

From (1)

$$B \sum_k \alpha_k Q_k \equiv B\,x = D = \sum_k \beta_k Q_k \qquad (4)$$

Using (2)

$$B \sum_k \alpha_k Q_k = \sum_k \alpha_k B Q_k = \sum_k \alpha_k \lambda_k Q_k = \sum_k \beta_k Q_k \qquad (5)$$

Since the Q_k are linearly independent, equation (5) may be reduced to (M+N) equations, one for each value of k

$$\alpha_k \lambda_k Q_k = \beta_k Q_k \qquad (6)$$

The right hand side of equation (6), which is the part of D which is parallel to the Q_k vector, will be called D_k. The part of X that is parallel to the vector Q_k is given by $\alpha_k Q_k$. The goal is to find the value of $\alpha_k Q_k$, the k^{th} component of our model or solution, once D_k which is the k^{th} component of data is known. In principle the solution is given by

$$X_k = \alpha_k Q_k = \frac{\beta_k Q_k}{\lambda_k} = \frac{1}{\lambda_k} D_k \qquad (7)$$

Consider the case where the data D contains errors so that $D = D_o + \Delta D$ where ΔD is the error in the data. The error in the k^{th} component of the model resulting from an error in the k^{th} component of data is given by

$$\Delta X_k = \frac{1}{\lambda_k} \Delta D_k \qquad (8)$$

If matrix B is nearly singular then one or more of the values of λ_k will be much smaller than the other values. Since the model vector ΔX_k is related to the data vector by the inverse of the eigenvalue, these small values of λ_k have the effect of introducing large errors in the resulting model due to small errors in the data. In order to decrease the effect of the error in the predicted model resulting from error in the data, a small positive quantity, ε^2, is added to each diagonal element of the matrix B. This has the effect of increasing each of the eigenvalues of A^TA by an amount ε^2. For large eigenvalues, the effect is negligible and, by (8), the changes in the model resulting from the additions of ε^2 are small. For small eigenvalues, the changes in values are large and the result will be to significantly decrease the

value of the X_k associated with the small eigenvalues. The net effect of adding ε^2 to each eigenvalue is to produce a poorer fit of the model to the data but at the same time the predicted error in the model resulting from errors in the data is decreased. To quantify these motions define the resolution matrix, R, and covariance matrix, C.

$$R = (B + \varepsilon^2 I)^{-1} B$$

$$C = \langle \Delta X \, \Delta\tilde{X} \rangle = \langle (B + \varepsilon^2 I)^{-1} \Delta D B \Delta\tilde{D} \, (B + \varepsilon^2 I)^{-1} \rangle \tag{9}$$

$$= (B + \varepsilon^2 I)^{-1} \Delta D B \Delta\tilde{D} \, (B + \varepsilon^2 I)^{-1}$$

The resolution matrix provides a measure of how close the inverse matrix, $(B + \varepsilon^2 I)^{-1}$ is to the true least squares inverse B^{-1}. If $\varepsilon^2 = 0$ the resolution matrix will be the identity matrix. The covariance matrix is a measure of how much the error in the data produces error in the model. If it is assumed that the components of the data vector, D, are statistically independent and share the same variance, σ^2, then

$$C = \sigma^2 (B + \varepsilon^2 I)^{-1} B (B + \varepsilon^2 I)^{-1} \tag{10}$$

This calculation of C enables one to place bounds on

possible models to fit the data. The inverse $(B + \varepsilon^2 I)^{-1}$ is called the damped least squares inversion of matrix B.

The eigenvalues of matrix $A^T A$ (see equation 8, Chapter 4) were typically in the range of 8×10^{-2} to 8×10^{2}. This large range of eigenvalues justifies use of the damped least squares inversion technique. The smallest eigenvalue corresponds to the model parameter giving the distance between the wellbores. In order to reduce the predicted error for the computed wellbore spacing, a value of .05 was chosen for ε^2. The result is a decrease by a factor of about 2 in the predicted error in wellbore spacing from the error predicted if ε^2 is chosen to be 0.

Biographical Note

The author spent his early days in Seattle and Tacoma, Washington before finally settling down in Portland, Oregon. Caught by the pioneering spirit of the early manned space flights, he decided to try to find his way into the aviation field and entered Benson Polytechnic High School with that as his goal. A couple of years of study of airplanes cured him of his fascination with aeronautics and he entered Pacific Lutheran University in Tacoma, Washington to study mathematics. After being convinced that physics would be a more interesting pursuit, the author transferred in 1971 to Reed College, that beatnick school less than a mile from his Portland home. During high school and college, the influence of the many beautiful ranges of mountains of the Northwest provied to be very strong. Much of his spare time was spent with pack on back, hiking along trails taking in the scenery that the mountains offer. Lacking great enthusiasm for the frontiers of physics, he looked for another field to study as a natural extension of his love of mountains and decided upon Geophysics. Family and friends convinced him that Boston would be a livable city so he moved from Northwest to Northeast to study at M.I.T. After leaving M.I.T., the author will join the faculty at the School of Oceanography at Oregon State University,

back in his home state.

Publications

Aki, K., M. Fehler and S. Das, Source mechanism of volcanic tremor: fluid driven crack models and their application to the 1963 Kilauea eruption, J. of Volcanology and Geothermal Research, 2, 259-287, 1977.

Aki, K., B. Chouet, M. Fehler, G. Zandt, R. Koyanagi, J. Colp and R. Hay, Seismic properties of a shallow magma reservoir in Kilauea Iki by active and passive experiments, J. Geophys. Res., 83, 2273-2282, 1978.

Fehler, M. and K. Aki, Numerical study of diffraction of plane elastic waves by a finite crack with application to location of a magma lens, Bull. Seism. Soc. Am., 68, 573-598, 1978.